The Development of Molecular Precursors for the Atomic Layer Deposition of Tin Monoxide and Related Studies

Parish, James

Award date:
2019

Awarding institution:
University of Bath

The Development of Molecular Precursors for the Atomic Layer Deposition of Tin Monoxide and Related Studies

James D. Parish

A thesis submitted for the degree of Doctor of Philosophy

University of Bath

Department of Chemistry

October 2018

Contents

Chapter 2

Chapter 3

Acknowledgements

It goes without saying that one person above all is most deserving of acknowledgement. Words cannot express my thanks to Dr Andrew Johnson, the man that took me on in the summer of 2013 and has yet to see the back of me. Your boundless wisdom and bottomless (and at times groundless) optimism has made the last five years some of the best of my life. As both a mentor and friend, thank you.

In a similar vein, I offer my thanks to the Johnson group (and related baggage) past and present: Sam, Ibbi, Joe, Andrew, Jeff, Dave, Jerome, Kerry, Hannah, Emily, Matt, Prem and Pete. I can't think of any people I would rather have worked alongside and consider all of you firm friends. I would also like to thank Michael Snook, who spent far too long having to do what I told him to.

My thanks must also go to those who made this work possible. I would like to thank John Lowe and Catherine Lyall for their tireless assistance with NMR, Mary Mahon and Gabriele Kociok-Köhn for their help with crystallography, and Remí Castaing and Shaun Reeksting for help with CCAF instrumentation. I would also like to thank everyone at PragmatIC Printing Ltd. and Dr Kham Niang for their help with electrical characterisation, alongside Dr David Morgan, Dr Mark Light and Chris Amey for assistance with XPS and XRR characterisation. I also owe a debt of gratitude to all the support staff – porters and stores staff, including Dave and Sarah Elkins, Lesley and Martin. Your behind the scenes work keeps us all afloat.

And finally, to my friends, parents, brothers – especially Robert – and grandparents, thank you for supporting this foolish endeavour. And Hannah, thank you for all your support and for accepting without question all the weekends, evenings and early mornings that have gone into this.

Declaration

The work contained within this thesis was conducted by the author at the University of Bath between October 2014 and October 2018. It represents the author's own work, except where specific reference is made to the contrary. This thesis does not exceed the prescribed limit, including tables, references and appendices.

Abstract

The research outlined within this report sought to achieve a number of objectives. Until recently, a single precursor existed within the literature for the atomic layer deposition (ALD) of tin(II) oxide. Subsequently, a second precursor has been reported, though this later process was demonstrably flawed and far inferior to that of the initial report.

With such a paucity of literature precedent, the main focus of this investigation in the first instance was to replicate the aforementioned ALD process on a commercially viable ALD tool, and through doing so gain a greater understanding of the nature of the deposition process and the effect of precursor properties on their efficacy. Concurrently, work set out on the development of a novel precursor to tin(II) oxide films that demonstrated greater efficiency, economy, ease of synthesis and commercial viability.

Chapter 2: Tin(II) Aminoalkoxides

The first body of work undertaken sought to explore the properties of the reported tin(II) oxide precursor, synthesising a range of related systems in order to elucidate the subtle effects of steric and electronic influences on the structure and reactivity of precursor systems.

Four related pro-ligands were reacted to give a variety of homo- and heteroleptic complexes, displaying a range of interesting properties, and were compared with interesting results to the established ALD precursor, which was for the first time fully characterised during the process. Simultaneous deposition investigations with the published precursor succeeded in replicating and improving the reported ALD process, allowing for a standard process for SnO deposition to be used to benchmark any novel precursor systems that may be identified within further research.

Chapter 3: Tin(II) Aminoamides

The second body of work details the synthesis and characterisation of a range of tin(II) amide systems as possible ALD precursor candidates. These demonstrated a range of interesting chemistries and identified patterns in reactivity and stability within reactive tin(II) systems. Consequently, viable precursor candidates were identified, and the resulting depositions characterised. Additionally, investigations were made into the deposition of tin(II) oxide onto graphitic substrates.

Chapter 4: Tin(II) Alkoxides

In an attempt to build on the understanding of tin(II) alkoxide precursors developed in Chapter 2, a range of simpler tin(II) systems, both novel and known, were synthesised, characterised and their ALD efficacy explored. This investigation into a hitherto overlooked application for simple tin(II) systems gives an interesting platform for further research.

Chapter 5: Tin(II) Pyrrolides

With the capabilities of tin(II) amide systems indicated previously within the investigation, alterations were made to the ligand environments in attempts to improve a number of properties. Results detailing the structural and thermal characterisation of a series of Sn(II) pyrrolides were collated and submitted for publication within the RSC journal *Dalton Transactions*, and are presented in their accepted form, with changes made to formatting.

List of Complexes

Chapter 2

(1) **$[Sn(OCH_2CH_2NMe_2)_2]$**

(2) **$[Sn(OCH_2CH_2NMe_2)N(SiMe_3)_2]$**

(3) **$[Sn(OCH_2CH_2NMe_2)NMe_2]$**

(4) **$[Sn\{OCH(Me)CH_2NMe_2\}_2]$**

(5) **$[Sn\{OCH(Me)CH_2NMe_2\}N(SiMe_3)_2]$**

(6) **$[Sn\{OCH(Me)CH_2NMe_2\}NMe_2]$**

(7) **$[Sn\{OC(Me)_2CH_2NMe_2\}_2]$**

(8) **$[Sn\{OC(Me)_2CH_2NMe_2\}N(SiMe_3)_2]$**

(9) **$[Sn\{OC(Me)_2CH_2NMe_2\}NMe_2]$**

(10) **$[Sn\{OC(CF_3)_2CH_2NMe_2\}_2]$**

(11) **$[Sn\{OC(CF_3)_2CH_2NMe_2\}N(SiMe_3)_2]$**

(12) **$[Sn\{OC(CF_3)_2CH_2NMe_2\}NMe_2]$**

Chapter 3

(13) **$[Sn(MeNCH_2CH_2NMe_2)NMe_2]$**

(14) **$[Sn(MeNCH_2CH_2NMe_2)_2]$**

(15) **$[Sn(EtNCH_2CH_2NMe_2)NMe_2]$**

(16) **$[Sn(EtNCH_2CH_2NMe_2)_2]$**

(17) **$[Sn(MeNCH_2CH_2NEt_2)NMe_2]$**

(18) **$[Sn(MeNCH_2CH_2NEt_2)_2]$**

(19) **$[Sn(C_6H_5CH_2NCH_2CH_2NMe_2)NMe_2]$**

(20) **$[Sn(C_6H_5CH_2NCH_2CH_2NMe_2)_2]$**

(21) **$[Sn\{dippNC(NMe_2)Ndipp\}(EtNCH_2CH_2NMe_2)]$**

Chapter 4

(22) **$[Sn\{OCH(Me)_2\}_2]$**

(23) **$[Sn\{OC(Me)_3\}_2]$**

(24) **$[Sn\{OCH(Me)Et\}_2]$**

(25) **$[Sn\{OCH(Me)CH(Me)_2\}_2]$**

(26) **$[Sn\{OC(Me)_2Et\}_2]$**

(27) **$[Sn\{OCH(CF_3)_2\}_2]$**

(28) **$[Sn\{OC(CF_3)_3\}_2]$**

(29) **$[Sn\{OCH(Me)CH_2NMe_2\}_2]$**

(30) **$[Sn\{OC(Me)_2CH_2NMe_2\}_2]$**

Chapter 5

(31*)/1 **$[Sn\{C_5H_3CH_2NMe_2\}N(SiMe_3)_2]$**

(32*)/2 **$[Sn\{C_5H_3CH_2NMe_2\}_2]$**

(33*)/3 **$[Sn\{C_5H_3CHNMe\}_2]$**

(34*)/4 **$[Sn\{C_5H_3CHNEt\}_2]$**

(35*)/5 **$[Sn\{C_5H_3CHNC(Me)_3\}_2]$**

(36*)/6 **$[Sn\{C_5H_3CHNCH(Me)Et\}_2]$**

(37*)/7 **$[Sn\{C_5H_3CHNCH_2CH_2CH_2Me\}_2]$**

(38*)/8 **$[Sn\{C_5H_3CHNC(dipp)\}_2]$**

*Complexes within this chapter have been named as published (**1**-**8**), in addition to be ascribed number consistent with this work (**31**-**38***)

Lists of Figures, Schemes, Equations and Tables

Abbreviations

IC	-	Integrated Circuit
TFT	-	Thin-film Transistor
FET	-	Field-Effect Transistor
IGFET	-	Insulated Gate Field Effect Transistor
MOSFET	-	Metal Oxide Semiconductor Field-Effect Transistor
NMOS	-	n-Type Metal Oxide Semiconductor (Transistor)
CVD	-	Chemical Vapour Deposition
AA-CVD	-	Aerosol-Assisted Chemical Vapour Deposition
LP-CVD	-	Low-Pressure Chemical Vapour Deposition
AP-CVD	-	Atmospheric-Pressure Chemical Vapour Deposition
PA/E-CVD	-	Plasma Assisted/Enhanced Chemical Vapour Deposition
MO-CVD	-	Metal-organic Chemical Vapour Deposition
PVD	-	Physical Vapour Deposition
ALD	-	Atomic Layer Deposition
VW	-	Volmer-Weber (Growth)
FM	-	Frank van-der-Merwe (Growth)
SK	-	Stranski-Krastanov (Growth)
NMR	-	Nuclear Magnetic Resonance
XRR	-	X-ray Reflectivity
XRD	-	X-ray Diffraction
PXRD	-	Powder X-Ray Diffraction
e.s.d.s.	-	Estimated Standard Deviations
TGA	-	Thermogravimetric Analysis
UV-Vis	-	UV-Visible
FE-SEM	-	Field-Emission Scanning Electron Microscopy
TEM	-	Transmission Electron Microscopy
XPS	-	X-ray Photoelectron Spectroscopy
EDX	-	Energy-Dispersive X-ray Spectroscopy
AFM	-	Atomic Force Microscopy
RMS	-	Root Mean Square
M	-	Metal
GO	-	Graphene Oxide
MG	-	Monolayer Graphene
Si	-	Silicon
SiO_2	-	Silicon Oxide (wafer)
Py	-	Pyrrole
Dipp	-	2,6-diisopropylphenyl
Bn	-	Benzyl

Ph	-	Phenyl
Me	-	Methyl
Et	-	Ethyl
^{t}Bu	-	Tert-butyl
^{s}Bu	-	Sec-butyl
^{i}Pr	-	Isopropyl
^{Fi}Pr	-	Hexafluoro isopropyl
^{Ft}Bu	-	Nonafluoro tert-butyl

Chapter 1

Chapter 1: Introduction

1.1. Preface

Michael Faraday's 1832 observation of the increasing conductivity of silver sulfide with temperature heralded the initial characterisation of an effect which would underpin one of the greatest technological revolutions since the internal combustion engine. The subsequent leveraging of the "semiconductor effect" within the first transistor in 1947, followed by its application just over a decade later into the first integrated circuits, marked an inflection point in a technology that would shortly emerge to be an indispensable pillar of 21st century society.[1]

Semiconducting devices, and in particular integrated circuitries, have permeated almost every aspect of modern-day life, emerging as the cornerstones of economies, medicine, telecommunications and, of course, science and computing. The explosive trajectory of the semiconductor industry led to a valuation of over $340 billion in 2017[2] – a value entirely dwarfed by the market for their applications, and by the intangible scale of their impact over the last 60 years.

This trajectory is set to continue, with the rise of the "Internet of Things (IoT)" set to be a key driver for growth. Within this, the demand for low power, low cost devices that are both flexible and transparent, provides substantial challenges for device manufacturers. Conventional technologies, with established footings in silicon-based semiconducting materials, have significant limitations in these regards, and attention is increasingly being directed to metal-oxides as the key enabling materials for the next generation of electronics.

1.2. Semiconducting Materials

1.2.1. An Introduction to Semiconductor Physics

Before the direct implications of the research undertaken within this report can be properly understood, it is necessary to have a cursory understanding of the fundamental physics behind semiconducting materials. Whilst the research carried out is of a primarily chemical and materials nature, the overarching objective is the deposition of a material of great importance to the semiconductor industry.

Metallic bonding is favoured by a large majority of the elements within the periodic table, disseminating from the alkali metals and extending towards the noble gases. As such, metallic elements tend to consist of a strong core of electronic structure with the presence of a number of more loosely-bound valence electrons. Building on this, metallic structures involve large numbers of adjacent atoms in largely non-directional positions, and with such large "coordination" numbers and few valence electrons, it can be postulated that bonding between ionic cores occurs somewhat uniformly. Testament to this is the malleability displayed by metallic structures contrasting sharply with the more brittle nature of ionic materials.[3] The conductivity of metals can be attributed to the continuous flow of electrons through overlapping, energetically similar atomic orbitals. This structure is a key feature of *band theory*, in which a *band* comprises a collection of energetically similar atomic orbitals, such that an effectively continuous and non-quantised variation of energy is possible within it.[4] A distinctive feature of metallic bonding is the decrease in conductivity observed as temperature increases. This is a phenomenon caused by the increased probability of collisions between electrons and vibrating atoms at elevated temperatures.[5,6]

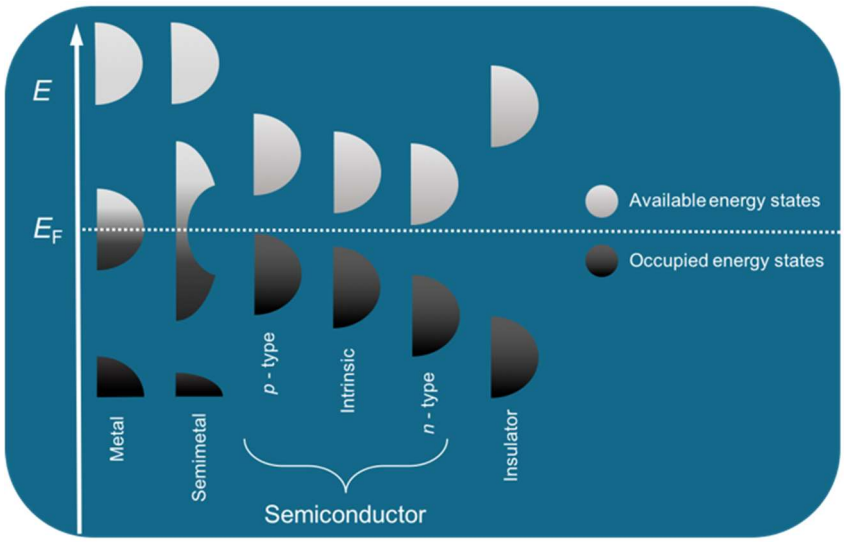

Figure 1.1 – Simplified band structures of an insulator (a), a metal (b), a metal (c), and a semiconductor.

Figure 1.1 depicts simplified band structures within metallic, semimetallic, insulating and semiconducting materials. Conduction is only possible within band structures wherein there is the ability for electrons or holes (electron vacancies) to flow. As such, conduction only occurs within materials where either the valence or conduction band is partially filled. Within metals, the valence and conduction bands are coincident and partially filled, allowing for conductivity to occur, whilst in semimetals, the two bands are close enough in energy for overlap to result in a similar structure to that of metallic materials.[6] Conversely, insulating materials consist of filled valence bands, with a large energetic separation, or "band gap", between valence and conduction bands. Residing within the band-gap of materials is the Fermi level, which for the purposes of semiconducting materials is defined as the energy at which there is an 50% probability of occupancy by an electron.[4,7]

Within intrinsically semiconducting materials, the band gap between valence and conduction bands is sufficiently narrow as to permit facile promotion of electrons into the conduction band, leaving behind holes within the valence band. As such, conductivity is permitted through both the conduction and valence bands, permitted by the presence of electrons and holes respectively. Concordantly, as promotion of electrons to the conduction band is increased, conductivity is also increased. Examples of intrinsic semiconducting materials include cubic tin (α-Sn), an interesting single element structure with a zinc-blende structure wherein a band gap of 8 kJmol^{-1} affords conductivity at room temperature.[4,8]

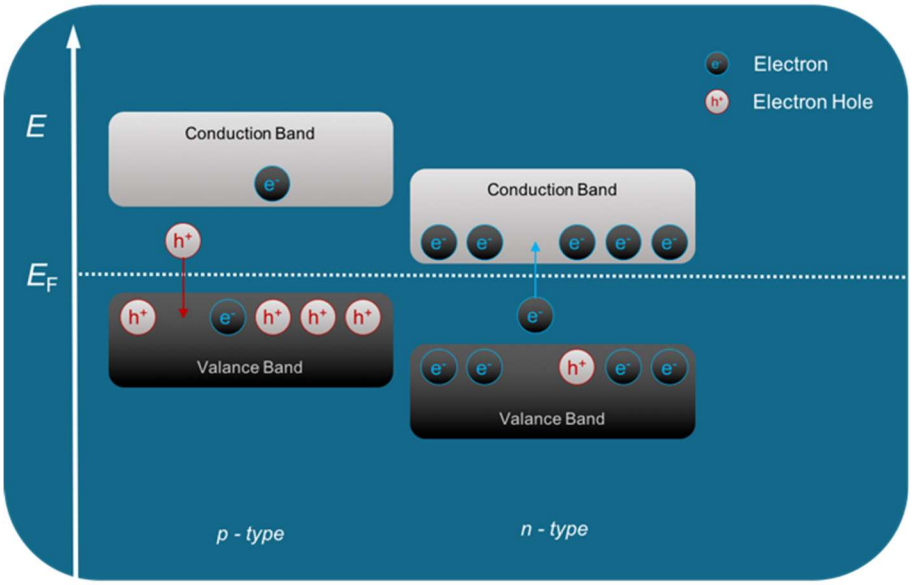

Figure 1.2 – Simplified band structures with p-type and n-type materials.

The presence of defects can significantly alter the electrical properties of semiconducting materials. In its most basic sense, "band gap engineering" entails the addition of dopant elements into the structures of semiconducting materials. This is most commonly achieved by

the incorporation of elements from neighbouring periodic groups forming “extrinsic” semiconductors, though it is also readily achieved through changes in material stoichiometry. More complex routes include the formation of multilayer materials or other physical constraints such as stress or strain.[6,9]

By inclusion of elements with a greater number of valence electrons, the conduction band becomes more energetically accessible, with the effective Fermi level shifted to a point between the donor valence level and conduction band. Excess electrons within these n-type materials reside in raised valence bands and are easily promoted. This not only gives the opportunity for electron flow to occur in the conduction band, but also creates positive vacancies, or holes, within the valence band, which in turn allow electrons to flow. Free electrons within n-type materials are the majority charge carriers, and conductivity is highly effective.[6,7]

In contrast, p-type materials are formed from the doping of semiconducting materials with elements with fewer valence electrons. This creates holes below the conduction band into which electrons are more easily promoted, creating holes within the valence band. As such, electron flow is primarily incurred by the presence of positive vacancies as the majority charge carriers within the valence band. With a high degree of bound electrons and conductivity determined by the “movement” of positive vacancies, conductivity, or mobility is far lower within p-type materials.[6,7]

1.2.2. The Transistor and the Evolution of CMOS Devices

The transfer-resistor, or transistor, is undoubtedly one of the most important applications of semiconducting materials within modern technology. In its most basic sense, these architectures act as electrical switches regulating the flow of current through a semiconducting *channel* between two terminals. The flow of current, through this channel layer, is regulated through the use of a third terminal, more commonly described as a *gate*.[7,10]

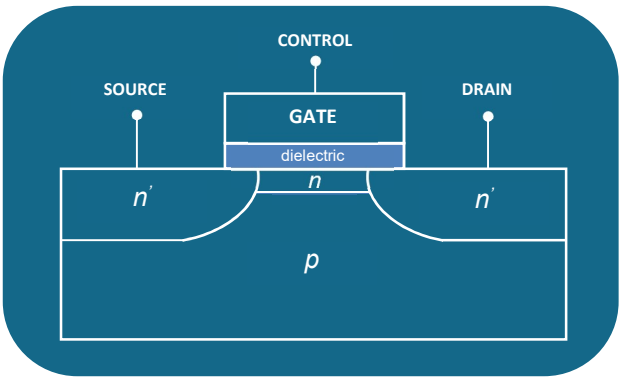

Figure 1.3 – Basic structure of an enhancement mode n-type (NMOS) Metal Oxide Field-Effect Transistor (MOSFET).

Whilst a number of manifestations of transistor architectures are employed across a range of integrated circuitries, the most ubiquitous is the Metal Oxide Field-Effect Transistor, or MOSFET. The term MOSFET is often used interchangeably with IGFET, an abbreviation of Insulated Gate Field Effect Transistor, though the latter may not always contain metal oxide materials. In the diagram given in Figure 1.3, which depicts an enhancement mode n-type field-effect transistor (NMOS) used in conventional silicon electronics, a substrate of p-type silicon is doped to create two highly n-type regions to serve as source and drain terminals. A dielectric layer (i.e. Al_2O_3 or HfO_2) is then deposited on the surface of the p-type silicon between the two terminals. A contact is then added to the top of the dielectric, creating an electrically insulated gate terminal. When a positive voltage is applied to the gate, an electric field is induced which repels holes from the underlying p-type material. Conversely, electrons are attracted from the two highly doped n-type regions, resulting in a conducting n-type channel layer between source and drain once the threshold voltage has been reached. This not only allows current to flow between source and drain, but also allows for the conductivity of the n-channel to be scaled with the magnitude of the voltage applied to the gate.[7,11]

MOSFET devices can also be formulated that rely on the semiconducting properties of p-type materials. These transistors are marginally more difficult to fabricate on conventional p-type substrates, with the entire transistor having to be placed in an n-type well. A structure similar to that of an NMOS is then used, with highly p-doped source and drain areas and capping insulator topped with a gate terminal. The advantage to this configuration lies in the fact that on application of a negative voltage to the gate, electrons from the n-type channel are repelled and holes from the p-type terminals are attracted, creating a conducting, p-type channel. This is in direct contrast to NMOS devices, where the threshold voltage is positive.[7,10,12]

Various combinations of transistor types and different circuit configurations afford control of voltage at different points across a circuit. Dependent on the desired outputs, a number generic logic gates can be employed to give binary (0 or 1) outputs under different conditions. Highly effective logic systems based entirely on NMOS devices have been used for a number of years, however the sole reliance on NMOS transistors creates a number of disadvantages. When a positive voltage is applied to the gate, the transistor is considered ON and the source and drain terminals allow a low impedance route for current to flow to the output. When the gate voltage is switched off, current is then routed through the resistor, meaning that power is consumed when the device is in the OFF state. As such, NMOS circuits generally have a high static power consumption, resulting in lower efficiencies. Furthermore, the necessity to incorporate resistors increases heat generation, wasting power and requiring device architectures to be configured in such a way as to dissipate heat efficiently. As a consequence of these considerations, device size is increased and the logic density therefore lower.[6,7,13]

Advances in PMOS technology enabled the integration of both technologies into Complementary Metal Oxide Semiconductor architectures, or CMOS. These complementary systems hold a number of advantages over the two individual elements, as by leveraging the conflicting operations of each component, the use of resistive logic is avoided, significantly reducing IC footprint, architectural complexity and heat generation. Additionally, whereas NMOS logic generally dissipates energy whilst in one of two states in addition to that lost through switching, CMOS logic instead relies on the PMOS component to switch ON whilst its NMOS counterpart is OFF, and visa-versa. The result of this is a logic system where static power consumption is negligible, and energy is mainly only lost through switching. CMOS devices benefit from reduced power consumption and heat generation and increased logic density, allowing more powerful and efficient devices to be realised.

CMOS off-Silicon

With the advent of CMOS having revolutionised the silicon IC sector a number of years previously, and as opportunities for off-silicon devices has grown, development of analogous devices has thus far been constricted by material limitations.[14] The burgeoning demand for flexible, transparent and low-cost electronics, ideally with energy scavenging capabilities, has driven research down two major routes. Metal oxide devices and organic electronics currently compete for dominance within the off-silicon IC landscape, with each displaying a number of advantages and disadvantages over the other.

Conventional silicon electronics are perfectly suited for the applications in which they are used, but an entirely different set of demands exist for a vast range of additional applications within which silicon electronics are not viable. With extensive markets in packaging, sensing, medical devices, banknotes, documents and supply chain logistics, the demand for flexible, transparent, low power and disposable circuitry is colossal.[10,14,15]

To achieve the low cost, low power consumption and high logic density of complementary logic for these applications, a number of technologies have been put forward:

- **Hybrid oxide-organic CMOS** – To address the current dearth of viable and processable p-type metal oxide materials, it has been shown to be possible to create complementary logic through the pairing of well-established n-type metal oxide materials with p-type organic systems. Whilst demonstrations have been shown to function, there is a significant mismatch in material performance, and the processing for organic materials is both significantly different and detrimental to metal oxide deposition and device fabrication.[16]

- **All organic CMOS** – Significant advances in printing technology have permitted the development of complementary logic based on n- and p-type organic materials. Due to physical fabrication methods, logic density is low and device performance poor as a consequence of organic semiconducting materials.[17]

- **"Printed" Silicon** – One of the closest to commercial readiness, printable silicon inks have been shown to allow for printable IC technology, though annealing temperatures of >500 °C are prohibitive and require printing to take place on metal substrates. Additionally, functionality is considerably inferior to significantly cheaper and more advanced conventional silicon.[18]

- **Unpackaged Silicon** – The most advanced option within the field to date is the use of unpackaged, or "thinned" silicon, which retains the high complexity and logic density of conventional silicon ICs, but is still constrained by the cost floor of high-purity silicon fabrication coupled with the lack of robustness associated with handling <50μm silicon.[19]

- **"True" CMOS** – CMOS circuitry based on devices fabricated completely from metal oxides is one of the most desirable technologies from a cost and fabrication perspective. This technology allows complementary processing, with minimal deviation from the well-established fabrication of "true" NMOS ICs. With fully oxide-based systems, transparency of devices also becomes possible. Techniques currently utilised in NMOS fabrication such as ALD are also desirable.[10]

"True" CMOS integrated circuitry has been demonstrated in number of literature publications but has not yet been realised commercially. Though NMOS is well established for all-oxide logic, the development of CMOS to date has been significantly impaired by the relative paucity of p-type metal oxide materials, the poor electrical characteristics of those that do exist, and undesirable fabrication processes.[20–22]

1.3. p-Type Metal Oxides

The development of p-type oxide materials is of great additional interest for purposes outside of the microelectronics industry. Purported uses in a multitude of applications including gas sensing, battery applications, optical displays, LEDs, photovoltaics and touch screens.[23–27] The use of n-type transparent conducting oxides and transparent semiconducting oxides is ubiquitous across the microelectronics and optoelectronics industries, amongst others, with materials such as indium tin oxide (ITO), fluorine-doped tin oxide (FTO), doped zinc oxide (ZnO) and indium-gallium-zinc-oxide (IGZO) widely used in a vast range of applications.[26]

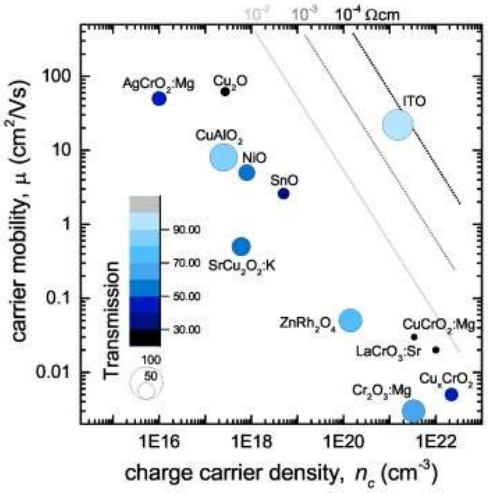

Figure 1.4 – Collation of carrier mobility vs. charge density for p-type TCO materials, with comparison to ITO. Transparency is proportional to colour and size of point. Taken from reference.[26]

Contrastingly, no real commercial examples of p-type metal oxide materials have been developed to date. Whilst a number of prospective materials have been trialled, p-type oxides are substantially inferior in a number of aspects to their n-type counterparts, partly due to intrinsic limitations of p-type semiconducting materials in general. Within n-type materials, oxide vacancies produce sufficient electrons for good conductivity, and the conduction band minimum (CBM) is comprised of predominantly metal s orbitals. With the use of heavier metal cations, a large degree of delocalisation and high dispersion of the CBM is achieved, even in amorphous materials, affording high mobilities.[22,28,29]

With the majority charge carriers with p-type materials being positive vacancies, p-type oxide materials are already disadvantaged in terms of mobility. This is compounded by the creation of holes being impaired by high formation energies of the acceptors responsible for hole propagation, and low formation energies of native donors responsible for the annihilation of holes, such as anion vacancies. This is compounded by the fact that the valence band maximum (VBM), the transport path for holes, comprises mainly localised and anisotropic oxygen 2p orbitals. The net effect of these multitude of considerations renders the realisation of p-type metal oxides problematic.[28,30–32]

A number of binary and multinary materials have been explored as p-type oxide materials, with the latter including delafossites such as $CuAlO_2$,[30,33,34] spinels such as Cr_2MNO_4,[35–37] corundum-type oxides including Cr_2O_3,[38–40] and perovskites including $LaCrO_3$.[26,41] A variety of design rationales have been employed in attempts to maximise the efficiency of p-type oxide materials. The first of these considerations aims to ensure that the cationic species hold closed-shell d^{10} configurations to avoid intra-atomic excitations, whilst the second aims to use cationic valence bands that are energetically comparable to the oxygen 2p orbitals. Furthermore, after the reportedly promising characteristics of delafossite materials, it is also

thought that tetrahedral coordination of oxide ions can reduce localisation of the valence band edge.[28,30,42]

Alternative approaches more relevant to the materials discussed herein have sought to employ binary oxide materials, which are preferred from a fabrication perspective. By application of metal cations with pseudo-closed ns^2 orbitals of similar energy to the oxygen 2p orbitals, strong hybridisation makes good mobility more achievable. Examples of these materials include lead oxide, later discovered to be primarily n-type, bismuth oxide, tin monoxide and copper(I) oxide.[28,43,44] With already low mobilities, p-type oxide investigations are additionally largely confined to crystalline materials to promote conductivity.

1.3.1. Tin(II) Oxide

One of the most promising binary p-type oxides to date is tin(II) oxide. It displays a relatively high hole mobility, which is due in part to the low defect formation energy of tin vacancies. This is assisted by a dispersed valence band maximum, caused by the hybridisation of oxygen 2p and tin 5s orbitals. The orbital structure within SnO and its impact on both valence band maximum and conduction band minimum are also responsible for the ambipolarity that has been observed within the system. This ambipolarity allows conduction of both electrons and holes within the same channel, giving the material both n- and p-type behaviour under some conditions. It is important that highly controllable deposition methods are developed to exercise control over these tendencies, though the ambipolarity offers a number of unique opportunities for further research.[28,44–46]

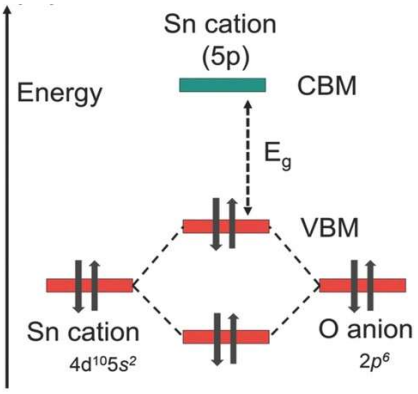

Figure 1.5 – Schematic of the hybridisation of the VBM in tin(II) oxide. Taken from reference.[28]

Crystalline SnO presents primarily with a tetragonal litharge structure comprising layers of alternating tin and oxygen atoms, with a large interplanar distance caused by directional lone pairs on the tin (Figure 1.6). The structure is layered along the (001) direction, and this layered structure has led to its purported use in battery materials and 2D devices.[47–49]

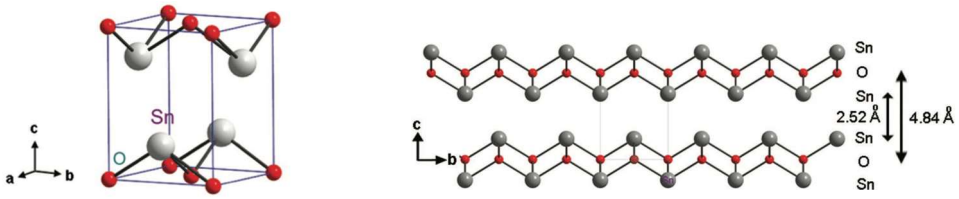

Figure 1.6 – Tetragonal SnO, unit cell (left) and layered structure (right). Taken from reference.[47]

A number of publications have demonstrated the efficacy of thin film transistors based on tin(II) oxide, with a recent publication by Kim et al.[12] detailing the high-performance of devices fabricated with an SnO channel layer deposited via the novel ALD precursor developed within the same group.[50] The SnO, deposited at 210 °C, demonstrated high on/off switching ratios (I_{on}/I_{off} = 2 x 10^6) and high field-effect mobilities (μ_{FE}) of ~1 cm^2 V^{-1} s^{-1}. These devices demonstrated superior performance in many aspects compared to a number of previous literature studies using SnO deposited by other means.[51–53] Whilst an extremely high mobility of 6.75 cm^2 V^{-1} s^{-1} was reported by Caraveo-Frescas et al,[54] switching ratios were reportedly low (~10^3) due to the presence of metallic tin, thought to be responsible for the high field-effect mobility.

The stability of tin(II) oxide with respect to oxidation to tin(IV) has long been a point of contention within the literature. Conflicting reports of its stability under ambient atmosphere at room temperature exist, though both oxidation and disproportionation are thermodynamically favoured.[55,56] However, in the absence of oxygen, as would be the case in encapsulated devices, disproportionation only becomes significant at temperatures above 300 °C. Additionally, whilst thermodynamically favoured, the disproportion process is kinetically disadvantaged in a highly ordered environment, with mobility of constituent atoms severely constrained.[55–58]

a) $SnO + 0.5\ O_2 \longrightarrow SnO_2$ $\quad -262.9$ kj mol^{-1}

b) $2\ SnO \longrightarrow SnO_2 + Sn$ $\quad -5.9$ kj mol^{-1}

Scheme 1.1 – a) Oxidation of SnO and b) Disproportionation of SnO.[55]

1.4. Deposition Methods

Dependant on the substrate, application and desired material, a wealth of different deposition techniques offer large degrees of adaptability within thin film fabrication, with many ideally suited to specific applications. It is beyond the scope of this discussion to give an overview of the less relevant techniques, and attention is instead drawn to vapour phase deposition methods. There are, however, a range of non-vapour phase techniques well-suited to large scale and bulk material depositions that are deserving of passing mention. The majority of these techniques rely on “wet” processes, ranging from electrodeposition to simple doctor-blading and printing, with the latter an important method within the organic semiconductor industry.[18,22]

More relevant to the deposition of inorganic materials are solution-based techniques such as sol-gel synthesis, wherein colloidal systems are used to precipitate solid materials out of solution, after which solvent is removed leaving behind extended networks of gel-type material. Commonly, post deposition treatment, usually thermal, is employed to further extend polymerisation or induce crystallisation. This technique is commonly directed towards the deposition of bulk metal oxide materials such as SiO_2 and TiO_2, alongside a number of organic polymers. As such, metal alkoxide and oxo-alkoxide systems are common molecular precursors for this process.[59,60]

Other solution deposition techniques are extensively employed within the semiconductor industry, including dip coating, spin coating and variants of spraying. Dip coating involves the immersion of a substrate in a coating solution, followed by withdrawal at a stipulated speed under controlled temperature and atmospheric conditions. The resulting evaporation of the solvent leaves a film of either desired material or precursor, whereupon thermal treatment creates a densified film. Similar methodology is employed in the spin coating technique, with the solution deposited in the centre of a spinning substrate, with a uniform distribution of material governed by centrifugal force. Surprising uniformity is achievable through spin coating, largely due to the lower shear forces and faster movement experienced by the surface solution in contrast to solution in contact with the substrate. Post-deposition treatments such as thermal exposure again result in either precursor decomposition and subsequent film formation, or the annealing of films to the required density and crystallinity.[61,62]

Spin coating is well-established within the semiconductor industry, forming an important step in device fabrications. Patterning of substrates is achieved through the use of photoresist polymers and UV exposure through a mask. The material changes stimulated by UV exposure create a non-soluble material over areas that need either protection from etching, or from subsequent deposition, whilst the unexposed photoresist can be washed away, leaving exposed substrate.[62,63]

In much the same way as in dip and spin coating, spray-related techniques such as spray pyrolysis are simple and versatile, relying on the spraying of a precursor solution, or a solution of the desired material, onto a substrate under a range of conditions. Simultaneous or subsequent thermal treatment results in the evaporation of the solvent and formation of the desired material through either precursor decomposition followed by annealing, or annealing alone.[64]

Solution-based deposition techniques hold a number of advantages over more involved and controlled processes, benefitting from the ability to deposit large volumes of material quickly and uniformly over large surface areas at low cost. Whilst these advantages hold true over the large scale deposition of thick films, generally >100 nm, a number of limitations manifest as textured substrates, thinner films, and more complex materials are required.[65] These requirements are met by a plethora of more advanced materials deposition techniques, falling under the classifications of physical and chemical vapour deposition methods.

1.4.1. Physical Vapour Deposition

Physical vapour deposition (PVD) processes are a well-established set of deposition techniques based around the condensation of vapourised material from a solid source onto a substrate. Usually carried out under high vacuum, techniques include sputtering, pulsed laser deposition and evaporation, and allow for a high degree of tunability and control over stoichiometries. However, due to their intrinsic methodology, techniques do not rely on chemical reactivity for film growth and often require post-deposition processing such as annealing. PVD processes are primarily also line-of-sight processes unsuitable for high aspect ratio substrates, and will not be discussed in any further depth.[66–68]

1.4.2. Chemical Vapour Deposition

Chemical Vapour Deposition (CVD) is a similarly well-established deposition technique, commonly employed across a vast range of disciplines. A number of variants on the methodology exist, but largely rely on the principle of the vapourisation of one or more materials followed by their transportation to a desired substrate.[68,69] In contrast to the PVD techniques discussed previously, CVD is not confined to being a line-of-sight process, and instead of condensation of material on the substrate, thermally initiated surface reactions are more commonly employed to afford growth of the desired material in a more controlled manner.

CVD in its most basic sense can be achieved through the evaporation of elemental components and their transportation to a heated substrate with a carrier gas or high vacuum, in a similar manner to a PVD evaporation process. Whilst this has been shown to be effective for more sufficiently volatile elements, it is of limited use for the CVD of non-volatile elements such as metals.[70] As such, the molecular precursor approach is an integral part of CVD, bestowing on elements a number of properties such as volatility and reactivity, properties that are dictated by the nature of the CVD process employed. CVD processes are generally characterised by the transportation mechanism and the method of inducing reaction of the chemical precursor to afford deposition. Consequently, a number of common CVD variants exist including Atmospheric-Pressure CVD (AP-CVD), Low-Pressure CVD (LP-CVD), High-Pressure CVD (HP-CVD), Aerosol-Assisted CVD (AA-CVD), Plasma-Assisted (or Enhanced) CVD (PA/E-CVD) and Photochemical CVD. Methodologies are in addition also often classed dependent on the precursors used, for example in the encompassing term Metal-Organic CVD (MO-CVD), which comprises many of the above techniques wherein organometallic precursor molecules are utilised. It is beyond the scope of this overview to give an in-depth discussion on the many manifestations of CVD processes and their relative merits and mechanisms, though some attention will be directed towards the necessity of astute precursor selection, and the important role precursor development plays within the field.[68,69,71]

The majority of CVD processes rely on the volatility of precursor molecules to afford transportation through either carrier gas or high-vacuum to the substrate surface. Concordantly, an important part of precursor design within MOCVD, particularly within low-pressure CVD, is the introduction of adequate volatility within the precursor complexes. This can, however be circumvented in some applications through the use of Aerosol-Assisted CVD, which relies on the solvation of precursor within a volatile solvent and the formation through sonication or atomisation of a fine dispersion of solvated precursor droplets that are transported via carrier gas to the heated substrate chamber. Subsequently, the solvent evaporates, leaving precursor free to react either in the vapour phase or on the substrate surface.[72–74]

Alongside obvious stipulations over cost, ease of synthesis and toxicity, molecular precursor design focusses on the development of complexes that are suitably stable until their decomposition is required. At this point, decomposition should be easily induced by chemical reaction with a second precursor (i.e. reducing gas), thermal, plasma, or photochemical stimulation. Decomposition must occur cleanly, resulting in volatile by-products that can be removed via carrier gas without contaminating the growing film. Furthermore, the nature of the film itself such as density and crystallinity can be hugely influenced by the nature of the precursor molecules employed.[71,73,75,76]

Additional considerations are introduced to precursor design dependent on the desired material. For many processes where binary or multinary films are required, two or more

precursors are needed. Unless volatility and reactivity can be matched, achieving uniform film growth is difficult and the relative composition over large areas can be impacted. These considerations have led to the large and sustained development of single-source precursors (SSPs), that contain all the required elements in a single molecule, such that chemical reaction on or above the substrate surface results in stoichiometric, well-controlled film growth.[77–79]

Whilst chemical vapour deposition is a hugely powerful thin film deposition technique providing a scalable and controllable method of fabricating complex materials, as device architectures become increasingly complex and the scale of electronic components diminishes, the evolution of more advanced techniques such as atomic layer deposition (ALD) has become increasingly important.[80]

1.5. Atomic Layer Deposition

1.5.1. Background and Theory

Atomic layer deposition emerged as a highly specific branch of chemical vapour deposition, gaining fast traction after its initial development in Finland in the early 1970s, before its widespread adoption by the semiconductor industry resulted in its rapid proliferation across the globe. Subsequently, its use has permeated into many different applications where conformal coatings of ultrathin films are required. Initially branded Atomic Layer Epitaxy (ALE), the first example of ALE literature was published in 1980 on the deposition of ZnTe thin films.[81,82]

ALD differs substantially from CVD. Whereas CVD processes rely on the decomposition and reaction of precursor compounds on or above the substrate surface to afford film growth, conventional ALD relies on reactivity with the substrate surface alone. There are a number of notable exceptions to this, *ibid*, but the majority of ALD processes conform to the concept of a series of self-limiting surface reactions (Figure 1.7), based on the sequential introduction of two or more reactive components to a substrate surface.[82]

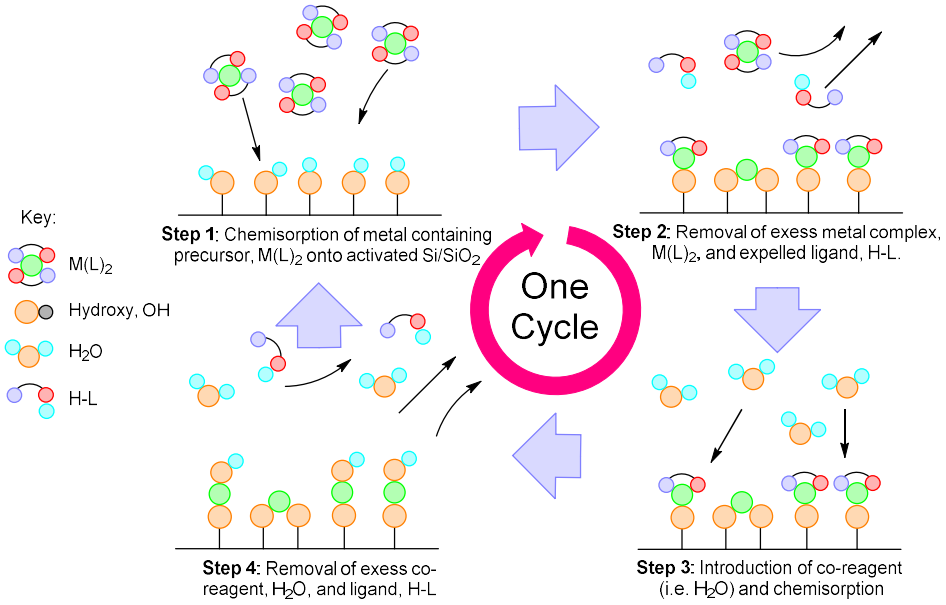

Figure 1.7 – Depiction of the ALD process.

A typical binary ALD process comprises four steps, the completion of which defines an ALD "cycle". Generally, a functionalised surface terminated in hydroxyl groups and adsorbed H_2O provides an adequate platform for growth. The first cycle introduces a pulse of reactive precursor "A" to the carrier gas and across the substrate, reacting with surface terminations to give a layer of material across the substrate, and liberating protonated ligands. As the precursor chemically reacts and does not decompose, excess precursor alongside liberated ligands can then be purged from the system by carrier gas in what becomes the second step. The third step introduces a second precursor "B" to the substrate that reacts with the remaining ligands of the adsorbed precursor "A", liberating any remaining ligands and forming A–B bonds. A further purge step removes any unreacted second precursor, and liberated ligands, readying the substrate for a repeat of the cycle. This binary approach allows material to be deposited in a sequential, "A-B-A-B" fashion.[82,83]

One of the most well-established ALD processes is the deposition of aluminium oxide (Al_2O_3). A vital dielectric material in the microelectronics industry, it provides a prime example of the textbook metal oxide process, wherein a highly reactive and volatile metal precursor ($AlMe_3$) is used in conjunction with H_2O to afford conformal films of amorphous Al_2O_3. Scheme 1.2 shows the typical surface reactions present within Al_2O_3 deposition.[82]

a) $AlOH^* + Al(CH_3)_3 \longrightarrow AlOAl(CH_3)_2^* + CH_4$

b) $Al(CH_3)_3^* + H_2O \longrightarrow AlOH^* + CH_4$

Scheme 1.2 – Surface reactions within the $AlMe_3/H_2O$ ALD process.[82]

The chemistry and mechanisms behind the ALD process give rise to a number of unique capabilities. As the process relies on reactions of each sequential precursor pulse with the respective surface terminations, once saturation of all accessible reactive sites is achieved, no further deposition occurs. Precursors do not decompose at the deposition temperature, and due to the purge steps do not react with any remaining precursor from previous cycles. As such, growth is only achieved at a monolayer level, and once surface saturation is achieved, excess reagent is carried away to the exhaust. This achieves not only highly controllable growth down to nanometre resolution, but also allows for the conformal coating of high aspect ratio substrates with no infilling, a feature that would occur with other conventional deposition techniques. Whilst CVD cannot be considered line-of-sight, deposition is still dictated by the "snowdrift" effect of precursor within a gas flow. Conversely, as a surface mediated technique, ALD allows for truly uniform deposition wherever it is possible for gas to permeate.[82,84]

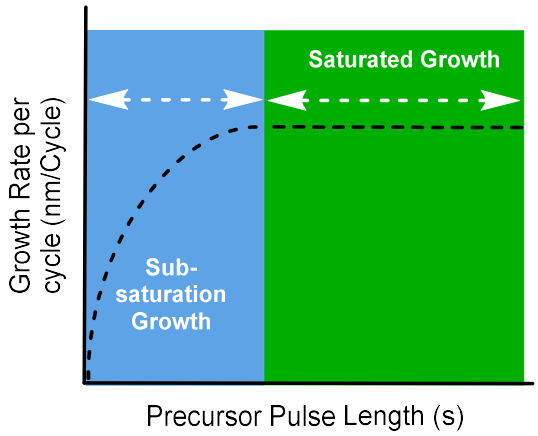

Figure 1.8 – Saturation curves for an ideal ALD process.[82]

The factors responsible for the unique properties of ALD give rise to a number of features that are representative of a "true" ALD process. The most common expected feature of an ALD process is a linear growth rate. This is important in precursor evaluation, as the linear relationship between number of cycles and film thickness should remain constant, with the amount of material deposited in each cycle the same. Though not always observed, this is largely a distinguishing feature of ALD and gives rise to a "growth rate" or "growth per cycle" value, which is used to indicate the efficiency of a precursor. Whilst this evaluation of an ALD process is consistent with highly reactive precursors, linear growth rates are not always observed at lower numbers of cycles if there is a lack of initial nucleation points on the substrate, or if the material deposited undergoes physical changes. Examples of the latter may be the sintering-type behaviour of a less dense amorphous material into crystallites after a certain volume of material has been deposited.[82,85–87]

Of similar importance within an ideal ALD process is the concept of surface saturation. This characterises the self-limiting nature of the deposition process, whereby film thickness will continue to increase with precursor pulse length until the substrate has been exposed to

sufficient volume of precursor to saturate every reactive site available. After this point, no further film growth will occur, and the film thickness with remain constant even with prolonged exposure to additional precursor. In less ideal ALD processes, such as in those with low-reactivity precursors, the concept of reaction time becomes a competing factor in this saturation, with prolonged exposure necessary to adequately saturate the surface. Whilst saturation experiments are an excellent way of characterising the ALD efficacy of a precursor, the method of defining saturation can prove contentious over larger substrates and different ALD reactor configuration. Whilst a uniform thickness may be achieved over a certain period of time, conformal density may require longer exposure at the further edges of the substrate. Furthermore, it is not uncommon for prolonged exposure to precursor pulses to actually facilitate etching of the deposited material, thereby reducing film growth after a certain point.[82,88,89]

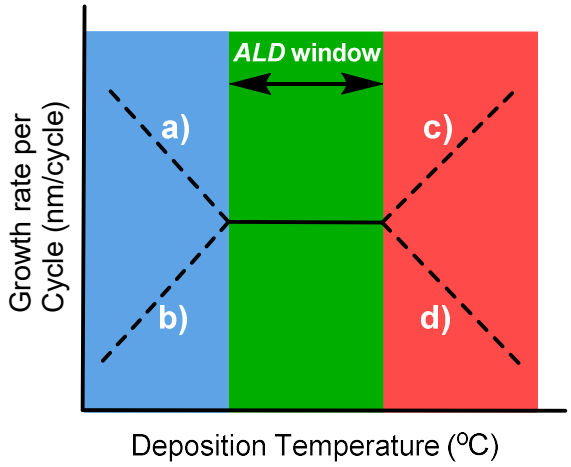

Figure 1.9 – Growth rate vs. temperature for an ideal ALD process depicting the "ALD window" and regions of non-optimal deposition: a) Precursor condensation, b) insufficient thermal activation, c) precursor decomposition and d) precursor desorption.[82]

Arguably one of the most frequently discussed features of the ALD process is the presence of a deposition window, commonly referred to as the "ALD window". This denotes a temperature region within which film growth rates remain largely consistent despite increasing temperature and can be seen in Figure 1.9. At lower temperatures, film growth is either kinetically impaired, with temperatures too low to enable reactions to take place, or alternatively film growth is significantly elevated due to condensation of precursor on the surface. The latter can also be compounded by CVD-style growth due to low temperatures reducing precursor diffusion from the surface and reactor, allowing for mixing of precursor pulses and uncontrolled growth. Conversely, at temperatures higher than the ALD window, two similar effects are often observed. Either growth rate is much diminished due to desorption of surface-bound species such as precursor or hydroxyl groups, or film growth increases substantially due to precursor decomposition at higher temperatures.[82,84]

A number of studies have sought to elucidate film growth mechanisms within ALD. Three main modes of growth are postulated within vapour-based thin film deposition in general: Volmer-Weber (VW) growth, Frank van-der-Merwe (FM) growth, and Stranski-Krastanov (SK) growth. These modes are governed by the relative strength of interactions between adatoms and between adatoms and the surface.[90]

- Volmer-Weber growth occurs when adatom–adatom interactions are greater than those between adatoms and the surface. This leads to the nucleation of three-dimensional clusters of adatoms on the surface, resulting in island-type growth.

- Conversely, Frank van-der-Merwe growth occurs when adatom–surface interactions are higher than those between adatoms. This is the expected growth mode within an ideal ALD system due to the chemical reactions of precursors with the substrate. As such, two-dimensional, monolayer growth is observed.

- Stranski–Krastanov growth is an intermediate growth mechanism between VW and FM growth, showing both 2D and 3D characteristics. Growth is initiated with a layer-by-layer process, which transitions to island growth after a critical thickness is reached, determined by chemical an physical properties.

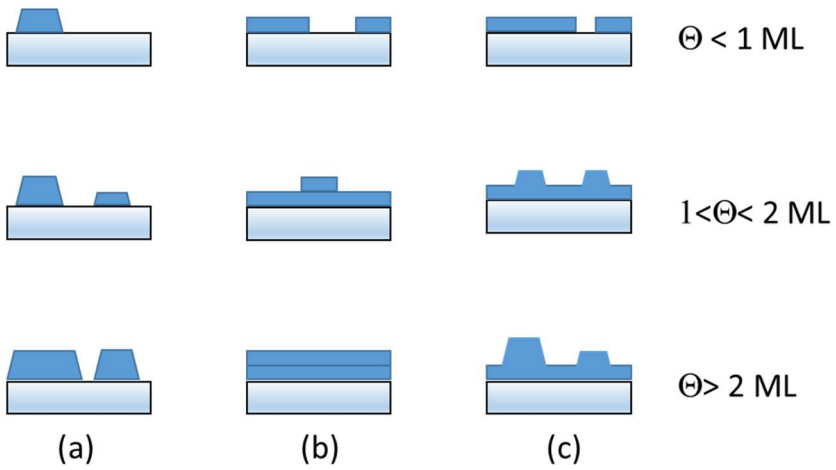

Figure 1.10 – Side on views of the three primary modes of thin-film growth: (a) Volmer–Weber (VW: island formation), (b) Frank–van der Merwe (FM: layer-by-layer), and (c) Stranski–Krastanov (SK: layer-plus-island). Each mode is shown for several different amounts of surface coverage, Θ (ML: Monolayer). Adapted from reference.[90]

1.5.2. Reactor Types

The self-limiting reaction sequences offered by ALD remove some of the reactor constraints that are often present in line-of-sight processes and CVD systems. Assuming that the substrate can be exposed for similar periods of time to reactant, and that gas flow over the substrate surface is sufficient to avoid precursor mixing, reactors can be designed to maximise precursor efficiency. This is particularly important due to the low economy of precursor usage over a single monolayer of material when compared to the size of the precursor dosage.

With primary applications within the semiconductor industry, commercial ALD tools are largely designed to take a range of sizes of silicon wafer. As such, tools are designated to be “single wafer” or “batch” reactors. Within the former, traditional configurations of either a showerhead reactor or crossflow reactor are used, whilst a number of configurations aim to maximise precursor flow over stacked wafers in batch systems.[82]

An interesting and more recent development within atomic layer deposition is the concept of “spatial ALD”. This technique aims to shuttle substrates between two continuous flows of precursor separated by a purge gas stream.[91–93] This theoretically minimises the length of the purge cycles that are necessary in conventional sequential systems. In practice, avoiding precursor mixing is difficult, and high growth per cycles have been observed that are more consistent with CVD-type behaviour. Avoidance of precursor mixing is important not only to maintain film conformality, but to avoid the mixing of pyrophoric precursors such as $ZnEt_2$ or $AlMe_3$ with H_2O.

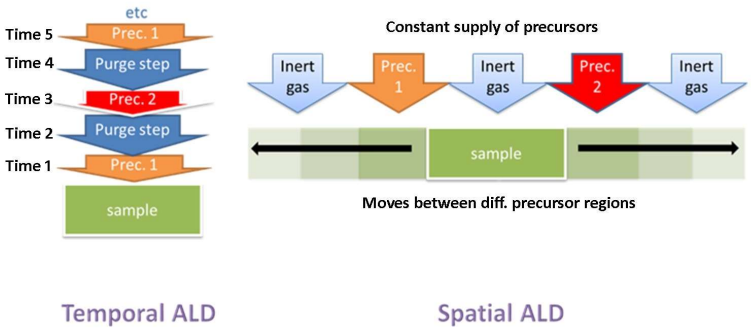

Figure 1.11 – Conventional temporal ALD process and Spatial ALD schematic. Taken from reference.[91]

1.5.3. ALD Variants

Thermal ALD

The ALD of a metal oxide material using a metal-containing precursor and H_2O is an example of a thermal ALD processes, in which simple ALD half-reactions take place between precursor and surface moieties at elevated temperatures. The thermal process is well-suited to the deposition of metal oxides due to the generally high enthalpies of formation of oxide materials, and as such, the deposition of materials such as TiO_2, ZnO and Al_2O_3 is thermodynamically favourable (Scheme 1.3). Similarly, other metal chalcogenide and pnictogenide materials are possible to deposit via thermal ALD, with the deposition of materials such as ZnS, CdS, TiN, W_2N, GaP and InP well documented.[82] Thermal ALD is by no means limited to simple binary materials, with more complex materials also easily deposited with precursor combinations of the correct reactivity.[82,84,94]

$$2AlMe_3 + 3H_2O \longrightarrow Al_2O_3 + 3CH_4 \qquad \Delta H = -376 \text{ kcal}$$

$$TiCl_4 + 2H_2O \longrightarrow TiO_2 + 4HCl \qquad \Delta H = -16 \text{ kcal}$$

$$ZnEt_2 + H_2O \longrightarrow ZnO + 2C_2H_6 \qquad \Delta H = -70 \text{ kcal}$$

Scheme 1.3 – Thermal ALD processes and enthalpies for Al_2O_3, TiO_2 and ZnO.[82]

Plasma and Radical Enhanced ALD

Whilst thermal ALD processes are simple and effective for highly reactive precursor combinations, it is sometimes necessary to improve growth rates, or indeed facilitate reactivity, through harsher conditions. Plasma enhanced ALD generally relies on the introduction of a hydrogen, oxygen or ammonia plasma in place of the second precursor step, and allows reactions to occur that may not necessarily be energetically favourable under normal thermal conditions. The process is used to great effect in the deposition of oxide materials, where reactivity with H_2O is limited, but has also proven of great use in the deposition of single-element films, where a normal binary process is unlikely to be possible. The generation of hydrogen radicals allows for the reduction of films to a metallic state, and for the decomposition or protonation of low-reactivity ligand systems. Similar effects can also be achieved through the generation of hydrogen radicals via a tungsten filament, negating the use of plasma for some applications. The use of plasma has also been shown to demonstrate an enhanced capability of film deposition at lower temperatures when compared to thermal processes, making the process of interest for substrates with low thermal tolerance, such as polymers.[82,95,96]

It has however been demonstrated that high-aspect ratio coverage can be impaired with plasma depositions due to radical recombination in deep substrates, resulting in non-conformal film growth. Furthermore, for materials sensitive to reduction or oxidation, the ability to use plasma enhancement can be impaired. This is of particular relevance to the research conducted in this investigation, where Sn(II) oxide is readily oxidised to Sn(IV).[50,97,98]

Advanced ALD Chemistries

The desire to apply the powerful capabilities of ALD to as vast a range of materials as possible has led to the evolution of a range of interesting variations on the traditional ALD process. Amongst these are techniques such as reductive ALD, which induces the reduction of adsorbed precursor with H_2 or organic reductants such as ethanol or formalin. This has been shown to be effective in the deposition of copper[99,100] and palladium amongst others,[101–103] whilst an alternative method relies on the reduction of a metal oxide in a third step after a traditional oxide deposition cycle has taken place.[104,105] Alternative methods have sought to employ combustion chemistry in the deposition of metallic films, which has been used to deposit films of Ru,[106] Pt,[107] Ir[108] and Rh,[109] with particular success arising from the complete combustion of cyclopentadienyl ligands to give CO_2 and H_2O.[82]

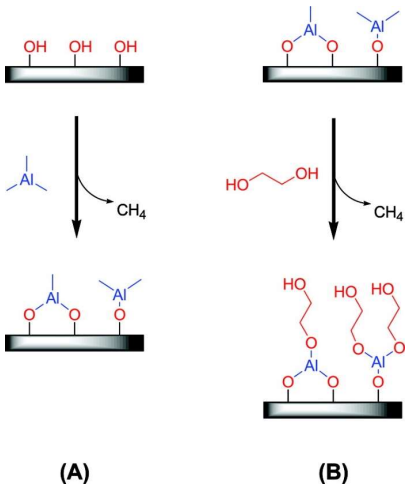

Figure 1.12 – Molecular Layer Deposition of inorganic-organic thin film. Initial $AlMe_3$ pulse (A), followed by organic pulse (B). Taken from references.[82,110]

An interesting avenue of ALD research has sought to move away from purely inorganic materials and towards "molecular" layer deposition. The same principles of ALD apply, but studies have sought to react organic molecules with reactive sites at each termination in much the same way as polymerisation occurs. Such processes allow for purely organic, or hybrid organic-inorganic systems to be deposited (Figure 1.12).[82,110,111]

1.5.4. Precursor Design

In order to achieve self-limiting growth, a number of stringent precursor requirements exist. These stipulations make identifying viable precursors a time-consuming and largely unknown process, with steric and electronic influences playing a hugely important part in the determination of precursor properties.

Effective ALD precursors are required to display the following properties:[65,112–114]

- **Volatility** – High volatility is necessary to ensure effective and efficient delivery from the source to the reaction chamber. Precursors must be able to diffuse readily over and into high aspect ratio substrates to ensure conformal growth. It is also important that precursor molecules do not condense onto the substrate, and that unreacted precursor can be transported away from the reaction chamber by the purge gas and vacuum pump. Typically, monomeric, low molecular weight species are sought. Additional volatility can be incorporated with fluorinated substituents, disordering molecular chains and asymmetry.

- **Stability** – Precursor compounds must have sufficient thermal stability such that decomposition does not occur under the process operating conditions. This would cause CVD-like behaviour and uncontrolled film growth. Precursors should also have reasonable storage-life, ensuring that deposition is repeatable.

- **Reactivity** – As ALD relies on chemical reactions with surface-bound species, precursor compounds must display a high reactivity in this respect. Within ALD processes that do not rely on the reactivity of the precursor to such an extent, such as in plasma enhanced ALD, the precursor must still react with the plasma pulse in a controlled and predictable manner. The relative reactivities of metal-alkyl > metal-amide > metal-oxygen are useful tools in designing reactivity and stability. Whilst chelation can enhance stability and allow for the retention of reactive ligand-metal bonds, it can also impact reactivity.

- **Clean Reactivity** – Once reaction with surface-bound species has occurred, any ligand or precursor fragment must be sufficiently volatile as to be removed from the system. Additionally, these by-products should not promote any further reactions that would compromise the integrity of the growing film through contamination or through etching processes.

In addition to properties that are considered a necessity, there are a number of desirable properties for precursor molecules to possess:

- **Low Cost** – For any commercially viable process, economically tenable systems are a requirement.

- **Efficient** – Dependent on the desirability of the deposited material, efficiency is always a consideration of high importance. As such, processes with low growth per cycles lack commercial viability.

- **Easily Synthesised** – The need for scalable, high-yielding and simple routes of synthesis are highly desired.

- **High Purity** – For any application that requires highly pure films, it is important that precursor can be easily purified to avoid contamination.

- **Safe** – Whilst completely non-hazardous precursors are always achievable in the search for highly reactive compounds, ideal precursors would not result in the emission of toxic by-products and should be safely storable and transportable.

A good degree of research has seen the adaptation of established chemical vapour deposition precursors to ALD processes. This has proved successful in a number of cases where high reactivity or reactivity with plasma is observed, but there are often disparities between volatility, thermal stability and reactivity of conventional CVD precursors and ALD requirements.[112,114] Means of addressing precursor properties through ligand design are addressed in greater detail within the introductory sections within each individual chapter.

1.6. Deposition of Tin(II) Oxide

1.6.1. PVD and CVD Routes to SnO

A large number of publications have investigated the deposition of SnO with a wide range of techniques. Solution state syntheses are less relevant to this research than PVD techniques, of which sputtering, evaporation and pulsed laser deposition play key roles.[51–54,115,116] These techniques are advantageous as stoichiometries can be precisely tailored through gas flow. Aside from the drawbacks of PVD techniques previously discussed, it is also often necessary to anneal samples to induce crystallinity.

More relevant to the research undertaken within this investigation are chemical vapour deposition routes to tin(II) oxide films. Two publications by Hill and co-workers[75,117] described the successful deposition of crystalline SnO from a variety of tin(II) precursors, though no electrical characterisations were conducted. These processes are discussed in more detail *ibid*.

1.6.2. ALD Routes to SnO

Further to the manifold advantages previously discussed offered by atomic layer deposition, ALD routes to tin(II) oxide are particularly desirable due to the metastable nature of the material. Oxidative control is of paramount importance, and the ability to integrate seamlessly into existing oxide fabrication routes allows for in situ encapsulation in order to protect material from unnecessary exposure to air and moisture. It has been shown through research undertaken herein that once encapsulated, device longevity is excellent and undiminished, and the thermal robustness of the material tolerates temperatures up to 250 °C, challenging the metastable designation of the material. ALD is also uniquely placed to explore 2D materials such as SnO, and offers exceptional access to the epitaxial growth important in layered materials.[47,84]

At the time of writing, only two published examples of tin(II) oxide deposition via ALD processes exist, and are discussed in detail within the relevant chapters.[50,118] Of these, only one has been shown to be truly effective, and the respective limitations of each precursor are discussed within the chapters to which they are most relevant.

1.7. References

1 M. Faraday, *Experimental Researches in Electricity, Volume 2*, Cambridge University Press, Cambridge, 2012.

2 SIA, 2017 SIA Factbook, Available at (17/09/2018): http://go.semiconductors.org/2017-sia-factbook-0-0-0.

3 J. Singleton, *Band Theory and Electronic Properties of Solids*, Oxford University Press, Oxford, 2001.

4 C. E. Housecroft and A. G. Sharpe, *Inorganic Chemistry*, Pearson, Harlow, 2nd edn., 2005.

5 D. F. Shriver, P. W. Atkins and C. H. Langford, *Inorganic Chemistry*, Oxford University Press, Oxford, 2nd edn., 1994.

6 D. J. Roulston, *An Introduction to the Physics of Semiconductor Devices*, Oxford University Press, Oxford, 1st edn., 1999.

7 K. K. Ng, *Complete Guide to Semiconductor Devices* , McGraw-Hill Education, 1st edn., 1995.

8 N. Oehl, L. Hardenberg, M. Knipper, J. Kolny-Olesiak, J. Parisi and T. Plaggenborg, *Cryst. Eng. Comm.*, 2015, **17**, 3695–3700.

9 Y. Liu, W. Xu, D. B. Liu, M. J. Yu, Y. H. Lin and C. W. Nan, *Phys. Chem. Chem. Phys.*, 2015, **17**, 11229–11233.

10 L. Petti, N. Münzenrieder, C. Vogt, H. Faber, L. Büthe, G. Cantarella, F. Bottacchi, T. D. Anthopoulos and G. Tröster, *Appl. Phys. Rev.*, 2016, **3**, 21303.

11 J. Sheng, H.-J. Jeong, K.-L. Han, T. Hong and J.-S. Park, *J. Inf. Disp.*, 2017, **18**, 159–172.

12 S. H. Kim, I.-H. Baek, D. H. Kim, J. J. Pyeon, T.-M. Chung, S.-H. Baek, J.-S. Kim, J. H. Han and S. K. Kim, *J. Mater. Chem. C*, 2017, **5**, 3139–3145.

13 E. Fortunato, P. Barquinha and R. Martins, *Adv. Mater.*, 2012, **24**, 2945–2986.

14 M. Lorenz, M. S. Ramachandra Rao, T. Venkatesan, E. Fortunato, P. Barquinha, R. Branquinho, D. Salgueiro, R. Martins, E. Carlos, A. Liu, F. K. Shan, M. Grundmann, H. Boschker, J. Mukherjee, M. Priyadarshini, N. Dasgupta, D. J. Rogers, F. H. Teherani, E. V. Sandana, P. Bove, K. Rietwyk, A. Zaban, A. Veziridis, A. Weidenkaff, M. Muralidhar, M. Murakami, S. Abel, J. Fompeyrine, J. Zuniga-Perez, R. Ramesh, N. A. Spaldin, S. Ostanin, V. Borisov, I. Mertig, V. Lazenka, G. Srinivasan, W. Prellier, M. Uchida, M. Kawasaki, R. Pentcheva, P. Gegenwart, F. Miletto Granozio, J. Fontcuberta and N. Pryds, *J. Phys. D. Appl. Phys.* 2016, **49** (43), 433001.

15 R. F. Aguilera and R. Aguilera, *Technol. Forecast. Soc.*, 2012, **79**, 579–586.

16 V. Pecunia, K. Banger, A. Sou and H. Sirringhaus, *Org. Electron.*, 2015, **21**, 177–183.

17 S. Abdinia, T.-H. Ke, M. Ameys, J. Li, S. Steudel, J. L. Vandersteen, B. Cobb, F. Torricelli, A. van Roermund and E. Cantatore, *J. Disp. Technol.*, 2015, **11**, 564–569.

18 A. Chandra, M. Takashima and A. Kamath, *MRS Adv.*, 2017, **2**, 1259–1265.

19 M. Jurczak, T. Skotnicki, M. Paoli, B. Tormen, J. Martins, J. Luis Regolini, D. Dutartre, P. Ribot, D. Lenoble, R. Pantel and S. Monfray, *Electron Devices, IEEE Trans.*, 2000, **47**, 2179-2187.

20 Z. Wang, H. A. Al-Jawhari, P. K. Nayak, J. A. Caraveo-Frescas, N. Wei, M. N. Hedhili and H. N. Alshareef, *Sci. Rep.*, 2015, **5**, 9617.

21 P. K. Nayak, J. A. Caraveo-Frescas, Z. Wang, M. N. Hedhili, Q. X. Wang and H. N. Alshareef, *Sci. Rep.*, 2014, **4**, 4672.

22 R. F. P. Martins, A. Ahnood, N. Correia, L. M. N. P. Pereira, R. Barros, P. M. C. B. Barquinha, R. Costa, I. M. M. Ferreira, A. Nathan and E. E. M. C. Fortunato, *Adv. Funct. Mater.*, 2012, **23**, 2153–2161.

23 S. A. Miller, P. Gorai, U. Aydemir, T. O. Mason, V. Stevanović, E. S. Toberer and G. J. Snyder, *J. Mater. Chem. C.*, 2017, **5**, 8854–8861.

24 Y. Cheng, J. Huang, J. Li, L. Cao and H. Qi, *Micro Nano Lett.*, 2018, **13**, 257–260.

25 T. S. Tripathi and M. Karppinen, *Adv. Mater. Interfaces*, 2017, **4**, 1700300.

26 K. Fleischer, E. Norton, D. Mullarkey, D. Caffrey and I. V. Shvets, *Materials*, 2017, **10**, 19–22.

27 S.-C. Wang and M. Shaikh, *Sensors*, 2015, **15**, 14286–14297.

28 Z. Wang, P. K. Nayak, J. A. Caraveo-Frescas and H. N. Alshareef, *Adv. Mater.*, 2016, **28** (20), 3831-3892.

29 K. Nomura, H. Ohta, A. Takagi, T. Kamiya, M. Hirano and H. Hosono, *Nature*, 2004, **432**, 488.

30 H. Kawazoe, M. Yasukawa, H. Hyodo, M. Kurita, H. Yanagi and H. Hosono, *Nature*, 1997, **389**, 939.

31 H. Raebiger, S. Lany and A. Zunger, *Phys. Rev. B*, 2007, **76**, 45209.

32 A. Togo, F. Oba, I. Tanaka and K. Tatsumi, *Phys. Rev. B*, 2006, **74**, 195128.

33 J. Tate, M. K. Jayaraj, A. D. Draeseke, T. Ulbrich, A. W. Sleight, K. A. Vanaja, R. Nagarajan, J. F. Wager and R. L. Hoffman, *Thin Solid Films*, 2002, **411**, 119–124.

34 M. K. Jayaraj, A. D. Draeseke, J. Tate and A. W. Sleight, *Thin Solid Films*, 2001, **397**, 244–248.

35 H. Peng, A. Zakutayev, S. Lany, T. R. Paudel, M. d'Avezac, P. F. Ndione, J. D. Perkins, D. S. Ginley, A. R. Nagaraja, N. H. Perry, T. O. Mason and A. Zunger, *Adv. Funct. Mater.*, 2013, **23**, 5267–5276.

36 T. Kamiya, S. Narushima, H. Mizoguchi, K. Shimizu, K. Ueda, H. Ohta, M. Hirano and H. Hosono, *Adv. Funct. Mater.*, 2005, **15**, 968–974.

37 S. Narushima, H. Mizoguchi, K. Shimizu, K. Ueda, H. Ohta, M. Hirano, T. Kamiya and H. Hosono, *Adv. Mater.*, 2003, **15**, 1409–1413.

38 L. Farrell, K. Fleischer, D. Caffrey, D. Mullarkey, E. Norton and I. V Shvets, *Phys. Rev. B*, 2015, **91**, 125202.

39 A. Holt and P. Kofstad, *Solid State Ionics*, 1997, **100**, 201–209.

40 E. Arca, K. Fleischer and I. V Shvets, *Appl. Phys. Lett.*, 2011, **99**, 111910.

41 K. H. L. Zhang, Y. Du, A. Papadogianni, O. Bierwagen, S. Sallis, L. F. J. Piper, M. E. Bowden, V. Shutthanandan, P. V Sushko and S. A. Chambers, *Adv. Mater.*, 2015, **27**, 5191–5195.

42 H. Yanagi, H. Kawazoe, A. Kudo, M. Yasukawa and H. Hosono, *J. Electroceramics*, 2000, **4**, 407–414.

43 Y. Ogo, H. Hiramatsu, K. Nomura, H. Yanagi, T. Kamiya, M. Hirano and H. Hosono, *Appl. Phys. Lett.*, 2008, **93**, 32113.

44 Y. Ogo, H. Hiramatsu, K. Nomura, H. Yanagi, T. Kamiya, M. Kimura, M. Hirano and H. Hosono, *Phys. Status Solidi a-Applications Mater. Sci.*, 2009, **206**, 2187–2191.

45 L. Y. Liang, H. T. Cao, X. B. Chen, Z. M. Liu, F. Zhuge, H. Luo, J. Li, Y. C. Lu and W. Lu, *Appl. Phys. Lett.*, 2012, **100** (26), 263502.

46 H. Luo, L. Liang, H. Cao, M. Dai, Y. Lu and M. Wang, *ACS Appl. Mater. Interfaces*, 2015, **7**, 17023–17031.

47 K. J. Saji, K. Tian, M. Snure and A. Tiwari, *Adv. Electron. Mater.*, 2016, **2**, 1500453.

48 M. Chen, D. Chao, J. Liu, J. Yan, B. Zhang, Y. Huang, J. Lin and Z. X. Shen, *Adv. Funct. Mater.*, 2017, **27**, 1606232.

49 X. Li, X. Meng, J. Liu, D. Geng, Y. Zhang, M. N. Banis, Y. Li, J. Yang, R. Li, X. Sun, M. Cai and M. W. Verbrugge, *Adv. Funct. Mater.*, 2012, **22**, 1646–1646.

50 J. H. Han, Y. J. Chung, B. K. Park, S. K. Kim, H. S. Kim, C. G. Kim and T. M. Chung, *Chem. Mater.*, 2014, **26**, 6088–6091.

51 P.-C. Hsu, C.-J. Hsu, C.-H. Chang, S.-P. Tsai, W.-C. Chen, H.-H. Hsieh and C.-C. Wu, *ACS Appl. Mater. Interfaces*, 2014, **6**, 13724–13729.

52 P.-C. Hsu, S.-P. Tsai, C.-H. Chang, C.-J. Hsu, W.-C. Chen, H.-H. Hsieh and C.-C. Wu, *Thin Solid Films*, 2015, **585**, 50–56.

53 H. Yabuta, N. Kaji, R. Hayashi, H. Kumomi, K. Nomura, T. Kamiya, M. Hirano and H. Hosono, *Appl. Phys. Lett.*, 2010, **97**, 72111.

54 J. A. Caraveo-Frescas, P. K. Nayak, H. A. Al-Jawhari, D. B. Granato, U. Schwingenschloegl and H. N. Alshareeft, *ACS Nano*, 2013, **7**, 5160–5167.

55 C. M. Campo, J. E. Rodríguez and A. E. Ramírez, *Heliyon*, 2016, **2**, e00112.

56 M. Becker, F. Michel, A. Polity and P. J. Klar, *J. Cryst. Growth*, 2018, **498**, 17–24.

57 M. S. Moreno, G. Punte, G. Rigotti, R. C. Mercader, A. D. Weisz and M. A. Blesa, *Solid State Ionics*, 2001, **144**, 81–86.

58 J. Geurts, S. Rau, W. Richter and F. J. Schmitte, *Thin Solid Films*, 1984, **121**, 217–225.

59 H. Yoshioka, T. Ishihara and M. Motoyama, *Advanced Materials '93*, 1994, 735–738.

60 A. Hassanzadeh, B. Moazzez, H. Haghgooie, M. Nasseri, M. Golzan and H. Sedghi, *Open Chem.*, 2008, **6** (4), 651-656.

61 K. Okamura, B. Nasr, R. A. Brand and H. Hahn, *J. Mater. Chem.*, 2012, **22**, 4607–4610.

62 D. E. Bornside, C. W. Macosko and L. E. Scriven, *J. Imaging Technol.*, 1987, **13**, 122–

130.
63 L. E. Scriven, *Better Ceram. Through Chem. III*, 1988, **121**, 717–729.
64 S. Liu, H. Zhang and M. T. Swihart, *Nanotechnology*, 2009, **20** (23), 235603.
65 V. Miikkulainen, M. Leskelä, M. Ritala and R. L. Puurunen, *J. Appl. Phys.*, 2013 **113** (2) 021301.
66 K. Reichelt and X. Jiang, *Thin Solid Films*, 1990, 191, 91–126.
67 J. F. Groves, G. Mattausch, H. Morgner, D. D. Hass and H. N. G. Wadley, *Surf. Eng.*, 2000, **16**, 461–464.
68 N. M. Hwang, *Non-Classical Crystallization of Thin Films and Nanostructures in CVD and PVD Processes*, Springer, 2016, 21-50.
69 A. C. Jones and M. L. Hitchman, in *Chemical Vapour Deposition*, 2009, pp. 1–36.
70 H. C. Aspinall, J. F. Bickley, J. M. Gaskell, A. C. Jones, G. Labat, P. R. Chalker and P. A. Williams, *Inorg. Chem.*, 2007, **46**, 5852–5860.
71 J. R. Creighton and P. HO, in *Chemical Vapour Deposition*, 2001, vol. 2, pp. 1–28.
72 C. E. Knapp and C. J. Carmalt, *Chem. Soc. Rev.*, 2016, 45, 1036–1064.
73 P. Marchand and C. J. Carmalt, *Coord. Chem. Rev.*, 2013, 257, 3202–3221.
74 Y. Xu and X.-T. Yan, in *Chemical Vapour Deposition, Vol. 2*, VCH, Weinheim, 2010, 1–28.
75 M. S. Hill, A. L. Johnson, J. P. Lowe, K. C. Molloy, J. D. Parish, T. Wildsmith and A. L. Kingsley, *Dalton Trans.*, 2016, **45**, 18252–18258.
76 I. Y. Ahmet, M. S. Hill, A. L. Johnson and L. M. Peter, *Chem. Mater.*, 2015, **27**, 7680–7688.
77 D. Barreca, A. Gasparotto, C. Maragno, R. Seraglia, E. Tondello, A. Venzo, V. Krishnan and H. Bertagnolli, *Appl. Organomet. Chem.*, 2005, **19**, 1002–1009.
78 S. L. Cumberland, K. M. Hanif, A. Javier, G. A. Khitrov, G. F. Strouse, S. M. Woessner and C. S. Yun, *Chem. Mater.*, 2002, **14**, 1576–1584.
79 C. J. Barrelet, Y. Wu, D. C. Bell and C. M. Lieber, *J. Am. Chem. Soc.*, 2003, **125**, 11498–11499.
80 M. Bueyuekyazi, T. Fischer, P. Yu, M. Coll and S. Mathur, *Dalton Trans.*, 2017, **46**, 12996–13001.
81 M. Ahonen, M. Pessa and T. Suntola, *Thin Solid Films*, 1980, **65**, 301–307.
82 S. M. George, *Chem. Rev.*, 2010, **110**, 111–131.
83 K. Knapas and M. Ritala, *Crit. Rev. Solid State Mater. Sci.*, 2013, **38**, 167–202.
84 R. W. Johnson, A. Hultqvist and S. F. Bent, *Mater. Today*, 2014, **17**, 236–246.
85 M. Copel, M. Gribelyuk and E. Gusev, *Appl. Phys. Lett.*, 2000, **76**, 436–438.
86 W. F. A. Besling, E. Young, T. Conard, C. Zhao, R. Carter, W. Vandervorst, M. Caymax, S. De Gendt, M. Heyns, J. Maes, M. Tuominen and S. Haukka, *J. Non. Cryst. Solids*, 2002, **303**, 123–133.
87 M. L. Green, M.-Y. Ho, B. Busch, G. D. Wilk, T. Sorsch, T. Conard, B. Brijs, W. Vandervorst, P. I. Räisänen, D. Muller, M. Bude and J. Grazul, *J. Appl. Phys.*, 2002,

92, 7168–7174.

88 K. Knapas, T. Hatanpää, M. Ritala and M. Leskelä, *Chem. Mater.*, 2010, **22**, 1386–1391.

89 J. Cho, T. Kim, T. Seegmiller and J. P. Chang, *J. Phys. Chem. C*, 2016, **120**, 11837–11846.

90 K. Oura, V. G. Lifshits, A. A. Saranin, A. V. Zotov and M. Katayama, *Surface science: An introduction, Vol. 4*, Springer, Berlin, 2003.

91 D. Muñoz-Rojas, V. H. Nguyen, C. Masse de la Huerta, S. Aghazadehchors, C. Jiménez and D. Bellet, *Comptes Rendus Phys.*, 2017, **18**, 391–400.

92 L. Hoffmann, D. Theirich, D. Schlamm, T. Hasselmann, S. Pack, K. O. Brinkmann, D. Rogalla, S. Peters, A. Raeupke, H. Gargouri and T. Riedl, *J. Vac. Sci. Technol. A.*, 2018, **36**, 01A112/1-01A112/6.

93 D. Muñoz-Rojas and J. MacManus-Driscoll, *Mater. Horizons*, 2014, **1**, 314–320.

94 K. J. Blakeney and C. H. Winter, *J. Vac. Sci. Technol. A Vacuum, Surfaces, Film.*, 2018, **36**, 01A104/1-01A104/6.

95 J.-G. Song, J. Park, J. Yoon, H. Woo, K. Ko, T. Lee, S.-H. Hwang, J.-M. Myoung, K. Kim, Y. Jang, K. Kim and H. Kim, *J. Lumin.*, 2014, **145**, 307–311.

96 K.-M. Jeon, J.-S. Shin, J.-Y. Yun, S. J. Lee and S.-W. Kang, *J. Vac. Sci. Technol. A Vacuum, Surfaces, Film.*, 2014, **32**, 031511/1-031511/6.

97 S. B. Kim, P. Sinsermsuksakul, A. S. Hock, R. D. Pike and R. G. Gordon, *Chem. Mater.*, 2014, **26**, 3065–3073.

98 J. Heo, A. S. Hock and R. G. Gordon, *Chem. Mater.*, 2010, **22**, 4964–4973.

99 P. Mårtensson and J.-O. Carlsson, *Chem. Vap. Depos.*, 2004, **3**, 45–50.

100 P. Mårtensson and J.-O. Carlsson, *J. Electrochem. Soc.* , 1998, **145**, 2926–2931.

101 J. W. Elam, A. Zinovev, C. Y. Han, H. H. Wang, U. Welp, J. N. Hryn and M. J. Pellin, *Thin Solid Films*, 2006, **515**, 1664–1673.

102 R. Solanki and B. Pathangey, *Electrochem. Solid-State Lett.*, 2000, **3**, 479–480.

103 J. Huo, R. Solanki and J. McAndrew, *J. Mater. Res.*, 2002, **17**, 2394–2398.

104 M. Utriainen, M. Kröger-Laukkanen, L.-S. Johansson and L. Niinistö, *Appl. Surf. Sci.*, 2000, **157**, 151–158.

105 J. Chae, H.-S. Park and S. Kang, *Electrochem. Solid-State Lett.*, 2002, **5**, C64–C66.

106 T. Aaltonen, P. Alén, M. Ritala and M. Leskelä, *Chem. Vap. Depos.*, 2003, **9**, 45–49.

107 T. Aaltonen, M. Ritala, T. Sajavaara, J. Keinonen and M. Leskelä, *Chem. Mater.*, 2003, **15**, 1924–1928.

108 T. Aaltonen, M. Ritala, V. Sammelselg and M. Leskelä, *J. Electrochem. Soc.*, 2004, **151**, G489–G492.

109 T. Aaltonen, M. Ritala and M. Leskelä, *Electrochem. Solid-State Lett.*, 2005, **8**, C99–C101.

110 A. A. Dameron, D. Seghete, B. B. Burton, S. D. Davidson, A. S. Cavanagh, J. A. Bertrand and S. M. George, *Chem. Mater.*, 2008, **20**, 3315–3326.

111 A. Kim, M. A. Filler, S. Kim and S. F. Bent, *J. Am. Chem. Soc.*, 2005, **127**, 6123–6132.

112 A. Devi, *Coord. Chem. Rev.*, 2013, **257**, 3332–3384.

113 T. Hatanpää, M. Ritala and M. Leskelä, *Coord. Chem. Rev.*, 2013, **257**, 3297–3322.

114 C. Dussarrat, *ECS Trans.*, 2014, **64**, 233–241.

115 E. Fortunato, R. Barros, P. Barquinha, V. Figueiredo, S.-H. K. Park, C.-S. Hwang and R. Martins, *Appl. Phys. Lett.*, 2010, **97**, 52105.

116 T. Yang, J. Zhao, X. Li, X. Gao, C. Xue, Y. Wu and R. Tai, *Mater. Lett.*, 2015, **139**, 39–41.

117 T. Wildsmith, M. S. Hill, A. L. Johnson, A. J. Kingsley and K. C. Molloy, *Chem. Commun.*, 2013, **49**, 8773–8775.

118 J. Tupala, M. Kemell, M. Mattinen, K. Meinander, S. Seppälä, T. Hatanpää, J. Räisänen, M. Ritala and M. Leskelä, *J. Vac. Sci. Technol. A*, 2017, **35**, 41506.

Chapter 2

Chapter 2: Tin(II) Aminoalkoxides

2.0. Background and Precedent

2.0.1. Alkoxide Chemistry

The use of metal alkoxide compounds is ubiquitous across the periodic table, with manifold applications in a variety of fields including catalysis, polymerisation, and as molecular precursors for liquid and vapour deposition techniques such as sol-gel synthesis and CVD/ALD.[1–4] Despite some drawbacks, alkoxide compounds have proven to be versatile and easily functionalised, and their chemistry well-understood.[5–7] In neutral ligand formalism, alkoxo species [OR] are considered L_2X ligands, donating up to five electrons to the metal centre, with anionic [$^{-}$OR] species donating up to six.[8,9] This $1\sigma2\pi$ arrangement led to the analogy by Wolczanski and co-workers that direct comparisons could be drawn between the possible interactions of alkoxide ligands and cyclopentadienyl ligands (Figure 2.1), subsequently initiating a flurry of renewed interest in alkoxide chemistry.[10]

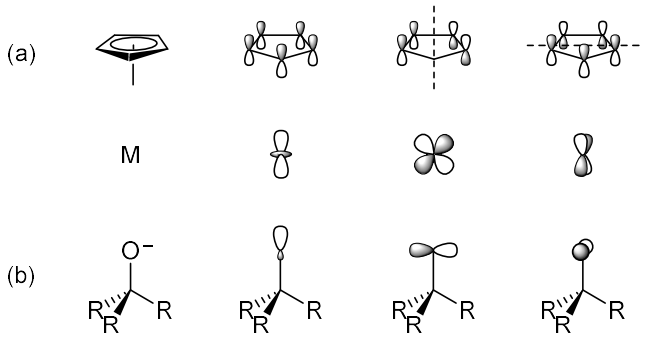

Figure 2.1 – a) Cyclopentadienyl-alkoxide orbital analogy, and b) depiction of σ and π orbital interactions between alkoxide moieties and metal centres, responsible for the 1 to 6 electron donating capabilities.[10,11]

Alongside amides and early halogens, alkoxo ligands fall into the category of hard ligands as defined by Pearson, with the strongly electronegative oxygen responsible for the induction of considerable polarity within the M–O bond.[11,12] This is somewhat mitigated by a high tendency to disseminate electron density by forming bridging species, though it is also responsible for the extreme sensitivity towards hydrolysis for most alkoxide species – an inclination exacerbated by highly oxophilic and coordinatively unsaturated metal centres. Facile reactions in this regard result in a wide range of cluster species containing bridging oxo species, many of which are self-forming and require no external influences, though are of great interest in their own right as chemical vapour deposition precursors and catalysts.[6,9,13,14]

Alkoxide compounds are often synthesised though salt metathesis reactions (Scheme 2.1a) from the corresponding metal halide and group 1 alkoxide. Salt metathesis routes are less favoured for higher oxidation state metals, with salt-like alcoholates leading to undesired redox and coordination reactions, and ionic -ate complexes (Scheme 2.1b). Alternative routes such as amide displacement (Scheme 2.1c) circumvent these issues, with displacement of volatile amines such as $HNMe_2$ and $HN(SiMe_3)_2$ providing an entropic driving force compensating for the loss of the lattice-enthalpic driving forces present in salt metatheses. This displacement route, colloquially known as the amide route, is the linchpin of the coordination chemist, and comprises much of the synthetic procedure outlined in this body of work. Alternative routes towards alkoxide complexes rely on the relative acidity of alcohols with respect to each other, allowing for ligand displacement of less acidic alkoxides by more acidic counterparts (Scheme 2.1d). Out of necessity, the equilibrium of the latter is usually driven by the distillation of the eliminated alcohol in an inert solvent.[9,13]

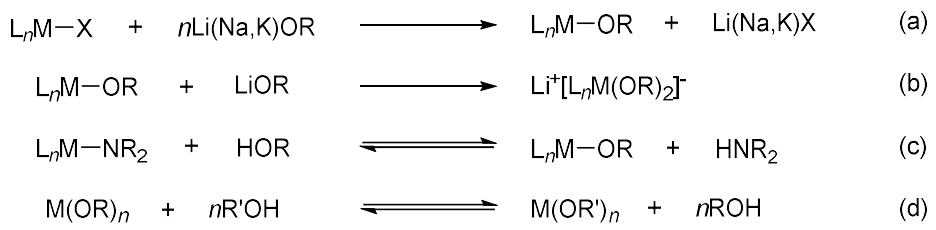

Scheme 2.1 – (a) Salt metathesis reaction between metal halide and group 1 alkoxide. (b) Ionic -ate complex as complication of salt metathesis route. (c) Amide ligand displacement. (d) alkoxide displacement by higher acidity alcohols.

Figure 2.2 depicts common metal-alkoxide binding modes, as dictated by steric and electronic influences, with metal-oxygen bond lengths increasing with degree of bridging. In the case of terminal species (Figure 2.2a), alkoxides most often exhibit non-linear geometry (<*ca*.170°) about the MOR angle, with the majority of more linear systems a product of steric influences. Very few examples can be found whereby a linear MOR arrangement arises from electronic influences, though an indication that this interaction is occurring can be inferred from short M-O bond lengths in conjunction with near-linear MOR arrangements in sterically unhindered species.[15,16] These artefacts could be interpreted as the use of both lone pairs of an *sp* hybridised oxygen involved in π-bonding with the metal, though this case is a rarity.[17,18] As a result of these solid-state steric considerations, interpretation of MOR bond angles within monodentate alkoxides as determined by single-crystal X-ray diffraction must be embarked upon with caution, as crystal-packing influence on bond angle may not be present on solvation or within liquid or gaseous form.[9] In contrast to the rare occasions in which O-M interactions comprising both oxygen lone pairs are seen within near-linear terminal alkoxides, there exist other instances, such as in the complex $[(dppe)_2Pt(OMe)Me]$, where no π-bonding was observed at all, with a 120° MOR angle being a direct result of a lack of vacant π-acceptor orbitals on the metal centre. More commonly seen within terminal alkoxide chemistry is a

middle-ground of π-bonding interaction, with proposed interaction from a single lone pair, leading to MOR angles in the region of 140°. As a general rule, M-O bond lengths decrease with increasing linearity of MOR angles as greater π-interactions between metal and alkoxide occur.[16,18] For more in-depth reviews of the chemistry of alkoxides, the reader is directed to the works of Mehrotra[7,8] and Bradley.[12,19]

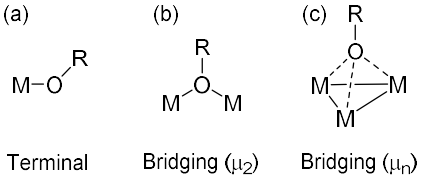

Figure 2.2 – Typical binding modes found in simple metal alkoxide species; a) terminal M-OR bond, b) μ_2 M-O-M bridge, symmetrical or asymmetrical, and c) M_3-O μ_3 bridge, representative of "capping" alkoxide.

There is great propensity for [RO^-] ligands to form bridges within metal alkoxide systems due to the high electron-donating potential of heteroatoms, a tendency which is exacerbated by the Lewis acidity, atomic radius and coordinative unsaturation of the metal centre (Figure 2.2b). This is often manifested in the formation of oligomeric species or clusters, which can present a lack of control over synthesis and, more significantly for the field of precursor chemistry, can result in undesirable properties such as a reduction in volatility or reactivity. Bridging species can either exhibit uniform bond lengths across the M-O-M bridge, or asymmetric bonding comprising one stronger and one weaker interaction between oxygen and each metal respectively. The occurrence of bridging alkoxides (Figure 2.2c) between three metal atoms or greater is particularly prevalent in compounds containing oxophilic metal centres and is often also encountered in alkoxide chemistry.[9,19] The side effects of this increasing inclination towards oligomerisation with decreasing size of –R group manifest themselves through solubility and volatility decreases from $^tBuO^- > {}^iPrO^- > EtO^- > MeO^-$.[20]

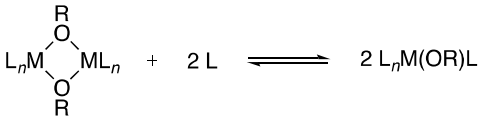

Equation 2.1[16] – Thermodynamic competition within the oligomerisation process where labile ligands compete for coordination sites.

As a result of the thermodynamic competition between monomer and oligomer, and in cases where labile ligands directly compete for coordination sites (Equation 2.1), a great deal of research, particularly in the field of precursor development, has been directed towards exerting control over the proclivity of various metal alkoxide complexes towards oligomerisation. In addition to the monomer–oligomer equilibrium shown in Equation 2.1, many other instances of monomer–oligomer equilibrium exist where free ligand is not liberated, and instead the coordination number of an electron-deficient metal centre is increased (Equation 2.2). A variety of methods have been employed in efforts to disrupt the

formation of oligomers, including attempts to coordinatively saturate metal centres of interest, sterically encumber the alkoxide species involved, or influence the electron-donating abilities of the alkoxide itself. One common technique includes the formation of adduct species with neutral bases, such as pyridine or dimethylamine, though this approach introduces additional decomposition steps and dissociations which are less desirable for molecular precursor applications.[21] Increasing the steric demands of the alkyl- or aryl-oxide ligand is a widely used method to disrupt oligomer formation, with varying degrees of success depending on the valency, atomic radius and Lewis acidity of the metal involved. For many metals, the steric bulk of tert-butyl alkoxide is sufficient for this purpose, though with a cone angle of *ca.* 125°, more demanding species such as the "tritox" group {$OC(CH_3)_3$} have long been used to exact significant steric influence on metals more predisposed to forming oligomeric alkoxides, after first being introduced into coordination chemistry by Power et al. and Wolczanski et al.[9,22–25]

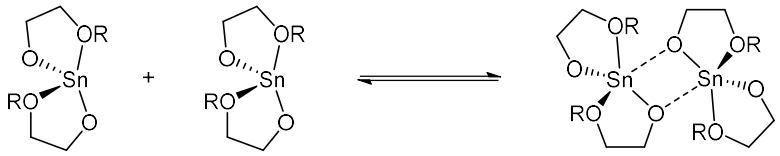

Equation 2.2 – Monomer–dimer equilibrium in pendant chelating alkoxides depicting increasing coordination number of Sn atom on dimerisation.

Alternative approaches have been applied to the prevention of oligomerisation aimed at influencing the electronic properties of the alkoxide species. The substituent alkyl or aryl groups of alkoxide species are capable of inducing varying degrees of electron-withdrawing and -donating effects, which significantly influence the chemistry of the metal-alkoxide bonding and in many instances the chemistry of the complex as a whole. This is particularly relevant in the field of catalysis, where metal electronics are frequently tailored by alkoxide moieties and their respective substituents.[14,26] For this reason, alkoxide systems with simple aromatic substituents often display differing properties to their alkyl counterparts due to conjugative π-overlap resulting in a resonance form extending to the metal centre. Aryloxides, of the form $M(OAr)_x$ (where Ar = aryl), tend to display limited volatility and it is mainly for this reason that aromatic alkoxide substituents have long been seen as less suitable for CVD and ALD processes.[9,16]

In addition to providing a well-established route towards increasing the volatility of precursor complexes, the inclusion of fluorinated substituents has also been employed in the prevention of oligomerisation within metal alkoxide species. The electronegative nature of fluorine results in an electron-deficient alkoxide ligand which exhibits a much reduced tendency to form bridging species. This can be achieved without the steric expense of bulky substituent groups as with a van der Waals radius of 135 pm, fluorine is only approximately 10% larger than hydrogen (120 pm).[9] However, this effect must be balanced with the reduced nucleophilicity

of the oxygen-based lone pairs, which reduces the π-donating character of the ligand and as such, highly fluorinated alkoxide ligands behave in a similar fashion to halide ligands, as opposed to ligands with good π-donating capacity. In turn, the lack of the additional electronic saturation provided by π-bonding alkoxides can lead to increased electrophilicity of the metal centre, increasing the desire to scavenge electron density though oligomerisation, cluster formation or other means.[11] Further to this, due to the relatively common occurrence of metal–fluorine interactions, particularly at elevated temperatures and within unexpected decomposition pathways, fluorine contamination within thin films can be an unintended consequence of the use of fluorine-containing precursors.[9,27] It is however possible that this could be avoided in low-temperature ALD processes that do not rely on harsh oxidants such as H_2O_2, O_3 and O_2–plasma. Further diligence is required when considering the use of fluorine-based precursors due the propensity of fluorine to etch silicon and other metal oxide substrates.[28]

One of the more facile routes towards tailoring an extensive range of physicochemical properties of metal complexes is to incorporate chelating pendant groups into ligand modifications. If the anionic number of the ligand is to remain the same as the parent monodentate alkoxide, then a neutral coordinating linkage must be used. Within the field of precursor development, these are commonly other heteroatoms within ketonic, ether, secondary imine, and tertiary amine moieties. One advantage leveraged by the incorporation of pendant chelating arms is the ability to alter the chelating arm chain length to suit the coordination demands of metal centres with differing atomic radii, or preferred geometrical configurations (i.e. square planar vs. tetrahedral). This ability to saturate electrophilic metal centres both electronically and coordinatively is particularly effective in the prevention of oligomerisation, whilst the extended ligand framework and additional heteroatom afford many further opportunities to develop the steric footprint of the system, which in turn offers further influence on properties such as volatility, reactivity and susceptibility to polymerisation.

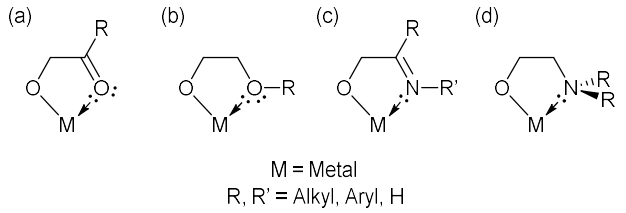

Figure 2.3 – Generic depictions of monoanionic alkoxide ligands containing pendant chelating arms: (a) ketonate, (b) alkoxyether, (c) ketiminate, and (d) alkoxyamine.

Though perhaps more subtle, the most interesting advantage offered by the inclusion of chelating functionalities is the unique opportunity to fine-tune ligand electronics through a wide variety of means. In much the same manner as found with the fluorination of alkoxides, the presence of electron-donating or -withdrawing groups in close proximity to heteroatoms has great effect on coordination abilities for both anionic and neutral binding sites, whilst simply

changing heteroatom affords significant electronic changes. Any steric strain arising from substituent bulk or inadequate ligand backbone length will also impact binding capabilities upon chelation. The effect of sub-optimal chelating site position can be further compounded by the hybridisation and directionality of heteroatom orbitals with respect to the coordination centre. This can be inferred from Figure 2.3, which depicts sp^2 and sp^3 heteroatoms as neutral donors in pendant substituents. Further fundamental alterations can be made to ligand systems, such as the inclusion of certain configurations of ligand backbone promoting delocalisation across the entire chelating system, examples of which exist in ligand classes such as carboxylates, xanthates, guanidinates and β-diketonates.[29–31]

Many aspects of ligand design discussed within this prelude significantly impact the efficacy of molecular precursors towards atomic layer deposition. In particular, factors that strengthen metal-ligand bonding and enhance thermal stability can also diminish the lability of the ligand and hence its ALD reactivity. This is particularly important in thermal ALD processes in which harsh oxidising agents must be avoided, such as in the deposition of quasi-metastable tin(II) oxide. To this end, precursor complexes with high reactivity towards H_2O are desirable. The two theoretical ALD half-reactions between alkoxide and surface-based hydroxyl groups, and between surface-based alkoxide and H_2O, are depicted in Scheme 2.2.

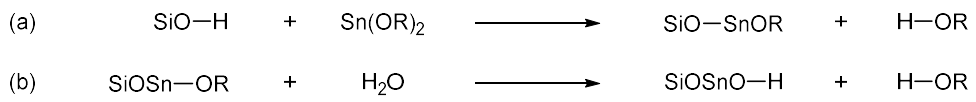

Scheme 2.2 – ALD half-reactions of tin(II) alkoxide with surface-based silicon hydroxyl species (a), and H_2O pulse (b).

Attention has previously been drawn to the importance of relative O–H acidity in the determination of alkoxide reactivity with respect to synthetic procedures. The same principle can in theory be applied to the protonation of alkoxide ligands by H_2O and surface hydroxyls, wherein an alkoxide ligand with a higher basicity will exhibit a greater driving force to abstract a proton from either H_2O or surface [OH] terminations than an alkoxide with lower basicity. Conversely, it could be postulated that more basic ligand species would form stronger metal–heteroatom bonds and result in lower affinity with the conjugate bases of either surface [O^-] or water [HO^-]. It must also be considered that any loss of multidentate ligands is in competition with the chelate effect, though this is likely to be somewhat compensated by the formation of the solid-phase SnO lattice. These competing electronic influences pose interesting avenues for further research, particularly in the optimisation of low-reactivity precursor systems.

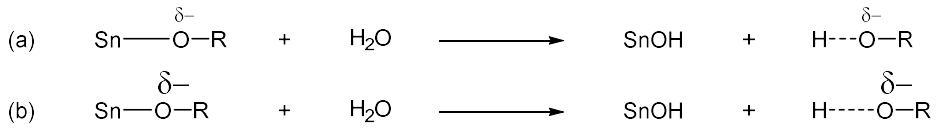

Scheme 2.3 – Alkoxide with low basicity resulting in weaker M–OR bonding and weaker acidity (a), cf. alkoxide with high basicity resulting in stronger M–OR bonding and stronger acidity.

2.1. Donor Functionalised Alkoxide Precursors

2.1.1. Alkoxyether Ligands

Donor functionalised ligands of the general parent form [$^{-}$O(CH$_2$)$_n$OR], with any degree of modification to the carbon backbone, are well established molecular precursors for a range of deposition processes, including CVD, ALD and solution-based synthesis.[32–34] The inclusion of the Lewis basic ether moiety is known to successfully promote metal centres with higher nuclearity than the parent alkoxides. The added functionality also allows greater control over rates of hydrolysis and decomposition, and ability to improve volatility and solubility.[35] Attention in this chapter is primarily focussed on saturated ligand systems with ethylene backbones, on which much of the research contained herein is based. As such, precursors such as β-diketonates, which often display low reactivities, and other related chelating systems are not covered here.[36,37]

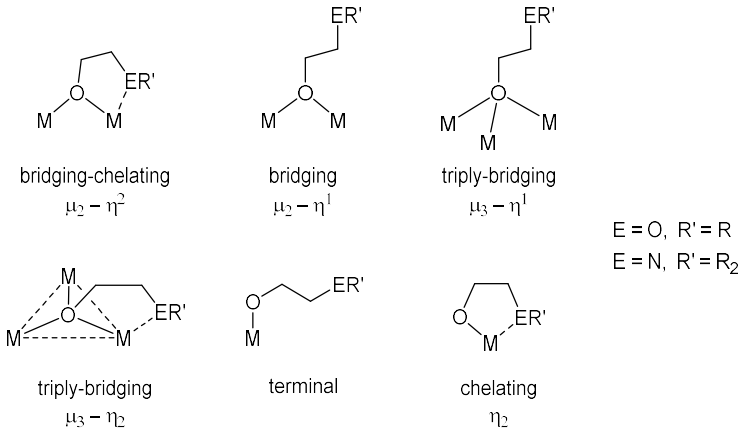

Figure 2.4 – Common binding modes of alkoxide ligands with pendant ether (OR) or pendant amine (NR$_2$) moieties.[20]

Many coordination modes are observed in alkoxyether compounds (Figure 2.4) giving great variety in the structure of complexes when multinuclearity arises. Despite occurrences of multinuclearity, alkoxyether ligands remain important tools in the prevention of oligomerisation. In general, metal–heteroatom bond lengths within alkoxyether complexes increase with dissemination of oxygen-based electron density through bridging in the expected manner: M–OR (terminal) < M–μ–OR < M–μ$_3$–OR.

As may be expected, alkoxyether systems have found wide application in sol-gel synthesis and in many other processes where the parent alcohol is used as both reagent and solvent. The attraction of these donor-functionalised systems is, for some applications, their ability to act as self-assembly linkages and routes to polymeric networks. These properties are obvious detriments when considering precursors for use in vapour deposition processes, however these properties can be mitigated by diligent alteration of steric demands, or by increasing the number of pendant donor sites.[9,35]

A vast number of alkoxyether compounds of many elements have been characterised, and a large number applied to chemical vapour deposition processes.[9] Elements deposited via 1-methoxy-2-methylpropan-2-oxide (mmp) (Figure 2.5) chelates alone include – though are by no means limited to – Al, Hf, Bi, Sc, Zr, Ti, Ga, In and many lanthanides.[32,33,46,38–45] It is noted, however, that with alkoxyether ligands the coordination chemistry of larger elements is far from straightforward. This is exemplified by Aspinall and co-workers in a 2007 study into the MOCVD and ALD of rare-earth oxides, which characterises a range of donor-functionalised complexes with varying coordination environments.[33]

Whilst a great number of MOCVD processes have made use of alkoxyether precursor systems, application of these systems in ALD has been more limited. The volatility of many of these compounds is often less compelling than alternative precursors, though successful depositions have been undertaken with a range of precursor systems where volatility has been sufficient, or where liquid-injection ALD is appropriate. Deposition of Al_2O_3 has been undertaken by Min et al. who applied the aluminium complex of 1-methoxy-2-methyl-2-propanol, [Al(mmp)$_3$], in a 0.1 M solution of ethylcyclohexane in a liquid-injection ALD process with H_2O, though notably both the film quality and growth-per-cycle (0.6 Å) of alumina films were lower than the traditional TMA/H_2O process.[46] Research from the same group has also reported the ALD of mmp complexes of Bi and Ti with a similar solution-based process, whilst heteroleptic hafnium mmp derivatives have been applied by others to the same process with limited effect.[38,47] Ce-HfO_2 composites have also been grown using [Ce(mmp)$_4$] and H_2O, in limited examples of traditional non-solution-based ALD processes using alkoxyether precursors. Volatility of [Ce(mmp)$_4$] proved adequate in these processes with bubbler temperatures of 130 °C sufficient to ensure precursor delivery.[48,49]

2.1.2. Aminoalkoxide Ligands

Considerably more attention in the field of donor functionalisation has been directed towards pendant amine ligands. These systems, of the general parent formula ($^{-}OCH_2CH_2NR_2$) typically exhibit higher volatilities than their alkoxyether counterparts, and lower propensity for self-assembly processes. This is due in part to the differing heteroatom electronic

predispositions, but also to the extra steric influence of the additional functionality on the amine (–OR vs. $–NR_2$).[20,35]

Amine functionalised systems have also been shown to disfavour oligomerisation when compared with the analogous alkoxyether compounds. This aids volatility and is exemplified in the praseodymium complexes of $^{-}OCH_2CH_2OMe$ and $^{-}OCH_2CH_2NMe_2$, where polynuclear oxo-clusters are formed with the alkoxyether, whilst the aminolkoxide was isolated as a trimer.[50] This is further illustrated in the copper complexes $[Cu(OCHRCH_2NMe_2)_2]$ (R = H, Me) which exist as monomeric, volatile compounds whilst the ethoxy derivatives are oligomeric or polymeric. The same observations have also been noted for Zn analogues.[35,51,52] As such, aminoalkoxide precursors have been used extensively in a range of CVD procedures.[45,52–55] Further studies have sought to improve the volatility of aminoalkoxide compounds by the addition of fluorinated substituents. Ligands such as $^{-}OC(CF_3)_2CHN(RR')_2$, where (R, R' = H, Me, ^{t}Bu) have been used within indium and gallium complexes to deposit oxide films via CVD methodologies.[56,57] Additionally, identical precursors have been responsible for the CVD of copper metal, where interestingly, the proton present in secondary amine (–NHR) pendant groups facilitated deposition in a non-reductive atmosphere, whereas tertiary amine ($–NR_2$) pendant groups required the use of an H_2 atmosphere to decompose efficiently.[58]

Donor functionality has been used to great effect to enhance the stability and limit the reactivity of a number of metal compounds. This is exemplified within group 13 elements, where traditional "gold standard" ALD precursors such as trimethylaluminium and trimethylindium are highly reactive and incredibly pyrophoric. As such, development of alternative processes utilising more benign precursors has been of some interest. Examples of such precursors are the donor functionalised aluminium and indium alkyls, $[M(Me_2)(dmp)]$, (dmp = dimethylaminopropyl) (Figure 2.5), and the aluminium species $[Al(NR_2)(dmp)]$, where R = Me, Et and ^{i}Pr. Importantly, these systems were shown to exhibit ALD-type growth in a range of processes (H_2O and O_2–plasma) with reasonable growth rates whilst remaining non-pyrophoric.[59,60] Further studies on a less hazardous substituted indium alkyl, $[Me_2In(edpa)]$, showed the efficacy of a novel donor functionalised ligand system that displayed good potential for further work within the field (Hedpa = N-ethoxy-2,2-dimethylcarboxylicpropanamide) (Figure 2.5).[61–63] A further example of the use of stabilising chelates to temper reactivity can be found within a series of novel zinc precursors based on delocalised ketoiminate systems, that also combine non-pyrophoric properties with good ALD characteristics.[64]

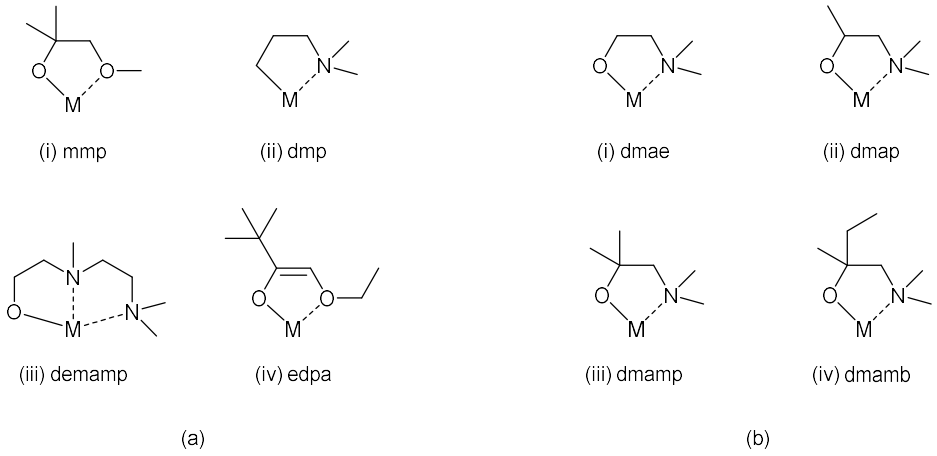

Figure 2.5 – Salient donor functionalised ALD ligands. (a) – (i) mmp, 1-methoxy-2-methyl-2-propoxide, (ii) dmp, 1-dimethylaminopropyl, (iii) demamp, 1-{[2-(dimethylamino)ethyl](methyl)amino}-2-methylpropan-2-oxide and (iv) edpa, N-ethoxy-2,2-dimethylcarboxylicpropanamide. (b) – (i) dmae, 1-dimethylamino-2-ethoxide, (ii) dmap, 1-dimethylamino-2-propoxide, (iii) dmamp, 1-dimethylamino-2-methyl-2-propoxide and (iv) dmamb, 1-dimethylamino-2-methyl-2-butoxide.

Due to the favourable properties displayed by aminoalkoxides in comparison to alkoxyether ligands, it is unsurprising that many ALD processes adopting these ligands have been developed. ALD of TiO_2 has been achieved using heteroleptic systems $[Ti(O^iPr)_2(dmae)_2]$ (Hdmae = 1-dimethylamino-2-ethanol) and $[Ti(NMe_2)_3(dmap)]$ (Hdmap = 1-dimethylamino-2-propanol), diverging from the standard $TiCl_4$ and $Ti(O^iPr)_4$ processes.[65,66] The chiral secondary alcohol dmap has also been shown to be effective in the ALD of copper(II) oxide with either H_2O or O_3 as oxidant, and the deposition of Cu metal films with borane dimethylamine/formic acid, formic acid/hydrazine, or tertiary-butyl hydrazine as reductants.[67–71] For larger, more coordinatively demanding and ionic metal centres, additional pendant moieties have been shown to be effective at stabilising dimeric ALD precursor systems whilst preserving precursor activity, as found in the case of $[\{Sr(demamp)(tmhd)\}_2]$, where Hdemamp = 1-{[2-(dimethylamino)ethyl](methyl)amino}-2-methylpropan-2-ol, and Htmhd = 2,2,6,6-tetramethyl-3,5-heptanedione) (Figure 2.5).[72]

Other variants of the aminoalcohol series under discussion, such as 1-dimethylamino-2-methyl-2-butanol (dmamb) (Figure 2.5), have demonstrated efficacy in ALD studies across the periodic table. Films of metallic copper were deposited using a combination of $[Cu(dmamb)_2]$ and H_2–plasma, whilst copper(I) oxide was deposited using the same precursor alongside H_2O pulses in a study that saw growth rates of 0.13 Å/cy at 140-160 °C.[73–75] A range of studies have used $[Ni(dmamb)_2]$ to deposit films of Ni with reducing conditions such as H_2 or NH_3, though of more relevance is the deposition of NiO under different process conditions.[76,77] Nickel(II) oxide has been grown in self-limiting processes using both H_2O (microcrystalline, 130-150 °C, ~1.3 Å/cy and; amorphous, 100-140 °C, ~1.4 Å/cy),[78,79] and ozone (polycrystalline, 140-200 °C, ~0.23-0.26 Å/cy).[80] Studies have also shown that the use

of H_2S as a co-reactant results in the formation of crystalline NiS films with growth rates of ~0.77 Å/cy at temperatures of 80-160 °C.[81] Further to this, closely related [Ni(dmamp)$_2$] (dmamp = 1-dimethylamino-2-methyl-2-propoxide) has found use in the deposition of amorphous NiO from H_2O with a growth per cycle of ca. 0.8 Å between 90 °C and 150 °C.[82]

In addition to its use in the deposition of NiO, the aminoalcohol Hdmamp (Figure 2.5) has been applied in the ALD of a number of other systems. In(dmamp)$_3$ and O_3 were used as precursors in a study by Han et al. that deposited In_2O_3 with a growth rate of ca. 0.27 Å/cy at 150-200 °C. The study also claimed that the dmamp precursor displays ALD activity with H_2O, though at a lower growth per cycle than with ozone.[83] In 2007, the first ALD studies of a late group 14 element using the dmamp ligand were reported by Hwang et al. in investigations that succeeded in the deposition of PbO at growth rates of ca. 0.2 Å/cy at temperatures of 200-280 °C.[84,85] The study focussed on the deposition of $PbTiO_3$ and formed the basis of subsequent studies using the [Pb(dmamp)$_2$]/H_2O combination to deposit ternary films via ALD.[86] The application of 1-dimethylamino-2-methyl-2-propanol as a ligand in group 14 precursor chemistry was further expanded with the use of the tin(II) complex [Sn(dmamp)$_2$] to deposit films of SnO, which is discussed in greater detail in the following section.

2.1.3. *Bis*(1-dimethylamino-2-methyl-2-propoxy) tin(II)

At the time of research, a single precursor for the deposition of tin monoxide had been reported in the literature. Subsequently, an additional process has been described, though both precursor and films were acknowledged to be of very poor quality. The latter is discussed in chapter 3 due to its pertinence to the ligand systems investigated therein.

A 2014 study by Han et al.[87] described the first example of the atomic layer deposition of tin(II) oxide thin films. This was achieved using a standard thermal ALD process consisting of alternate pulses of *bis*(1-dimethylamino-2-methyl-2-propoxy)tin(II), or [Sn(dmamp)$_2$] (Figure 2.6), and H_2O. Films grown at 150-210 °C obtained from this process showed clear p-type behaviour, with Hall mobilities of 0.4-2.9 cm^2/V s and resistivities of 4.9-14.5 Ω cm for films grown at either extreme of the aforementioned temperature window respectively.

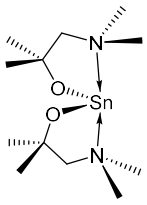

Figure 2.6 – [Sn(dmamp)$_2$]

Deposited SnO films showed preferential orientation by p-XRD, consistent with tetragonal α-SnO (JCPDS 06-0395) with peaks at 18.3° and 37.1°, corresponding to the (001) and (002) planes respectively. Crystallinity of the films became evident above 150 °C, at which temperature the growth per cycle was found to be 0.18 Å. Films were grown between 90 °C and 210 °C with growth rates decreasing from 0.61-0.08 Å/cy over this range, though it is noted that the aforementioned rate of 0.18 Å/cy is the highest achieved for the crystalline material necessary for the purported applications of SnO. The precursor [$Sn(dmamp)_2$] is described as a volatile liquid distilled at 100 °C (10^{-2} mbar), and is synthesised from the reaction of [$Sn(N(SiMe_3)_2)_2$] and 2 equivalents of 1-methoxy-2-methyl-2-propanol.[87]

Subsequent investigations have also showed [$Sn(dmamp)_2$] to be effective when used in conjunction with a number of alternative oxidants. A 2017 publication by Baek et al.[88] described the deposition of SnS through the use of H_2S as a co-reactant. The Sn(II) oxidation state was conserved throughout the process, facilitating the deposition of multiphase SnS at temperatures between 90-210 °C, and purely orthorhombic SnS between 210 °C and 240 °C. A growth per cycle of 0.36 Å was observed, notably higher that that observed for the reaction between [$Sn(dmamp)_2$] and H_2O. In addition, it is recognised by the authors that the length of H_2O pulse required to saturate the film was significantly longer than that required for an H_2S pulse (>5 s and 1 s respectively), leading to the conclusion that H_2S is significantly more reactive than H_2O within these processes.[87,88]

Further control over the oxidation state of Sn can be exerted through the use of more oxidative processes. Research by Lee et al.[89] applied a low temperature [$Sn(dmamp)_2$]/O_2–plasma process to deposit films of SnO_2 at 70–130 °C for use in thin film transistors, whilst a thermal ALD process using O_3 at 100–200 °C was described by Choi et al.[90] to result in the deposition of SnO_2 at growth rates of 0.18–0.42 Å/cy.

The development of *bis*(1-dimethylamino-2-methyl-2-propoxy)tin and its application in the atomic layer deposition of SnO represents a significant step in the field of p-type metal oxide deposition, and consequently the viability of its more widespread uptake and application within the semiconductor industry. Central to this achievement has been the ability to selectively retain the Sn(II) oxidation state in the as-deposited films, made possible through the use of H_2O as a co-reactant. This is a step previously unachievable with other Sn(II) precursor systems such as [$Sn(II)(acetylacetonate)_2$], in which reactivity is exceedingly limited in all but the most strongly oxidising conditions.[91] As [$Sn(dmamp)_2$] remains the only viable precursor for the atomic layer deposition of SnO, there exists considerable scope for further investigation into Sn(II) precursor development. The creation of a library of different precursors operating under different conditions is highly desirable, as subtle changes in film properties such as composition, density and morphology have largely untested effects on the electrical characteristics of materials when used in devices. Further to this, the low reactivity of

[Sn(dmamp)$_2$] towards H_2O results in long precursor exposure times and low growth rates (0.18 Å/cy), factors which severely limit the commercial viability of the process as a whole.[87,88]

With studies into the atomic layer deposition of SnO significantly limited, an initial investigation centred around the [Sn(dmamp)$_2$] system was devised, with a number of objectives:

- To develop a large-scale synthetic route towards both pro-ligand and tin complex.
- To repeat characterisation of the precursor complex.
- To replicate and improve upon atomic layer deposition studies carried out by Han et al.[87] on a Beneq TFS 200 commercial atomic layer deposition tool.
- To synthesise and characterise a range of related precursor systems with cost-effective and simple pro-ligands.
- Collaborate with PragmatIC Printing Ltd. to fabricate the first demonstrator of a commercial CMOS device with p-type SnO channel layer.

2.2. Case Study: *Bis*(1-dimethylamino-2-methyl-2-propoxy)tin(II)

2.2.1. Refinement of synthetic procedures

An important property sought in the development of precursors for any industrially relevant deposition method is the ability to synthesise large quantities of compound efficiently in high yield and at low cost, and to date, no precursors for the atomic layer deposition of tin(II) oxide are commercially available.

As the pro-ligand 1-dimethylamino-2-methyl-2-propanol is not itself commercially available, routes towards its synthesis were explored. At the time of investigation, two viable procedures (Scheme 2.4) were identified, though other more intensive routes have been reported.[92] Both routes identified involve the use of lithium-containing reagents, and recently the use of lithium perchlorate-diethyl ether (LDPE) has been phased out in organic synthesis due to its capricious and explosive nature. The route proposed by Anwander et al.[93] involves the synthesis of $LiNMe_2$ from butyl lithium and solvated dimethylamine, followed by the addition of the substituted epoxide and aqueous work up. Though this multi-step process involves the use and synthesis of pyrophoric substances, one advantage lies in the formation of a fully lithiated pro-ligand before aqueous work up, which would afford the opportunity to synthesise the desired tin complex from a salt metathesis reaction between lithiated ligand and metal halide. However, the development of a simple one-step reaction without the use of pyrophoric substances and yielding the alcoholic pro-ligand was desirable.

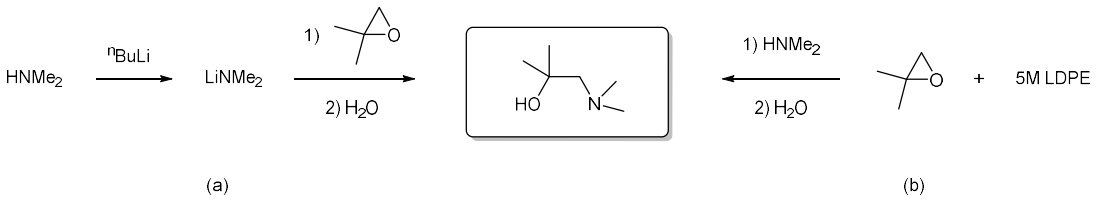

Scheme 2.4 – Published synthetic routes to 1-dimethylamino-2-methyl-2-propanol by Anwander et al.[93] (a) and Heydari et al.[94] (b).

Due to the indication that the presence of lithium was an important factor in the nucleophilic attack of the epoxide by the dimethylamine, a catalytic quantity (5% mol) of lithium trifluoromethanesulfonate was trialled in a neat reaction between condensed dimethylamine and 2-methyl-1-propenoxide at 0 °C. Despite literature precedent[93,94] never displaying a sub-stoichiometric presence of lithium, the reaction proceeded to good yield (>90%) after aqueous work up and extraction with chloroform. The investigation also discovered that neat reaction of dimethylamine and 2-methyl-1-propenoxide did not yield the desired product after 12 hours.

Interestingly, research published by Kim et al.[95] after the development of the aforementioned methodology described the synthesis of 1-dimethylamino-2-methyl-2-propanol through the heating of an aqueous mixture of dimethylamine and 2-methyl-1-propenoxide for 120 hours at 50 °C (Scheme 2.5b). This route presented an equally attractive method of pro-ligand synthesis, though the long reaction time and removal of water under vacuum limit the advantage of this method, particularly in view of the fact that it is of great importance that the pro-ligand be dry when used in further synthesis. It is, however, worth consideration that a work-up involving an organic extraction followed by addition of a drying agent before removal of volatiles would be an appropriate deviation from the method in this instance, replicating that used in the synthetic route developed in this investigation (Scheme 2.5a). Both the route developed throughout this research, and that published subsequently by Kim et al.[95] present facile and cost-effective routes towards large scale production of 1-dimethylamino-2-methyl-2-propanol.

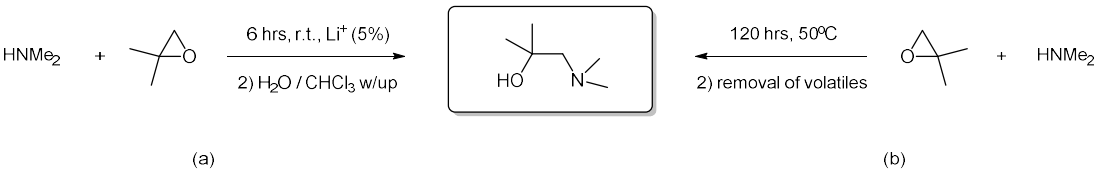

Scheme 2.5 – Synthetic routes to 1-dimethylamino-2-methyl-2-propanol. (a) Lithium catalysed route developed during the investigation, and (b) uncatalysed, aqueous reaction published by Han et al.[95] during the course of research (50 °C, 120 hrs).

With the development and implementation of a multigram-scale process for the production of 1-dimethylamino-2-methyl-2-propanol, a straightforward amide substitution, followed by appropriate removal of volatiles and distillation affords *bis*(1-dimethylamino-2-methyl-2-

propoxide)tin(II) in high yields, which are conserved in reactions exceeding a 30g scale (Scheme 2.6).

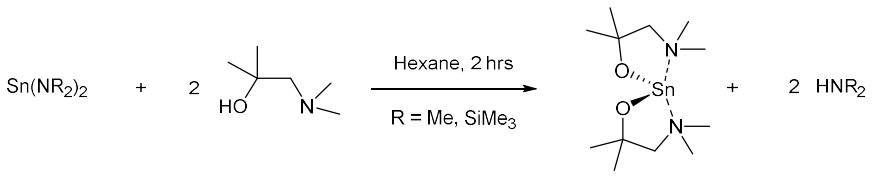

Scheme 2.6 – Amide ligand displacement reaction between [Sn(NR$_2$)$_2$] and 1-dimethylamino-2-methyl-2-propanol affording [Sn(dmamp)$_2$].

2.2.2. Characterisation of *Bis*(1-dimethylamino-2-methyl-2-propoxy)tin(II)

^{1}H NMR spectroscopy of [Sn(dmamp)$_2$] proved consistent with that reported within the US Patent for its preparation,[96] displaying broad singlet resonances at δ = 2.34 ppm (2 H) and δ = 2.24 (6 H), attributed to the C*H*$_2$ backbone and –N*Me*$_2$ moiety respectively, in addition to the presence of a singlet at δ = 1.39 ppm (6 H), indicative of the two backbone methyl substituents (Appendix, 7.2). In similar accordance with the published data, the ^{13}C{^{1}H} NMR spectrum displays resonances at δ = 74.28 ppm (O*C*(Me)$_2$), 71.02 ppm (*C*H$_2$), 46.78 ppm (N*Me*$_2$) and 34.45 ppm (C*Me*$_2$). With no literature precedent, the ^{119}Sn NMR spectrum was found to consist of a single, well defined resonance at –218.3 ppm in C_6D_6. A more detailed analysis of both NMR spectroscopy and structural data takes place later in the chapter, where full discussions are made in consideration of relevant compounds found within the literature and compounds synthesised within the investigation.

Despite previous reports by Han et al.[87] describing [Sn(dmamp)$_2$] as a colourless liquid, distillation at 120 °C (10^{-2} mbar) into liquid nitrogen was found to yield a white-colourless crystalline material of high purity with a melting point of ca. 70 °C. Subsequent states of material exhibit unusual solid-liquid behaviour, with some crystalline samples remaining solid above 100 °C and samples remaining liquid at room temperature, crystallising in response to agitation or other external stimuli. A brief acknowledgement of these interesting properties is made within the US patent 8030507B2, though no further discussion exists within the literature.[96]

As a result of these unusual properties, the previously unreported solid-state structure of Sn(dmamp)$_2$ was determined by single crystal X-ray diffraction (Figure 2.7). The compound was found to exist as a monomer in the solid state, crystallising in the orthorhombic *P*2$_1$2$_1$2$_1$ space group. Whilst a more detailed discussion on the structural data of Sn(dmamp)$_2$ can be found later in the chapter, a cursory inspection of the geometry about the metal centre reveals

a four-coordinate tin centre consistent with the expected chelation of two bidentate dmamp ligands. Despite a formal coordination number of four, the complex appears to display a coordination environment best described as distorted pseudo trigonal bipyramidal, with equatorially bound oxygen atoms and axially coordinated –NMe_2 moieties (Figure 2.8, left). The presence of a lone pair that is often stereochemically active is an important consideration in tin(II) chemistry, though the extent of its involvement is not necessarily easily inferred.[97,98]

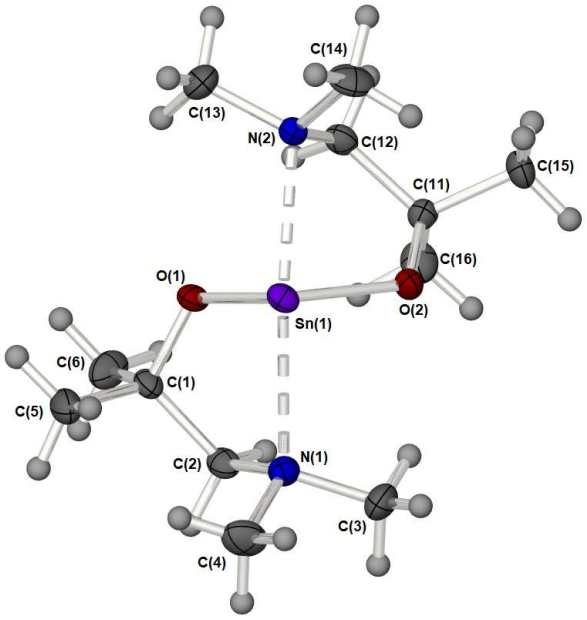

Figure 2.7 – Molecular structure of bis*(1-dimethylamino-2-methyl-2-propoxy)tin(II)* ***(7)****. Thermal ellipsoids are shown at 50% probability.*

Study of the bonding angles within the [$Sn(dmamp)_2$] complex can reveal some details as to the bonding environment within the complex and give an indication as to the geometry adopted by the system (Figure 2.8). Analysis of the structural data shows the angle formed between both equatorially bound nitrogen atoms (β) to be ~144.25(9)°, and the angle formed between axially bound oxygen atoms (α) to be ~98.30(9)°. It is to be expected that the formally covalent Sn–O bonds adopt largely the most energetically preferable orientation available, after which the dative N–Sn bonds from the pendant –NMe_2 groups coordinate within both the constraints of the freedom of direction and movement permitted by the ligand backbone, and within the confines of suitably oriented orbitals. Support for this assumption is found on analysis of the bonding around the oxygen itself, which is indicative of sp^2 hybridisation with an C–O–Sn angle of 122.1(2)° and no obvious distortion on interaction with the tin centre. Reinforcing this, the sp^3 –NMe_2 (C–N–C angles 109.8°, 109.7° and 112.6°) displays a C(backbone)–N–Sn angle of 101.1(2)°, which is less than the expected ~109° that would be expected for unencumbered coordination of the nitrogen-based lone pair within the sp^3 nitrogen-based group present.

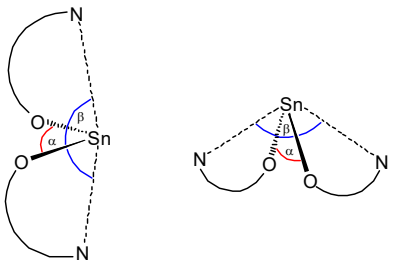

Figure 2.8 – Distorted pseudo trigonal bipyramidal and distorted square-based pyramidal geometries of four-coordinate tin(II) species. Comparison of the angle between equatorial atoms (α), and the angle between axial atoms (β), gives an indication of the extent of one particular geometrical configuration and orbital interactions involved.

The analysis of the oxygen and nitrogen bonding environments suggest an unconstrained sp^2 oxygen well-coordinated to the tin centre, coupled with an sp^3 nitrogen that shows non-linear lone-pair donation to the central metal atom. The extent of sp^3 nature of the nitrogen is estimated from the C–N–C angles and their deviation towards values greater than ~109.5°. A convenient mechanism to gauge this deviation is to calculate the sum of all three angles about the central nitrogen atom, as seen in Table 2.1.

*Table 2.1 – Relevant bond angles and lengths within $Sn(dmamp)_2$ **(7)**. (Atom labels where appropriate).*

Bond Angle (deg.)		**Bond Angle (deg.)**	
N–Sn–N	144.25(9)	C(2/12)–N–C(3/13)	110.6(2), 109.8(3)
O–Sn–O	98.30(9)	C(2/12)–N–C(4/14)	112.2(3), 112.6(3)
		C(3/13)–N–C(4/14)	109.0(3), 109.7(3)
C(1/11)–O–Sn	119.02(2), 122.1(2)		
C(2/12)–N–Sn	101.7(2), 101.1(2)	∑ C–N–C (sp^3 = ~328.5°)	331.8, 332.1

Bond Length (Å)	
N(1/2)–Sn	2.580(3), 2.436(3)
O(1/2)–Sn	2.050(2), 2.038(2)
C(1/11)–O	1.412(4), 1.412(3)

The analysis of the oxygen and nitrogen bonding environments suggest an unconstrained sp^2 oxygen well-coordinated to the tin centre, coupled with an sp^3 nitrogen that shows non-linear lone-pair donation to the central metal atom. The extent of sp^3 nature of the nitrogen is estimated from the C–N–C angles and their deviation towards values greater than ~109.5°. A convenient mechanism to gauge this deviation is to calculate the sum of all three angles about the central nitrogen atom, as seen in Table 2.1.

Two likely orbital configurations that could account for the coordination environment within [Sn(dmamp)$_2$] and similar four-coordinate tin(II) systems can be seen in Figure 2.9. In the case of an sp^2 hybridised tin centre (Figure 2.9a), hybridisation of the 5p$_x$- and 5p$_y$-orbitals with the 5s-orbital gives rise to a planar, equatorial distribution of orbitals with expected angles of ca. 120° between adjacent orbitals. This would result in a directional non-bonding electron pair taking an equatorial position, potentially compressing the angle between the remaining two orbitals responsible for the alkoxide Sn–O bonding. The unhybridised and empty p$_z$ orbital would therefore occupy the axial position, accepting electron density from axially positioned donors, such as the –NMe$_2$ pendant groups.

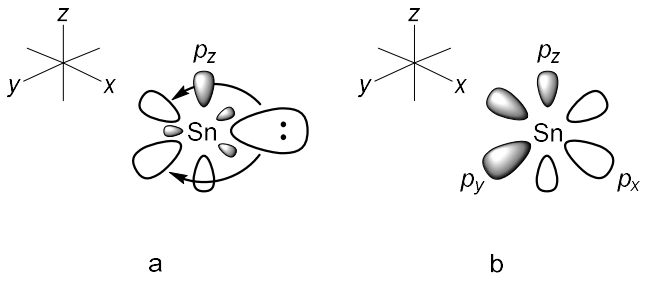

Figure 2.9 – Possible orbital configurations within four-coordinate Sn(II) complexes, showing an sp^2 hybridised tin centre with vacant, unhybridized p$_z$ orbital and directional lone pair (a), and unhybridized p-orbitals with lone pair based on the non-directional 5s orbital (b).

Alternatively, a system with a much lower degree of hybridisation would exhibit traditional p-orbital configurations with a significantly less directional lone pair inhabiting the 5s^2 orbital (Figure 2.9). This would give rise to an axial, equally unoccupied 5p$_z$-orbital, with equatorial 5p$_x$- and 5p$_z$-orbitals lying at ca. 90° to each other. In this case, equatorial orbitals would still account for the alkoxide bonding, with a vacant 5p$_z$-orbital available to accept donation from pendant chelating groups.

It is interesting to note that in both the hybridised and non-hybridised orbital configurations depicted in Figure 2.9, the axial position of the 5p$_z$-orbital remains unchanged. Significant differences are only observed in the equatorial bonding angles, with a non-hybridised system giving rise to an O–Sn–O angle of close to 90°, whereas a hybridised system would be expected to display values of <120° due to the compression of the O–Sn–O angle by a directional lone pair. The similar positioning of the 5p$_z$-orbital within both hybridised and non-hybridised orbital configurations allows for a discussion of the possible nature of the N→Sn bonding present within the system.

A basic partial molecular orbital diagram can be described and applied to understand the interactions between the lone pair of each sp^3 nitrogen atom and the vacant 5p$_z$-orbital of the tin centre (Figure 2.10). As can be seen from the diagram, only one case of compatible orbital symmetry exists for the N–Sn–N bonding, resulting in a three-centre-two-electron interaction.

This leaves remaining electron density residing in non-bonding purely nitrogen-based orbitals. This, exacerbated by a limited axial overlap (N–Sn–N angle ~144°), results in relatively long Sn–N bond lengths (2.580(3) Å and 2.436(3) Å) when compared with formally covalent Sn–N single bonds in molecules such as the $Sn(NMe_2)_2$ dimer (2.068 Å) and the $[Sn(HMDS)_2]$ monomer (2.087 Å). Indeed, the bond distance between tin and μ_2-bridging nitrogen within $[Sn(NMe_2)_2]$ is shorter than that observed within $[Sn(dmamp)_2]$, with a length of 2.266 Å.[99,100]

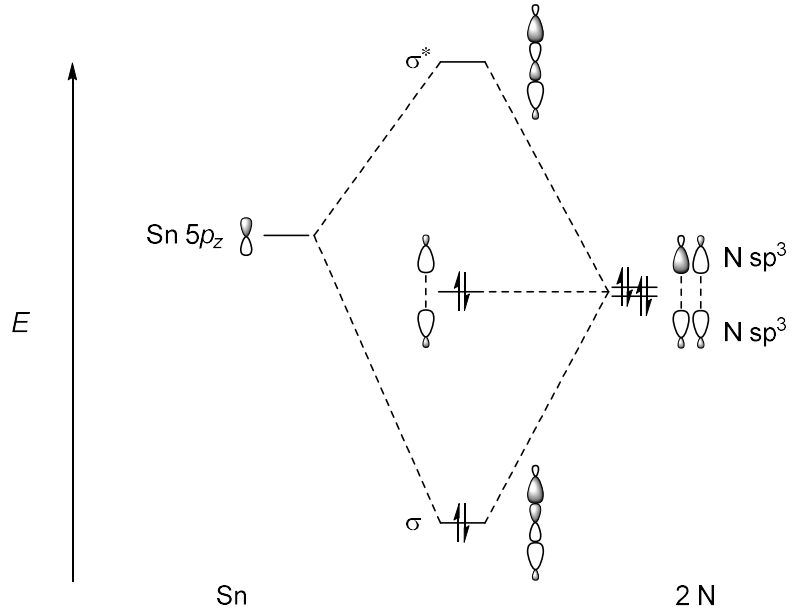

Figure 2.10 – Depiction of likely 3-centre-2-electron N–Sn–N bonding present within four-coordinate Sn(II) complexes such as $[Sn(dmamp)_2]$.

A mathematical concept known as a geometry index is often applied to four- and five-coordinate compounds in an attempt to quantify the extent of a particular geometry displayed by a complex. Scrutiny of the largest bonding angles (where $\beta > \alpha$) and submission into the appropriate equation below gives a numerical τ value between 0 and 1. For five-coordinate systems (τ_5), a value of 0 represents a purely square pyramidal geometry, whereas a value of 1 represents a purely trigonal bipyramidal geometry. Similarly, for four-coordinate systems (τ_4 and τ'_4), values from 0 to 1 are indicative of a transition from square planar to tetrahedral, via an intermediate “seesaw” geometry.

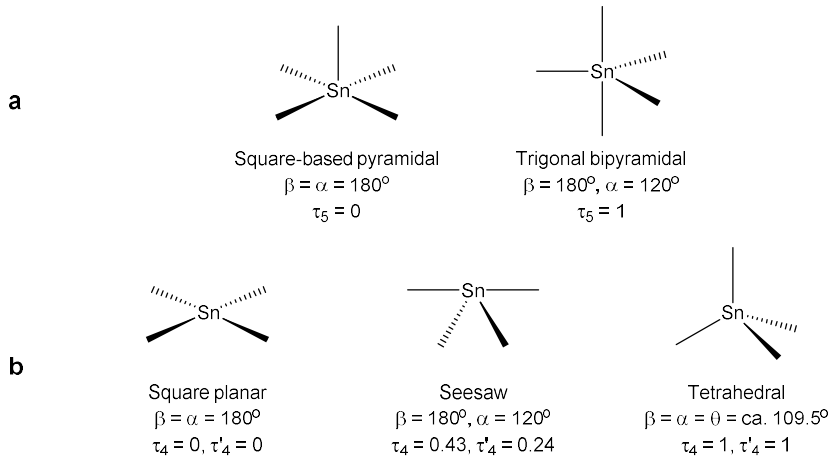

Figure 2.11 – Five- and four-coordinate systems with corresponding τ values – (a and b respectively).

Whilst the assignment of values within a five-coordinate system is relatively straightforward (Equation 2.3),[101] difficulties arise from the over-simplification of four-coordinate geometries. The original formula developed by Yang et al.[102] (τ_4 – Equation 2.4) makes no distinction between α and β angles, resulting in the possibility that molecules with substantially different geometries could display the similar τ values. For this reason, a later publication by Rosiak and co-workers[103] described an alternative formula (τ'_4 – Equation 2.5) for four-coordinate systems, using the two greatest valence bonding angles as before, but ensuring that the larger of the angles, where applicable, was assigned the value of β.

$$\tau_5 = \frac{\beta - \alpha}{60^o} \qquad \textit{Equation 2.3}$$

$$\tau_4 = \frac{360^o - (\alpha + \beta)}{360^o - 2\theta} \qquad \textit{Equation 2.4}$$

$$\tau'_4 = \frac{\beta - \alpha}{360^o - \theta} + \frac{180^o - \beta}{180^o - \theta} \qquad \textit{Equation 2.5}$$

$$where: \theta = cos^{-1}\left(-1/3\right) \approx 109.5^o$$

However, the presence of a lone pair that could be either directional or non-directional presents a significant challenge when determining whether formally four-coordinate systems such as $Sn(dmamp)_2$ are to be considered four-coordinate, or pseudo five-coordinate for the purposes of calculating a τ value. Table 2.2 displays calculated τ_4, τ'_4 and τ_5 values for $Sn(dmamp)_2$.

Table 2.2 – Calculated τ values for four- and pseudo five-coordinate [Sn(dmamp)$_2$].

	β, α	τ_x
τ_4	β = 144.25°, α = 98.30°	0.83
τ'_4	β = 144.25°, α = 98.30°	0.69
τ_5	β = 144.25°, α = 130.85°*	0.22

*calculated largest equatorial angle with inclusion of lone pair ((360°-98.30°)/2).

Whilst the calculated τ values for both four-coordinate and five-coordinate geometries are somewhat inconclusive, application of the methodology could prove useful in the comparison of [Sn(dmamp)$_2$] with related species. A number of factors are likely to influence the outcome of such calculations, such as the constrained chelation angles permitted by a ligand backbone length of only two methylene groups, and the unknown influence of the lone pair. This is particularly evident in the equatorial bond angles, where a ~98° O–Sn–O angle could either be the result of an unhybridized tin(II) centre with oxygen–tin interactions formed through 5p-orbitals at 90°, or could alternatively arise from a stereoactive lone pair compressing a 120° trigonal bipyramidal angle to ~98°.

It is currently unknown as to what extent a stereochemically active lone pair would influence the surface chemistry and reactivity within atomic layer deposition, however there would be particular merit in a computational study to this effect. The development and characterisation of a catalogue of suitable tin(II) oxide precursors is of great importance to the field, and could provide a suitable platform on which further studies could build.

2.2.3. Thermogravimetric analysis of [Sn(dmamp)$_2$]

Thermogravimetric analysis is an invaluable technique in the assessment of novel precursors for application in thermal deposition processes such as CVD or ALD. By monitoring changes in mass with increases in temperature, thermal stability and mechanisms of decomposition can be probed, whilst isothermal temperature studies can be used to determine the degree of volatility displayed by a precursor.

In contrast to chemical vapour deposition, atomic layer deposition relies on the chemical reactivity of a precursor with the growing film surface rather than thermal decomposition to drive film deposition. As such, processes must be carried out below the decomposition temperature of a precursor to prevent CVD-style growth. Due to the publication of differing thermogravimetric profiles for [Sn(dmamp)$_2$],[87,96] it was necessary to replicate the characterisation in order to embark upon deposition studies and comparison with any precursors synthesised as part of subsequent research.

Previous thermal characterisation of air- and moisture-sensitive compounds had necessitated TGA experiments to be undertaken by the filling and crimping of pierced aluminium crucibles within a glove-box, before withdrawal and loading at ambient atmosphere, and thermal analysis undertaken under a flow of argon. It was soon determined that this procedure was not appropriate for the high sensitivity of the precursors necessary for effective ALD. As a result of this, a Perkin Elmer TGA4000 thermal analyser was installed in a modified glove box under an argon atmosphere (Figure 2.12) with ambient pressure maintained by an oil-filled bubbler.

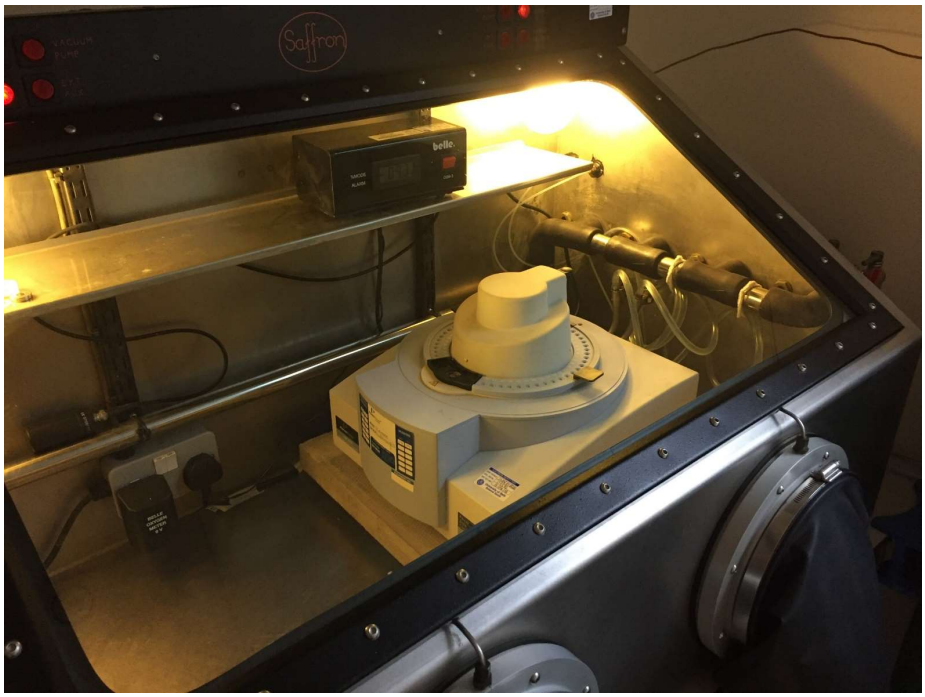

Figure 2.12 – Perkin Elmer TGA4000 installed in pressure-equalised Ar glovebox.

An example of the significant disparity between TGA conditions can be seen in Figure 2.13, which shows thermogravimetric profiles of [Sn(dmamp)$_2$] carried out in crimped pans under an argon flow in ambient atmosphere, and in open pans within an argon filled glovebox. Inspection of the former shows no appreciable mass loss until ca. 200 °C, indicating limited volatility, whilst the profile of the fully inert, open pan sample exhibits an immediate and steadily increasing loss of mass more representative of a volatile compound.

Also noteworthy is the large difference in residual mass between the two experiments, with masses stabilising at ~11% and ~31% for the inert and crimped samples respectively. The residual mass for the fully inert sample is well below any decomposition product that might reasonably be expected, indicative of significant volatility. In contrast to this, the residual mass for the crimped sample, whilst lower than that expected for either tin(II) or tin(IV) oxide (Table 2.3), is close to that of metallic tin (~34%). It is however, important to recognise that a combination of volatility in addition to reactions with ambient atmosphere could result in a wide

range of residual masses, highlighting the importance of an inert-atmosphere thermogravimetric installation. With volatility impaired by the crimped and pierced pan, the decomposition temperature of [Sn(dmamp)$_2$] can be seen around 230 °C, which correlates well with visual decomposition studies undertaken in a sealed glass tube (233 °C).

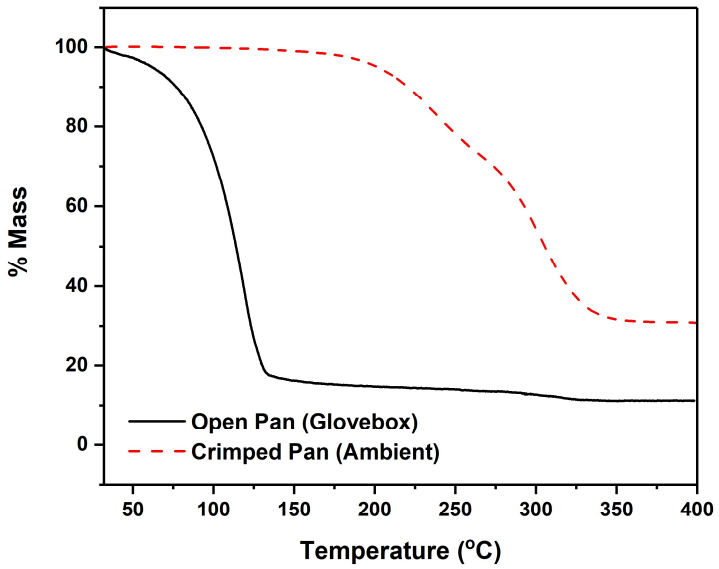

Figure 2.13 – TGA plots of [Sn(dmamp)$_2$] carried out in closed and open pans outside and inside glovebox respectively.

Table 2.3 – Residual masses from the TGA of [Sn(dmamp)$_2$] with expected masses of decomposition products under air and argon atmospheres.

Residual Mass (%)		Expected Mass (%)		
Crimped Pan (Ambient)	Open Pan (Glove Box)	Sn	SnO	SnO_2
31.0	17.0 (11.0)*	33.8	38.4	52.0

**Residual mass after final mass loss event at 325 °C.*

2.2.4. Process optimisation: [Sn(dmamp)$_2$]

A window of crystallinity for SnO deposited using [Sn(dmamp)$_2$] was defined by Han et al. to exist between 150 °C and 210 °C, though growth rates were noted to decrease with increasing temperature from 0.18 Å/cy at 150 °C to ca. <0.08 Å/cy at 210 °C.[87,104] The lack of a discernible "ALD window" consisting of a steady growth rate between two temperatures was rationalised by the low reactivity of the precursor, in conjunction with the reliance on surface bound hydroxyl sites, the density of which decreases with increasing temperature. This is an observation also made in a study by Nyns et al. on HfO_2 deposition from $HfCl_4$ and H_2O.[87,105]

At deposition temperatures of greater than 150 °C, crystalline films reported by Han et al. displayed highly preferential orientation with powder X-ray diffraction showing reflections at 2θ values of 18.3° and 37.1°, corresponding to the (001) and (002) planes respectively.[87] Tetragonal α-SnO exists in a layered structure, with laminar sheets of tin and oxygen atoms extending parallel to the *a* and *b* axes. The presence of primarily (001) and (002) reflections is consistent with what would be expected for the deposition of this layered structure lying parallel to the substrate surface (Figure 2.14).

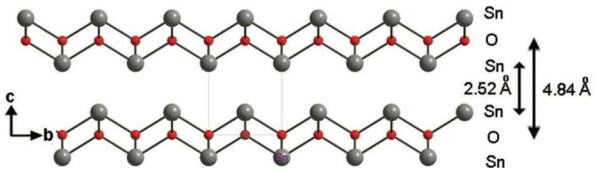

Figure 2.14 – SnO layered structure, with a and b axes lying parallel to substrate.[106]

Table 2.4 displays published parameters for the deposition of SnO using *bis*(1-dimethylamino-2-methyl-2-propoxy)tin(II).[87] The ALD tool used in the development of [Sn(dmamp)$_2$] is undisclosed by the authors, and as a result of this an initial process was devised for use on the Beneq TFS200 tool with a number of slight modifications. A nitrogen process gas was used in place of argon, as per the machine specifications, and an H_2O pulse of 0.15 s was initially used, as opposed to the published 5 s. This considerably shorter H_2O pulse was known to be sufficient for full surface saturation on the ALD tool within standard processes such as TMA/H_2O and DEZ/H_2O. In further support of this, many publications within the field utilise home-built ALD reactors with far less efficient surface saturation abilities than commercial tools such as the Beneq TFS200. Due to the decreasing growth rates with temperature, a 170 °C process was initially selected in order to attempt to replicate deposition on the commercial Beneq ALD tool. This was based on the assumption that deposition at this temperature gave the greatest likelihood to obtain crystalline growth at a rate that was still reasonably efficient.

Table 2.4 – Published process parameters for ALD of crystalline SnO from [Sn(dmamp)$_2$].[87]

Precursor	[Sn(dmamp)$_2$]
Precursor temp. (°C)	70
Reactor temperature (°C)	150-210
Pulse Sequence (s)	5:10:5:10
	Precursor:Purge:H_2O:Purge
Process gas	Ar 300 sccm
Substrate	SiO_2 (300nm) on Si

Whilst visibly yellow-tinted films were deposited after 425 cycles at a temperature of 170 °C using the modified process, no crystallinity was observed by p-XRD. In a bid to achieve this, anneals of 60 minutes were carried out on the amorphous films at a range of temperatures under ambient atmosphere, resulting in the evolution of detectable crystallinity (Figure 2.15). Despite the metastable nature of SnO with respect to further oxidation, there is limited evidence of the presence of crystalline SnO_2 until an annealing temperature of 350 °C, where a loss of SnO crystallinity occurs in tandem with the appearance of a reflection attributable to the (200) plane within crystalline SnO_2.[107,108] It is to be noted that the absence of crystalline SnO_2 is not evidence of a lack of oxidation of SnO however, which is highly likely to occur at high temperatures in the presence of O_2.

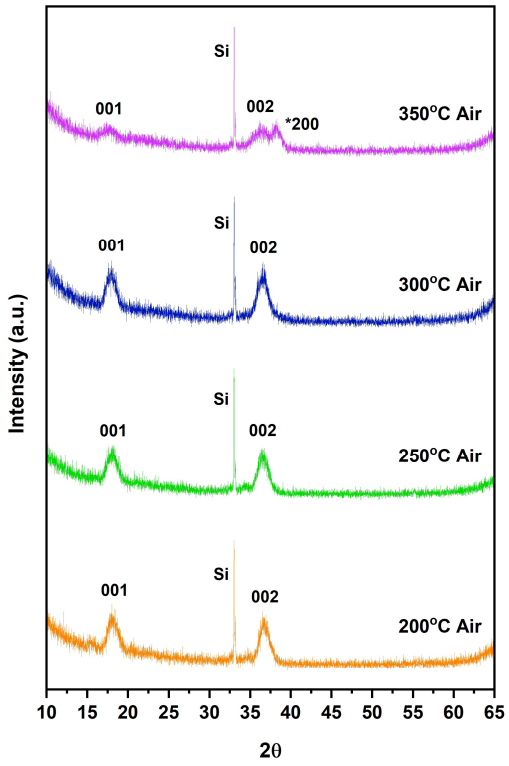

*Figure 2.15 – p-XRD patterns of post-annealed films deposited at 70 °C (JCPDS 06-0395). *Reflection ascribed to SnO_2 (200) (JCPDS 41-1445).*

Whilst the modified ALD parameters were not as successful at the deposition of crystalline SnO as the published process, the ability to anneal the as-deposited film to give the desired material was indicative of successful SnO deposition, with the lack of crystallinity a factor of processing conditions other than temperature. In order to address this, an identical pulse sequence to the published process was applied, including the full 5 s H_2O pulse, which resulted in the deposition of a film of low crystallinity displaying the expected (001) and (002) diffraction peaks (Figure 2.16, top).

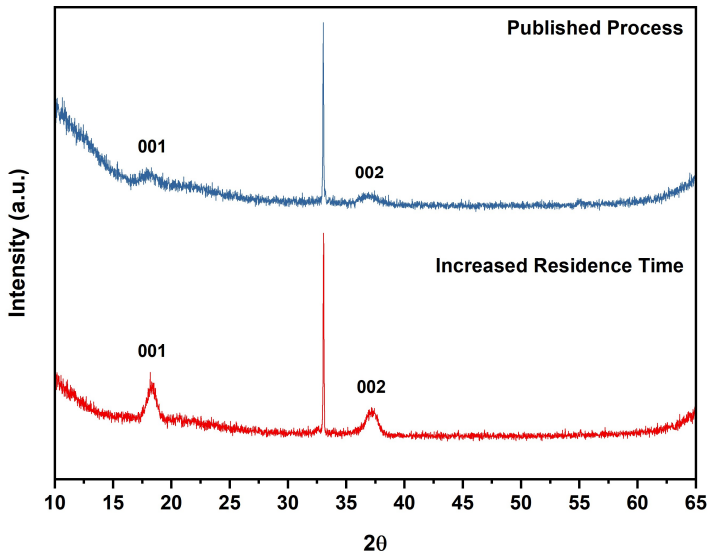

Figure 2.16 – Powder X-Ray Diffraction Patterns of published $Sn(dmamp)_2$ process and process with prolonged chamber residence time.

The crystalline films obtained from direct replication of the published pulse sequence displayed a thickness of 5.90 nm as measured by variable angle spectroscopic ellipsometry (VASE). This is equivalent to a growth per cycle of ca. 0.14 Å, which corresponds well to that reported for the same temperature by Han et al.[87]

Closer inspection of the p-XRD patterns of crystalline films can reveal further information about crystallinity beyond orientation. The diffraction peaks of a perfect, infinitely extending crystal are expected to appear as singular, symmetrical, well-defined peaks with no broadening. Any broadening of peaks that is observed occurs as a result of a combination of instrumental broadening, and to a far greater extent, the physical properties of the crystalline material. Properties responsible for peak broadening primarily include crystallite dimensions and strain caused by lattice defects such as twinning, grain boundaries, internal stresses and chemical heterogeneities.[109]

For crystallites with dimensions under ca. 1 μm, peak broadening as a function of size becomes increasingly prevalent. According to the principle that every fraction of crystallite with the same thickness will result in a defined contribution to peak broadening, the effective broadening of a peak is a weighted depiction of the sums of each thickness. This allows the mean dimension of a crystallite to be calculated for the reflection on which it operates. As an example, the thickness calculated from the peak broadening of the (001) plane correlates to the thickness of the crystallite with respect to the *C* axis.[109]

By applying a Gaussian fit to broadened diffraction peaks, a value for the full-width half-maximum (FWHM), or measure of the extent of broadening can be extracted. This can then

be applied, after the subtraction of any instrumental broadening, to a formula published by Paul Scherrer in 1918 that quantifies the extent of the phenomenon (Equation 2.6). A number of more modern derivatives exist, though for simple estimates such as those undertaken within this investigation, the Scherrer formula in its original form is still relevant and widely applied. This formula states that average grain size (*D*), relating to a particular set of *hkl* values, was found to be a function of; the Scherrer constant, (*K*), which is related to assumptions about crystal shape and most often ascribed values of ~0.9, the wavelength of incident X-rays, the 2θ value of the reflection in radians, and the observed broadening (*B*) in radians. The observed broadening can be defined by a number of techniques, but for simple dimensional analysis, the FWHM value is often applied.[110,111]

$$D_{hkl} = \frac{K\lambda}{B_{hkl}cos(\theta_{hkl})} \qquad \textit{Equation 2.6}$$

As reflections for the (001) and (002) planes can be clearly observed in the p-XRD pattern for the film deposited from direct replication of the published process (Figure 2.16), a basic estimate of the average crystallite dimension along the *C* axis can be made. The peak observed at 2θ = 33°, ascribed to that of the (200) plane of the crystalline silicon substrate, gives a good qualitative standard by which to gauge the impact of instrumental broadening, the extent of which is clearly reasonably limited with respect to the observed broadening of the (001) and (002) SnO reflections. Estimations of peak broadening are most accurate between 2θ values of ca. 30° and 50°, and hence the most appropriate reflection of deposited SnO to estimate crystallite dimensions is the (002) plane ($2\theta \approx 37°$), though analysis of the (001) plane ($2\theta \approx 18°$) will be included for comparison.[112]

Analysis of the FWHM value for the (001) reflection gives an approximate value of the *C* axis dimension to be ~4.8 nm. Interestingly, as mentioned previously, ellipsometry measurements estimate the film thickness to be ~5.9 nm. Accounting for the preferential orientation observed within the material, which places the *C* axis primarily perpendicular to the substrate surface, it could be suggested that much of the thickness of the film comprises single crystal domains. With reported surface roughness values of 3-5 nm for films deposited via this process, further research into this could prove interesting for the study of 2D materials. This proposition is discussed in greater depth in Chapter 3, where more extensive analysis of films is provided.

Despite the initial process comprising pulses expected to deliver sufficient volumes of water to the substrate, it was determined that on replicating the published process, including longer H_2O pulses, crystalline material could be obtained, as discussed previously. It was suspected that this was as a result of the low reactivity of precursor and its reaction rates with surface moieties, or with gaseous H_2O when it itself was adsorbed. This would account for the less efficient deposition and reduced crystallinity. This theory could also contribute to the lack of

visible “ALD window” observed by Han et al., with diffusion away from the substrate prior to reaction more pronounced at higher temperatures. It is also possible that this could additionally account for the lower than theoretical material density (~5.5 g/cm^3 cf. 6.45 g/cm^3) observed within the same publication.[87]

Table 2.5 – Optimised process parameters for increased residence time ALD process

Precursor	[Sn(dmamp)$_2$]
Precursor temp. (°C)	70
Reactor temperature (°C)	150-210
Pulse Sequence (s)	5:10:5:10
	Precursor:Purge:H_2O:Purge
Valve Sequence	Close Exhaust
	Pulse Boost Gas **2 s**
	Wait **50 ms**
	Pulse Precursor 1 **5 s**
	Wait **3 s**
	Open Exhaust
	Purge **10 s**
	Repeat with Precursor 2
Process gas	Ar 300 sccm
Substrate	SiO_2 (300nm) on Si

In an attempt to increase both the growth rate and crystallinity, a process attempting to maximise reactant time in the chamber was devised and is shown in Table 2.5. The process relies on identical pulse lengths, but includes the closing of an exhaust valve for 3 seconds after the introduction of the precursor to the chamber over the pulse length and into the purge time. This effectively increases the residence time of precursor in the chamber and results in a pressure increase in the reaction chamber from ~1.5 mbar to ~12 mbar with the continued flow of process N_2. This step is followed by the continuation of the purge cycle after which the process is repeated for the second precursor. This process, based on increased chamber residence time, resulted in films of higher crystallinity (Figure 2.16) and successfully raised the effective growth per cycle for films deposited at 170 °C from 0.14 Å to 0.17 Å. With an optimised process in place, further characterisation of [Sn(dmamp)$_2$] deposition was undertaken alongside alternative precursor development.

As used previously, the p-XRD analysis for the films obtained from the optimised ALD process (Figure 2.16, bottom) can be used to estimate crystallite dimensions along the *C* axis. After submission to the Scherrer formula, an average value of ~6.9 nm emerges, which, as was found for the film obtained via the published process, is approximately equal to the film thickness of as determined by spectroscopic ellipsometry (7.0 nm).

2.2.5. Deposition Studies: $Sn(dmamp)_2$

With the development of an optimised ALD process for [$Sn(dmamp)_2$], deposition was carried out at a range of temperatures to further explore process parameters and establish basic electrical characteristics of the material. Depositions were carried out at 90°, 130°, 170° and 200 °C. This allowed for relevant comparisons to be made with material deposited by Han et al.[87] at the same temperatures, and for an appropriate selection of material with which to undertake device fabrication.

Films deposited at 90 °C were amorphous by p-XRD, whilst films deposited at 170 °C and 200 °C exhibited the expected highly-oriented (001) crystallinity in findings consistent with those reported at the same temperatures by Han et al.[87] Interestingly, films deposited at 130 °C using the optimised methodology displayed high crystallinity and orientation, in contrast to the aforementioned published work, which reports the evolution of consistent crystallinity above temperatures of 150 °C (Figure 2.17).

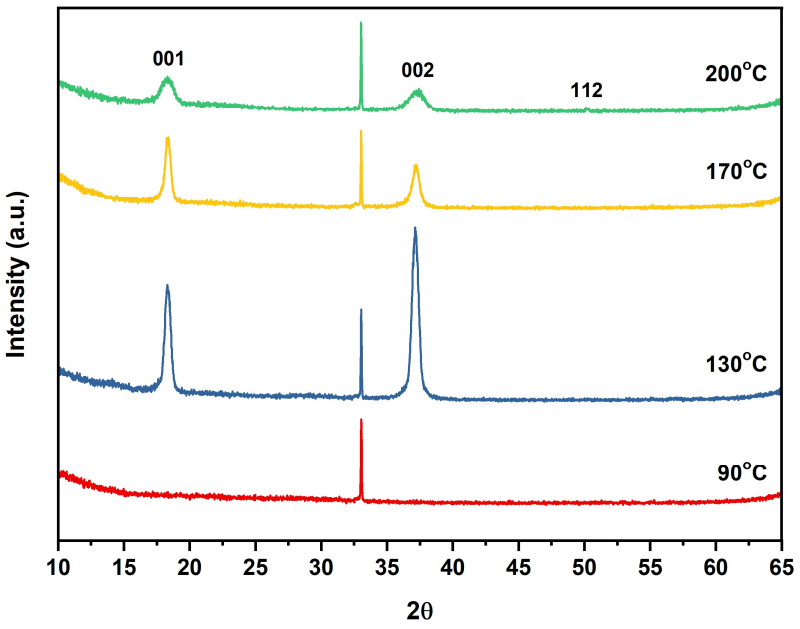

Figure 2.17 – Powder X-ray diffraction patterns of as-deposited films after 850 ALD cycles at 90 °C, 130 °C, 170 °C and 200 °C.

The thickness of each film was determined by variable-angle spectroscopic ellipsometry with a model corroborated by XRR measurements. After 850 ALD cycles at each given temperature, film thicknesses were found to be 30.2, 28.5, 14.3 and 7.0 nm for increasing temperatures respectively. As applied previously, rudimental Scherrer analysis of the (002) reflections affords an estimate of crystallite dimensions in the *C*-axis. These were found to be

13.6, 10.5 and 5.4 nm for films grown at 130 °C, 170 °C and 200 °C respectively. Annealing of the amorphous film grown at 90 °C for 1 h under an N_2 atmosphere in situ was found to yield films of the same orientation and crystallinity, with crystallite dimensions in the *C*-axis estimated to be 5.3 nm.

The densities of films deposited at 90, 150, 170 and 200 °C were estimated via X-ray reflectivity experiments carried out by J. Troughton, Durham University on behalf of PragmatIC Printing Ltd. As can be seen from Table 2.6, the densities of all crystalline films (130-200 °C) are near identical with values of ca. 6.5 g/cm^{-3}, whilst the amorphous film displays a lower density of ~5.2 g/cm^{-3}. This would be consistent with the expected increase in density on the evolution of a highly crystalline material. The densities are higher than those reported by Han et al.,[87] who report densities of 4.3-4.6 g/cm^{-3} for amorphous films, and densities of 5.4-5.5 g/cm^{-3} for crystalline films. The values of ~6.5 g/cm^{-3} are in good corroboration with the theoretical density of SnO, at ~6.5 g/cm^{-3}.[87]

Table 2.6 – Density and sheet resistance of SnO films vs. deposition temperature.

Temperature (°C)	**90**	**130**	**170**	**200**
Density (g/cm^{-3})	5.18±0.04	6.50±0.06	6.53±0.05	6.50±0.06
Sheet Resistance (Ω/sq)	2.6 x10^6	40 x10^3	4.3 x10^6	2.5 x10^6

The sheet resistance of the as-deposited films gives an indication of one aspect of the conductivity of the film. Whilst it is desirable for semiconducting films for transistor applications to display a high conductivity when in the “on” state, the latent conductivity of the films as deposited can be a significant disadvantage, resulting in gate leakage. As such, high sheet resistance films are sought for transistor applications. Whilst the sheet resistances for films grown at 90 °C and 200 °C were optimal, the two deposition temperatures were discounted. The amorphous nature of the films grown at 90 °C would significantly impair the already theoretically low mobility of the material, whilst the low (0.08 Å/cy) growth rates observed for deposition at 200 °C precluded its effective use in scaled up applications. Unsurprisingly, the exceedingly high (40 kΩ/sq) sheet resistance of the highly crystalline 130 °C deposition was more suited to TCO applications than CMOS devices.[113]

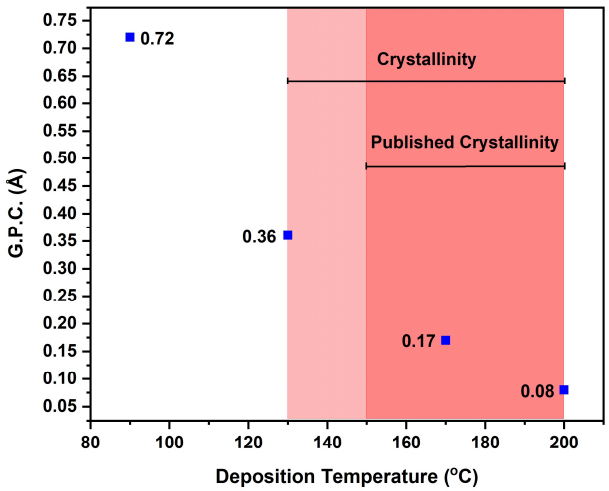

Figure 2.18 – Growth per cycle estimates and region of crystallinity after 850 ALD cycles at 90 °C, 130 °C, 170 °C and 200 °C.

The estimated growth per cycle pot (Figure 2.18) displays a largely similar profile to that observed within the initial publication. No obvious "ALD window" of consistent growth rate over a temperature span was observed in either the data published by Han et al. or within the replication contained herein.[87] Greater discussion on possible reasons for this observation is given in Chapter 4, though the surface-level interactions of low-reactivity precursors within ALD processes is the focus of a good degree of research within the field.[114–116] The degree of chemi- versus physisorption of precursors and the consequential effects of increasing temperature, purge times and reactivity times is fast proving to hold particular importance for low-reactivity precursors.

Testament to these considerations are the improved growth rates over published values demonstrated in this research. All temperatures demonstrated that the increased reactivity time offered by the newly formulated process offered an improvement in film growth. Furthermore, the temperature at which crystalline material is deposited has been decreased to 130 °C, where highly oriented films are grown at a rate of 0.36 Å/cy (reported rates of 0.22 Å/cy).

To fully characterise the enhanced aspect of these depositions, a series of experiments were undertaken to establish the linearity of the growth per cycle at 130 °C (Figure 2.19). The series of depositions confirmed the linear growth rate characteristic of ALD-type growth. The growth per cycle was confirmed to be 0.36 Å/cy, the most efficient growth of crystalline SnO films via ALD to date.

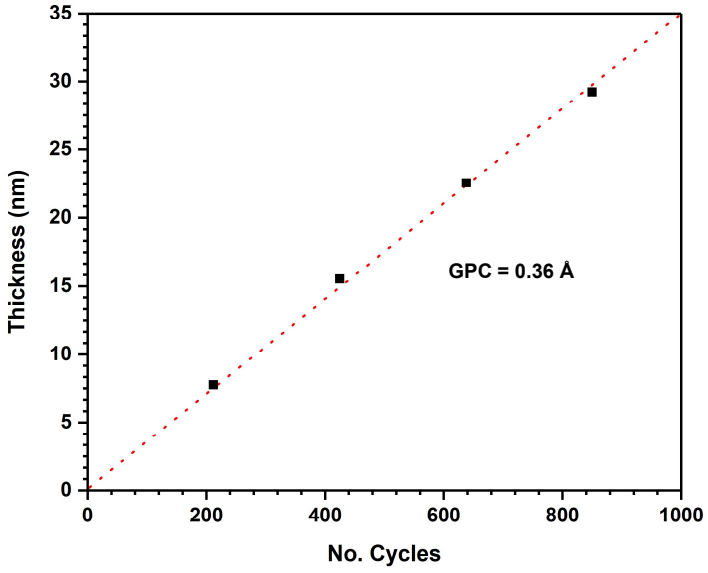

Figure 2.19 – Plot of film thickness as a function of number of ALD cycles at 130 °C.

2.2.6. Device Integration

In order to assess the electrical performance of the ALD SnO thin films, deposition was carried out onto device substrates fabricated by PragmatIC Printing Ltd. 850 ALD cycles (~15 nm) were undertaken at 170 °C using [$Sn(dmamp)_2$]. Device fabrication, which included the deposition of a passivation layer of Al_2O_3 as the top gate dielectric and annealing at 300 °C for 1 h, was undertaken by PragmatIC Printing Ltd., whilst electrical characterisations were carried out by Dr. Kham Niang, University of Cambridge.

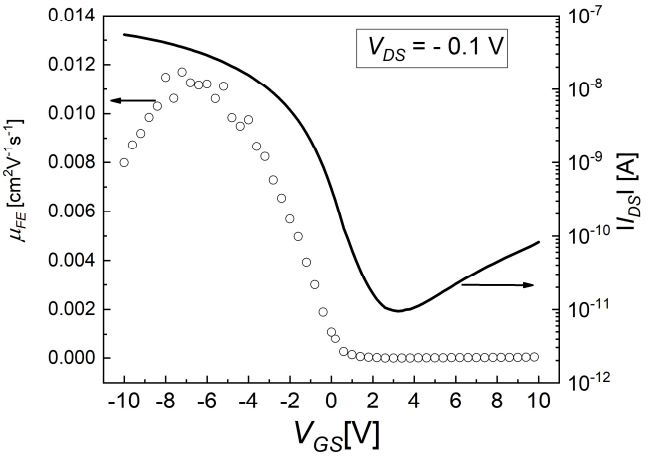

Figure 2.20 – Plot of field effect mobility (μ_{FE}) and source-drain current ($I_{DS}I$) vs voltage sweep.

Figure 2.20 shows a combined plot of field effect mobility (μ_{FE}) and source-drain current ($I/_{DS}I$) as a function of voltage. As a negative gate bias is applied, the field effect mobility of the SnO increases to a maximum of 0.012 $cm^2\ V^{-1}\ s^{-1}$. This is significantly lower than many reported devices incorporating SnO channel layers, including those fabricated using $[Sn(dmamp)_2]$ deposited at 210 °C by Kim et al., which display μ_{FE} values of ca. 1 $cm^2\ V^{-1}\ s^{-1}$.[104] It must however be noted that this is an initial proof-of-concept device at the first iteration, after transport in ambient atmosphere. The on/off current ratio was found to be 5 x 10^3, which is in good accordance with other SnO channel TFTs fabricated by traditional deposition techniques, which report values between 10^2 and 10^4.[117–121] The TFTs fabricated by Kim et al. report values as high as 2 x 10^6, though this is after significant optimisation in terms of deposition temperature and post-deposition annealing. Despite the lower performance, the SnO deposited at 170 °C through the optimised process described herein was shown to successfully act as a p-type oxide channel in a TFT device with a reasonable switching ratio despite low mobility.

2.3. Ligand Modification

2.3.1. Target compounds

With a reliable deposition process in place for the use of low reactivity precursors such as [Sn(dmamp)$_2$], a greater understanding of the electronic and steric balances that influenced reactivity was desirable. As such, a series of inexpensive and readily obtainable pro-ligands based around the dmamp ligand backbone were obtained and used to form a combination of novel and reported Sn(II) complexes.

In addition to the synthesis and characterisation of a range of bis-substituted homoleptic Sn(II) species such as [Sn(dmamp)$_2$], for completeness and to further understanding within the field, the heteroleptic mono-substituted systems, based on the Sn(II) amide reagent used were also catalogued. It was hypothesised that a full distribution of systems with subtle changes in ligand electronics would result in interesting structural observations, and as such, a number of subtly differing pro-ligands were selected, of the form HOC(R^1R^2)CH_2NMe_2, where: R^1, R^2 = H (dmae), R^1 = H and R^2 = Me (dmap), R^1, R^2 = Me (dmamp), and R^1, R^2 = CF_3 (Fdmamp). The four relevant pro-ligands are depicted in Figure 2.21.

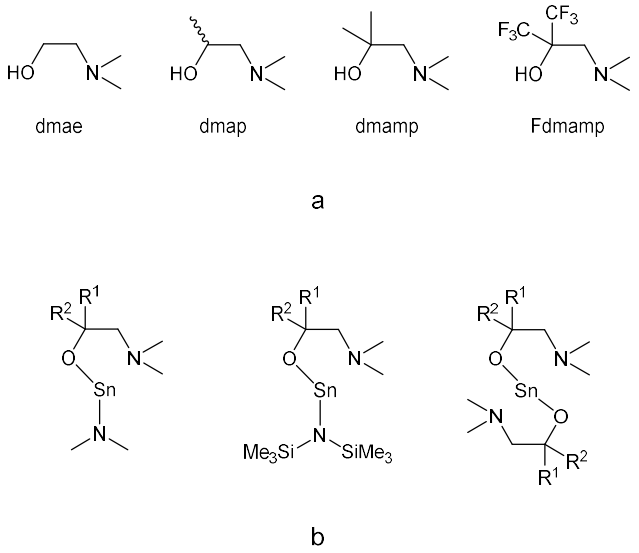

Figure 2.21 – (a) Pro-ligands dmae, dmap, dmamp and Fdmamp, and (b) target hetero- and homoleptic Sn(II) systems.

2.3.2. Sn(II) Aminoalkoxides: Synthesis

All complexes were synthesised through simple, high yielding ligand metathesis reactions between the aminoalcohol pro-ligand and a tin(II) amide of the form $Sn(NR_2)_2$ where R = Me, $SiMe_3$ (Scheme 2.7). Pro-ligands 2-dimethylaminoethanol (dmae) and (1-dimethylamino-2-propanol (dmap) were purchased from Sigma Aldrich and stored over activated 4 Å molecular sieves, whilst 1-dimethylamino-2-methyl-2-propanol (dmamp) and 3,3,3-trifuoro-1-dimethylamino-2-trifuoromethyl-2-propanol (Fdmamp) were synthesised from the appropriate epoxide as described in section 2.2.1. (Scheme 2.5a). In order to draw useful insights from the characterisation of compounds **1-12**, comparisons will be made between similar families of compounds.

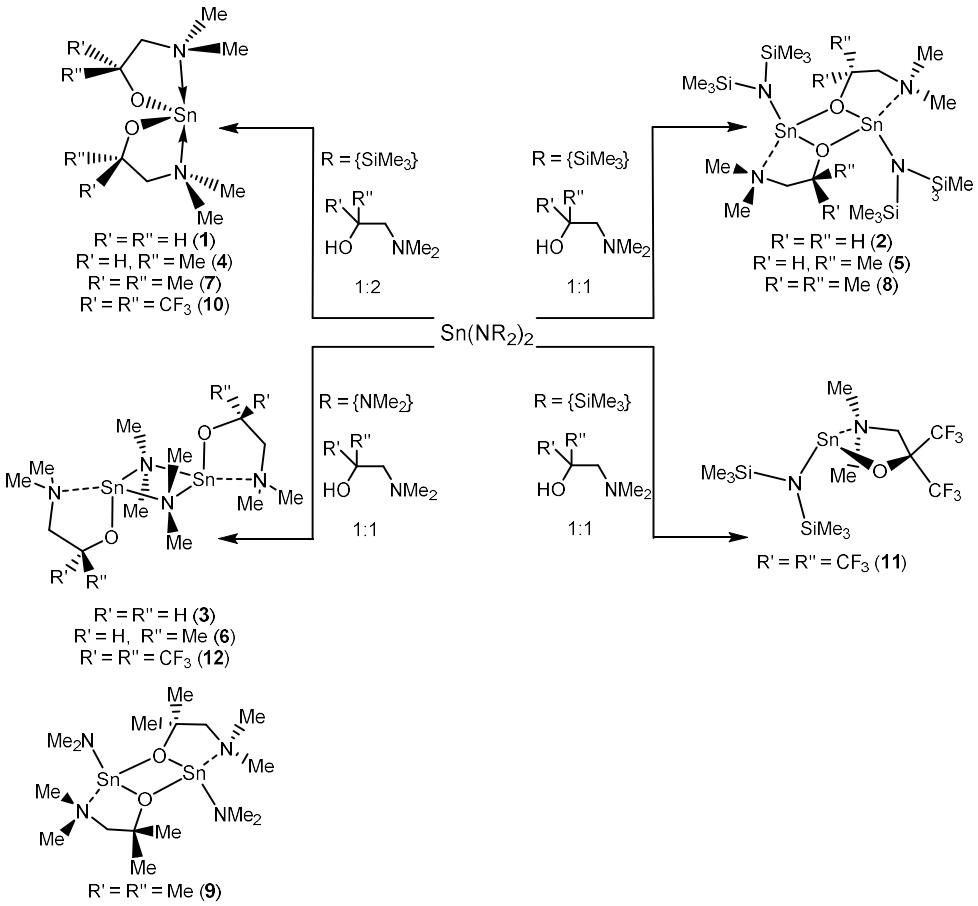

*Scheme 2.7 – Synthetic approaches to compounds **1-12**.*

2.3.3. Characterisation of Homoleptic Aminoalkoxides (SnL_2): 1, 4, 7 and 10

NMR Spectroscopy

^{1}H NMR spectroscopy of bis-substituted compounds **1**, **4**, **7** and **10** displays the expected resonances associated with the ^{1}H environments present within the ligand systems, including the omission for all complexes of the alcoholic proton lost upon amide liberation in the process of ligand metathesis.

The ^{1}H NMR spectrum of [Sn(dmae)$_2$] **(1)** demonstrates a triplet resonance at δ = 4.24 ppm (J = 5.3 Hz), ascribed to the C*H*$_2$ backbone nearest the alkoxide, with the remaining C*H*$_2$ defined by a broad multiplet at δ = 2.35 ppm (Appendix, 7.2). A singlet peak associated with the N*Me*$_2$ moiety completes the spectrum at δ = 2.10 ppm. Similarly, the ^{13}C{^{1}H} NMR spectrum displays resonances at δ = 63.4, 62.3 and 43.4 ppm. The ^{13}C{^{1}H} NMR resonances for both methylene backbone moieties appear shifted marginally downfield from their positions as observed in the free ligand, whilst interestingly the N*Me*$_2$ resonance can be found upfield from its uncomplexed position, indicative of a greater degree of shielding observed on complexation of the tertiary amine to the Sn(II) centre, contrary to what might perhaps be expected after donation of lone pair electron density to the central tin atom.

The various stereochemical configurations possible for [Sn(dmap)$_2$] **(4)** result in a complex ^{1}H NMR spectrum at room temperature. The chiral secondary carbon of the alkoxide ligand gives rise to a number of stereoisomers between two chelated ligands, with *RR*, *SS*, *RS* and *SR* configurations all likely to be present in solution. High temperature ^{1}H NMR in D_8-toluene (90 °C) allowed for full characterisation, clearly showing multiplets of equal integration for the chiral proton and the two protons of the methylene backbone, which appear as inequivalent due to influences of the chiral methyl substituent (δ = 4.18, 2.47 and 1.91 ppm respectively). Further to this, the expected resonances of the –N*Me*$_2$ and chiral methyl substituent are observed at δ = 2.16 and 1.21 ppm respectively (Appendix, 7.2). As observed in the ^{13}C{^{1}H} NMR spectrum of dmae discussed previously, the ^{13}C{^{1}H} resonances appear at high temperature in the expected order, with the deshielded alkoxide carbon appearing at the most downfield position, followed by the methylene group, the –N*Me*$_2$ groups and the backbone methyl substituent (δ = 68.9, 68.2, 44.1 and 24.4 ppm respectively).

The ^{1}H NMR spectrum of [Sn(dmamp)$_2$] **(7)** has been discussed previously (Section 2.2.2.), though a more in depth assessment of salient observations reveals that interestingly, on complexation to tin, the ^{13}C{^{1}H} resonance of the tertiary alkoxide carbon appears to shift downfield (δ = 70.26→74.28 ppm), indicative of a loss of electron density with the coordination of the adjacent oxygen to the central tin. Similarly, these inductive effects also result in a loss of electron density from the backbone CH_3 groups, with both the ^{1}H and ^{13}C{^{1}H} NMR spectra

displaying a shift of resonances downfield on complexation (^{1}H NMR δ = 1.13→1.38 and ^{13}C{^{1}H} NMR δ = 28.24→34.45). Conversely, and as observed in the analysis of [Sn(dmae)$_2$] (**4**), above, the ^{13}C{^{1}H} NMR spectrum exhibits an upfield resonance shift associated with increased electron density about the –N*Me*$_2$ moiety when compared to the free ligand (δ = 49.3→46.8). This is not, however, reflected in the ^{1}H NMR resonance, where slight deshielding is observed through a downfield shift from δ = 2.10 ppm to δ = 2.24 ppm. Whilst a very limited shift is seen the ^{13}C{^{1}H} resonance of the methylene backbone, the ^{1}H NMR spectrum shows a significant shift (δ = 2.01→2.34) on complexation, consistent with the induction of electron density through both heteroatoms.

The ^{1}H NMR spectrum of [Sn(Fdmamp)$_2$] **(10)** displays three environments, with a broad singlet at δ = 2.54 ppm (methylene C*H*$_2$) and two very broad signals of equal integration ascribed to the methyl groups of the chelating amine (δ = 2.07 and 1.75 ppm), which exist in inequivalent environments, a feature not observed in compounds **1**, **4** and **7** (Appendix, 7.2). This represents a considerable deviation from the characterisation of the free ligand, in which only two sharp multiplets centred at δ = 2.44 and 1.86 ppm are observed and assigned to the methylene backbone and equivalent –C*H*$_3$ groups respectively. The ^{19}F NMR spectrum again shows deviation, with the sharp multiplet of the free ligand (δ = –78.86 ppm) shifting marginally downfield and splitting into two resonances at δ = –76.40 and –77.55 ppm, indicative of further inequivalence on the ^{19}F NMR timescale within the complex. This is supported by the ^{13}C{^{1}H} NMR spectrum, which exhibits two broad resonances at δ = 47.8 and 46.0 ppm corresponding to the inequivalence within the –N*Me*$_2$ moiety. The multiplet resonance of the tertiary carbon shifts downfield on complexation from δ = 71.8 to 82.8 ppm, whilst only a negligible shift of the ^{13}C{^{1}H} environment attributed to the –*C*F$_3$ groups is observed (ca. 1 ppm), which presents in both spectra as a quartet (J = 290 Hz and 286 Hz uncomplexed).

It was discovered throughout the course of this research that the vast majority of the aminoalkoxide compounds investigated are extremely sensitive to hydrolysis normally induced by the presence of trace amounts of water in the pro-ligands. This hydrolysis results in the facile formation of oxo-bridged cluster compounds as determined by single-crystal X-ray diffraction. This fact is acknowledged by other studies within the field, such as the publication by Hollingsworth et al., which catalogues oxo- species formed during the synthesis of previously reported [Sn(dmae)$_2$] **(1)**. The formation of these species is usually evident through the presence of highly defined, sharp resonances in ^{119}Sn NMR spectroscopy, significantly differing from the broadened features more generally observed in the type of target compounds under investigation.[122–124]

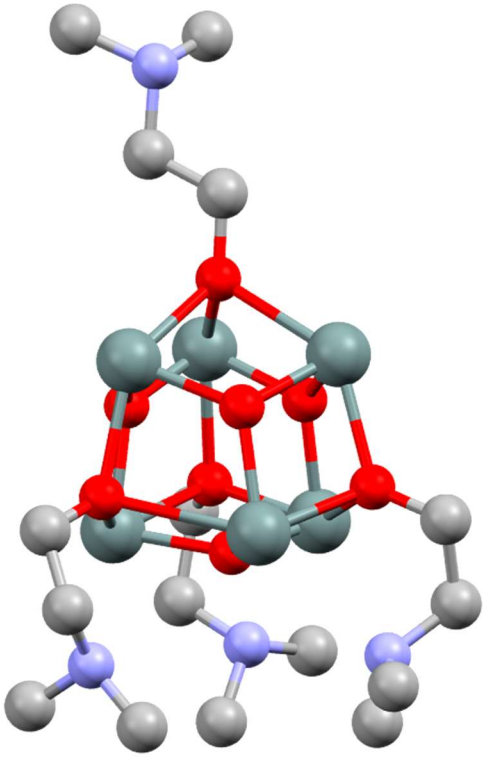

Figure 2.22 – Molecular structure of $Sn_6(O)_4(dmae)_4$.[122]

The synthesis and characterisation, including the ^{119}Sn NMR spectroscopy, of [Sn(dmae)$_2$] **(1)** was previously reported by Zemlyansky et al. and Hollingsworth et al.,[122,123] with both studies reporting a ^{119}Sn resonance for the desired compound at δ = –309 ppm, with an additional resonance reported by the latter study at $\delta \approx$ –161 ppm, attributed to the oxo-cluster [$Sn_6(O)_4(dmae)_4$] (Figure 2.22). Similar spectra were observed in the ^{119}Sn NMR of compound **(1)** as characterised in the course of this research, with an unexplained downfield shift of the [Sn(dmae)$_2$] resonance to δ = –279 ppm observed, alongside the characteristically sharp oxo-cluster resonance at δ = –156 ppm. This downfield resonance could be as a result of the facile interchange between coordination environments postulated in computational calculations by Zemlyansky et al., where the cleavage of the Sn←NMe_2 dative bond requires little energetic input.[123] As such, changes in concentration and solvent may influence the ^{119}Sn resonance observed. The ^{119}Sn NMR of [Sn(dmap)$_2$] **(4)**, displays two distinct tin environments, in addition to the presence of an additional cluster species at δ = –172 ppm. With the addition of a single methyl substituent to the ligand backbone resulting in the formation of a chiral ligand system, a number of different stereoisomers of complex **4** become possible. This, or alternatively the aforementioned labile Sn←NMe_2 bonding, could prove responsible for the two ^{119}Sn resonances associated with the target compound, which occur at δ = –231 and –259 ppm. Due to the broadened nature of these resonances, it is not immediately obvious whether concentration influences the relative intensities of these peaks, however high-temperature

^{119}Sn NMR observes a coalescence into a single, broad resonance positioned between the two initial shifts at δ = –246 ppm, making the explanation of different stereoisomers likely.

The ^{119}Sn NMR of [Sn(dmamp)$_2$] **(7)** is considerably more straightforward, with a single sharp resonance at δ = –218 ppm with no detectable presence of cluster by-products, likely due to the fact that the pro-ligand Hdmamp was synthesised and dried in-house. Whilst the complex as a whole exhibits chirality in an identical manner to the other systems described herein, there exists no additional chirality induced by the pro-ligand as seen in [Sn(dmap)$_2$] **(4)**. Similarly, the ^{119}Sn NMR of [Sn(Fdmamp)$_2$] **(10)** exhibits a single, well defined resonance at δ = –322 ppm. Interestingly, with the electron donating effects of backbone substituent towards the alkoxide expected to increase from $(CF_3)_2$ **(10)** << H **(1)** < Me **(4)** <Me_2 **(7)**, it would be reasonable to suggest a resultant shielding of the tin centre as this order is traversed, with the highly electronegative fluorinated system **(10)** appearing most downfield. Conversely to this hypothesis, ^{119}Sn resonances are observed to shift downfield as the series progresses (**10**-**1**-**4**-**7**), necessitating the analysis of structural data to attempt an explanation.

Single-Crystal X-Ray Diffraction

Homoleptic compounds **1**, **4**, **7** and **10** all display similar molecular configurations, with a pseudo trigonal bipyramidal geometry consisting of axially bound –NMe_2 groups and equatorially placed Sn-alkoxide bonds. Many of the concepts relevant to this discussion have been covered in the initial characterisation of [Sn(dmamp)$_2$] **(7)**, the molecular structure of which can be found in Figure 2.7, and will not be covered in depth.

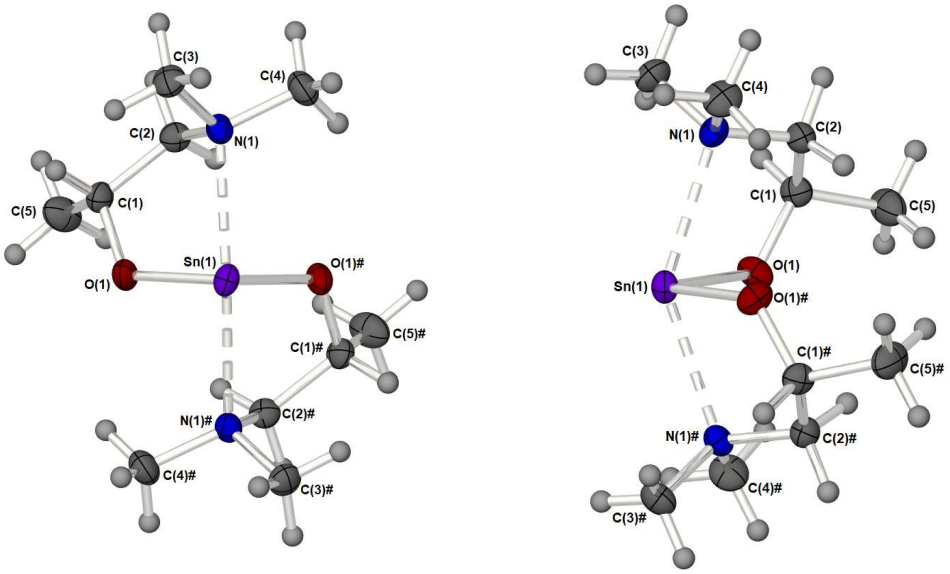

*Figure 2.23 – Molecular structure of [Sn(dmap)$_2$] **(4)**. Thermal ellipsoids are shown at 50% probability. Symmetry equivalent atoms are generated by the operator: #1–X, Y, ½–Z*

The solid-state structure of [Sn(dmae)$_2$] **(1)** was first described by Zemlyansky et al. in 2003, and analogous data was recollected throughout the course of this investigation.[123] When published, the monomeric compound was an important example of the stabilising effect of pendant donating groups in the prevention of dimerisation within simple, sterically undemanding tin(II) systems. Identical ligand environments are exhibited within compounds **1** and **4**, whilst slight deviations of the ligand environment on either side are seen in the geometries of **7 (**Figure 2.7**)** and **10 (**Figure 2.25). This is most likely due to the added steric influence of the Me_2 and $(CF_3)_2$ substituents, and in the case of the latter, the added complication of electronic repulsion observed within fluorinated molecules.

Table 2.7 displays relevant structural data relating to the bonding angles present within the homoleptic tin species discussed in this section, whilst salient bond lengths and torsion angles can be found in Table 2.8. The similarities between the sterically unencumbered systems [Sn(dmae)$_2$] **(1)** and [Sn(dmap)$_2$] **(4)** are evident, with two equivalent ligand systems in each. Many of the major bond and plane angles are exceedingly close, or even identical, though a small difference is seen in the marginally larger N–Sn–N angle observed for **1** (145.9° cf. 143.2°). As discussed previously, the calculation of either four- or pseudo five-coordinate τ values is of limited value when examining systems such as these.

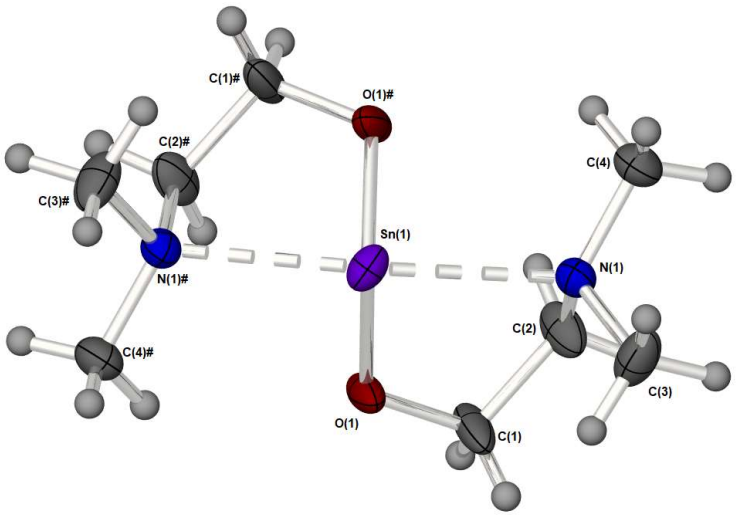

*Figure 2.24 – Molecular structure of [Sn(dmae)$_2$] **(1)**. Thermal ellipsoids are shown at 50% probability. Symmetry equivalent atoms are generated by the symmetry operator: #1–X, 1–Y, Z.*

*Table 2.7 – Relevant bond angle data for compounds **1**, **4**, **7** and **10**. (Atom labels where appropriate).*

	Angle (°) / Compound			
	1	**4**	**7**	**10**
N–Sn–N	145.86(19)	143.24(7)	144.25(9)	141.9(1)
O–Sn–O	96.4(2)	96.39(7)	98.30(9)	98.3(1)
N–Sn–N/O–Sn–O*	87.2	87.0	84.26	84.55
C(1)–O–Sn	118.8(3)	120.81(10)	-	-
C(1/11)–O–Sn	-	-	119.02(2), 122.1(2)	126.4(2), 121.4(2)
C(2)–N–Sn	101.0(3)	100.49(10)	-	-
C(2/12)–N–Sn	-	-	101.7(2), 101.1(2)	108.1(2), 105.7(4)
C(2)–N–C(3)	111.8(4)	110.6(1)	-	-
C(2/12)–N–C(3/13)	-	-	110.6(2), 109.8(3)	113.2(3), 113.2(6)
C(2)–N–C(4)	110.6(4)	112.0(1)	-	-
C(2/12)–N–C(4/14)	-	-	112.2(3), 112.6(3)	109.4(3), 111.8(6)
C(3)–N–C(4)	109.9(4)	110.0(1)	-	-
C(3/13)–N–C(4/14)	-	-	109.0(3), 109.7(3)	107.8(3), 108.7(6)
∑ C–N–C (sp^3 = ~328.5°)	332.3	332.6	331.8, 332.1	330.4, 333.7

*Smallest angle between N–Sn–N and O–Sn–O planes

It would be reasonable to assume from the C–O–Sn angles within the four systems (118.8°, 120.8°, ~119°/~122°, ~126.4°/~121.4°) that each alkoxide oxygen atom exhibits an sp^2 hybridisation. In both $[Sn(dmamp)_2]$ **(7)** and $[Sn(Fdmamp)_2]$ **(10)**, there is a divergence away from equivalent ligand environments, and this is reflected in the intramolecular difference between C–O–Sn angles. This is far more pronounced within the fluorinated system, though it still remains close to the expected ~120°. Interestingly, the Sn–O bond distances across all four molecules are strikingly similar (~2.05 Å), with small deviations seen in one of the two ligands in both **7** and **10**. This conformality in Sn–O bond environments across all four systems highlights the thermodynamic preferences of the alkoxide bonding taking precedence in spite of the change in ligand sterics and electronics.

It was hoped that these subtle alterations in ligand electronics would result in noticeable changes in Sn–O bond strengths and perhaps the reactivity of the molecule as a whole. The consistency in Sn–O bonding would imply that there is limited impact on bond strength, even with the introduction of the highly electron-withdrawing CF_3 substituents. Despite this, a clear shortening is observed of the O–C bond distances within the alkoxide ligands when fluorinated substituents are added (~1.36 Å cf. ~1.41 Å). It would appear that the withdrawal of electron density by the substituent groups acts on the oxygen in a manner that does not affect the nature of the Sn–O bonding. This likely involves one or both of the oxygen lone pairs and implies that at least one of these is not involved in any donation of electron density to tin. This

would be expected for the sp^2 lone pair, which is oriented away from the tin centre, but not necessarily for any lone pair residing in an unhybridized p_z orbital.

*Table 2.8 – Relevant bond length data for compounds **1**, **4**, **7** and **10**. (Atom labels where appropriate).*

	Bond Length (Å) and Torsion Angle (°) / Compound			
	1	**4**	**7**	**10**
Sn–O(1/2)	2.052(4)	2.0548(12)	2.050(2), 2.038(2)	2.050(2), 2.081(3)
Sn–N(1/2)	2.464(4)	2.4772(15)	2.580(3), 2.436(3)	2.449(3), 2.509(3)
O(1)–C(1)	1.412(7)	1.409(2)	-	-
O(1/2)–C(1/11)	-	-	1.412(4), 1.412(3)	1.361(4), 1.360(4)
OCCN (torsion)	52.0(6)°	51.3(2)°	50.7(3)°, 24.0(4)°	20.1(4)°, 40.4(7)°

The Sn–O bond lengths are reasonably commensurate with reported terminal alkoxide bonds within Sn(II) monodentate alkoxide complexes, such as $[Sn(O^tBu)_2]_2$ (2.010 Å) and $[Sn(OCRPh_2)_2]_2$ (where R = Ph (2.049 Å) and R = H (2.015 Å)).[2,125] Of the limited examples of similar monomeric and bi-chelating alkoxides with sp^3 nitrogen chelating group, $[Sn(OC(CH_2NH^tBu)_3)_2]$ exhibits a similar Sn–O bond length of 2.073 Å.[126] In addition, some examples exist of rigid-backbone analogues featuring aromatic, quinolin ligand frameworks and sp^2 nitrogen atoms, and typically exhibit slightly longer Sn–O bonds in the region of ca. >2.1 Å.[127,128]

The added steric and electronic effects of changing the backbone substituent from a single methyl to Me_2 and finally $(CF_3)_2$ cause an increasing disruption of the ligand environment. This not only manifests itself in the inequivalence of each ligand, but also in a degree of encumbrance to the uniform OCCN torsion across the ligand backbone. Torsion angles of 51-52° are present in **1** and **4**, and in one ligand within **7**, however the second ligand within $[Sn(dmamp)_2]$ exhibits a much smaller torsion of ~24°. Torsion angles across the ligand backbone within $[Sn(Fdmamp)_2]$ **(10)** are more significantly altered at ~20° and ~40°.

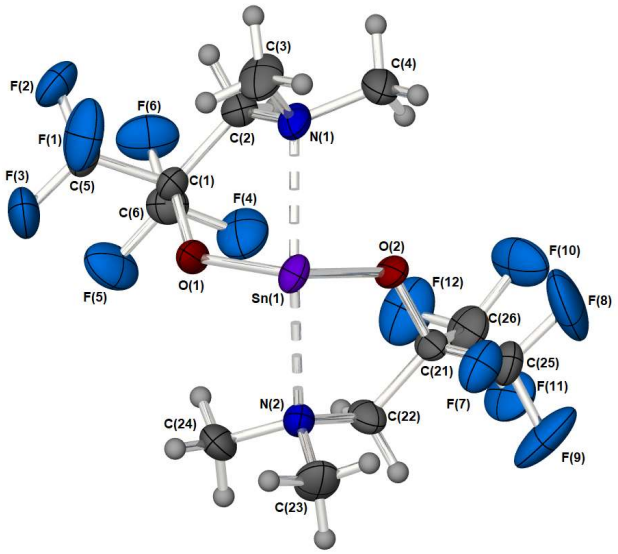

*Figure 2.25 – Molecular structure of [Sn(Fdmamp)$_2$] **(10)**. Thermal ellipsoids are shown at 50% probability. There is disorder in the CH$_2$NMe$_2$ moiety of the O(2) alkoxide ligand. The larger of the two components is shown (70:30).*

Study of the pendant –NMe$_2$ environment within complexes **1**, **4**, **7** and **10** shows that all nitrogen atoms display the expected bonding angles consistent with an sp^3 hybridisation, though once again [Sn(Fdmamp)$_2$] **(10)** exhibits a slight deviation between ligands. There appears to be no discernible pattern to Sn–N bond lengths across the series, with the only notable elongation appearing within [Sn(dmamp)$_2$] **(7)**, with one Sn–N bond appearing longer than its intramolecular counterpart. A more significant difference in chelating environment is observed between the C–N–Sn angles formed across the pendant nitrogen between the ligand backbone and tin centre. Whilst all non-fluorinated compounds display largely similar bond angles of ~101°, compound **10** exhibits angles of 108.1° and 105.7°, resulting in the nitrogen-based lone pair trained directly at the central tin atom, which is not seen in compounds **1**, **4** and **7**. It is possible that this feature is responsible for the unexpected upfield ^{119}Sn NMR shift (δ = –322 ppm) associated with an increased electron density at the nucleus.

Of particular interest amongst the homo- and heteroleptic compounds characterised throughout this investigation is the impact of alkoxide substituents on oligomerisation. It is worth noting that simple alkoxides such as tin neo-pentoxide [Sn(OCH$_2$CMe$_3$)$_2$] and [Sn(O^{i}Pr)$_2$] exist as oxygen-bridged polymers in the solid state, whilst bulkier [Sn(O^{t}Bu)$_2$] exists as a dimer.[124,125] Alkoxyethers, discussed later in this work, appear to also exist as dimers, whilst more recently reported aminoalkoxides of similar forms to those discussed in this section also present as systems of higher nuclearity. A publication on the latter by Han et al.[129] describes the aminoalkoxide compound [Sn(OCH$_2$CH$_2$CH$_2$NMe$_2$)$_2$], a compound analogous to [Sn(dmae)$_2$] **(1)**, which was found to exist as a polymer with no chelation of the pendant NMe$_2$. However, it was found that on addition of sterically encumbering methyl substituents on the alkoxide carbon, and a single methyl addition to the nitrogen-bonded backbone carbon atom, a dimeric species was obtained. Interestingly, this complex displayed marginally shorter

Sn–O bonds than those previously discussed, but similar length or longer Sn–N bonds (2.531(3) Å and 2.628 Å), despite a N–Sn–N bite angle of 164° allowing a far greater alignment with the p_z axis on the central tin atom.

With monomeric species desirable for ALD applications, the characterisation of compounds **1**, **4**, **7** and **10** provides a useful insight into the tolerance of the $^{-}OCR_2CR_2NMe_2$ pro-ligand to functionalisation, and as such could provide interesting alternatives to $[Sn(dmamp)_2]$ as an ALD precursor. To this end, thermogravimetric analysis was undertaken to determine the thermal stability and volatility of compounds **1**, **4** and **10**, and compared to that of the established precursor $Sn(dmamp)_2$ **(7)**.

2.3.4. Thermogravimetric Characterisation of Homoleptic Compounds 4, 7 and 10

Thermogravimetric Analysis – Mass/Temperature

The impact of ligand functionalisation on stability and volatility within the aminoalkoxide systems synthesised were probed with thermogravimetric analysis. Figure 2.26 shows the thermal profiles of $[Sn(dmae)_2]$ **(1)**, $[Sn(dmap)_2]$ **(4)**, $[Sn(dmamp)_2]$ **(7)** and $[Sn(Fdmamp)_2]$ **(10)**, which were carried out under an inert atmosphere in open aluminium crucibles as described in section 2.2.3.

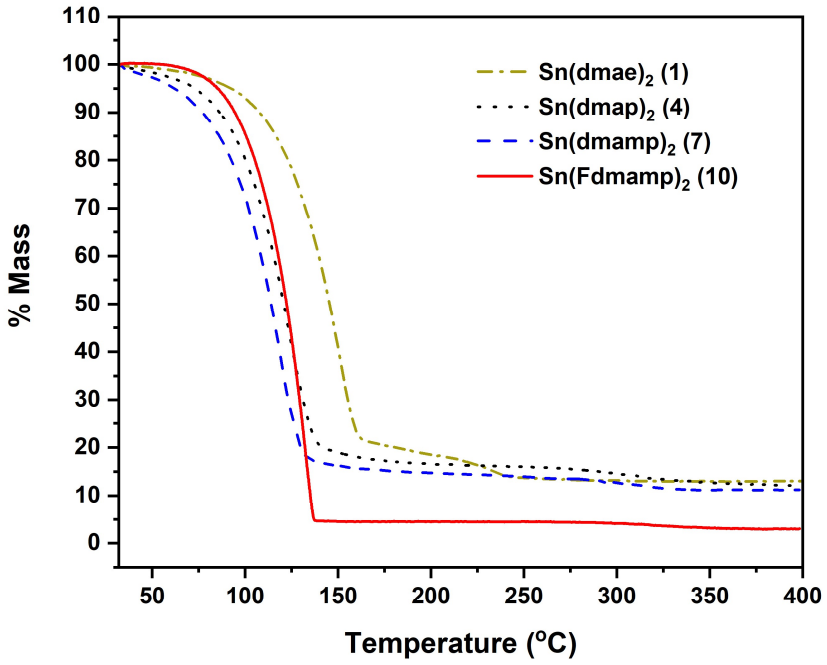

*Figure 2.26 – Mass loss/temperature plots of $[Sn(dmae)_2]$ **(1)**, $[Sn(dmap)_2]$ **(4)**, $[Sn(dmamp)_2]$ **(7)** and $[Sn(Fdmamp)_2]$ **(10)**. Ramp: 5°C min^{-1}, Ar flow 20 ml min^{-1}.*

With the exception of [Sn(dmae)$_2$] **(1)**, all complexes display a single large mass loss event consistent with volatility or extensive one-step decomposition. The low residual masses (Table 2.9) indicate that the former is more likely, with the final masses for all four complexes presenting well below that which would be expected for metallic tin.

*Table 2.9 – Residual masses from the TGA of **1**, **4**, **7** and **10**, with expected masses of decomposition products.*

		Expected Residual Mass (%)		
Compound	Residual Mass (%)	SnO	SnO_2	Sn
1	13.1	45.7	51.1	40.2
4	12.1	41.7	46.7	36.8
7	11.2	38.4	42.9	33.8
10	3.0	23.7	26.6	20.9

Whilst all complexes seem to display adequate degrees of volatility, it would appear that the volatility increases in the order [Sn(dmae)$_2$] **(1)** < [Sn(Fdmamp)$_2$] **(10)** < [Sn(dmap)$_2$] **(4)** < [Sn(dmamp)$_2$] **(7)**. Whilst volatile compounds should theoretically display a residual percentage mass of ~0%, reactivity with trace amounts of O_2 and H_2O, in addition to possible reactivity with surface bound species from the crucibles may account for the >0% residual masses encountered. Furthermore, it is highly likely that undetected cluster species remain present within the alkoxide samples, in addition to the propensity for these species to self-synthesise through elimination reactions. This is likely to be responsible for the second decomposition step seen in the TGA of [Sn(dmae)$_2$] **(1)**, as cluster species within this system are well-known, and to a large extent, unavoidable.[126] All complexes display promising TGA profiles for consideration as potential ALD precursors, though the profiles for complexes **4**, **7** and **10** are cleaner and appear most volatile.

Thermogravimetric Analysis – Isothermal

Isothermal analysis provides a simple method of quantifying volatility by measuring mass loss over time at a consistent temperature. With samples of differing weights, the most consistent method of displaying data is shown in Figure 2.27, with the rate of evaporation at a set temperature given by the gradient of each plot. Whilst more accurate quantification of evaporation rates and a value for enthalpy of evaporation can be gained through the collection of isothermal TGA measurements at a range of temperatures, screening of precursors based on relative volatilities is facile technique in order to assess initial compound viability.

It is also worth noting that a number of publications carry out isothermal TGA measurements with the results displayed in a plot of weight percentage against time, as opposed to the plot of mass against time contained herein.[130,131] The former is significantly flawed unless the

weight of each sample is identical, a variable that is incredibly difficult to control on the when loading microlitre-scale samples of reactive liquids. Even small differences in mass can lead to unrepresentative percentage mass changes when comparing rates between samples. As such, the plot of mass against time is the more accurate method of assessing relative volatilities (Figure 2.27).

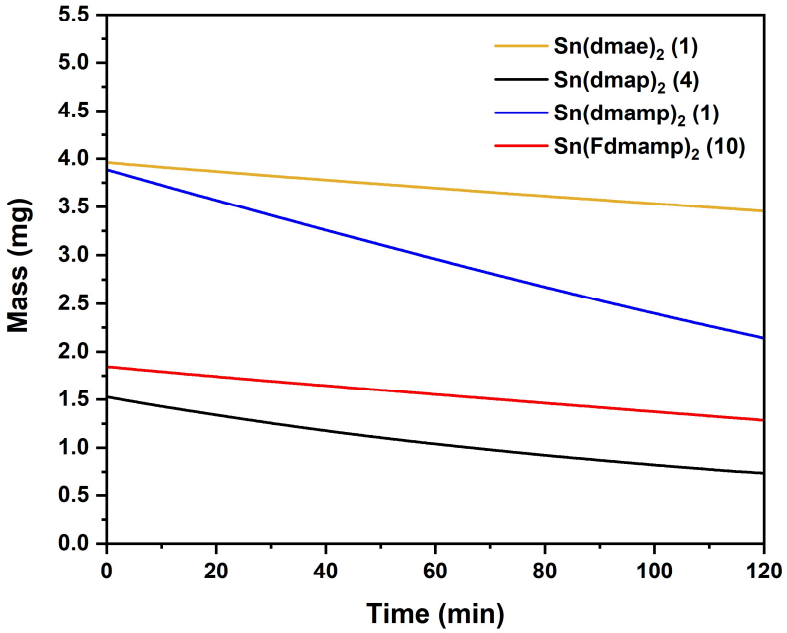

*Figure 2.27 – Isothermal plots at 70 °C of [Sn(dmae)$_2$] **(1)**, [Sn(dmap)$_2$] **(4)**, [Sn(dmamp)$_2$] **(7)** and [Sn(Fdmamp)$_2$] **(10)**. Ar flow 20 ml min^{-1}.*

*Table 2.10 – Evaporation rates of compounds **1**, **4**, **7** and **10** at 70 °C.*

Compound	Evaporation rate (μg min^{-1} cm^{-2})
1	33.7
4	55.0
7	118.7
10	36.8

Isothermal analyses were undertaken at a temperature of 70 °C, consistent with the precursor source temperature for [Sn(dmamp)$_2$] depositions. As indicated by the initial variable temperature thermogravimetric analysis (Figure 2.26), all compounds displayed degrees of volatility, with evaporation rates decreasing in the order [Sn(dmamp)$_2$] **(7)** >> [Sn(dmap)$_2$] **(4)** > [Sn(Fdmamp)$_2$] **(10)** > [Sn(dmae)$_2$] **(1)**. This order is consistent with the observed onsets of volatility in the variable temperature TGA. Whilst it is unsurprising that the complex with the straight chain ligand system dmae **(1)** is the least volatile (33.7 μg min^{-1} cm^{-1}), it is unexpected

that the volatility of the fluorinated system **(10)** is only marginally greater at 36.8 μg min^{-1} cm^{-1}. Despite the asymmetry introduced on the chiral ligand system dmap, the volatility is over half that demonstrated by $[Sn(dmamp)_2]$ **(7)**, which is the most volatile of the four species characterised (118.7 μg min^{-1} cm^{-1}).

2.3.5. Deposition Trials of $[Sn(dmap)_2]$ (4)

As discussed in the introduction to this chapter, dmap is an established and successful ALD precursor, and is the second-most volatile Sn(II) species studied after $[Sn(dmamp)_2]$ **(7)**. This fact, coupled with the substantial cost reductions offered by the commercially available alcoholic pro-ligand, dmapH, made $[Sn(dmap)_2]$ **(4)** the most obvious choice for further studies into its efficacy as an ALD precursor to SnO thin films. Further to this, the expense of synthesis of the fluorinated system, coupled with its obvious lower reactivity than its protonated counterparts made the selection of **(10)** unattractive. Similarly, despite the facile and cost-efficient synthesis, the lack of volatility in addition to the high tendency to form cluster species eliminated $[Sn(dmae)_2]$ **(1)** from further study without significant synthetic improvements.

ALD experiments were carried out using the optimised process parameters developed for $[Sn(dmamp)_2]$. A number of processes were trialled in attempts to deposit crystalline SnO, and whilst deposition of visible films was observed, the lack of crystallinity under any conditions prevented any further exploration of $[Sn(dmap)_2]$ as a precursor towards crystalline SnO thin films. Processes attempted in addition to variations in processing parameters included the deposition of a seed-layer of crystalline SnO using $[Sn(dmamp)_2]$, annealing of amorphous films under a range of conditions and the use of H_2O_2 as the oxidising precursor instead of H_2O.

2.3.6. Characterisation of Heteroleptic Aminoalkoxides $[Sn(L)N(SiMe_3)_2]$: 2, 5, 8 and 11

NMR Spectroscopy

The initial screening and consideration of potential ALD precursors focussed on homoleptic systems such as those covered in the previous section. This was largely due to the high likelihood of unequal reactivity between different tin-ligand bonds and the potential impact of this inequivalence on ALD processes. However, throughout the course of the investigation a number of heteroleptic systems were characterised which provided an interesting insight into the effect of steric and electronic factors within tin aminoalkoxide systems. The application of the ligand metathesis route from metal amides allows for facile synthesis of compounds which contain a single chelating aminoalkoxide and a single terminal amide ligand, such as –

$N(SiMe_3)_2$ or $–NMe_2$. As such, the heteroleptic systems [Sn(L)(HMDS)] were synthesised, where HMDS = $N(SiMe_3)_2$ and L = dmae **(2)**, dmap **(5)**, dmamp **(8)** and Fdmamp **(11)**. All NMR characterisation correlates with the molecular structures collected and the ^{1}H NMR spectra show clean loss of alcoholic protons and changes in chemical shifts from the unchelated pro-ligands.

As was found for the homoleptic [Sn(dmae)$_2$] **(1)** system, the heteroleptic [Sn(dmae)HMDS] **(2)** system has been previously characterised in a publication by Khrustalev et al., which found the complex to exist as an oxygen-bridged dimer in the solid state. Further to this, the monomeric germanium analogue was also characterised.[132] Structural and spectroscopic data for the [Sn(dmae)(HMDS)] complex were independently collected in this investigation and found to concur with the results described within the previous publication, with the ^{1}H NMR spectrum consisting of a triplet resonance at δ = 3.73 ppm (2H, C*H*$_2$O, $^3J_{HH}$ = 5.3 Hz), a broad multiplet at δ = 2.21 ppm (C*H*$_2$N), a singlet ascribed to –N*Me*$_2$ at δ = 1.99 ppm and a final singlet at δ = 0.46 ppm displaying $^2J_{SiH}$ (5.8 Hz) coupling arising from the $SiMe_3$ fragment. A similarly simple $^{13}C\{^1H\}$ NMR spectrum was found, comprising resonances at δ = 61.15, 57.99, 44.29 and 7.37 ppm, accounting for environments belonging to O*C*H$_2$, N*C*H$_2$, N*Me*$_2$ and Si*Me*$_3$ respectively. The resonance for the latter exhibits two sets of coupling; $^1J_{SiC}$ = 54.6 Hz and $^3J_{SnC}$ = 37.3 Hz. The ^{119}Sn NMR spectrum, previously unreported, was found to contain a single, broad resonance at δ = –168 ppm.

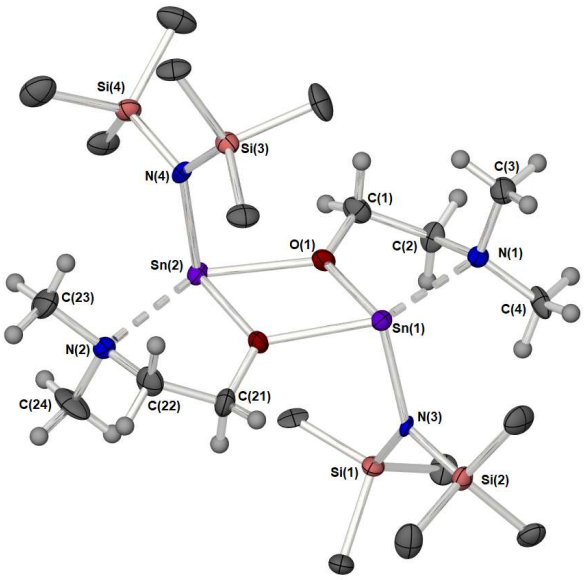

*Figure 2.28 – Molecular structure of [Sn(dmae)HMDS] **(2)**. Thermal ellipsoids are shown at 50% probability.*

The ^{1}H NMR spectrum of [Sn(dmap)HMDS] **(5)** displays clear differences in chemical shifts when compared to the protonated pro-ligand. A complex multiplet at δ = 4.11 ppm was observed for the chiral OC(*H*)Me, whilst the backbone methylene C*H*$_2$ was observed as two

distinct resonances depending on the *cis/trans* relationship to the chiral substituent. These resonances occur as a triplet at δ = 2.24 ($^{3}J_{HH}$ = 11.78 Hz) and a complex doublet at δ = 1.71 ppm. The remaining resonances at δ = 1.97, 1.31 (d, $^{3}J_{HH}$ = 6.1 Hz) and 0.46 ppm correspond to the –N*Me*$_2$, C(H)*Me* and SiMe$_3$ groups respectively. The $^{13}C\{^{1}H\}$ NMR spectrum is expectedly less convoluted, with resonances at δ = 68.87 and 67.25 ppm, both of which appear downfield from the comparable shifts within [Sn(dmae)HMDS] **(2)**, followed by resonances at δ = 45.25, 22.44 and 7.02 ppm (–N*Me*$_2$, OC(H)*Me* and Si*Me*$_3$). As was observed in the $^{13}C\{^{1}H\}$ of compound **2**, ^{1}J silicon-carbon and ^{3}J tin-carbon coupling can be seen on either side of the SiMe$_3$ peak, with values of 54.7 Hz and 33.5 Hz respectively. Further to this, the ^{29}Si NMR reveals a doublet ($^{1}J_{SiH}$ = 1.16 Hz) at δ = –3.51 ppm. The ^{119}Sn NMR occurs significantly downfield to that observed for compound **2**, at δ = –92 ppm, indicative of a more electron rich tin centre.

[Sn(dmamp)HMDS] **(8)** was found to exhibit a simple ^{1}H NMR spectrum consisting of four singlets at δ = 2.01, 1.98, 1.23 and 0.42 ppm, allocated to the –N*Me*$_2$, C*H*$_2$, OC*Me*$_2$ and Si*Me*$_3$ moieties respectively. A similarly self-explanatory $^{13}C\{^{1}H\}$ spectrum is observed, with resonances at δ = 75.61, 71.56, 47.90, 32.42 and 6.40 ppm. The $^{13}C\{^{1}H\}$ environments are allocated in an identical order to that described in the spectrum of **5**, with the most downfield assigned to the tertiary O*C*(Me$_2$), followed by the *C*H$_2$, N*Me*$_2$, C(*Me*)$_2$ and Si*Me*$_3$ groups. Interestingly, the tertiary and methylene carbon environments occur even more downfield than seen in compound **5**, indicative once again of a greater degree of electron density. As seen previously, ^{1}J silicon-carbon and ^{3}J tin-carbon coupling are observed around the Si*Me*$_3$ peak ($^{1}J_{SiC}$ = 55.0 Hz and $^{3}J_{SnC}$ = 25.4 Hz), in addition to a peak at δ = –2.55 ppm found in the ^{29}Si NMR spectrum. ^{119}Sn NMR shows a considerably further downfield resonance than is seen in compounds **2** and **5** at δ = 123 ppm, appearing as a triplet in accordance with similar systems described by Wang et al., who report a ^{119}Sn–^{14}N coupling of 256 Hz in the complex [Sn(μ-O^{i}Pr)(N(SiMe$_3$)$_2$)]$_2$.[133] However, closer inspection reveals the peak to be a complicated multiplet, presumably due to coupling both the nitrogen of the HMDS group and the nitrogen of the NMe$_2$ group coordinated to the tin in complex **8**.

The NMR characterisation of [Sn(Fdmamp)HMDS] **(11)** displays a simplified ^{1}H NMR spectrum, with singlet resonances at δ = 2.34, 1.84 and 0.29 ppm assigned to the methylene, amino and Si*Me*$_3$ groups respectively. The ^{19}F NMR displays a complex multiplet centred around δ = –76.88 ppm, believed to be due to coupling between inequivalent {CF$_3$} groups as well as ^{119}Sn and ^{117}Sn centres. Despite numerous attempts to obtain a full $^{13}C\{^{1}H\}$ NMR spectrum, only resonances for the protonated environments can be observed, with the methylene environment appearing at δ = 57.93 ppm and the –N*Me*$_2$ and Si*Me*$_3$ groups appearing at δ = 46.27 and 5.29 ppm. The ^{119}Sn NMR spectrum displays a resonance at δ = 94 ppm, which is marginally more upfield than that found for the non-fluorinated analogue **(8)**.

Single-Crystal X-ray Diffraction

The solid-state structures of compounds **2**, **5**, **8** and **11** were unambiguously determined via single-crystal X-ray diffraction. Whereas the structures of the bis-substituted, homoleptic species **1**, **4**, **7** and **10** were found to be largely similar, existing as monomers with only minor variations in ligand geometries, the structures of the heteroleptic analogues display a clear change in coordination environment with substituent group. For all but the fluorinated system **(11)**, which was found to be monomeric, the heteroleptic {HMDS} species **(2**, **5** and **8)** exist as oxygen-bridged dimers in the solid state. As mentioned in the discussion of spectral data, the molecular structure of [Sn(dmae)HMDS] **(2)** has been previously reported by Khrustalev et al. and was found to be consistent with the structure collected as part of this research.[132]

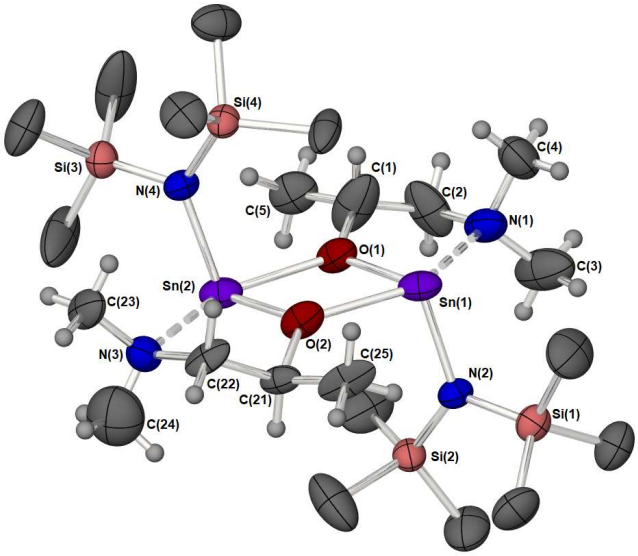

*Figure 2.29 – Molecular structure of [Sn(dmap)HMDS] **(5)**. Thermal ellipsoids are shown at 50% probability. Disorder is present in the ligand based on O(2) in addition to one of the $SiMe_3$ groups (Si(4)). Disorder is in a 55:45 occupancy ratio for both sets of disorder. Furthermore, the crystal exhibits twinning.*

The molecular structures of compounds **2**, **5** and **8** consist of a planar central $\{Sn_2O_2\}$ heterocycle, with μ_2–bridging, chelating alkoxide ligands. As seen in the homoleptic systems, the tin atoms adopt a distorted, pseudo trigonal bipyramidal geometry with an axially-coordinated $–NMe_2$ group from a chelated aminoalkoxide, and an axially-coordinated alkoxide bridge from the second aminoalkoxide ligand on the adjacent tin atom. The bulky $–N(SiMe_3)_2$ ligand and second alkoxide bridge, formed from the chelated aminoalkoxide, occupy equatorial positions about the tin centre, alongside a stereoactive lone-pair. Due to substantial structural constraints such as the $\{Sn_2O_2\}$ ring, the chain length of the bidentate ligand and the steric demands of the HMDS group, the pseudo trigonal bipyramidal geometry is significantly distorted, as can be seen in Figure 2.30.

The structure adopted by compounds **2**, **5** and **8** is a common arrangement for tin(II) dimers, with many species such as $[Sn(O^tBu)_2]_2$,[125] $[Sn(NMe_2)_2]_2$,[100] $[Sn(O^tBu)HMDS]$,[134] and $[Sn(dmae)OR]_2$ (where R = ^{t}Bu, Ph)[135] crystallising in an identical manner. These dimers almost universally display a transoid arrangement, with terminal ligands directed on opposite faces of the $\{Sn_2O_2\}$ heterocycle. This is reflected in the structures of **2**, **5** and **8**, where bulky HMDS ligands adopt this transoid conformation. However, a recent exception to this can be seen in a publication by Hill et al., which characterised the cisoid tin(II) alkoxide dimer $[Sn(OCPh_3)_2]_2$, which despite the presence of bulky phenyl substituents, was found to exist with both terminal species on the same side of the $\{Sn_2O_2\}$ ring. It was tentatively suggested that this conformation was stabilised by dispersion forces between phenyl rings.[2] Of further relevance to this discussion, it is also worth noting that $[Sn(HMDS)_2]$ has been shown to be monomeric with a two-coordinate tin centre due to the steric stabilisation offered by the bulky $–N(SiMe_3)_2$ fragments.[99]

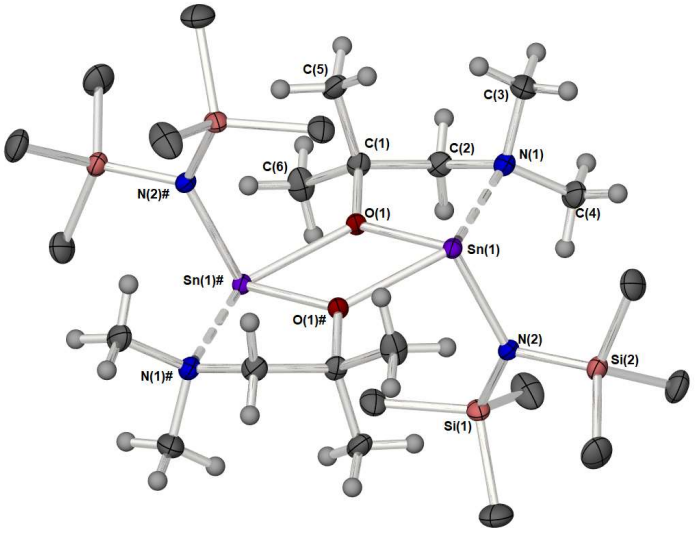

Figure 2.30 – Molecular structure of [Sn(dmamp)HMDS] ***(5)****. Thermal ellipsoids are shown at 50% probability. Symmetry equivalent atoms are generated by the operator: #1–X, 1–Y, 1–Z*

Salient bond lengths and angles found within compounds **2**, **5** and **8** can be seen in Table 2.11. Whilst all adopt identical structures, both [Sn(dmae)HMDS] **(2)** and [Sn(dmap)HMDS] **(5)** display marginally different, though statistically indistinguishable, environments on each half of the molecule, as divided by tin centres. Conversely, [Sn(dmamp)HMDS] shows greater symmetry, with the completely identical environments on each half of the complex. On further scrutiny, and as was seen in the homoleptic systems discussed previously, no appreciable difference in Sn–O bond lengths was observed between compounds **2**, **5** and **8**, though all were longer than the ca. 2.05 Å lengths seen in the monomeric species **1**, **4**, **7** and **10**. This is an expected change, as each alkoxide oxygen within the dimeric systems forms a μ_2 bridge between the two tin atoms associated with the loss of electron density through dative interactions that this incurs. From the bonding angles about each oxygen atom, it is to be expected that an sp^2 hybridisation is adopted, and as such, a planar $\{Sn_2O_2\}$ heterocycle could

be expected to comprise both covalent and dative Sn–O bonds. This is supported by an inequivalence in bond lengths around the heterocycles, which is also observed in related systems in which similar bond lengths are observed ([Sn(dmae)OPh]$_2$, 2.118(1) Å and 2.245(1) Å; [Sn(OR)HMDS]$_2$, R = CC(Me)$_2$CH$_2$SC$_6$H$_4$-*o*-CH$_2$NMe$_2$, 2.168(4) and 2.250(4)).[135,136] Whilst commensurate with these similar systems, little difference is observed in Sn–O bond lengths between compounds **2**, **5** and **8**.

No meaningful correlation presents itself when comparing dative axial Sn←NMe$_2$ bond lengths, though the related systems [Sn(dmae)OR]$_2$ (where R = ^{t}Bu, Ph) and [Sn(dmae)Cl]$_2$ display slightly shorter bonds at 2.503(1) Å, 2.472(1) Å and 2.499(4) Å respectively. A noticeable, if small, trend however is observed within the Sn–Sn distances across the {Sn$_2$O$_2$} heterocycles, with distances increasing along with steric bulk of ligand backbone substituent (dmae **(2)**, 3.6529(8) Å; dmap **(5)**, 3.6679(8) Å and dmamp **(8)**, 3.7152(2) Å). On examination of the molecular structures, it can be seen that these backbone moieties sterically interact with the HMDS groups, accounting for the slight expansion of the tin–tin distance across the series. The Sn–N(SiMe$_3$)$_2$ bonds show an elongation with the progression from dmap to dmamp ligands (**5** to **8**), and are similar to those found in sterically strained systems such as [Sn{C(SiMe$_3$)$_2$C$_5$H$_4$N-2}HMDS] (2.144(5) Å)[137] and [Sn{^{t}BuC(NCy)$_2$}HMDS] (2.134(4) Å).[138] These values are however significantly longer than those observed in systems such as [Sn(OAr)HMDS] (Ar = C$_6$H$_2$-*o*-^{t}Bu-*p*-Me, 2.079(3) Å)[139] and Sn[N(SiMe$_3$)$_2$]$_2$ (2.088(6) Å and 2.096(1) Å).[99]

By far the most significant impact of ligand backbone substituent is observed on the incorporation of fluorinated moieties. Whereas the compounds **2**, **5** and **8** exist as μ–O dimers, [Sn(Fdmamp)HMDS] **(11)** was found to crystallise as a monomeric species (Figure 2.31), the structure of which is much more reminiscent of the reported [Ge(dmae)HMDS] analogue of compound **2**, which was reported to be monomeric.[132]

*Table 2.11 – Relevant bond lengths and angles within compounds **2**, **5** and **8**.*

Angle (°) / Bond (Å) / Compound	**2**	**5**	**8**
Distance			
$Sn_1–N_{(NMe2)}$	2.634(6), 2.613(6)	2.596(8), 2.64(3)	2.592(2)
Sn–O	O(1): 2.126(5) O(2): 2.145(5)	O(1): 2.136(7), O(2): 2.120(6)	2.130(1)
$Sn–N_{(HMDS)}$	O(1): 2.150(5) O(2): 2.155(5)	O(1): 2.147(7) O(2): 2.158(7)	2.183(2)
Sn–O	O(1): 2.264(4) O(2): 2.304(4)	O(1): 2.339(6) O(2): 2.320(6)	2.381(1)
Sn–Sn	3.6529(8)	3.6679(8)	3.7152(4)
O–C	1.401(8), 1.399(7)	1.43(1), 1.48(2)	1.440(2)
∑ Sn_2O_2 ring	359.51	359.93	360
Angle			
O–Sn–O	68.8(2), 67.8(2)	69.0(2), 69.6(2)	69.23(5)
Sn–O–Sn	111.0(2), 111.8(2)	110.7(3), 110.6(3)	110.77(6)
Sn–O–C	123.9(4), 121.1(4)	117.4(7), 114.7(7)	122.1(1)
$N_{(NMe2)}–Sn–O_{(trans)}$	139.5(2), 138.8(2)	141.5(2), 146.0(6)	142.72(5)
$O–Sn–N_{(HMDS)}$	O(1), N(2): 105.8(2) O(2), N(4): 103.2(2)	O(1), N(2): 104.2(3) O(2), N(4): 104.8(2)	O(1), N(2) 105.64(6)
Sn–O–C	125.6(4), 124.3(4)	129.3(7), 129.7(7)	125.4(1)
$C–N_{(NMe2)}–Sn$	102.6(4), 104.6(4)	105.1(7), 98(1)	102.8(1)
∑ $C–N_{(NMe2)}–C$ (sp^3 = ~328.5°)	332.8	332.6	330.9

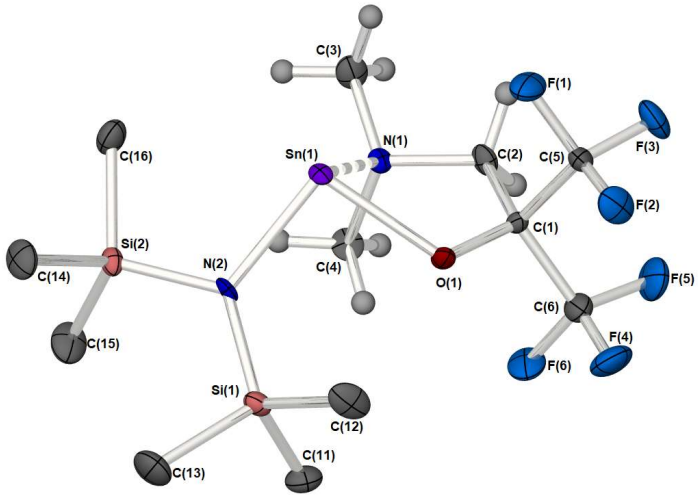

*Figure 2.31 – Molecular structure of [Sn(Fdmamp)HMDS] **(11)**. Thermal ellipsoids are shown at 50% probability.*

As was seen in the homoleptic fluorinated system **(10)**, a considerably shortened (1.364(5) Å) C–O bond within the ligand is present. This bond length is commensurate with the fluorinated alkoxide compound [Sn{OCH(CF_3)$_2$}$_2$HNMe_2], which exists a divalent monomer stabilised by a coordinated molecule of dimethylamine (1.381(8) Å and 1.367(9) Å).[21]

Compound **11** adopts a geometry best described as trigonal pyramidal, though with consideration of a stereoactive lone pair can be considered distorted pseudo-tetrahedral. The Sn–O bond length is significantly shorter than that observed within the dimerised compounds, as would be expected for a non-bridging alkoxide, though at 2.087(2) Å remains slightly longer than the Sn–O bond lengths observed in monodentate tin(II) alkoxides[2,125] (2.01-2.05 Å), and is comparable to the limited examples of bidentate aminoalkoxide complexes (2.073 Å) and the fluorinated alkoxide mentioned above (2.107(4) Å and 2.060(5) Å).[21,126] The Sn–N($SiMe_3$)$_2$ bond length (2.090(3) Å) is considerably shorter than the same bond in the dimeric systems **2**, **5** and **8** (~2.15-2.18 Å), and more similar to monomeric and sterically unstrained systems such as [Sn{N($SiMe_3$)$_2$}$_2$] (2.088(6) Å and 2.096(1) Å), as discussed previously.[99]

*Table 2.12 – Relevant bond angles and lengths within [Sn(Fdmamp)HMDS] **(11)**.*

Angle (°)		Bond Length (Å)	
O–Sn–N(1)	72.1(1)	Sn–O	2.087(2)
O–Sn–N(2)	94.3(1)	Sn–N(1)	2.433(4)
N(1)–Sn–N(2)	102.3(1)	Sn–N(1)	2.090(3)
Sn–O–C(1)	117.4(2)	O–C	1.364(5)
C–N(1)–Sn	103.8(2)		
C(2)–N(1)–C(3)	111.6(3)		
C(2)–N(1)–C(4)	108.1(3)		
C(3)–N(1)–C(4)	109.8(3)		
∑ C–N–C (sp^3 = ~328.5°)	329.5		

It is interesting to note that no appreciable difference in Sn–O bond length was observed in the homoleptic compounds **1**, **4**, **7** and **10**, indicating that the relative strengths of these bonds were likely to be similar, a factor worth considering when looking towards ALD reactivity. It was hypothesised that on progression to a fluorinated substituent, a lower electron density on the alkoxide oxygen would contribute to a weaker and more reactive Sn–O bond, in addition to the volatility advantages offered by precursor fluorination. Evidence of this induction of electron density towards the fluorinated substituent was provided in the considerably shortened O–C bond lengths observed within the fluorinated ligands in systems **10** and **11**. Despite this being the case, it would appear that this effect has no direct implication for the strength of Sn–O bonds despite the indicated loss of oxygen-centred electron density.

With an atomic radius merely ~10% larger than that of hydrogen,[9] it is unlikely that steric influences are responsible for the monomeric form of **11** when all other complexes in the heteroleptic series (**2**, **5** and **8**) exist as dimers. The findings support the supposition that electron density is withdrawn by the fluorinated groups from the oxygen-based lone pairs that have limited interaction with the tin centre, and as such are unable to participate in bridging behaviour to coordinatively satisfy the other tin centres. Interestingly, this leads to the three-coordinate Sn(II) species seen in the molecular structure of **11**, which may well be expected to display heightened reactivity due to its coordinative unsaturation.

A similar example of this delicate balance can be seen in the molecular structure of [Sn(O^{i}Pr)$_2$], which, due to limited steric bulk and low coordination, was found to exist as an oxygen-bridged polymer in the solid state.[2] It was subsequently found that if fluorinated isopropoxide ligands were used, higher nuclearity species were unable to form and instead electron density was scavenged from liberated amine by-products to form the reactive monomeric adduct [Sn(O^{Fi}Pr)$_2$HNMe$_2$], mentioned previously.[2,21]

Due to the propensity for silicon-containing precursors to result in silicon contamination within ALD processes, thermogravimetric analyses were not undertaken on complexes **2**, **5**, **8** and **11**. Furthermore, heteroleptic species with differing metal–heteroatom bonds are not as desirable as species with complementary bonding due to substantial differences in reactivity across the system. However, characterisation of these complexes provides valuable insight into the effect of subtle ligand variations on structure and possible ALD capabilities of related compounds. Of particular interest is the potential to synthesise low coordinate tin compounds without the necessity for overly sterically demanding ligands or excessively obstructive chelating groups.

2.3.7. Characterisation of Heteroleptic Aminoalkoxides [Sn(L)NMe$_2$]: 3, 6, 9 and 12

NMR Spectroscopy

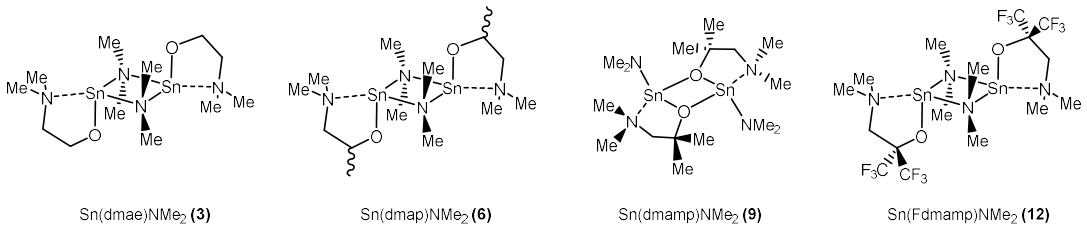

*Figure 2.32 – Molecular structures of compounds **3**, **6**, **9** and **12**.*

The synthesis and characterisation of the heteroleptic derivatives of dmae, dmap, dmamp and Fdmamp pro-ligands was of particular interest with a sterically undemanding amine (–NMe_2), in order to provide contrast with the high steric constraints exerted by –$N(SiMe_3)_2$ and observed in compounds **2**, **5**, **8** and **11**. The molecular structures of all four systems were determined via single-crystal X-ray diffraction and characterised by NMR spectroscopy.

Whilst the only notable difference observed in the structures of **2**, **5**, **8** and **11** was the manifestation of a monomeric species with the use of a fluorinated ligand, significant structural differences are evident between the –NMe_2 derived systems **3**, **6**, **9** and **12** (Figure 2.32). and due to the subtle nature of the alterations are likely to result in a certain degree of interchange between the respective structures in solution, a feature which is demonstrated in many of the NMR spectra.

The ^{1}H NMR spectrum of [Sn(dmae)NMe_2] **(3)** appears as expected, with resonances at δ = 4.01-4.03, 2.91, 2.20-2.22 and 1.98 ppm accounting for the OCH_2, SnNMe_2, NCH_2 and CH_2NMe_2 groups respectively. Similarly, the ^{13}C{^{1}H} NMR data show the expected signals for the environments NCH_2, OCH_2, CH_2NMe_2 and SnNMe_2 at δ = 62.46, 61.22, 44.14 and 42.42 ppm. In addition to a sharp peak in the ^{119}Sn NMR spectrum at δ = –156 ppm attributed to the hydrolysed [Sn(dmae)$_2$] cluster species, a very broad (ca. 40 ppm) and weak signal is observed at $\delta \approx$ –68 ppm.

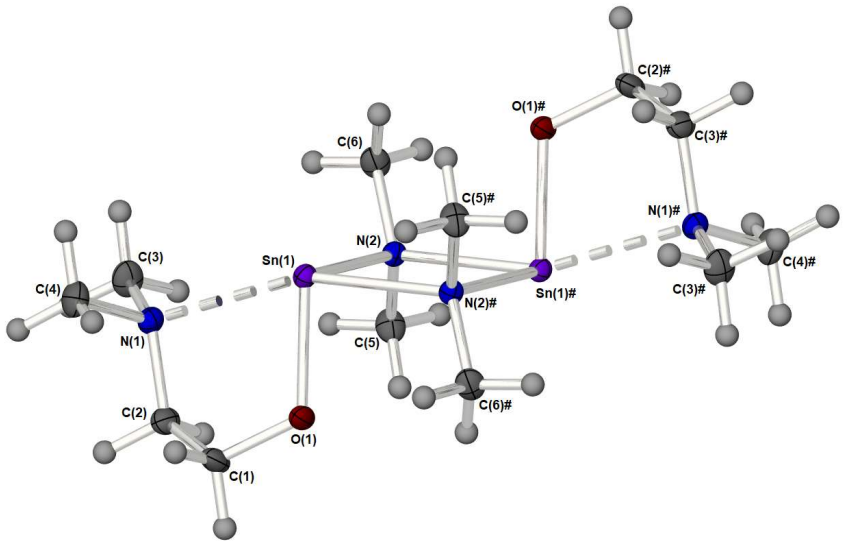

*Figure 2.33 – Molecular structure of [Sn(dmae)NMe_2] **(3)**. Thermal ellipsoids are shown at 50% probability. Symmetry equivalent atoms are generated by the operator: #–X, 1–Y, 1–Z.*

As observed for the previously discussed dmap derivatives **(4** and **5)**, [Sn(dmap)NMe_2] **(6)** displays a well-defined ^{1}H NMR spectrum consisting of a multiplet at δ = 4.17-4.19 ppm ascribed to the chiral C*H*Me, with the remaining methylene group giving rise to a broad multiplet at δ = 2.19-2.31 ppm and a doublet of doublets (J = 11.6, 2.5 Hz) at δ = 1.82 ppm. The $SnNMe_2$ and CH_2NMe_2 are found at δ = 2.82 and 2.01 ppm, whilst the chiral CH*Me*

substituent presents as a doublet at δ = 1.30 ppm (J = 6.0 Hz). The ^{119}Sn NMR displays a large, broad (ca. 40 ppm) signal at δ = –65 ppm in conjunction with a smaller broad signal at δ = 125 ppm and sharp cluster resonance at δ = –171 ppm.

The ^{1}H NMR spectrum of [Sn(dmamp)NMe$_2$] **(9)** is also much as expected, with broad signals observed at δ = 2.78, 2.19, 2.13 and 1.37 ppm and attributed to the SnNMe$_2$, CH$_2$, CH$_2$NMe$_2$ and CH$_3$ groups respectively. The resonances ascribed to the *C*H$_2$ and *C*Me$_2$ appear to coalesce in the ^{13}C{^{1}H} NMR spectrum, with the tertiary environment appearing more downfield (δ = 72.80 ppm) than the methylene (δ = 72.19 ppm), in contrast to compounds **3** and **6**, in which the alkoxide carbon environment is found further upfield of the methylene group. These resonances are followed by peaks at δ = 47.81, 42.96 and 33.88 ppm, allocated in the order CH$_2$N*Me*$_2$, SnN*Me*$_2$ and *C*H$_3$. Once again, the ^{119}Sn NMR spectrum consists of a number of broad resonances, which, excluding the characteristic cluster peak at δ = –166 ppm, can be observed at δ = +127, –46, –66 and –217 ppm.

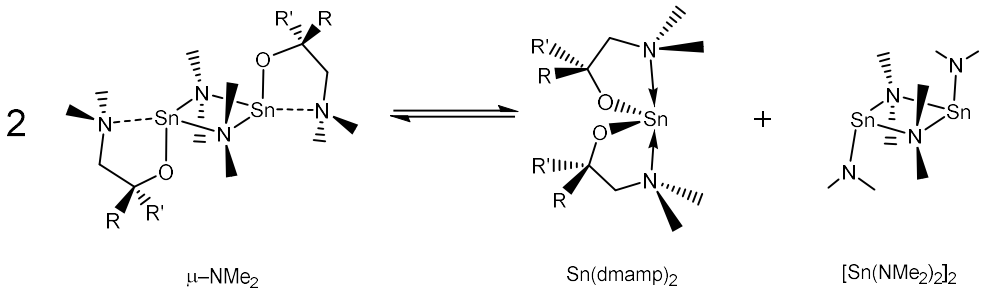

*Equation 2.7 – Possible Schlenk-type equilibrium within heteroleptic tin(II) systems **3**, **6**, **9** and **12**.*

The ^{119}Sn NMR resonance at δ ≈ +125 that is present in both [Sn(dmap)NMe$_2$] **(6)** and [Sn(dmamp)NMe$_2$] **(9)** is coincidental with the ^{119}Sn NMR signal of [Sn(NMe$_2$)$_2$]. The presence of [Sn(NMe$_2$)$_2$] within the solution to this degree is not unexpected, due to the high likelihood of a Schlenk-type equilibrium taking place for these heteroleptic compounds whereby a combination of Sn(NMe$_2$)$_2$ and Sn(L)$_2$ are in constant exchange with the target heteroleptic systems Sn(L)NMe$_2$. This supposition is most clearly demonstrated in the ^{119}Sn NMR spectrum of [Sn(dmamp)NMe$_2$], where four peaks excluding that of the cluster species can be seen. In this spectrum, the resonances at δ = +125 and –217 ppm match very closely with those observed for [Sn(NMe$_2$)$_2$] and [Sn(dmamp)$_2$], whilst two overlapping peaks at δ = –46 and –66 ppm are likely to correspond to the dimeric target system with two different bridging modes, μ–O and μ–N. The latter observation is explained in more detail in the following structural discussion.

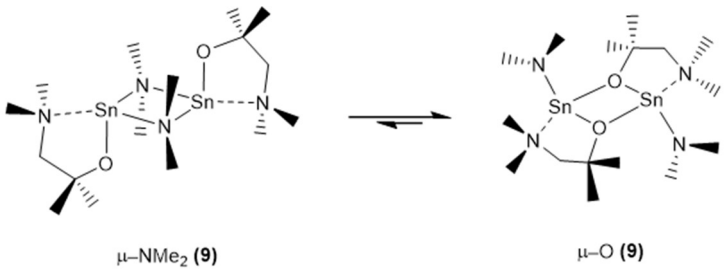

*Figure 2.34 – Possible bridging modes of dimeric [Sn(dmamp)NMe$_2$] **(9)**, showing the likely major (μ–O) and minor (μ–NMe$_2$) isomers.*

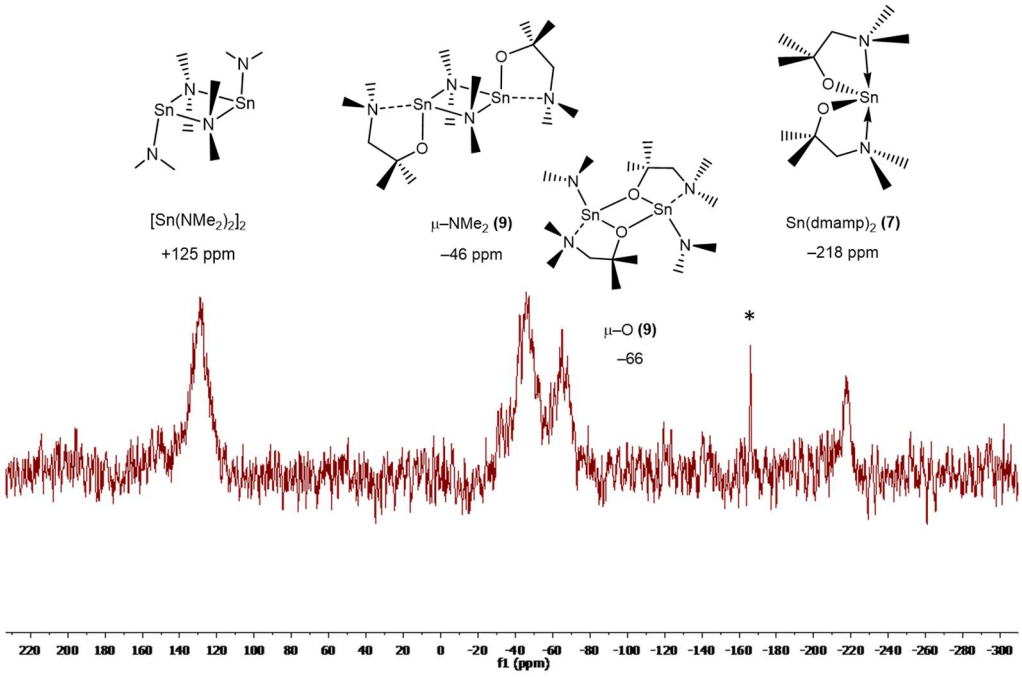

*Figure 2.35 – ^{119}Sn NMR (C$_6$D$_6$, 25 °C) spectrum of Sn(dmamp)NMe$_2$ **(9)**. *Denotes Sn$_6$(O)$_4$(dmamp)$_4$ cluster.*

Slightly more convoluted are the NMR spectra for [Sn(Fdmamp)NMe$_2$], with the room temperature ^{1}H NMR spectrum displaying a pattern of signals consistent with a fluxional system. When repeated in d$_8$-toluene at 90 °C, the peaks resolve into the expected methylene and CH$_2$N*Me*$_2$ signals at δ = 2.66 and 2.08 ppm, and an inequivalence in the SnNMe$_2$ environments giving rise two broad signals in a 2:4 ratio between δ = 2.52 and 2.26 ppm. Though difficult to obtain in its entirety, the ^{13}C{^{1}H} NMR spectrum displays a signal for the bridging NMe$_2$ moiety at δ = 41.68 ppm and methylene backbone at δ = 57.50 ppm, whilst the ^{19}F spectrum exhibits two peaks, one of much greater intensity, indicative of inequivalence within the ^{19}F environments or an alternative product. The latter would not be unreasonable,

as the room temperature ^{119}Sn NMR spectrum contains four signals at δ = +80, +70, –117 and –132, and though further investigation would be needed to deconvolute these fully, high temperature ^{119}Sn NMR in d_8-toluene reveals a coalescence of the downfield two peaks to a single broad peak at δ = +85, and the disappearance of the upfield peaks. A tentative hypothesis suggests the presence of a monomer-dimer equilibrium between the two positive and negative peaks, where the weak dimerisation is dispelled at high temperature.

Single-Crystal X-ray Diffraction

The molecular structures of heteroleptic compounds **3**, **6**, **9** and **12** were unambiguously determined and found to exist as dimers via single-crystal X-ray diffraction. [Sn(dmae)NMe_2] **(3)**, [Sn(dmap)NMe_2] **(6)** and [Sn(Fdmamp)NMe_2] **(12)** were shown to dimerise via μ_2–NMe_2 bridges, whilst [Sn(dmamp)NMe_2] **(9)** was shown to bridge through a μ_2 alkoxide.

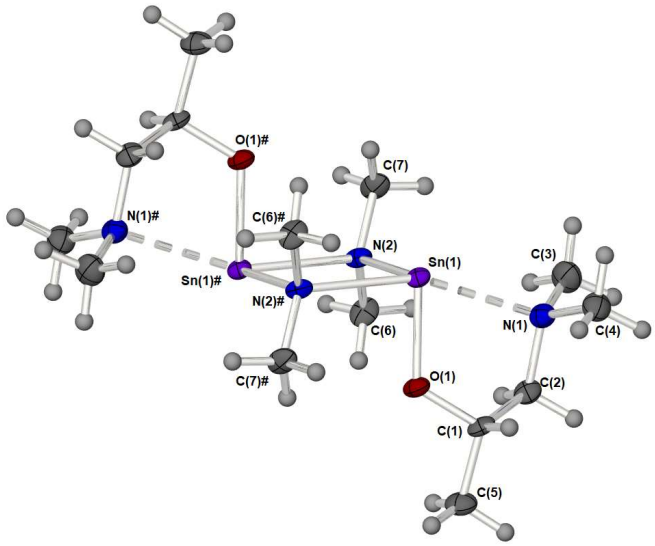

*Figure 2.36 – Molecular structure of [Sn(dmap)NMe_2] **(6)**. Thermal ellipsoids are shown at 50% probability. Symmetry equivalent atoms are generated by the operator: #1–X, 1–Y, 1–Z*

As was seen in all of the four-coordinate systems discussed previously, each tin atom adopts a pseudo trigonal bipyramidal geometry, with an axially-coordinated pendant –NMe_2. In compounds **3**, **6** and **12**, which contain bridging NMe_2 species, the remaining axial site is occupied by this bridging coordination, whilst in compound **9**, where bridges are formed through the alkoxide, a dative O→Sn bond occupies this position. As a consequence, within the latter compound, non-bridging NMe_2 ligands and tin–alkoxide bonds are arranged equatorially, whilst in compounds **3**, **6** and **12**, tin–alkoxide bonds and bridging NMe_2 groups occupy these positions.

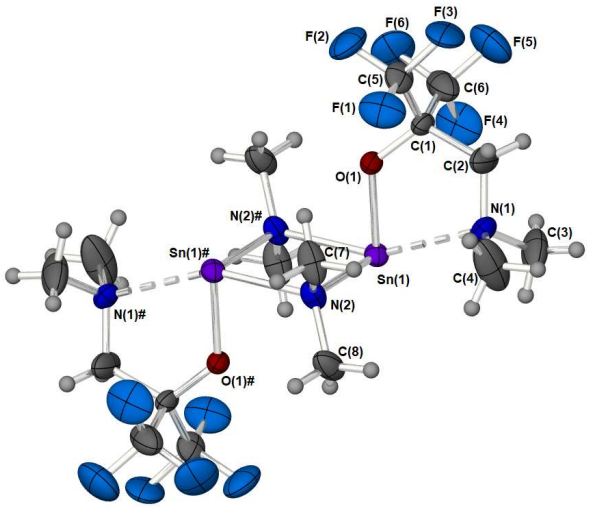

*Figure 2.37 – Molecular structure of complex **12**. Possible O–H interactions can be seen between alkoxide and bridging NMe_2 groups on either side of the $\{Sn_2N_2\}$ plane. Thermal ellipsoids are shown at 50% probability. Symmetry equivalent atoms are generated by the operator: #1–X, 2–Y, 1–Z.*

The molecular structures of compounds **3**, **6** and **12** all consist of an entirely planar $\{Sn_2N_2\}$ heterocycle with Sn–alkoxide bonds sitting trans to each other on either side of the plane, at angles nearing 90° (91.1(4)° **(3)**, 89.27(8)° **(6)**, 87.8(1)° **(12)**). All axial tin–pendant NMe_2 bonds are noticeably longer than those observed in the homoleptic and heteroleptic HMDS systems, with the [Sn(dmae)NMe_2] system **(3)** displaying the longest bond, at 2.795(2) Å. The elongation of this bond can be explained by the more constrained C–N–Sn angle at the pendant nitrogen, which at 96.7(1)° is imperfect for directing the lone pair of an sp^3 nitrogen atom towards the central tin. Despite being of notable length, with some reported Sn←N bonds displaying lengths of up to 3.10 Å, these bonds are still well within reasonable bounds.[140] The terminally coordinated Sn–O bond lengths are commensurate with those found within the homoleptic $Sn(L)_2$ complexes, whilst in compound **9**, the bridging μ_2–alkoxide–tin bonds show good correlation with those found in the oxygen-bridged HMDS compounds **2**, **5** and **8**. A slight elongation of the Sn–O is however seen in the fluorinated compound **12** when compared to compounds **3** and **6**, which could be as a result of an imperfect angle of 126.1(5)° between the alkoxide and tin centre. It is possible that there is a small degree of interaction between the lone pairs of the alkoxide oxygen and the hydrogen atoms of the bridging NMe_2, with long through-space distances of 2.582 and 2.620 Å (Figure 2.37). In support of this, distances of 2.5-3.2 Å are not unusual for moderate electrostatic H-bonding.[141]

*Table 2.13 – Relevant bond lengths and angles within compounds **3**, **6** and **12**.*

Angle (°) / Bond (Å) / Compound	3	6	12
Distance*			
$Sn–N_{(NMe2)}$	2.795(2)	2.720(3)	2.717(6)
Sn–O	2.045(2)	2.048(2)	2.067(5)
$Sn–N(1)_{(\mu\text{-}NMe2)}$	2.218(2)	2.217(3)	2.212(7)
$Sn(1)\#–N(1)_{(\mu\text{-}NMe2)}$	2.320(2)	2.350(3)	2.323(7)
Sn–Sn	3.4826(4)	3.4825(4)	3.4525(7)
O–C	1.409(3)	1.412(4)	1.363(9)
∑ Sn_2N_2 ring	360	360	360
Angle			
$N_{(NMe2)}$–Sn(1)–N(2)#$_{(\mu\text{-}NMe2)}$	158.36(6)	157.8(1)	154.5(2)
Sn–N–Sn	100.25(7)	80.7(1)	99.1(3)
O(1)–Sn–N(2)	93.56(6)	92.6(1)	91.5(2)
Sn–O–C	118.0(1)	121.0(2)	126.1(5)
C(2)–N(1)–Sn	96.7(1)	100.5(2)	105.8(5)
C(2)–N(1)–C(3)	111.6(2)	111.9(3)	111.7(8)
C(2)–N(1)–C(4)	111.1(2)	112.1(3)	112.7(8)
C(3)–N(1)–C(4)	108.3(2)	109.0(3)	107.9(9)
∑ C–N(1)–C (sp^3 ~328.5°)	331.0	333.0	332.3

Of greatest interest within the structures of complexes **3**, **6**, **9** and **12** is the observed change in bridging environment as the series is progressed. Whilst it would be reasonable to expect the greatest change to take place on the addition of fluorinated substituents, as was seen in the heteroleptic HMDS systems, the most informative change occurs as the alkoxide ligand backbone is changed from CHMe to CMe_2. Despite the increased steric demand of an additional methyl group on the alkoxide, it becomes more favourable to form an alkoxide bridge where before a bridging NMe_2 group was most stable. This change points strongly to the impact of electronic effects within the alkoxide ligand and supports the initial hypothesis that the direction of electron density onto the alkoxide is increased in the order CH_2 < CHMe < $CHMe_2$. Subsequently, the process is reversed on the inclusion of fluorinated substituents, whereupon withdrawal of electron density from the alkoxide results in a diminished ability to donate electron density through bridging, and the restoration of the NMe_2 bridge. The latter observation is also supported by the monomeric nature of the [Sn(Fdmamp)HMDS] complex **(11)**, when contrasted with dimeric **2**, **5** and **8**. There is great scope for computational studies on the back of these observations, which could give significant insight into the effects of

electron-directing groups on alkoxide ligands, with particular emphasis on a tailored approach to precursor reactivity.

Minimal changes in bond lengths and angles are observed within the homoleptic and heteroleptic-HMDS species on progression from dmae to dmamp, which is indicative of the fact that electronic influences within these systems are expectedly subtle. This could be suggestive that whilst the molecular structure of [Sn(dmamp)NMe_2] **(9)** was found to contain alkoxide bridges, a relatively low energy barrier may exist between this conformation and the NMe_2-bridged systems observed in the rest of the series. This suggestion could account for many of the observations in the solution NMR of compounds **6** and **9**. The ^{119}Sn NMR spectrum of [Sn(dmamp)NMe_2] **(9)** displays overlapping peaks at δ = –46, –66 ppm, in addition to those observed for [Sn$(NMe_2)_2$] and the bis-substituted [Sn$(dmamp)_2$]. The two central resonances could tentatively be ascribed to the target compound [Sn(dmamp)NMe_2] in each of its possible bridging forms. Equally, the same may be true of [Sn(dmap)NMe_2] **(6)**, which crystallises with an NMe_2 bridge that may prove to be in equilibrium with an alkoxide bridge in solution.

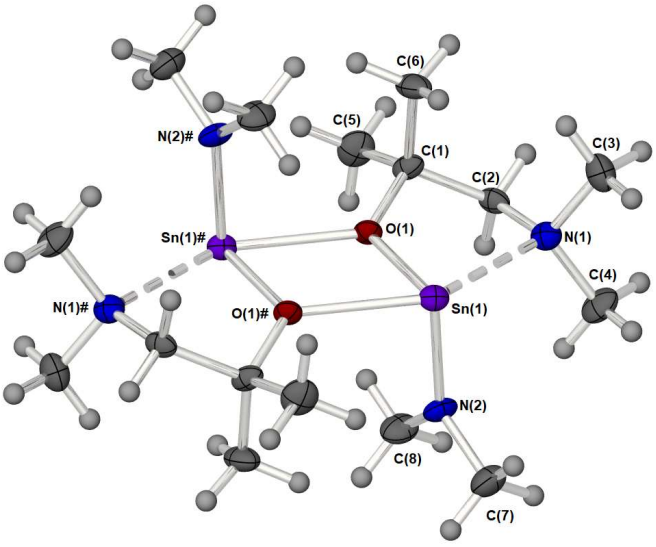

*Figure 2.38 – Molecular structure of complex **9**. Thermal ellipsoids are shown at 50% probability. Symmetry equivalent atoms are generated by the operator: #1–X, 1–Y, 1–Z.*

*Table 2.14 – Relevant bond lengths and angles within compound **9**.*

Angle (°)		Distance (Å)	
N(1)–Sn–O(1)#	142.3(1)	Sn–O(1)	2.111(2)
O(1)–Sn–N(2)	94.7(1)	Sn–O(1)#	2.338(2)
Sn–O–C	120.7(2)	Sn–N(1)	2.619(3)
Sn–O–Sn	110.0(1)	Sn–N(2)	2.058(3)
O–Sn–O	69.97(9)	Sn–Sn	3.6474(5)
C(2)–N(1)–Sn	103.1(2)	O–C	1.427(4)
C(2)–N(1)–C(3)	110.1(3)		
C(2)–N(1)–C(4)	112.7(3)		
C(3)–N(1)–C(4)	108.7(3)		
∑ C–N–C (sp^3 = ~328.5°)	331.5		

2.4. Conclusion

The research described within this chapter set out initially to replicate, on a commercially available ALD tool, the only effective reported atomic layer deposition procedure for tin(II) oxide. After full structural characterisation was obtained for the reported precursor, [Sn(dmamp)$_2$], facile synthetic routes towards scaled-up synthesis were sought. Subsequent deposition investigations determined effective ALD parameters for the growth of crystalline SnO, which allows for comparative screening of novel precursors. These investigations also enabled improved growth per cycles and densities, and allowed high growth grates (0.36 Å/cy) of crystalline tin(II) oxide at temperatures as low as 130 °C.

In order to gain an appreciation of the electronic and steric implications of the incorporation of the dmamp ligand, and in an attempt to elucidate the factors that allow for successful ALD activity, a range of closely related systems were synthesised and characterised. Ligand electronics and sterics were probed by the addition or removal of {CH_3} or {CF_3} moieties to the dmamp framework, affording complexes **1-12**. The molecular structure of these species showed clear transitions of preference for dimerisation configurations in both the {HMDS} and {NMe_2} heteroleptic species **(2**, **5**, **8** and **11)** and **(3**, **6**, **9** and **12)** respectively. Deposition was trialled with the Sn(dmap)$_2$ complex **(4)**, which, though structurally very similar, and displaying identical Sn–O bond lengths, failed to deposit crystalline material in the same manner as [Sn(dmamp)$_2$] **(7)**, highlighting the extremely subtle nature of ALD precursor design.

Computational studies into the series of ligands, their electronic considerations and their effect on reactivity would be of great interest, not only for precursor design, but in understanding the tendency towards oligomerisation within the series. Such ligands, or related systems could prove useful in catalysis of materials such as PLA, or within other deposition techniques, such as CVD. Further studies into the atomic layer deposition of the {NMe_2} heteroleptic species

would be desirable, avoided in this research to date due to the inequivalence between Sn–N and Sn–O bond reactivity. Finally, a proof-of-concept SnO-channel TFT was fabricated by PragmatIC Printing Ltd. and demonstrated moderate switching ratios, though low mobilities, using SnO deposited at a reactor temperature of 170 °C.

Reactions and complexes described within Chapter 2 are summarised in Scheme 2.8.

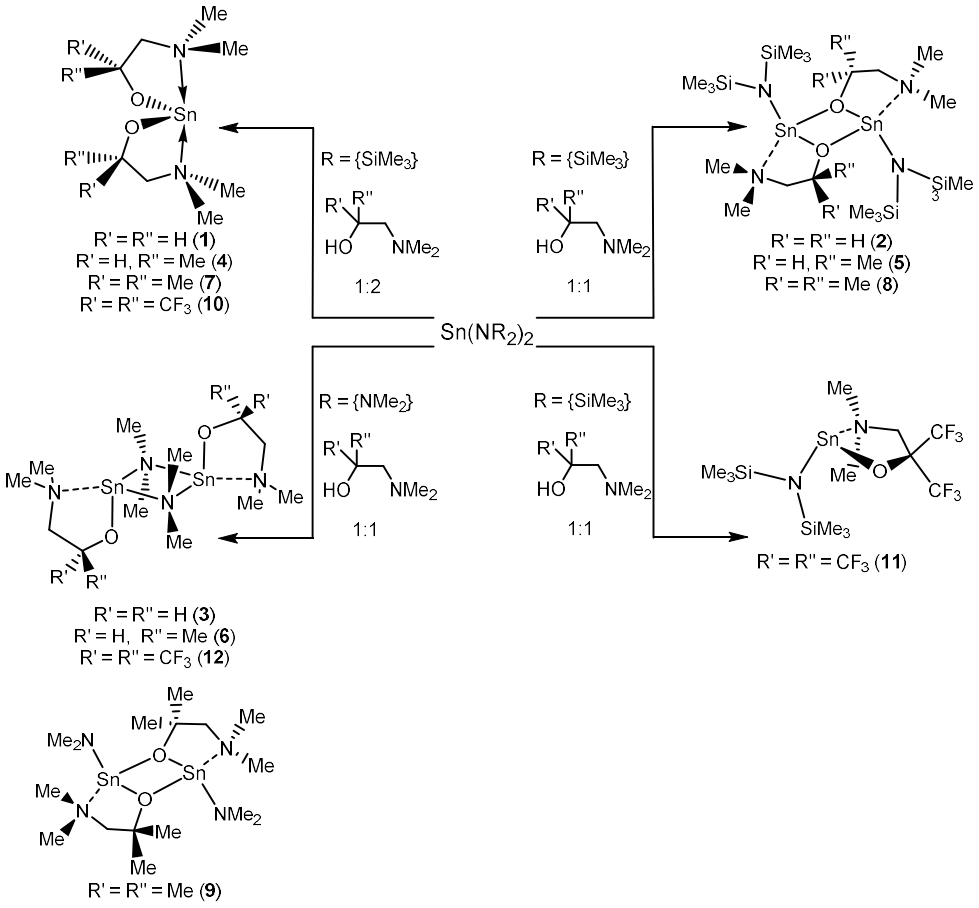

Scheme 2.8 – Summary of reactions and complexes presented within Chapter 2.

2.5. Experimental

Generic experimental details are given in the Appendix, but it is necessary to explain that due to the highly air and moisture sensitive nature of complexes **1**-**12**, significant difficulty was encountered in obtaining sufficiently consistent elemental analysis results, despite numerous attempts for each novel compound. The high sensitivity of these compounds is exacerbated by the inability to fully separate the desired complex from volatile self-forming cluster species. However, the molecular structures of all novel complexes have been confirmed with single-crystal X-ray diffraction, which is corroborated by multinuclear NMR and 2D NMR spectroscopy.

$[Sn(NMe_2)_2]_2$

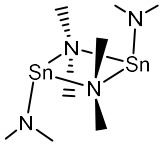

Tin(II) dimethylamide was synthesised according to adapted literature procedures.[100,142]

A stirring suspension of $SnCl_2$ (18.96 g, 100 mmol) in Et_2O (150 ml) was cooled and added to a –78 °C solution of lithium dimethylamide (10.20 g, 200 mmol) in Et_2O (200 ml). The solution was stirred for 8 h and the volatiles removed *in vacuo*. 3 x hexane aliquots (30 ml) were added and removed under vacuum before the white solid was dissolved in hexane (300 ml). After removal of the LiCl via filtration through Celite®, the pale yellow solution was reduced to yield crystalline material at –28 °C. (17.51 g, 85%)

^{1}H NMR (500 MHz, THF-d_8); δ_{ppm} 2.80 (br s, 12H, *Me*)
^{13}C{^{1}H} NMR (125.7 MHz, THF-d_8); δ_{ppm} 44.77 (4C, *Me*)
^{119}Sn NMR (186.3 MHz, C_6D_6); δ_{ppm} 125

$[Sn\{N(SiMe_3)_2\}_2]$ – $[Sn(HMDS)_2]$

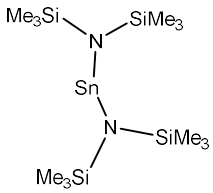

Bis[bis(trimethylsilylamido)]tin(II) was synthesised according to an adapted literature procedure.[143]

A stirring suspension of $SnCl_2$ (18.96 g, 100 mmol) in Et_2O (150 ml) was cooled and added to a –78 °C solution of lithium bis(trimethylsilylamide) (33.47 g, 200 mmol) in Et_2O (200 ml). The solution was stirred for 8 h and the volatiles removed *in vacuo*. 3 x hexane aliquots (30 ml) were added and removed under vacuum before the white solid was dissolved in hexane (300 ml). After removal of the LiCl via filtration through Celite®, the dark orange solution distilled under reduced pressure (10^{-2} mbar) into liquid N_2 at 150 °C.

^{1}H NMR (500 MHz, C_6D_6); δ_{ppm} 0.30 (s, 36H, Si*Me*$_3$)
^{119}Sn NMR (186.3 MHz, C_6D_6); δ_{ppm} 779

1-dimethylamino-2-methyl-2-propanol (dmamp)

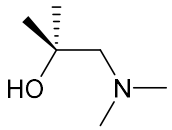

Dimethylamine (10ml, 150mmol) was condensed at 0 °C into a high-pressure Youngs ampoule containing a catalytic amount of lithium bis(trifluoromethylsulfonyl)amine 5% after which 2-methyl-1-propenoxide (7.21g, 100 mmol) was added with stirring. The vessel was sealed and reacted overnight. An excess of water was added and the product extracted with dichloromethane and dried over $MgSO_4$. After filtration, the solvent was removed *in vacuo* yielding a pure liquid. (13.47 g, 87 %)

^{1}H NMR (500 MHz, C_6D_6); δ_{ppm} 2.73 (s, 1H, O*H*), 2.10 (s, 6H, C(C*H*$_3$)$_2$), 2.02 (s, 2H, C*H*$_2$), 1.12 (s, 6H, N(C*H*$_3$)$_2$)
^{13}C{^{1}H} NMR (125.7 MHz, C_6D_6); δ_{ppm} 70.19 (1C, CH_2), 69.69 (1C, O*C*), 48.12 (2C, N*Me*$_2$), 28.19 (2C, C*Me*$_2$)

HOC(CF$_3$)$_2$CH$_2$NMe$_2$ – (Fdmamp)

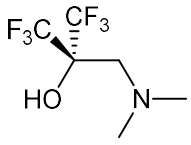

Dimethylamine (10ml, 150mmol) was condensed at 0°C into a high-pressure Youngs ampoule containing a catalytic amount of lithium bis(trifluoromethylsulfonyl)amine 5% after which hexafluoropropylene oxide (16.6 g, 100 mmol) was added with stirring. The vessel was sealed and reacted overnight. An excess of water was added and the product extracted with

dichloromethane and dried over $MgSO_4$. After filtration, the solvent was removed *in vacuo* yielding a pure liquid. (13.47 g, 87 %)

^{1}H NMR (500 MHz, C_6D_6); δ_{ppm} 6.11 (s, 1H, O*H*), 2.27 (s, 2H, CH_2), 1.63 (s, 6H, NMe_2)
^{13}C{^{1}H} NMR (75.5 MHz, C_6D_6); δ_{ppm} 127.21 (q, $^1J_{CF}$ = 290 Hz, 2C, CF_3), 71.77 (sept, $^2J_{CF}$ = 28.47 Hz, 1C, *C*$(CF_3)_2$), 55.12 (1C, *C*H_2), 45.61 (2C, NMe_2)
^{19}F NMR (470.6 MHz, C_6D_6); δ_{ppm} –78.82

[Sn(OCH$_2$CH$_2$NMe$_2$)$_2$] – [Sn(dmae)$_2$] – (1)

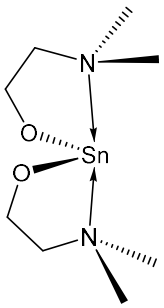

Compound **1** was synthesised according to an adapted literature procedure.[126]

A stirring solution of Sn(HMDS)$_2$ (0.89 g, 2 mmol) in hexane (20 ml) was added to a cooled solution of dimethylaminoethanol (0.36 g, 4 mmol) in hexane (20 ml) and left to stir for 2 h. After removal of the volatiles *in vacuo*, the solid residue was redissolved in hexane and filtered through Celite®. The volume was subsequently reduced and colourless crystals obtained at –28 ^{o}C. (0.45 g, 76 %)

^{1}H NMR (500 MHz, C_6D_6); δ_{ppm} 4.24 (t, J = 5.3 Hz, OCH_2), 2.31-2.39 (m, 4H, CH_2N), 2.10 (s, 12H, NMe_2)
^{13}C{^{1}H} NMR (125.7 MHz, C_6D_6); δ_{ppm} 63.43 (2C, O*C*H$_2$), 62.28 (2C, *C*H$_2$N), 43.46 (4C, NMe_2)
^{119}Sn NMR (186.3 MHz, C_6D_6); δ_{ppm} –279

[Sn(OCH$_2$CH$_2$NMe$_2$)HMDS] – [Sn(dmae)HMDS] – (2)

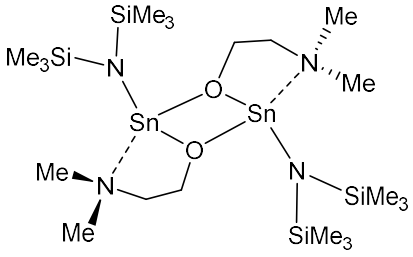

Compound **2** was synthesised according to an adapted literature procedure.[132]

A solution of dimethylaminoethanol (0.18 g, 2 mmol) in hexane (20 ml) was added to a cooled solution of $Sn(HMDS)_2$ (0.89 g, 2 mmol) in hexane (20 ml) and left to stir for 2 h. After removal of the volatiles *in vacuo*, the solid residue was redissolved in hexane and filtered through Celite®. The volume was subsequently reduced and colourless crystals obtained at –28 °C. (0.59 g, 80 %)

^{1}H NMR (500 MHz, C_6D_6); δ_{ppm} 3.73 (t, J = 5.3 Hz, 2H, OC*H*$_2$), 2.21 (br m, 2H, C*H*$_2$N), 1.99 (s, 6H, N*Me*$_2$), 0.46 (s, 18H, $^2J_{SiH}$ = 5.8 Hz, $SiMe_3$)
^{13}C{^{1}H} NMR (125.7 MHz, C_6D_6); δ_{ppm} 61.15 (1C, O*C*), 57.99 (1C, *C*H$_2$N), 44.29 (2C, N*Me*$_2$), 7.37 (6C, $^1J_{SiC}$ = 54.6 Hz and $^3J_{SnNSiC}$ = 37.3 Hz, $SiMe_3$)
^{119}Sn NMR (186.3 MHz, C_6D_6); δ_{ppm} –168

[Sn(OCH$_2$CH$_2$NMe$_2$)NMe$_2$] – [Sn(dmae)NMe$_2$] – (3)

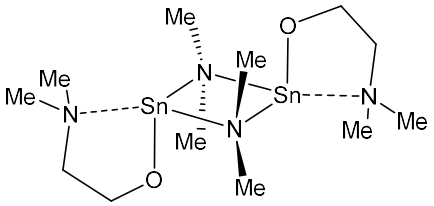

A solution of dimethylaminoethanol (0.18 g, 2 mmol) in hexane (20 ml) was added to a cooled solution of $Sn(NMe_2)_2$ (0.41 g, 2 mmol) in hexane (20 ml) and left to stir for 2 h. After removal of the volatiles *in vacuo*, the solid residue was redissolved in hexane and filtered through Celite®. The volume was subsequently reduced and colourless crystals obtained at –28 °C. (0.28 g, 55 %)

^{1}H NMR (500 MHz, C_6D_6); δ_{ppm} 4.01-4.03 (m, 2H, OC*H*$_2$), 2.91 (br s, 6H, SnNMe$_2$), 2.20-2.22 (m, 2H, NC*H*$_2$), 1.98 (s, 6H, CH$_2$N*Me*$_2$)
^{13}C{^{1}H} NMR (125.7 MHz, C_6D_6); δ_{ppm} 62.46 (1C, N*C*H$_2$), 61.22 (1C, O*C*H$_2$), 44.14 (2C, CH$_2$N*Me*$_2$), 42.42 (2C, SnN*Me*$_2$)
^{119}Sn NMR (186.3 MHz, C_6D_6); δ_{ppm} –68 (br)

[Sn(OCH(CH$_3$)CH$_2$NMe$_2$)$_2$] – [Sn(dmap)$_2$] – (4)

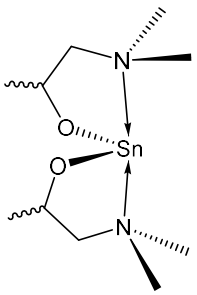

A solution of Sn(HMDS)$_2$ (0.89 g, 2 mmol) in hexane (20 ml) was added to a cooled solution of 1-dimethylamino-2-propanol (0.41 g, 4 mmol) in hexane (20 ml) and left to stir for 2 h. After removal of the volatiles *in vacuo*, the solid residue was redissolved in hexane and filtered through Celite®. The volume was subsequently reduced and colourless crystals obtained at –28 ^{o}C. (0.41 g, 64 %)

^{1}H NMR (500 MHz, D$_8$–tol, 90 °C); δ_{ppm} 4.18 (m, 1H, C*H*Me), 2.47 (m, 2H, C*H*$_2$), 2.16 (s, 12H, N*Me*$_2$), 1.91 (m, 2H, C*H*$_2$), 1.21 (m, 6H, CH*Me*)
^{13}C{^{1}H} NMR (125.7 MHz, 90 °C); δ_{ppm} 68.90 (2C, O*C*), 68.23 (2C, *C*H$_2$), 44.14 (4C, N*Me*$_2$), 24.37 (2C, CH*Me*)
^{119}Sn NMR (186.3 MHz, 90 °C); δ_{ppm} –246

[Sn(OCH(CH$_3$)CH$_2$NMe$_2$)HMDS] – [Sn(dmap)HMDS] – (5)

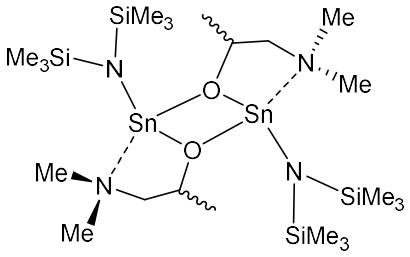

A solution of 1-dimethylamino-2-propanol (0.21 g, 2 mmol) in hexane (20 ml) was added to a cooled solution of Sn(HMDS)$_2$ (0.89 g, 2 mmol) in hexane (20 ml) and left to stir for 2 h. After removal of the volatiles *in vacuo*, the solid residue was redissolved in hexane and filtered through Celite®. The volume was subsequently reduced and colourless crystals obtained at –28 ^{o}C. (0.57 g, 75 %)

^{1}H NMR (500 MHz, C$_6$D$_6$); δ_{ppm} 4.11 (m, 1H, C(*H*)Me)), 2.24 (t, J = 11.78 Hz, 1H, C*H*HNMe$_2$), 1.97 (s, 6H, N*Me*$_2$), 1.71 (m, 1H, CH*H*NMe$_2$), 1.31 (d, J = 6.1 Hz, 3H, C(H)*Me*)), 0.46 (s, 18H, Si*Me*$_3$)

$^{13}C\{^{1}H\}$ NMR (125.7 MHz, C_6D_6); δ_{ppm} 68.87 (1C, O*C*), 67.25 (1C, *C*H_2), 45.25 (2C, NMe_2), 22.44 (1C, OC(H)*Me*), 7.02 (6C, $^{1}J_{CSi}$ = 54.7 Hz, $^{3}J_{CSn}$ = 33.5 Hz, Si*Me*$_3$)

^{29}Si NMR (99.4 MHz, C_6D_6); δ_{ppm} –3.51 (d, J = 1.16 Hz, *Si*Me_3)

^{119}Sn NMR (186.3 MHz, C_6D_6); δ_{ppm} –92

[Sn(OCH(CH$_3$)CH$_2$NMe$_2$)NMe$_2$] – [Sn(dmap)NMe$_2$] – (6)

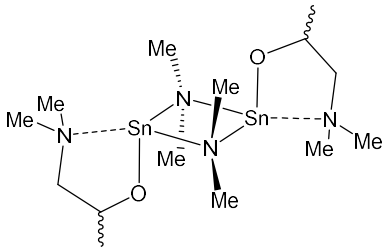

A solution of 1-dimethylamino-2-propanol (0.21 g, 2 mmol) in hexane (20 ml) was added to a cooled solution of $Sn(NMe_2)_2$ (0.41 g, 2 mmol) in hexane (20 ml) and left to stir for 2 h. After removal of the volatiles *in vacuo*, the solid residue was redissolved in hexane and filtered through Celite®. The volume was subsequently reduced and colourless crystals obtained at –28 ^{o}C. (0.37 g, 70 %)

^{1}H NMR (500 MHz, C_6D_6); δ_{ppm} 4.17-4.19 (m, 1H, C*H*Me), 2.82 (br s, 6H, $SnNMe_2$), 2.19-2.31 (br m, 1H, C*H*$HNMe_2$), 2.01 (br s, 6H, CH_2N*Me*$_2$), 1.82 (dd, J = 11.6, 2.5 Hz, 1H, CH*H*NMe_2), 1.30 (d, J = 6.0 Hz, 3H, CH*Me*)

$^{13}C\{^{1}H\}$ NMR (125.7 MHz, C_6D_6); δ_{ppm} 68.84 (1C, *C*H_2) 66.64 (1C, *C*HMe), 44.78 (2C, CH_2N*Me*$_2$), 42.57 (2C, $SnNMe_2$), 24.18 (1C, CH*Me*)

^{119}Sn NMR (186.3 MHz, C_6D_6); δ_{ppm} –65 major, 125 minor ($Sn(NMe_2)_2$)

[Sn(OC(CH$_3$)$_2$CH$_2$NMe$_2$)$_2$] – [Sn(dmamp)$_2$] – (7)

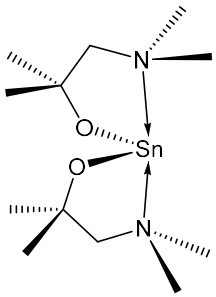

A solution of $Sn(HMDS)_2$ (0.89 g, 2 mmol) in hexane (20 ml) was added to a cooled solution of 1-dimethylamino-2-methyl-2-propanol (0.47 g, 4 mmol) in hexane (20 ml) and left to stir for

2 h. After removal of the volatiles *in vacuo*, the solid residue was redissolved in hexane and filtered through Celite®. The solvent was removed and the viscous oil distilled (10^{-2} mbar, 120 °C) into liquid N_2, yielding a white crystalline solid. (0.51 g, 72 %)

^{1}H NMR (500 MHz, C_6D_6); δ_{ppm} 2.34 (s, 4H, C*H*$_2$), 2.24 (s, 12H, N*Me*$_2$), 1.39 (s, 12H, C*Me*$_2$)
^{13}C{^{1}H} NMR (125.7 MHz, C_6D_6); δ_{ppm} 74.28 (2C, O*C*(Me)$_2$), 71.02 (2C, *C*H$_2$), 46.78 (4C, N*Me*$_2$), 34.45 (4C, C*Me*$_2$)
^{119}Sn NMR (186.3 MHz, C_6D_6); δ_{ppm} –218

[Sn(OC(CH$_3$)$_2$CH$_2$NMe$_2$)HMDS] – [Sn(dmamp)HMDS] – (8)

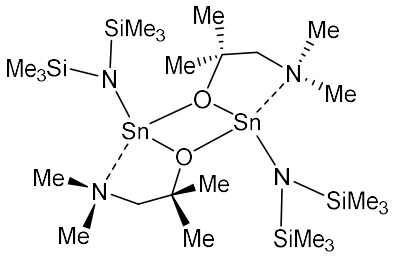

A solution of 1-dimethylamino-2-methyl-2-propanol (0.24 g, 2 mmol) in hexane (20 ml) was added to a cooled solution of Sn(HMDS)$_2$ (0.89 g, 2 mmol) in hexane (20 ml) and left to stir for 2 h. After removal of the volatiles *in vacuo*, the solid residue was redissolved in hexane and filtered through Celite®. The volume was subsequently reduced and colourless crystals obtained at –28 °C. (0.52 g, 66 %)

^{1}H NMR (500 MHz, C_6D_6); δ_{ppm} 2.01 (s, 6H, N*Me*$_2$), 1.98 (s, 2H, C*H*$_2$), 1.23 (s, 6H, C*Me*$_2$), 0.42 (s, 18H, SiMe$_3$)
^{13}C{^{1}H} NMR (125.7 MHz, C_6D_6); δ_{ppm} 75.61 (1C, O*C*), 71.56 (1C, *C*H$_2$), 47.90 (2C, N*Me*$_2$), 32.42 (2C, C*Me*$_2$), 6.40 (6C, $^{1}J_{SiC}$ = 55.0 Hz and $^{3}J_{CSn}$ = 25.4 Hz, Si*Me*$_3$)
^{29}Si NMR (99.4 MHz, C_6D_6); δ_{ppm} –2.55
^{119}Sn NMR (186.3 MHz, C_6D_6); δ_{ppm} 123 (m)

[Sn(OC(CH$_3$)$_2$CH$_2$NMe$_2$)NMe$_2$] – [Sn(dmamp)NMe$_2$] – (9)

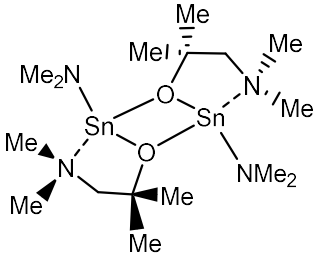

A solution of 1-dimethylamino-2-methyl-2-propanol (0.24 g, 2 mmol) in hexane (20 ml) was added to a cooled solution of $Sn(NMe_2)_2$ (0.41 g, 2 mmol) in hexane (20 ml) and left to stir for 2 h. After removal of the volatiles *in vacuo*, the solid residue was redissolved in hexane and filtered through Celite®. The volume was subsequently reduced and colourless crystals obtained at –28 °C. (0.40 g, 71 %)

^{1}H NMR (500 MHz, C_6D_6); δ_{ppm} 2.78 (s, 6H, SnN*Me*$_2$), 2.19 (s, 2H, CH_2), 2.13 (s, 6H, CH_2N*Me*$_2$), 1.37 (s, 6H, C*Me*$_2$)
^{13}C{^{1}H} NMR (125.7 MHz, C_6D_6); δ_{ppm} 72.80 (1C, O*C*), 72.19 (1C, *C*H_2), 47.81 (2C, CH_2N*Me*$_2$), 42.96 (2C, SnN*Me*$_2$), 33.88 (2C, C*Me*$_2$)
^{119}Sn NMR (186.3 MHz, C_6D_6); δ_{ppm} 127 ($Sn(NMe_2)_2$), –46, –66, –217 $Sn(dmamp)_2$ **(7)**)

[Sn(OC(CF$_3$)CH$_2$NMe$_2$)$_2$] – [Sn(Fdmamp)$_2$] – (10)

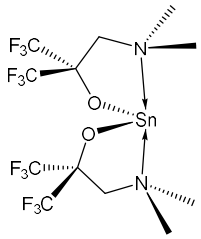

A solution of $Sn(HMDS)_2$ (0.89 g, 2 mmol) in hexane (20 ml) was added to a cooled solution of $HOC(CF_3)_2CH_2NMe_2$ (0.90 g, 4 mmol) in hexane (20 ml) and left to stir for 2 h. After removal of the volatiles *in vacuo*, the solid residue was redissolved in hexane and filtered through Celite®. The volume was subsequently reduced and colourless crystals obtained at –28 °C. (0.57 g, 50 %)

^{1}H NMR (500 MHz, C_6D_6); δ_{ppm} 2.54 (br s, 4H, C*H*$_2$), 2.07 (br s, 6H, N*Me*), 1.75 (br s, 6H, N*Me*)
^{13}C{^{1}H} NMR (125.7 MHz, C_6D_6); δ_{ppm} 124.89 (q, $^1J_{CF}$ = 290 Hz, 4C, CF_3), 82.83 (2C, O*C*), 47.78 (2C, NMe), 45.97 (2C, NMe)
^{19}F NMR (470.6 MHz, C_6D_6); δ_{ppm} –76.40 (6F, CF_3), –77.55 (6F, CF_3)
^{119}Sn NMR (186.3 MHz, C_6D_6); δ_{ppm} –322

[Sn(OC(CF$_3$)$_2$CH$_2$NMe$_2$)HMDS] – [Sn(Fdmamp)HMDS] – (11)

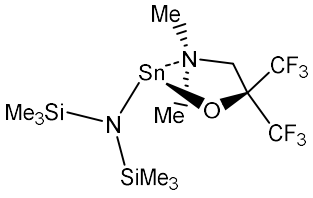

A solution of $HOC(CF_3)_2CH_2NMe_2$ (0.45 g, 2 mmol) in hexane (20 ml) was added to a cooled solution of $Sn(HMDS)_2$ (0.89 g, 2 mmol) in hexane (20 ml) and left to stir for 2 h. After removal of the volatiles *in vacuo*, the solid residue was redissolved in hexane and filtered through Celite®. The volume was subsequently reduced and colourless crystals obtained at –28 °C. (0.35 g, 35 %)

^1H NMR (500 MHz, C_6D_6); δ_{ppm} 2.34 (s, 2H, C*H*$_2$), 1.84 (s, 6H, N*Me*$_2$), 0.29 (s, 18H, Si*Me*$_3$)
$^{13}C\{^1H\}$ NMR (125.7 MHz, C_6D_6); δ_{ppm} 57.93 (1C, *C*H_2), 46.27 (2C, N*Me*$_2$), 5.29 (6C, Si*Me*$_3$)
^{19}F NMR (470.6 MHz, C_6D_6); δ_{ppm} δ = –76.88
^{119}Sn NMR (186.3 MHz, C_6D_6); δ_{ppm} 94

[Sn(OC(CF$_3$)$_2$CH$_2$NMe$_2$)NMe$_2$] – [Sn(Fdmamp)NMe$_2$] – (12)

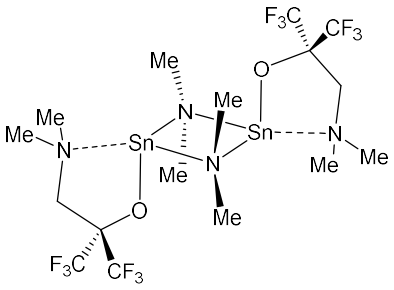

A solution of $HOC(CF_3)_2CH_2NMe_2$ (0.45 g, 2 mmol) in hexane (20 ml) was added to a cooled solution of $Sn(NMe_2)_2$ (0.41 g, 2 mmol) in hexane (20 ml) and left to stir for 2 h. After removal of the volatiles *in vacuo*, the solid residue was redissolved in hexane and filtered through Celite®. The volume was subsequently reduced and colourless crystals obtained at –28 °C. (0.22 g, 28 %)

^1H NMR (500 MHz, D_8–tol, 90 °C); δ_{ppm} 2.66 (br s, 2H, C*H*$_2$), 2.08 (br s, 6H, CH_2N*Me*$_2$), 2.52 and 2.26 (2:4, br s, 6H, SnN*Me*$_2$)
$^{13}C\{^1H\}$ NMR (125.7 MHz, D_8–tol, 90 °C); δ_{ppm} 41.68 (2C, SnN*Me*$_2$), 57.50 (1C, *C*H_2)
^{19}F NMR (470.6 MHz, D_8–tol, 90 °C); δ_{ppm} –76.29 major, –76.75 minor
^{119}Sn NMR (186.3 MHz, C_6D_6); δ_{ppm} 80, 70, –117, –132
^{119}Sn NMR (186.3 MHz, D_8–tol, 90 °C); δ_{ppm} 85 (br), –117, –132

2.6. References

1 T. J. Boyle, T. Q. Doan, L. A. M. Steele, C. Apblett, S. M. Hoppe, K. Hawthorne, R. M. Kalinich and W. M. Sigmund, *Dalton Trans.*, 2012, **41**, 9349–9364.

2 M. S. Hill, A. L. Johnson, J. P. Lowe, K. C. Molloy, J. D. Parish, T. Wildsmith and A. L. Kingsley, *Dalton Trans.*, 2016, **45**, 18252–18258.

3 R. M. Kissling and M. R. Gagné, *J. Org. Chem.*, 1999, **64**, 1585–1590.

4 A. Hassanzadeh, B. Moazzez, H. Haghgooie, M. Nasseri, M. Golzan and H. Sedghi, *Open Chem.*, 2008, **6** (4), 651-656.

5 D. C. Bradley, R. C. Mehrotra and D. P. Gaur, *Acad. Press*, 1978, 322–325.

6 R. C. Mehrotra and A. Singh, *Chem. Soc. Rev.*, 1996, **25**, 1–13.

7 R. C. Mehrotra, *J. Non. Cryst. Solids*, 1990, **121**, 1–6.

8 R. C. Mehrotra, *J. Non. Cryst. Solids*, 1988, **100**, 1–15.

9 W. A. Herrmann, N. W. Huber and O. Runte, *Angew. Chemie Int. Ed. Engl.*, 1995, 34, 2187–2206.

10 P. T. Wolczanski, *Polyhedron*, 1995, **14**, 3335–3362.

11 J. Bellow, Ph.D. Thesis, Wayne State University, 2016.

12 D. C. Bradley, in *Advances in Inorganic Chemistry and Radiochemistry*, 1972, vol. 15, pp. 259–322.

13 D. C. Bradley, in *Metal-Organic Compounds, vol. 23*, ACS publishing, New York, 1959, 2–10.

14 V. G. Kessler, in *Comprehensive Inorganic Chemistry II (Second Edition)*, Eds. J. Reedijk and K. Poeppelmeier, Elsevier, Amsterdam, Second Edi., 2013, pp. 455–470.

15 G. B. Deacon, T. C. Feng, B. W. Skelton and A. H. White, *Aust. J. Chem.*, 1995, **48**, 741–756.

16 M. H. Chisholm and I. P. Rothwell, *in Comprehensive Coordination Chemistry, Vol. II*, Pergamon Press, Oxford, 1987.

17 P. C. Wailes, H. Weigold and A. P. Bell, *J. Organomet. Chem.*, 1972, **34**, 155–164.

18 A. L. Johnson, Ph.D. Thesis, Durham University, 2000.

19 D. C. Bradley, *Chem. Rev.*, 1989, **89**, 1317–1322.

20 L. G. Hubert-Pfalzgraf, *Appl. Organomet. Chem.*, 1992, **6**, 627–643.

21 S. Suh and D. M. Hoffman, *Inorg. Chem.*, 1996, **35**, 6164–6169.

22 J. Hvoslef, H. Hope, B. D. Murray and P. P. Power, *J. Chem. Soc., Chem. Comm.*, 1983, 1438–1439.

23 T. V Lubben and P. T. Wolczanski, *J. Am. Chem. Soc.*, 1987, **109**, 424–435.

24 B. D. Murray, H. Hope and P. P. Power, *J. Am. Chem. Soc.*, 1985, **107**, 169–173.

25 R. E. LaPointe, P. T. Wolczanski and G. D. Van Duyne, *Organometallics*, 1985, **4**, 1810–1818.

26 M. Mirzaee, M. Norouzi, A. Amoli and A. Ashrafian, *Advanced Catalytic Materials*, Scrivener Publishing LLC and Wiley, Hoboken, New Jersey, 2015.

27 L. G. Hubert-Pfalzgraf, *J. Mater. Chem.*, 2004, **14**, 3113–3123.
28 Y. Lee and S. M. George, *ACS Nano*, 2015, **9**, 2061–2070.
29 Y. S. Tan, S. N. A. Halim, K. C. Molloy, A. L. Sudlow, A. Otero-de-la-Roza and E. R. T. Tiekink, *Cryst. Eng. Comm.*, 2016, **18**, 1105–1117.
30 Y. Zhang, L. Du, X. Liu and Y. Ding, *New J. Chem.*, 2018, **42**, 9110–9115.
31 I. Y. Ahmet, M. S. Hill, P. R. Raithby and A. L. Johnson, *Dalton Trans.*, 2018, **47**, 5031–5048.
32 H. C. Aspinall, J. Bacsa, A. C. Jones, J. S. Wrench, K. Black, P. R. Chalker, P. J. King, P. Marshall, M. Werner, H. O. Davies and R. Odedra, *Inorg. Chem.*, 2011, **50**, 11644–11652.
33 H. C. Aspinall, J. F. Bickley, J. M. Gaskell, A. C. Jones, G. Labat, P. R. Chalker and P. A. Williams, *Inorg. Chem.*, 2007, **46**, 5852–5860.
34 P. Marchand and C. J. Carmalt, *Coord. Chem. Rev.*, 2013, **257**, 3202–3221.
35 L. G. Hubert-Pfalzgraf, *Coord. Chem. Rev.*, 1998, **178**–**180**, 967–997.
36 J. Aarik, A. Aidla, A. Jaek, M. Leskela and L. Niinisto, *J. Mater. Chem.*, 1994, **4**, 1239–1244.
37 T. Aaltonen, M. Ritala and M. Leskelä, *Electrochem. Solid-State Lett.* , 2005, **8**, C99–C101.
38 R. O'Kane, J. Gaskell, A. C. Jones, P. R. Chalker, K. Black, M. Werner, P. Taechakumput, S. Taylor, P. N. Heys and R. Odedra, *Chem. Vap. Deposition*, 2007, **13**, 609–617.
39 J. Thery, C. Dubourdieu, T. Baron, C. Ternon, H. Roussel and F. Pierre, *Chem. Vap. Deposition*, 2007, **13**, 232–238.
40 S. Van Elshocht, P. Lehnen, B. Seitzinger, A. Abrutis, C. Adelmann, B. Brijs, M. Caymax, T. Conard, S. De Gendt, A. Franquet, C. Lohe, M. Lukosius, A. Moussa, O. Richard, P. Williams, T. Witters, P. Zimmerman and M. Heyns, *J. Electrochem. Soc.*, 2006, **153**, F219–F224.
41 Y. Otani, K. Uchiyama, S. Okamura and T. Shiosaki, *Integr. Ferroelectr.*, 2006, **81**, 261–270.
42 C. Dubourdieu, E. Rauwel, C. Millon, P. Chaudouet, F. Ducroquet, N. Rochat, S. Rushworth and V. Cosnier, *Chem. Vap. Deposition*, 2006, **12**, 187–192.
43 R. J. Potter, P. A. Marshall, P. R. Chalker, S. Taylor, A. C. Jones, T. C. Q. Noakes and P. Bailey, *Appl. Phys. Lett.*, 2004, **84**, 4119–4121.
44 J. S. Zhao, D.-Y. Park, M. J. Seo, C. S. Hwang, Y. K. Han, C. H. Yang and K. Y. Oh, *J. Electrochem. Soc.*, 2004, **151**, C283–C291.
45 P. Marchand and C. J. Carmalt, *Coord. Chem. Rev.*, 2013, 257, 3202–3221.
46 Y. S. Min, Y. J. Cho and C. S. Hwang, *Chem. Mater.*, 2005, **17**, 626–631.
47 Y.-S. Min, Y. J. Cho, J.-H. Ko, E. J. Bae, W. Park and C. S. Hwang, *J. Electrochem. Soc.*, 2005, **152**, F124–F128.
48 W.-H. Kim, M.-K. Kim, I.-K. Oh, W. J. Maeng, T. Cheon, S.-H. Kim, A. Noori, D.

Thompson, S. Chu and H. Kim, *J. Am. Ceram. Soc.*, 2014, **97**, 1164–1169.

49 P. J. King, N. Sedghi, S. Hall, I. Z. Mitrovic, P. R. Chalker, M. Werner and S. Hindley, *J. Vac. Sci. Technol. B*, 2014, **32**, 03D103/1-03D103/5.

50 L. G. Hubert-Pfalzgraf, S. Daniele, A. Bennaceur, J.-C. Daran and J. Vaissermann, *Polyhedron*, 1997, **16**, 1223–1234.

51 S. C. Goel, M. Y. Chiang and W. E. Buhro, *Inorg. Chem.*, 1990, **29**, 4646–4652.

52 V. L. Young, D. F. Cox and M. E. Davis, *Chem. Mater.*, 1993, **5**, 1701–1709.

53 K. C. Molloy and P. A. Williams, *Appl. Organomet. Chem.*, 2008, **22**, 676–683.

54 L. G. Hubert-Pfalzgraf, A. Abrutis, S. Pasko, N. Touati and D. Luneau, *Polyhedron*, 2006, **25**, 293–299.

55 S. H. Yoo, H. Choi, H.-S. Kim, B. K. Park, S. S. Lee, K.-S. An, Y. K. Lee, T.-M. Chung and C. G. Kim, *Eur. J. Inorg. Chem.*, 2011, 1833–1839.

56 T. Y. Chou, Y. Chi, S. F. Huang, C. S. Liu, A. J. Carty, L. Scoles and K. A. Udachin, *Inorg. Chem.*, 2003, **42**, 6041–6049.

57 Y. Chi, T.-Y. Chou, Y.-J. Wang, S.-F. Huang, A. J. Carty, L. Scoles, K. A. Udachin, S.-M. Peng and G.-H. Lee, *Organometallics*, 2004, **23**, 95–103.

58 Y. Chi, P.-F. Hsu, C.-S. Liu, W.-L. Ching, T.-Y. Chou, A. J. Carty, S.-M. Peng, G.-H. Lee and S.-H. Chuang, *J. Mater. Chem.*, 2002, **12**, 3541–3550.

59 M. Lukas, G. Maximilian, de los A. Teresa, G. Ignacio, M. Felix, W. Manuela, P. Harish, A. Peter, G. Guido and D. Anjana, *Chem. Eur. J.*, 2017, **23**, 10768–10772.

60 W. J. Maeng, D. Choi, J. Park and J.-S. Park, *Ceram. Int.*, 2015, **41**, 10782–10787.

61 H. Y. Kim, E. A. Jung, G. Mun, R. E. Agbenyeke, B. K. Park, J.-S. Park, S. U. Son, D. J. Jeon, S.-H. K. Park, T.-M. Chung and J. H. Han, *ACS Appl. Mater. Interfaces*, 2016, **8**, 26924–26931.

62 R. E. Agbenyeke, E. A. Jung, B. K. Park, T.-M. Chung, C. G. Kim and J. H. Han, *Appl. Surf. Sci.*, 2017, **419**, 758–763.

63 G. S. Mary, N. J. Hyeun, L. G. Yeon, H. J. Hwan, P. B. Keun, K. C. Gyoun, J. D. Ju and C. Taek-Mo, *Eur. J. Inorg. Chem.*, 2016, **2016**, 5539–5546.

64 R. O' Donoghue, D. Peeters, D. Rogalla, H.-W. Becker, J. Rechmann, S. Henke, M. Winter and A. Devi, *Dalton Trans.*, 2016, **45**, 19012–19023.

65 J. P. Lee, M. H. Mi, T.-M. Chung, Y.-S. Kim and M. M. Sung, *Bull. Korean Chem. Soc.*, 2004, **25**, 4, 475-479.

66 M. Gebhard, F. Mitschker, M. Wiesing, I. Giner, B. Torun, T. de los Arcos, P. Awakowicz, G. Grundmeier and A. Devi, *J. Mater. Chem. C*, 2016, **4**, 1057–1065.

67 J. R. Avila, A. W. Peters, Z. Li, M. A. Ortuño, A. B. F. Martinson, C. J. Cramer, J. T. Hupp and O. K. Farha, *Dalton Trans.*, 2017, **46**, 5790–5795.

68 T. Iivonen, J. Hamalainen, B. Marchand, K. Mizohata, M. Mattinen, G. Popov, J. Kim, R. A. Fischer and M. Leskela, *J. Vac. Sci. Technol. A*, 2016, **34**, 01A109/1-01A109/7.

69 L. C. Kalutarage, S. B. Clendenning and C. H. Winter, *Chem. Mater.*, 2014, **26**, 3731–3738.

70 K. Vayrynen, K. Mizohata, J. Raisanen, D. Peeters, A. Devi, M. Ritala and M. Leskela, *Chem. Mater.*, 2017, **29**, 6502–6510.

71 T. J. Knisley, T. C. Ariyasena, T. Sajavaara, M. J. Saly and C. H. Winter, *Chem. Mater.*, 2011, **23**, 4417–4419.

72 W. Lee, W. Jeon, C. H. An, M. J. Chung, H. J. Kim, T. Eom, S. M. George, B. K. Park, J. H. Han, C. G. Kim, T.-M. Chung, S. W. Lee and C. S. Hwang, *Chem. Mater.*, 2015, **27**, 3881–3891.

73 B. K. Lee, S. H. Kim, B. K. Park, S. S. Lee, J.-H. Hwang, T.-M. Chung, Y. K. Lee, C. G. Kim and K.-S. An, *J. Nanosci. Nanotechnol.*, 2011, **11**, 5887–5891.

74 S.-E. Jin, D. Lee, S. Lee, J.-M. Choi, B. Kim, C. G. Kim, T.-M. Chung and D.-J. Byun, *Surf. Rev. Lett.*, 2010, **17**, 307–310.

75 H. Kim, M. Y. Lee, S.-H. Kim, S. I. Bae, K. Y. Ko, H. Kim, K.-W. Kwon, J.-H. Hwang and D.-J. Lee, *Appl. Surf. Sci.*, 2015, **349**, 673–682.

76 W.-H. Kim, H.-B.-R. Lee, K. Heo, Y. K. Lee, T.-M. Chung, C. G. Kim, S. Hong, J. Heo and H. Kim, *J. Electrochem. Soc.*, 2010, **158**, D1–D5.

77 H.-S. Kang, J.-B. Ha, J.-H. Lee, C. K. Choi, J. Y. Lee and K.-M. Lee, *Thin Solid Films*, 2011, **519**, 6658–6661.

78 M.-H. Ko, B. Shong and J.-H. Hwang, *Ceram. Int.*, 2018, **44** (14), 16342-16351.

79 T.-M. Chung, S. S. Lee, W. Cho, M. Kim, Y. K. Lee, J.-H. Hwang, K.-S. An and C. G. Kim, *Bull. Korean Chem. Soc.*, 2011, **32**, 783–784.

80 P. Antony Premkumar, M. Toeller, C. Adelmann, J. Meersschaut, A. Franquet, O. Richard, H. Tielens, B. Brijs, A. Moussa, T. Conard, H. Bender, M. Schaekers, J. A. Kittl, M. Jurczak and S. Van Elshocht, *Chem. Vap. Deposition*, 2012, **18**, 61–69.

81 M.-H. Ko, B. Shong and J.-H. Hwang, *Ceram. Int.*, 2018, **44** (14), 16342-16351.

82 T. S. Yang, W. Cho, M. Kim, K.-S. An, T.-M. Chung, C. G. Kim and Y. Kim, *J. Vac. Sci. Technol. A*, 2005, **23**, 1238–1243.

83 J. H. Han, E. A. Jung, H. Y. Kim, D. H. Kim, B. K. Park, J.-S. Park, S. U. Son and T.-M. Chung, *Appl. Surf. Sci.*, 2016, **383**, 1–8.

84 G. W. Hwang, H. J. Lee, K. Lee and C. S. Hwang, *J. Electrochem. Soc.*, 2007, **154**, G69–G76.

85 H. J. Lee, G. H. Kim, K. Lee and C. S. Hwang, *Electrochem. Solid-State Lett.*, 2007, **10**, G89–G92.

86 H. J. Lee, M. H. Park, Y.-S. Min, G. Clavel, N. Pinna and C. S. Hwang, *J. Phys. Chem. C*, 2010, **114**, 12736–12741.

87 J. H. Han, Y. J. Chung, B. K. Park, S. K. Kim, H. S. Kim, C. G. Kim and T. M. Chung, *Chem. Mater.*, 2014, **26**, 6088–6091.

88 I.-H. Baek, J. J. Pyeon, Y. G. Song, T.-M. Chung, H.-R. Kim, S.-H. Baek, J.-S. Kim, C.-Y. Kang, J.-W. Choi, C. S. Hwang, J. H. Han and S. K. Kim, *Chem. Mater.*, 2017, **29**, 8100–8110.

89 B. K. Lee, E. Jung, S. H. Kim, D. C. Moon, S. S. Lee, B. K. Park, J. H. Hwang, T.-M.

Chung, C. G. Kim and K.-S. An, *Mater. Res. Bull.*, 2012, **47**, 3052–3055.

90 M.-J. Choi, C. J. Cho, K.-C. Kim, J. J. Pyeon, H.-H. Park, H.-S. Kim, J. H. Han, C. G. Kim, T.-M. Chung, T. J. Park, B. Kwon, D. S. Jeong, S.-H. Baek, C.-Y. Kang, J.-S. Kim and S. K. Kim, *Appl. Surf. Sci.*, 2014, **320**, 188–194.

91 S. Kannan Selvaraj, A. Feinerman and C. G. Takoudis, *J. Vac. Sci. Technol. A*, 2014, **32**, 01A112/1-01A112/6.

92 B. K. Campbell and K. N. Campbell, *J. Am. Chem. Soc.*, 1938, **60**, 1372–1376.

93 R. Anwander, F. C. Munck, T. Priermeier, W. Scherer, O. Runte and W. A. Herrmann, *Inorg. Chem.*, 1997, **36**, 3545–3552.

94 A. Heydari, M. Mehrdad, A. Maleki and N. Ahmadi, *Synthesis*, 2004, **2004**, 1563–1565.

95 S. H. Kim, S. Y. Han, J. H. Kim, Y. Y. Kang, J. Lee and Y. Kim, *Eur. J. Inorg. Chem.*, 2015, **2015**, 2323–2329.

96 C. G. Kim, T.-M. Chung, K. L. Young and S. L. Sun, *US Pat. 8030507B2*.

97 J. D. Donaldson and S. M. Grimes, in *Chemistry of Tin, 2nd edn.*, Ed. P. G. Harrison, Springer, Dordrecht, 1998, 62–92.

98 R. Day, R. R. Holmes, A. Schmidpeter, K. Stollb and L. Howea, *Chem. Ber.*, 1991, **124**, 2443-2448.

99 T. Fjeldberg, H. Hope, M. F. Lappert, P. P. Power and A. J. Thorne, *J. Chem. Soc. Chem. Commun.*, 1983, 639–641.

100 M. M. Olmstead and P. P. Power, *Inorg. Chem.*, 1984, **23**, 413–415.

101 A. W. Addison, T. N. Rao, J. Reedijk, J. van Rijn and G. C. Verschoor, *J. Chem. Soc. Dalton Trans.*, 1984, 1349–1356.

102 L. Yang, D. R. Powell and R. P. Houser, *Dalton Trans.*, 2007, 955–964.

103 D. Rosiak, A. Okuniewski and J. Chojnacki, *Polyhedron*, 2018, **146**, 35–41.

104 S. H. Kim, I.-H. Baek, D. H. Kim, J. J. Pyeon, T.-M. Chung, S.-H. Baek, J.-S. Kim, J. H. Han and S. K. Kim, *J. Mater. Chem. C*, 2017, **5**, 3139–3145.

105 L. Nyns, A. Delabie, M. Caymax, M. M. Heyns, S. Van Elshocht, C. Vinckier and S. De Gendt, *ECS Trans.*, 2008, **16**, 257–267.

106 K. J. Saji, K. Tian, M. Snure and A. Tiwari, *Adv. Electron. Mater.*, 2016, **2**, 1500453.

107 A. A. Yadav, S. C. Pawar, D. H. Patil and M. D. Ghogare, *J. Alloys Compd.*, 2015, **652**, 145–152.

108 X.-T. Chen, K.-X. Wang, Y.-B. Zhai, H.-J. Zhang, X.-Y. Wu, X. Wei and J.-S. Chen, *Dalton Trans.*, 2014, **43**, 3137–3143.

109 T. Ungár, *Scr. Mater.*, 2004, **51**, 777–781.

110 D.-M. Smilgies, *J. Appl. Crystallogr.*, 2009, **42**, 1030–1034.

111 P. Scherrer, *Göttinger Nachrichten Gesell.,* 1918, **2,** 98–100.

112 M. A. Lemes, M. S. Godinho, D. Rabelo, F. T. Martins, A. Mesquita, F. N. De Souza Neto, O. A. Araujo and A. E. De Oliveira, *Acta Chim. Slov.*, 2014, **61**, 778–785.

113 K. Fleischer, E. Norton, D. Mullarkey, D. Caffrey and I. V. Shvets, *Materials*, 2017, **10**, 19–22.

114 R. Timm, A. R. Head, S. Yngman, J. V Knutsson, M. Hjort, S. R. McKibbin, A. Troian, O. Persson, S. Urpelainen, J. Knudsen, J. Schnadt and A. Mikkelsen, *Nat. Commun.*, 2018, **9**, 1412.

115 T. Eom, T. Gwon, S. Yoo, B. J. Choi, M.-S. Kim, I. Buchanan, M. Xiao and C. S. Hwang, *Chem. Mater.*, 2014, **26**, 1583–1591.

116 K. Knapas and M. Ritala, *Crit. Rev. Solid State Mater. Sci.*, 2013, **38**, 167–202.

117 J. A. Caraveo-Frescas, P. K. Nayak, H. A. Al-Jawhari, D. B. Granato, U. Schwingenschlögl and H. N. Alshareeft, *ACS Nano*, 2013, **7**, 5160–5167.

118 E. Fortunato, R. Barros, P. Barquinha, V. Figueiredo, S.-H. K. Park, C.-S. Hwang and R. Martins, *Appl. Phys. Lett.*, 2010, **97**, 52105.

119 Y. Ogo, H. Hiramatsu, K. Nomura, H. Yanagi, T. Kamiya, M. Hirano and H. Hosono, *Appl. Phys. Lett.*, 2008, **93**, 32113.

120 H. Yabuta, N. Kaji, R. Hayashi, H. Kumomi, K. Nomura, T. Kamiya, M. Hirano and H. Hosono, *Appl. Phys. Lett.*, 2010, **97**, 72111.

121 P.-C. Hsu, C.-J. Hsu, C.-H. Chang, S.-P. Tsai, W.-C. Chen, H.-H. Hsieh and C.-C. Wu, *ACS Appl. Mater. Interfaces*, 2014, **6**, 13724–13729.

122 N. Hollingsworth, G. A. Horley, M. Mazhar, M. F. Mahon, K. C. Molloy, P. W. Haycock, C. P. Myers and G. W. Critchlow, *Appl. Organomet. Chem.*, 2006, **20**, 687–695.

123 N. N. Zemlyansky, I. V Borisova, M. G. Kuznetsova, V. N. Khrustalev, Y. A. Ustynyuk, M. S. Nechaev, V. V Lunin, J. Barrau and G. Rima, *Organometallics*, 2003, **22**, 1675–1681.

124 T. J. Boyle, T. M. Alam, M. A. Rodriguez and C. A. Zechmann, *Inorg. Chem.*, 2002, **41**, 2574–2582.

125 T. Fjeldberg, P. B. Hitchcock, M. F. Lappert, S. J. Smith and A. J. Thorne, *J. Chem. Soc. Chem. Comm.*, 1985, 939–941.

126 N. Hollingsworth, G. Kociok-Köhn, K. C. Molloy and A. L. Sudlow, *Dalton Trans.*, 2010, **39**, 5446–5452.

127 C. Kitamura, N. Maeda, N. Kamada, M. Ouchi and A. Yoneda, *J. Chem. Soc., Perkin Trans. 1*, 2000, 781–785.

128 C. Kitamura, A. Yoneda, K. Sugiura and Y. Sakata, *Acta Crystallogr. Sect. C*, 1999, **55**, 876–878.

129 S. H. Han, E. A. Jung, J. H. Lee, D. H. Kim, G. Y. Lee, B. K. Park, C. G. Kim, S. U. Son and T.-M. Chung, *Chemistry Select*, 2018, **3**, 7836–7839.

130 K.-H. Park, A. Z. Bradley, J. S. Thompson and W. J. Marshall, *Inorg. Chem.*, 2006, **45**, 8480–8482.

131 Z. Li, A. Rahtu and R. G. Gordon, *J. Electrochem. Soc.*, 2006, **153**, C787.

132 V. N. Khrustalev, I. A. Portnyagin, N. N. Zemlyansky, I. V. Borisova, M. S. Nechaev, Y. A. Ustynyuk, M. Y. Antipin and V. Lunin, *J. Organomet. Chem.*, 2005, **690**, 1172–1177.

133 L. Wang, C. E. Kefalidis, T. Roisnel, S. Sinbandhit, L. Maron, J.-F. Carpentier and Y. Sarazin, *Organometallics*, 2015, **34**, 2139–2150.

134 M. J. McGeary, K. Folting and K. G. Caulton, *Inorg. Chem.*, 1989, **28**, 4051–4053.

135 O. V. Chernov, A. Y. Smirnov, I. A. Portnyagin, V. N. Khrustalev and M. S. Nechaev, *J. Organomet. Chem.*, 2009, **694**, 3184–3189.

136 A. Pop, L. Wang, V. Dorcet, T. Roisnel, J.-F. Carpentier, A. Silvestru and Y. Sarazin, *Dalton Trans.*, 2014, **43**, 16459–16474.

137 L. M. Engelhardt, B. S. Jolly, M. F. Lappert, C. L. Raston and A. H. White, *J. Chem. Soc. Chem. Comm.*, 1988, 336–338.

138 S. R. Foley, G. P. A. Yap and D. S. Richeson, *Organometallics*, 1999, **18**, 4700–4705.

139 H. Braunschweig, R. W. Chorley, P. B. Hitchcock and M. F. Lappert, *J. Chem. Soc. Chem. Comm.*, 1992, 1311.

140 J. Jastrzebski and G. van Koten, in *Advances in Organometallic Chemistry, Vol. 35*, Eds. F. G. A. Stone and R. West, Academic Press, Inc., London, 1993, 258–270.

141 George A. Jeffrey, *An Introduction to Hydrogen Bonding*, OUP, Oxford, 1997.

142 P. Foley and M. Zeldin, *Inorg. Chem.*, 1975, **14**, 2264–2267.

143 P. J. Davidson, D. H. Harris and M. F. Lappert, *J. Chem. Soc., Dalton Trans.*, 1976, 2268–2274.

Chapter 3

Chapter 3: Tin(II) Aminoamides

3.0. Introduction

3.0.1. Metal Amide Chemistry

The chemistry of metal amides is as commonplace across the periodic table as that of the metal alkoxides, with amido complexes known for nearly every naturally occurring element.[1] With the rich and varied chemistry offered by metal amide species, a wealth of applications are found in wide-ranging fields including catalysis,[2–4] synthesis,[1,5,6] biological reactions[7,8] and hydrogen storage[9,10] amongst many others.

Amido ligands have the form $[NH_2]^-$, $[N(H)R]^-$ or $[N(R)R']^-$ (where R may be identical or different), with possible substituents comprising alkyl, aryl, and importantly, silyl. Such species can be found coordinated in terminal or bridging configurations, as seen in complexes such as $[Sn(NMe_2)(\mu\text{-}NMe_2)]_2$[11] and those encountered previously in Chapter 2, where both bridging and terminal arrangements were observed. The two principal bonding modes of terminal metal amides can be seen in (Figure 3.1). With a single covalent bond to a metal centre, an sp^3 NR_2 environment can be classed as a one-electron, or X, ligand. Alternatively, a planar sp^2 NR_2 environment affords the possibility of lone pair π-donation into an appropriate metal acceptor orbital, thus giving classification as a three-electron, LX, ligand. This arrangement is most commonly observed in high oxidation state early transition metals, where vacant d-orbitals are available for π-acceptance.[1,12]

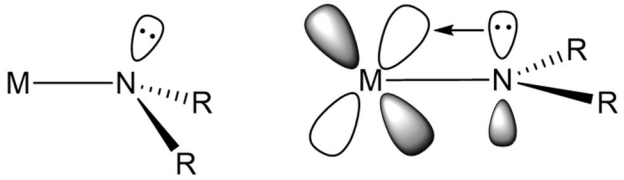

Figure 3.1 – Termial amido bonding configurations with sp^3 and sp^2 nitrogen atoms.

Substantial differences in available heteroatomic electron density, coupled with an increased steric crowding around the donor atom, leads to a much lower tendency for amido systems to form bridged species than is observed for alkoxide compounds. As such, the propensity to form cluster species is significantly decreased. Astute application of electronic and steric factors has seen a wealth of chemistry develop around the $\{N(SiMe_3)_2\}$ ligand, more commonly referred to as HMDS, or hexamethyldisilylamide. This sterically demanding ligand is ubiquitous across synthetic chemistry and has found particular use in the transition metals, where the strong σ- and π- donating tendencies of conventional amide ligands result in strong

bonds to the π-accepting early transition metals, but relatively weak bonds to the poorly π-accepting later transition metals. The incorporation of silicon may well provide an explanation for this, with the π-electrons of the nitrogen partially delocalising onto the silicon atom, allowing for the $N(SiMe_3)_2$ ligand to act as a weak π-acceptor. These influences, coupled with the kinetically stabilising effects of the bulky $SiMe_3$ groups make conventional decomposition pathways more energetically unfavourable than in simpler amide species. These effects are compounded by the lack of available ß-hydrogen atoms, preventing ß-hydride eliminations from taking place.[12]

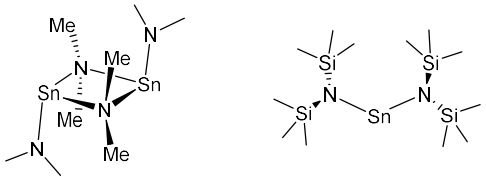

Figure 3.2 – Dimeric $[Sn(NMe_2)(\mu\text{-}NMe_2)]_2$ and monomeric $[Sn\{N(SiMe_3\}_2]_2$.

Metal amide species are extensively used within synthesis, with the lability of the M–N bond affording facile ligand substitution. The strength of M–N bonds is lower than that of M–O and as such, amide-based synthetic routes were applied in the synthesis of alkoxide complexes **1-12** (Chapter 2), and underpin the majority of the reactions undertaken throughout the remainder of the investigation.[13] The benefits of simple amide displacement are also found in the expulsion of volatile amine species on ligand protonation, such as $HNMe_2$ and $HN(SiMe_3)_2$, which act as thermodynamic driving forces for the reaction.

This lability often presents as a lack of stability towards thermal stress on the part of simple metal amides. Notable exceptions to this include the $^{-}N(SiMe_3)_2$ ligand for reasons outlined above. Testament to this, and of particular relevance to this investigation, are the relative stabilities of $[Sn(NMe_2)(\mu\text{-}NMe_2)]_2$ and $[Sn\{N(SiMe_3)_2\}_2]$, with the former decomposing as a solid over ca. 100 °C, and the latter withstanding distillation at temperatures well in excess of 200 °C.[11,14] The lack of stability exhibited by simple, sterically undemanding amides is often mitigated by the functionalisation of these ligands through electronic, steric or coordinative means, in much the same way as was discussed in relation to alkoxide compounds previously. Whilst keeping steric demands as minimal as possible, the alteration of ligand electronics alongside the inclusion of multidenticity allows the reactivity of metal-amide bonding to be leveraged, whilst improving certain other physical properties of the resultant complexes. This is particularly relevant in deposition applications, where the volatility, thermal stability and solubility of precursor complexes can be fine-tuned with functionalisation of nitrogen-based ligand systems

3.0.2. Metal Amides as Precursors for Atomic Layer Deposition

The lability and versatility of metal amides has unsurprisingly been exploited for use in the development and application of M–N complexes for utilisation in a variety of deposition methods. The use of such complexes is well-established within the field of chemical vapour deposition, with many CVD precursors finding a resurgence in atomic layer deposition over recent years.[15]

Simple alkyl amides are ubiquitous across ALD processes. Atomic layer deposition using amide ligands of the form $^{-}$NRR' (where R,R' = Me or Et) has been demonstrated with a vast number of elements including titanium,[16–18] hafnium,[19,20] zirconium,[21] vanadium,[22,23] niobium,[24] tantalum,[25,26] aluminium,[27] indium[28] and silicon.[29,30] Furthermore, –N(SiMe$_3$)$_2$, systems are reliably used across the periodic table for the atomic layer deposition of a number of desirable elements.[31,32]

Constraints over the volatility, reactivity, stability and availability of the simple alkyl and silyl amides of a number of elements has seen a burgeoning in the development of more adaptive precursor systems. Whilst a plethora of amide-based precursors have been reported in the literature, a selection of the most relevant systems is given in Figure 3.3. With a few isolated exceptions, amidinates, formamidinates and guanidinates appear to be the most pervasive nitrogen-bound ligands after those of the simple amides. Amidinate precursors have been applied in the deposition of Zr,[33] Mg,[34] Ca,[35,36] V,[37–39] Mo,[40,41] In,[39] Sn,[42] Ti,[16,43] Sc,[44] Y,[45–48] Dy,[49,50] La,[45,46,51] Er,[52] Pr,[49] Gd,[45,46] W,[40] Ni,[53–55] Co[53,56–58] and Fe[53], whilst guanidinate systems have been developed and tested for Ta,[59] Ti,[17] Y,[60] Hf,[20] Er,[61] In[62] and Zr,[18,21] and a single formamidinate precursor exists for calcium deposition.[36] Cobalt and nickel metal films have also been deposited with precursors taking the form [M(RNCHCHNR)$_2$] (where R = ^{t}Bu and M = Ni, Co, and R = ^{i}Pr and M = Co), though are not directly relevant to the course of this research. ALD was undertaken via a three-step reaction utilising formic acid followed by the reducing agent 1,4-bis(trimethylsilyl)dihydropyrazine.[63–65]

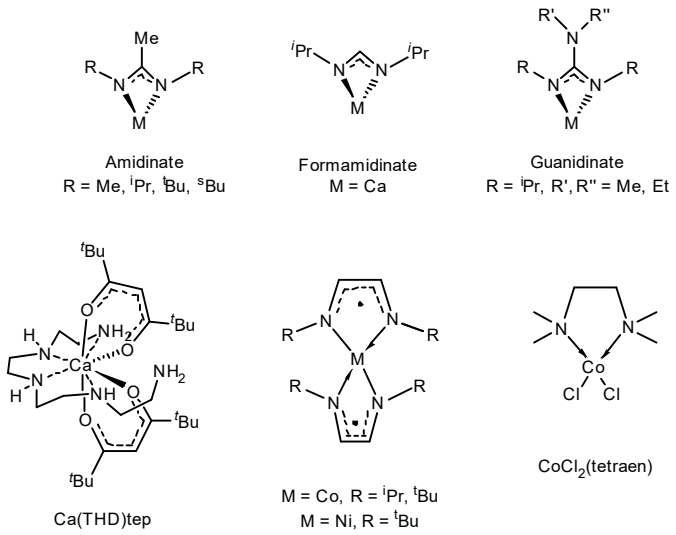

Figure 3.3 – A selection of nitrogen-based ALD precursors.

It would be remiss not to mention that whilst nitrogen-based ligands for ALD applications are predominantly charged species that form formal, largely covalent bonds with the metals of choice, neutral ligands play an occasionally important part in precursor design, assisting with coordinative saturation of metal centres and in enhancing stability and volatility. This is demonstrated in the coordination of tetramethylethylenediamine to cobalt(II) chloride and its application in the atomic layer deposition of cobalt oxide with H_2O by Väyrynen et al.[66] The coordination of neutral amines within ALD precursors has also been demonstrated by Hänninen et al., where the large coordination sphere of calcium was saturated by tetraethylenepentamine within the complex [Ca(THD)$_2$tep] (Figure 3.3).[67]

3.0.3. Tin(II) Amides in Atomic Layer Deposition

The reactive Sn–N bond is well established as an indispensable starting reagent in numerous synthetic procedures, and its lability has been used to great effect in a number of deposition applications. Indeed, insertions of this bond into a range of reagents leads to the synthesis of guanidinate,[68,69] ureide[70] and thioureide[71] species, which have in turn been successfully applied to chemical vapour deposition processes towards tin-chalcogenide materials such as SnO, SnS, SnSe and SnTe.[69,70,72] Further to this, tin(IV) dimethylamide is a widely used liquid precursor used in the atomic layer deposition of tin(IV) materials such as SnO_2 and SnS_2. ALD processes with H_2O,[73] H_2O_2,[74,75] O_3[75] and H_2S[76,77] as chalcogenide sources have been reported.

More relevant to the work contained within this chapter is the development of an N-heterocyclic Sn(II) precursor by Gordon et al., depicted in Figure 3.4. The precursor, of the form [Sn(^{t}BuNCH(Me)CH(Me)N^{t}Bu)] features a dianionic ligand with chiral backbone moieties. The precursor was found not to be reactive towards H_2O, instead utilising the greater acidity

of H_2S to deposit tin(II) sulfide.[78] In attempts to deposit tin oxide materials, H_2O_2 was used as a co-reactant, resulting in the deposition of SnO_2 films between 50-150 °C (~1.8 Å/cy).[78,79] In an attempt to combat the harsh oxidation exhibited by H_2O_2, in addition to circumventing the suspected instability of hydrogen peroxide at high temperatures, NO was subsequently used as an oxidant, again resulting in SnO_2 deposition at a rate of ~1.4 Å/cy at temperatures of 200-250 °C.[78,80] Work within the group undertaken at the same time, saw the development of the Sn(II) amidinate, [Sn{(^{i}PrN)$_2$CMe}$_2$], which was again applied to the ALD of tin chalcogenide materials, reacting with H_2S to yield crystalline films of SnS at a growth per cycle of ~0.9 Å in the temperature range of 100-250 °C.[78,81]

The two aforementioned compounds serve to highlight the capricious nature of Sn(II) oxide deposition and precursor development. Both the amidinate and N-heterocyclic precursors displayed a lack of reactivity towards H_2O, necessitating the use of harsher oxidants such as H_2O_2, NO and H_2S, leading to either SnS, or SnO_2 films.[42,78,80]

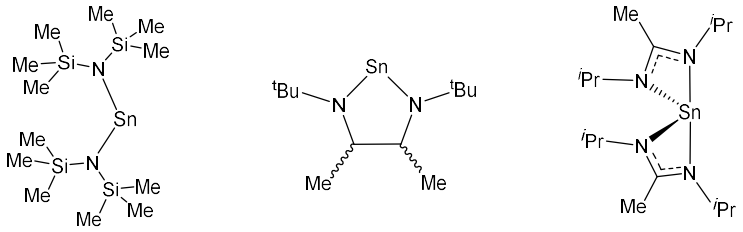

Figure 3.4 – Reported Sn(II) amide ALD precursors.

The most significant development within the field of tin(II) oxide deposition, and one most relevant to this research, was a report by Tupala et al.[82] in 2017 applying Sn(HMDS)$_2$ to the ALD of SnO. The Sn(II) amide precursor was reacted with H_2O at temperatures between 100 and 250 °C, with growth rates varying from 0.05-0.18 Å/cy. Crystallinity was observed within a temperature window of 125-175 °C, with growth rates within this window decreasing from ca. 0.07-0.05 Å/cy (150-175 °C). Amorphous tin oxide films were also deposited using ozone as an oxidant, though this caused significant silicon incorporation due to the decomposition of the HMDS ligand. Alongside the sub-optimal growth rates, non-linear deposition towards the higher temperatures was observed. This was rationalised by the reaction of HN(SiMe$_3$)$_2$ with surface –OH terminations. This results in silicon incorporation into the film and disrupts film growth. The surface passivation effects of HMDS have been previously confirmed by studies by Crowe and Tolbert, which demonstrated that silicon passivation efficiency increases with temperature.[83]

Of the three existing Sn(II)–N systems covered in this synopsis, only [Sn(HMDS)$_2$] demonstrates any degree of viability as a precursor to SnO films, and presents with significant limitations. As such, attention was directed towards a range of novel Sn(II) amide systems,

attempting to emulate the simplicity and reactivity of $[Sn(NMe_2)_2]_2$, and avoid the steric and electronic stability afforded by the more developed ligand systems discussed in this preface.

3.0.4. Target Compounds

Given the low reactivity towards H_2O of the divalent N-heterocyclic stannylene and amidinato complexes developed by Gordon and co-workers discussed previously (Figure 3.3), a range of non-delocalised ligand systems were targeted in an attempt to reduce stability.

The low thermal stability of $[Sn(NMe_2)_2]_2$, coupled with its solid form and low volatility preclude its use within atomic layer deposition. It does however, display the high reactivity towards H_2O and O_2 desirable in an efficient Sn(II) precursor. The analogous compound $[Sn\{N(Me)Et\}_2]$ is far less stable, and any attempts to form longer chain, terminal amido systems in a search for a volatile liquid have failed.[84] As such, research was directed towards similarly simple, silicon-free systems capable of enhancing stability with non-delocalised pendant nitrogen groups. A cursory coverage of some aspects of metal amide bonding was given in Chapter 2, where the dative donating capabilities of an sp^3 nitrogen pendant group were discussed. The same considerations are relevant in this chapter, with a range of inexpensive, commercially available aminoamide molecules identified and targeted (Figure 3.5).

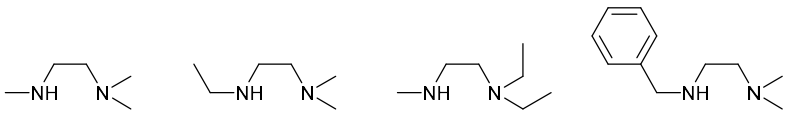

Figure 3.5 – Target pro-ligands for simple tin(II) amides.

Volatile liquid aminoamines targeted were N,N,N-trimethylethylenediamine (tmed), N,N-dimethyl-N'-ethylethylenediamine (deed), N,N-diethyl-N'-methylethylenediamine (dmed), and aromatic N,N-dimethyl-N'-benzylethylenediamine (bded). Attempted reactions in 1:1 and 2:1 ratios with $Sn(NMe_2)_2$ would afford the homo- and heteroleptic species, with the latter allowing the retention of the greatest degree of Sn–N reactivity as possible in conjunction with minimised steric bulk.

3.1. Synthesis and Characterisation of Tin(II) Amides

3.1.1. Synthesis

A range of simple tin(II) aminoamides were identified and synthesised by direct mono- or bis-substitution of tin(II) dimethylamide with bidentate pro-ligands of the form $RNHCH_2CH_2NR'_2$ (where R may be identical or different to R'). Reactions proceed with good yield at room temperature in tetrahydrofuran (Figure 3.6), which after removal of volatiles and distillation afford clear yellow liquids in the case of compounds **13-18**, and solid material in the case of **19** and **20**, which after recrystallisation from hexanes yields orange crystals of suitable quality for single-crystal X-ray diffraction studies.

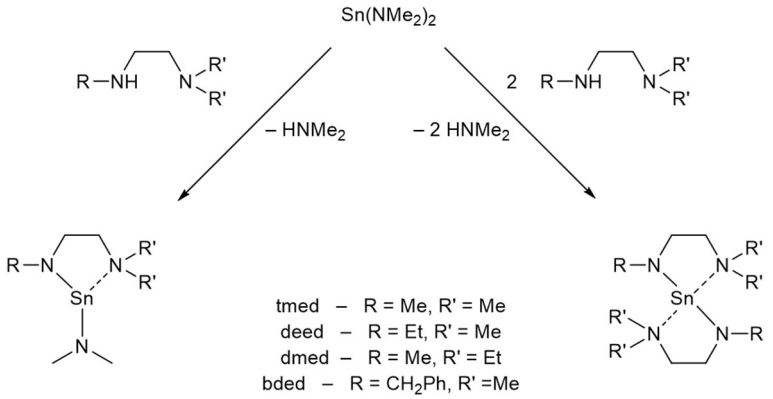

*Figure 3.6 – Generic synthetic procedures for compounds **13-20***

Compounds **13-20** proved to be highly air and moisture sensitive, with liquids **13-18** visibly oxidising on contact with inadequately dried glassware and fuming when handled in all but the most robust of gloveboxes. This sensitivity demonstrates high potential for application as atomic layer deposition precursors, though astute selection is necessary as liquid compounds **13-18** display varying degrees of stability with time, temperature and light.

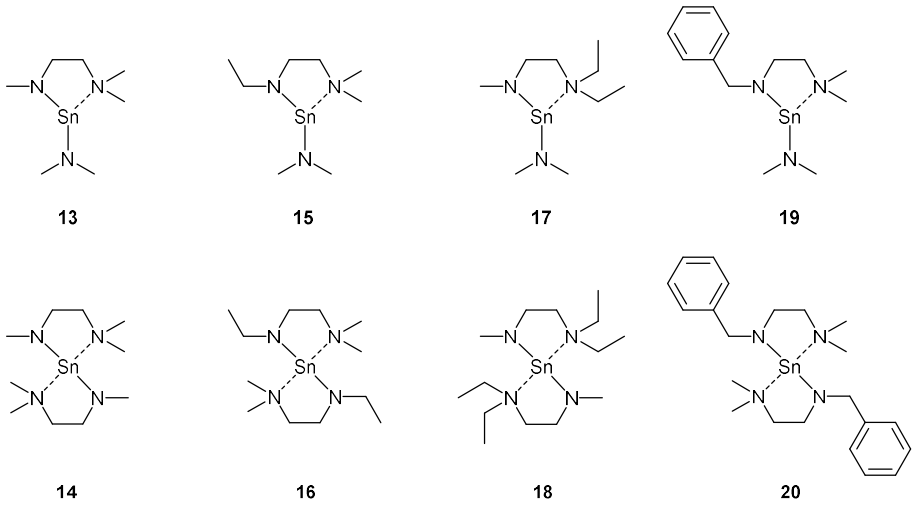

*Figure 3.7 – Compounds **13-20***

3.1.2. Characterisation

The ^{1}H NMR spectra (Appendix, 7.2) of both homo- and heteroleptic tmed systems (**13** and **14**) show clear differences from that of the aminoamine pro-ligand N,N,N-trimethylethylenediamine (tmed). The pro-ligand displays triplet resonances at δ = 2.50 and 2.27 ppm (J = 5.77 Hz) associated with the NHC*H*$_2$ and C*H*$_2$NMe$_2$ backbone environments, in addition to singlet signals at δ = 2.28, 2.03 and 1.28 ppm ascribed to the *Me*NH, CH$_2$N*Me*$_2$ and N*H* environments respectively. Contrastingly, the ^{1}H NMR spectrum of the heteroleptic NMe$_2$ complex **(13)** displays the triplet resonances at δ = 3.22 and 2.28 ppm (J = 5.60 Hz), with a broad SnN*Me*$_2$ signal and C*H*$_3$NCH$_2$ peak lying between at δ = 3.02 and 2.99 ppm. The final CH$_2$N*Me*$_2$ resonance is shifted similarly downfield of its uncomplexed position, at δ = 1.96 ppm. The ^{13}C{^{1}H} NMR spectrum again shows the expected resonances, which are fully disclosed later in the experimental procedures. The ^{119}Sn NMR displays a single, well-defined resonance at δ = +84 ppm.

Similarly, the ^{1}H NMR spectrum of the homoleptic tmed complex **14** gives rise to the expected resonances, which though similarly downshifted from those of the free amine, differ from those observed for the heteroleptic species **(13)**. Aside from the anticipated loss of the SnNMe$_2$ resonance, concise multiplets are observed at δ = 3.32-3.36 and 2.35-2.38 ppm and are ascribed to the backbone CH$_3$NC*H*$_2$ and C*H*$_2$NMe$_2$ methylene groups respectively, whilst peaks at δ = 3.02 and 2.07 ppm account for the C*H*$_3$NCH$_2$ and N*Me*$_2$ groups. Once again, a well-defined ^{13}C{^{1}H} spectrum presents as expected, whilst the ^{119}Sn NMR displays a single resonance at δ = +88 ppm.

Complexes **15** and **16** again display well-defined ^{1}H NMR spectra that differ significantly from the uncomplexed pro-ligand N,N-dimethy-N-ethylethylenediamine (deed), which displays an

overlapping triplet (δ = 2.58 ppm, J = 5.63 Hz) and quartet (δ = 2.54 ppm, J = 7.11 Hz), corresponding to the EtNHC*H*$_2$ and CH_3C*H*$_2$NH groups respectively, in addition to a further triplet at δ = 2.30 ppm (J = 5.63 Hz) and singlet at δ = 2.05 ppm belonging to the CH_2C*H*$_2$$NMe_2$ and CH_2N*Me*$_2$ environments. These resonances are followed by the amine N*H* at δ = 1.16 ppm and a C*H*$_3CH_2$ triplet at δ = 1.02 ppm (J = 7.11 Hz). The ^{1}H NMR spectrum of complex **15** displays downshifted signals, with the ethyl quartet appearing at δ = 3.33 ppm (J = 6.60 Hz) and an overlapped multiplet at δ = 3.07-3.28 ppm comprising the SnN*Me*$_2$ and EtNC*H*$_2$ environments (Appendix, 7.2). Broad signals can also be found at δ = 2.21 ppm (C*H*$_2$$NMe_2$), 1.75 ppm ($CH_2$N*Me*$_2$) and a triplet at δ = 1.41 ppm (J = 6.60, CH_3CH_2N). The ^{13}C{^{1}H} NMR spectrum is once again without remark, and the ^{119}Sn NMR spectrum displays another well-defined asymmetric resonance at δ = +106 ppm, alongside a minor signal at δ = +124 ppm. Due to the significance of compound **15** in subsequent research, a greater resolution ^{1}H NMR spectrum was obtained from neat, unsolvated liquid compound at 400 MHz. This spectrum displayed well-defined resonances at δ = 3.50 (t, J = 5.56 Hz), 3.41 (q, J = 6.88 Hz) and 3.10 ppm, corresponding to the EtNC*H*$_2$, CH_3C*H*$_2$N and SnN*Me*$_2$ environments, in addition to further resonances at δ = 2.76 (t, J = 5.56 Hz), 2.55 (br, s) and 1.41 (t, J = 6.88 Hz), ascribed to the C*H*$_2$$NMe_2$, CH_2N*Me*$_2$ and C*H*$_3CH_2$N protons respectively.

[Sn(deed)$_2$] **(16)** was found to decompose over a period of 48 h, resulting in the formation of metallic tin deposits. Nevertheless, the relevant NMR data were collected, revealing the ^{1}H NMR spectrum of the homoleptic deed complex **16** to display similarly downshifted proton environments from the pro-ligand. This is in conjunction with similar broadening of multiplets caused by a combination of fluxional environments and proximity to nitrogen atoms. Overlapped multiplets at δ = 3.32-3.41 ppm denote the CH_3C*H*$_2$N and EtNC*H*$_2$ protons, whilst a multiplet at δ = 2.31-2.39 ppm is indicative of the remaining methylene C*H*$_2$$NMe_2$ group. The spectrum is completed by a large broad singlet at δ = 2.05 ppm and triplet at δ = 1.33 ppm (J = 7.0 Hz), allocated to the CH_2N*Me*$_2$ and C*H*$_3CH_2$N groups respectively. The ^{13}C{^{1}H} NMR spectrum appears as expected, with the ^{119}Sn resonance appearing in the ^{119}Sn NMR spectrum at δ = 104 ppm.

In a similar vein to the observations made for complex **16**, N,N-diethyl-N-methylethylenediamine derivatives **17** and **18** were also found to exhibit limited stability over time, and as such NMR spectra were collected within a limited timeframe, revealing the expected downshift of environments from their positions observed for the uncoordinated pro-ligand. The ^{1}H NMR of the pro-ligand exhibits a complex series of resonances between δ = 2.28 and 2.55 ppm, comprising the respective shifts of the methylene protons in conjunction with the quartet and singlet resonances for the ethyl and C*H*$_3$NH groups. The amino proton, lost on complexation appears at δ = 1.51 ppm, whilst the triplet attributed to the ethyl chains is found at δ = 0.92 ppm.

The overlapping pro-ligand ^{1}H NMR spectrum becomes somewhat less convoluted on complexation, with the heteroleptic species **17** displaying a MeNC*H*$_2$ triplet resonance at δ = 3.25 ppm (J = 6.00 Hz), followed by broad singlets at δ = 3.04 and 2.99 ppm assigned to the *Me*N and SnN*Me*$_2$ groups respectively. Further upfield, a multiplet comprising signals from the methylene backbone C*H*$_2$NEt$_2$ and CH$_2$N(C*H*$_2$CH$_3$)$_2$ groups can be found at δ = 2.38-2.49 ppm, whilst the final CH$_2$C*H*$_3$ triplet presents at δ = 0.80 ppm, further upfield than its pro-ligand counterpart. Despite a relatively uninformative ^{13}C{^{1}H} NMR, the ^{119}Sn spectrum displays a broad asymmetric resonance at δ = +95 ppm, in addition to a smaller broad signal at δ = +124 ppm. The latter resonance is likely to be caused by the presence of [Sn(NMe$_2$)$_2$]$_2$, indicative of a Schlenk-type equilibrium between heteroleptic [Sn(dmed)NMe$_2$] **(17)**, [Sn(dmed)$_2$] **(18)** and [Sn(NMe$_2$)$_2$]$_2$. The asymmetric resonance centred at δ = 95 ppm, which spans between δ = 101 ppm and δ = 90 ppm could tentatively be assigned to a coalescence of both hetero- and homoleptic species, with the ^{119}Sn NMR of the latter presenting at δ = 102 ppm. Similar observations within heteroleptic aminoalkoxide systems were discussed in Chapter 2, whilst this theory is further supported by the NMR analysis of complexes **19** and **20**, *vide infra*. It is also important to note that all ^{119}Sn NMR resonances displayed by the amino compounds studied within this chapter present as broad signals, typically spanning 10-20 ppm.

The ^{1}H NMR spectrum of homoleptic [Sn(dmed)$_2$] **(18)** exhibits typical downshifted resonances from those observed for both the heteroleptic species and pro-ligand, with the methylene CH$_3$NC*H*$_2$ triplet appearing at δ = 3.40 ppm (J = 6.2 Hz), and the C*H*$_3$N singlet and N(CH$_2$C*H*$_3$)$_2$ triplet (J = 7.2 Hz) presenting at δ = 3.12 and 0.80 ppm respectively. Between the latter two resonances, at δ = 2.47-2.57 ppm, a multiplet comprising the methylene groups about the tertiary amine (C*H*$_2$N(C*H*$_2$CH$_3$)$_2$) is found. The broad ^{119}Sn resonance can be observed at δ = 102 ppm, approximately 7 ppm downfield of the heteroleptic system **(17)**.

*Table 3.1 – ^{119}Sn chemical shifts of compounds **13-21**.*

Compound		δ_{119Sn} (ppm)
-	[Sn(NMe$_2$)$_2$]$_2$	+125
13	[Sn(tmed)NMe]$_2$	+84
14	[Sn(tmed)]$_2$	+88
15	[Sn(deed)NMe]$_2$	+106, +124*
16	[Sn(deed)]$_2$	+104
17	[Sn(dmed)NMe]$_2$	+95, +124*
18	[Sn(dmed)]$_2$	+102
19	[Sn(bded)NMe]$_2$	+60, +88, +117*, +124*
20	[Sn(bded)]$_2$	+60
21	[Sn(DippG)deed]	–145

*Minor resonances

*Characterisation of [Sn(bded)NMe_2] **(19)** and [Sn(bded)$_2$] **(20)**.*

With compounds **13**-**18** presenting as highly sensitive liquids, a pro-ligand likely to induce crystallisation was selected and reacted in the same manner in an attempt to gain an insight into the structural parameters within the liquid compounds. Subsequently, the molecular structures of the hetero- **(19)** and homoleptic **(20)** tin derivatives of N-benzyl-N,N-dimethylethylenediamine (bded) were successfully determined via single-crystal X-ray crystallography, despite displaying a similarly high reactivity towards air and moisture as their aliphatic counterparts.

Both the ^{1}H NMR and ^{119}Sn NMR of heteroleptic [Sn(bded)NMe_2] **(19)** appear to consist of a mixture of [Sn$(NMe_2)_2$], mono- and bis-substituted species. The ^{119}Sn NMR displays two large resonances at δ = +60 ppm and δ = +88 ppm, likely to correlate with the presence of the bis species **(20)** and target compound respectively. Two lower intensity resonances are also observed at δ = +117 and +124 ppm, with the latter consistent with the presence of the [Sn$(NMe_2)_2]_2$ dimer. With the proximity of this to the signal at δ = +117 ppm, it is tentatively suggested that the undetermined resonance at δ = +117 ppm could be attributed to either the monomeric form of [Sn(bded)NMe_2] **(19)**, or more likely a mixed dimer comprising [Sn$(NMe_2)_2$] and [Sn(bded)NMe_2] **(19)**. The ^{1}H and ^{119}Sn NMR spectra of [Sn(bded)$_2$] **(20)** are considerably less convoluted than those of the heteroleptic species, with well-defined peaks at δ = 4.44, 3.19 (t, J = 5.60 Hz), 2.28 (t, J = 5.60 Hz) and 1.97 ppm, ascribed to the PhCH_2, PhCH_2NCH_2, CH_2NMe_2 and NMe_2 moieties respectively. The ^{119}Sn NMR displays a single resonance at δ = +60 ppm.

Figure 3.8 shows the molecular structure of [Sn(bded)NMe_2] **(19)**, which crystallises as a NMe_2-bridged dimer, comprising a central {Sn_2N_2} ring as was seen in the heteroleptic aminoalkoxide systems **3**, **6** and **12** (Chapter 2). A similar arrangement can be seen in dimeric [Sn$(NMe_2)_2]_2$, though the central {Sn_2N_2} heterocycle within this compound displays four uniform Sn–N bond lengths of 2.266 Å in contrast to the asymmetric bonding present in **19** (2.306(3) Å and 2.234(3) Å).[11] The reason for this asymmetry becomes immediately apparent when the coordination around the tin centres is taken into account. Whereas each tin atom within [Sn$(NMe_2)_2]_2$ exists as three-coordinate, the tin centres in **19** present as four-coordinate, with each adopting a well-documented pseudo trigonal bipyramidal geometry with stereoactive lone pair.

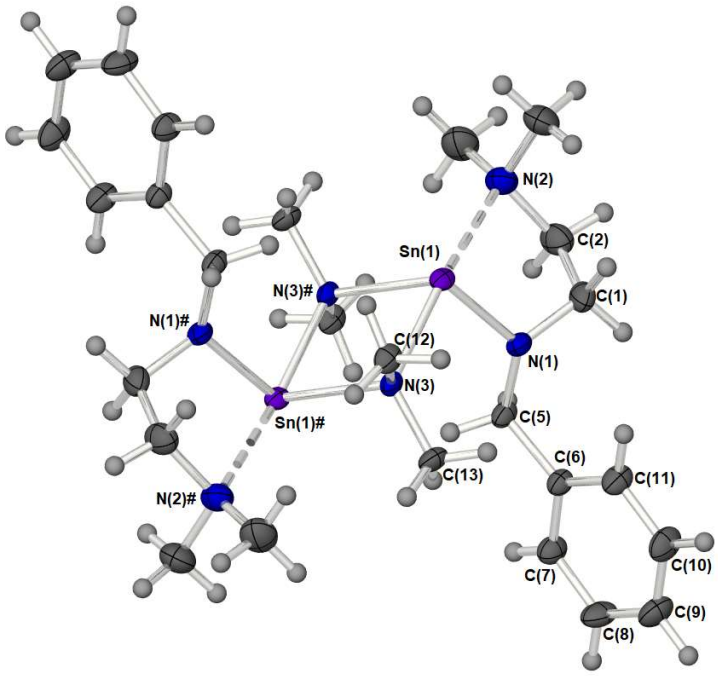

*Figure 3.8 – Molecular structure of [Sn(bded)NMe$_2$] **(19)**. Thermal ellipsoids are shown at 50% probability. Symmetry equivalent atoms are generated by the symmetry operator: #–X, 1–Y, 1–Z.*

Each metal centre within **19** shows equatorially-bound μ–NMe$_2$ and ligand (L) amide groups, displaying the shorter two of the four Sn–N interactions, at 2.078(3)Å and 2.234(3) Å respectively. These are commensurate with the expected covalent nature of the equatorial interactions, whilst the longer axial bonds (3.022(3) Å and 2.306(3) Å) are formed from dative coordination of the L–NMe$_2$ and μ–NMe$_2$ moieties. The presence of two dative heteroatoms on the axial positions results in the likely formation of a 3-centre-2-electron bonding configuration, as discussed in Chapter 2, accounting for the inequality of bond lengths within the {Sn$_2$N$_2$} ring, with each tin atom displaying one conventional covalent Sn–N interaction, and one dative interaction (2.234(3) Å and 2.306(3) Å). The Sn–Sn distance within this heterocycle appears only marginally longer than that observed within [Sn(NMe$_2$)$_2$]$_2$ at 3.4805(4) Å cf. 3.471 Å. Similarly, the N–Sn–N angle formed within the {Sn$_2$N$_2$} ring (79.9(1)^o) is almost identical to that reported within the tin bis(dimethylamide) dimer.[11]

*Table 3.2 – Relevant bond lengths and angles within compound **19**.*

Angle (°)		Distance (Å)	
N(3)–Sn–N(2)	161.01(9)	Sn–Sn	3.4805(4)
N(1)–Sn–N(3),	103.2(1)	Sn–N(1)	2.078(3)
Sn–N–Sn	100.1(1)	Sn–N(3)	2.234(3)
N(3)–Sn–N(3)#	79.9(1)	Sn–N(3)	2.306(3)
		Sn–N(2)	3.022(3)
Pendant –NMe_2 (Axial)			
C(2)–N(2)–Sn	95.7(2)		
C(2)–N(2)–C(3)	111.6(3)		
C(2)–N(2)–C(4)	110.7(3)		
C(3)–N(2)–C(4)	108.4(3)		
∑ C–N–C (sp^3 = ~328.5°)	330.7		
Sn–L (bded) (Equatorial)			
Sn–N(1)–C(1)	112.3(2)		
Sn–N(1)–C(5)	129.3(2)		
C(1)–N(1)–C(5)	112.5(3)		
∑ X–N–X (sp^3 = ~328.5°)	354.1		

The angle formed between the axial pendant –NMe_2 moiety and the dative μ–NMe_2 (161.01(9)°) is marginally closer to the ideal 180° expected for true trigonal bipyramidal geometry than seen in the aminoalkoxide analogues **3**, **6** and **12** in Chapter 2, though the L–NMe_2–tin bond length within **19** is longer, at 3.022(3) Å, than those observed in the aminoalkoxide analogues (2.717(6)-2.795(2) Å). This elongation is likely to arise from the sub-optimal direction of the dative lone pair of the nitrogen towards the tin (C(2)–N(2)–Sn angle = 95.7(2)°), considering the sp^3 nature of the –NMe_2 moiety.

In contrast to the sp^3 nature of the pendant –NMe_2, the nitrogen atom of the formal covalent Sn–N(1) bond of the aminoamide ligand bded displays a near-planar geometry, with the sum of bonding angles close to 360° (354.1°). This arrangement is common in terminal amide interactions, and is seen in both $[Sn(NMe_2)_2]_2$ and monomeric $[Sn\{N(SiMe_3)_2\}_2]$, and it has been tentatively suggested that this allows for π-donation into appropriate tin orbitals where available.[11,14]

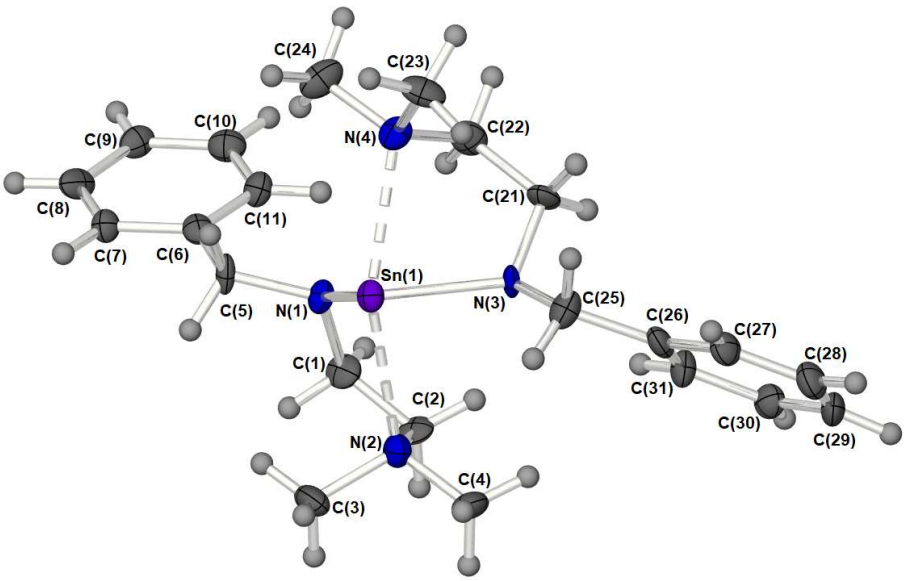

*Figure 3.9 – Molecular structure of monomeric [Sn(bded)$_2$] **(20)**. Thermal ellipsoids are shown at 50% probability.*

Figure 3.9 shows the molecular structure of [Sn(bded)$_2$] **(20)**, which crystallises as a monomeric system with asymmetric ligand environments. In an identical manner to the majority of the four-coordinate tin(II) systems encountered within these investigations, complex **20** adopts a pseudo trigonal bipyramidal geometry highly indicative of the presence of a stereoactive lone pair. The axial N–Sn–N angle that comprises both dative pendant –NMe$_2$ groups was found to be 144.5(4)°, commensurate with values found for the monomeric bis-aminoalkoxide complexes **1**, **4**, **7** and **10** discussed in Chapter 2.

Both pendant –NMe$_2$ groups exhibit C–N–Sn angles of around 100° between the ligand backbone and metal centre, which coupled with the sp^3 nature of the nitrogen atom ($\sum$ C–N–C ≈ 330°) indicates reasonable directionality of the lone pair towards the tin centre, contributing to shortened Sn–N distances of ~2.5 Å when compared to those of the heteroleptic dimer **19** (3.022(3) Å, C–N–Sn = 95.7(2)°).

Tin–nitrogen covalent bond lengths of 2.14(1) Å between metal and ligand fall once again within the expected ranges, though appearing longer than the Sn–aminoamide distances within **19** (2.078(3) Å) and the terminal Sn–N bonds within [Sn(NMe$_2$)$_2$]$_2$ and [Sn{N(SiMe$_3$)$_2$}$_2$] (2.068 Å and 2.095 Å respectively).[11,14] A contributing factor to this may be the deviation away from the planarity of the bonding nitrogen atom ($\sum$ C–N–C ≈ 342°) that was evident in the heteroleptic species **19** and in both aforementioned tin amides, and the possible consequences on any π-donation between nitrogen and tin that may be occurring. It is interesting to note the elongation in Sn–N bond length within the bis-substituted system, and to what extent this would offset any stability gained through chelation. This is particularly pertinent in the case of [Sn(deed)$_2$] **(16)**, which, despite being of lower steric bulk than

[Sn(bded)$_2$] **(20)**, decomposes over a short period of time, whilst mono-substituted [Sn(deed)NMe$_2$] **(15)** remains indefinitely stable.

*Table 3.3 – Relevant bond lengths and angles within compound **20**.*

Angle (°)	
N(2)–Sn–N(4)	144.5(4)
N(1)–Sn–N(3)	101.4(4)
Pendant –NMe$_2$ (L1) (Axial)	
C(2)–N(2)–Sn	100.5(8)
C(2)–N(2)–C(3)	109(1)
C(2)–N(2)–C(4)	113(1)
C(3)–N(2)–C(4)	108(1)
∑ C–N–C (sp^3 = ~328.5°)	330
Sn–L1 (bded) (Equatorial)	
Sn–N(1)–C(1)	119.(1)
Sn–N(1)–C(5)	113.5(9)
C(1)–N(1)–C(5)	111(1)
∑ X–N–X (sp^3 = ~328.5°)	343.6
Pendant –NMe$_2$ (L2) (Axial)	
C(22)–N(4)–Sn	100.1(9)
C(22)–N(4)–C(24)	109(1)
C(22)–N(4)–C(23)	113(1)
C(23)–N(4)–C(24)	108(1)
∑ C–N–C (sp^3 = ~328.5°)	330

Angle (°)	
Sn–L2 (bded) (Equatorial)	
Sn–N(3)–C(21)	118(1)
Sn–N(3)–C(25)	113(1)
C(21)–N(3)–C(25)	111(1)
∑ X–N–X (sp^3 = ~328.5°)	342
Distance (Å)	
Sn–N(1)	2.14(1)
Sn–N(3)	2.13(1)
Sn–N(2)	2.50(1)
Sn–N(4)	2.49(1)

3.1.3. Thermogravimetric Analysis

Of the simple aminoamide complexes synthesised and characterised **(13-20)**, only five compounds within the series demonstrated suitable longevity and stability to undergo thermal analysis. Traditional thermal stability tests were carried out under inert atmosphere on the aliphatic complexes [Sn(tmed)NMe$_2$] **(13)**, [Sn(tmed)$_2$] **(14)**, [Sn(deed)NMe$_2$] **(15)**, and on the aromatic complexes [Sn(bded)NMe$_2$] **(19)** and [Sn(bded)$_2$] **(20)**.

Complexes **13**, **14** and **15** display singular mass loss events consistent with evaporation, with residual masses of 3.1%, 6.7% and 5.6% respectively (Figure 3.10). The thermal profiles are indicative of high volatility and display limited signs of decomposition within the thermal

window necessary for full evaporation. Due to the lack of oxygen within the precursor systems, the likely thermolysis product of any decomposition would most likely be metallic tin, which accounts for 45.0%, 36.9% and 42.7% of each system by mass respectively, and as such was not observed in any meaningful capacity (Table 3.4). The exceedingly low residual masses and reasonable thermal stability, coupled with the aforementioned high reactivity, identified all three compounds as potential ALD precursor candidates and worthy of further study.

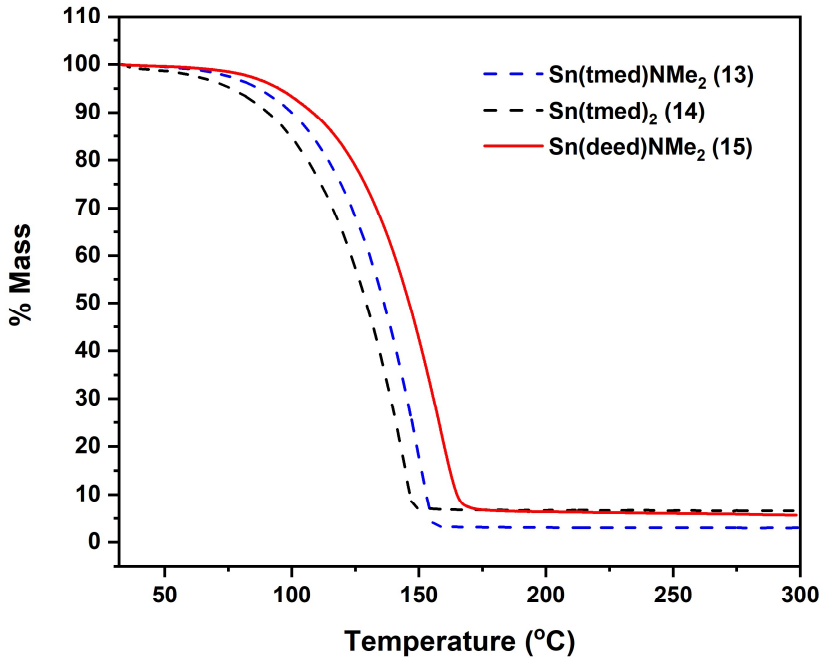

*Figure 3.10 – Mass loss/temperature plots of [Sn(tmed)NMe$_2$] **(13)**, [Sn(tmed)$_2$] **(14)** and [Sn(deed)NMe$_2$] **(15)**. Ramp: 5 °C min^{-1}, Ar flow 20 ml min^{-1}.*

*Table 3.4 – Residual percentage masses from the TGA of **13**, **14** and **15**, with expected percentage masses of metallic tin.*

Compound	Residual Mass (%)	% Sn
13	3.1	45.0
14	6.7	36.9
15	5.6	42.7
19	34.3	34.9
20	27.9	25.1

In direct contrast to the thermal profiles of the three aliphatic systems, both aromatic analogues (**19** and **20**) display a more convoluted decomposition occurring over a wide

temperature range (Figure 3.11), with limited evidence of volatility. The heteroleptic system (**19**) undergoes a well-defined ~50% loss of mass between 100 °C and 170 °C, before a slow decomposition yields a rest mass of 34.3%, remarkably close to the percentage composition of tin within the system (34.9%), making thermal reduction of the metal the likely process taking place. Similarly, the thermal profile of **20** reveals an ill-defined loss of mass of ca. 20% beginning at 75 °C before a further sharp decomposition at ~170 °C to ~35%, followed by a gradual decline to a residual mass close to that of metallic tin at (27.9% cf. 25.1% Sn^0). The lack of volatility and thermal stability precludes complexes **19** and **20** from any further consideration for use as ALD precursors, though the presence of markedly different decomposition processes on the inclusion of aromatic substituents is an interesting feature to note.

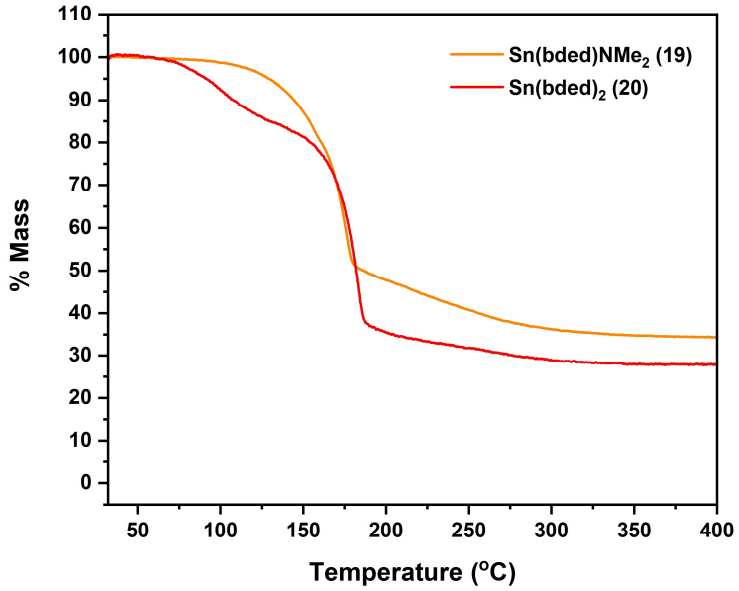

*Figure 3.11 – Mass loss/temperature plots of [Sn(bded)NMe$_2$] **(19)** and [Sn(bded)$_2$] **(20)**. Ramp rate 5 °C min^{-1}, Ar 20 ml min^{-1}.*

Aliphatic complexes **13**, **14** and **15** were shown by initial thermal profiles to be promising precursor candidates and as such, their relative volatility was further quantified with isothermal thermogravimetric analysis. Samples were held in open aluminium pans of identical surface area to allow for accurate analysis and comparison of evaporation rates between samples. Isothermal plots for complexes **13**, **14** and **15** can be found in Figure 3.12.

All three complexes demonstrated a steady loss of mass over 2 h at 70 °C, with the heteroleptic systems [Sn(tmed)NMe$_2$] **(13)** and [Sn(deed)NMe$_2$] **(15)** displaying a greater rate of evaporation than the homoleptic complex [Sn(tmed)$_2$] **(14)**. Evaporation rates of 133.0, 82.4 and 150.2 μg min^{-1} cm^{-1} were calculated for complexes **13**, **14** and **15** respectively (Table 3.5). Rates such as these are well within acceptable ranges for precursor volatilities, and

indeed are a high degree greater than a number of demonstrated precursor systems.[27,85,86] The greater volatility displayed by the heteroleptic systems is to be somewhat expected, with marginally lower molecular masses coupled with the inherent asymmetry of the molecular systems accounting for this. However, given the expected dimeric nature of the heteroleptic complexes at room temperature, a significantly larger molecular mass and lower volatility would be expected than would be for the homoleptic complex **14**. A number of factors could account for this. It could be inferred that complexes **13** and **15** exist as monomeric at 70 °C, or that complex **14** exists as a dimer up to at least 70 °C.

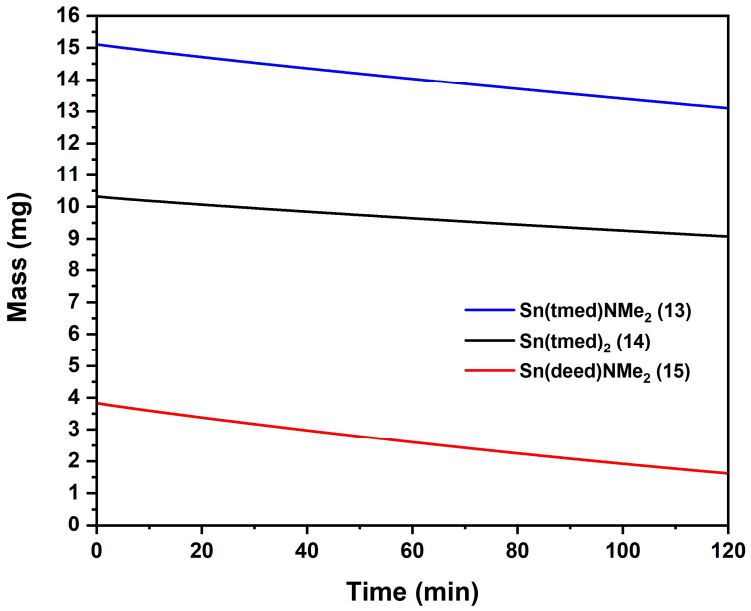

*Figure 3.12 – TG plot of the relative volatilities (70 °C) of [Sn(tmed)NMe$_2$] **(13)**, [Sn(tmed)$_2$] **(14)**, and [Sn(deed)NMe$_2$] **(15)**. Ar flow 20 ml min^{-1}.*

*Table 3.5 – Evaporation rates of compounds **13**, **14** and **15** at 70 °C.*

Compound	Evaporation rate (μg min^{-1} cm^{-2})
13	133.0
14	82.4
15	150.2

With the volatility of complexes **13**-**15** established, decomposition studies of complexes **13**, **14** and **15** were undertaken in sealed glass melting point tubes to establish estimates of decomposition temperatures in the absence of volatility. These tests revealed thermal limits of ~130 °C, ~135 °C and ~145 °C respectively, though it is important to note that the conditions within an ALD process are substantially different, and despite the substrate surface being held at the stipulated deposition temperature, a combination of gas flow, vacuum and volatility is likely to significantly increase the thermal tolerances of prospective precursor compounds.

With a higher stability than tmed derivatives **13** and **14**, [Sn(deed)NMe_2] **(15)** was identified as the most promising candidate for ALD trials. With this in place a brief computational investigation was commissioned in an attempt to further elucidate the nuclearity of the tin(II) complex.

3.1.4. Computational Studies

Computational studies were carried out by Dr Antoine Buchard, Department of Chemistry, University of Bath, as part of an ongoing collaboration into ligand design and electronics. Geometry optimisation was performed at the PBE0-D3 and B3PW91-D3 levels, using mixed valence triple basis set 6-311++G(2d,p) for C, H and N atoms, whilst the SDD basis set alongside the effective core potential were used for Sn. Solution calculations in benzene were conducted at 298.15 K using a conductor-like polarisable continuum model (CPCM).[87–89] The author would like to extend their gratitude to Dr Buchard for his time and efforts within the collaboration.

With the identification of a range of novel, volatile and highly reactive simple amides of tin(II), the intermolecular interactions taking place within these systems and their potential implication on physical properties was of increasing interest. Much focus within ALD precursor design is directed towards the development of monomeric systems, and one of the disadvantages of the selection of [Sn(deed)NMe_2] **(15)** as a precursor is the high likelihood of its existence in dimeric form. This was attested to by the X-ray characterisation of the analogous complex [Sn(bded)NMe_2] **(19)**, which crystallises as a NMe_2-bridged dimer.

It was however hypothesised that with the high lability of Sn–N interactions, coupled with the observed fluxionalities within NMR studies, it was possible that at elevated temperatures the monomeric system may exist as the dominant phase. As such, the Gibbs free energies of a range of different bridging modes were assessed through density functional theory (DFT) calculations as part of an internal collaboration.

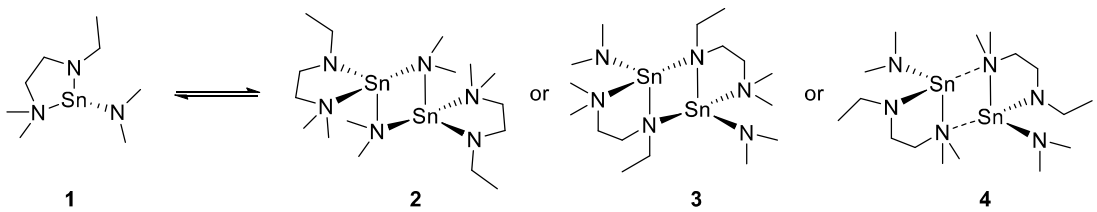

*Figure 3.13 – Monomeric **(1)** and possible dimeric forms of [Sn(deed)NMe_2], exhibiting μ–NMe_2 **(2)**, μ–N(Et)R **(3)** and μ–N(R)Me_2 **(4)** bridging.*

DFT studies were carried out at 25 °C in benzene, displaying a very low energy barrier between monomer and μ–NMe_2 dimer, with two different functionals giving rise to values of –0.2 and +1.4 kcal mol^{-1} (PBE0-D3 and B3PW91-D3 functionals respectively). It is therefore likely that a monomer-dimer equilibrium is present in solution at room temperature.

Table 3.6 – DFT computed Gibbs free energies of dimerisation of 1 into 2, 3 or 4, in the gas phase at 70 °C.

Functional	Dimerisation into 2	Dimerisation into 3	Dimerisation into 4
PBE0-D3	+1.0	+14.7	+14.8
B3PW91-D3	+1.9	+13.7	+14.5
B3LYP-D3	+4.0	-	-
M062X	+2.0	-	-
M062X-D3	+0.5	-	-

With a seemingly low energetic barrier to the formation of the monomeric species, DFT calculations were carried out at in the gas phase at a representative precursor source temperature of 70 °C, a temperature at which reasonable volatility was evident from experimental studies. It is also worth noting that whilst the precursor source may be heated to only 70 °C, typical ALD deposition temperatures for SnO range between 130 °C and 210 °C, further increasing the likelihood of monomeric species being delivered to the substrate. The results of the gas phase DFT study are collated in Table 3.6, where it can not only be seen that the NMe_2-bridged system is the most thermodynamically stable of the three postulated dimers, but also that the monomeric species is most favoured at temperatures of 70 °C and above, with Gibbs free energies of dimerisation of between +0.5 and +4.0 kcal mol^{-1}.

Density functional computations also predicted likely gas phase structures for [Sn(deed)NMe_2] **(15)** in both monomeric and dimeric forms. A short summary of angles and distances can be found in Table 3.7. The two forms were found to adopt the expected geometries, with the three-coordinate monomer displaying a distorted pseudo tetrahedral geometry with the expected presence of a stereoactive lone pair, and the dimeric form displaying similar geometry to that observed in the analogous [Sn(bded)NMe_2] **(19)**. The latter exhibits a pseudo trigonal bipyramidal geometry, with axially coordinated bridging–NMe_2 moieties and dative –NMe_2 pendant groups, and equatorial Sn–$N_{(bded)}$ and Sn–bridging-NMe_2 bonds.

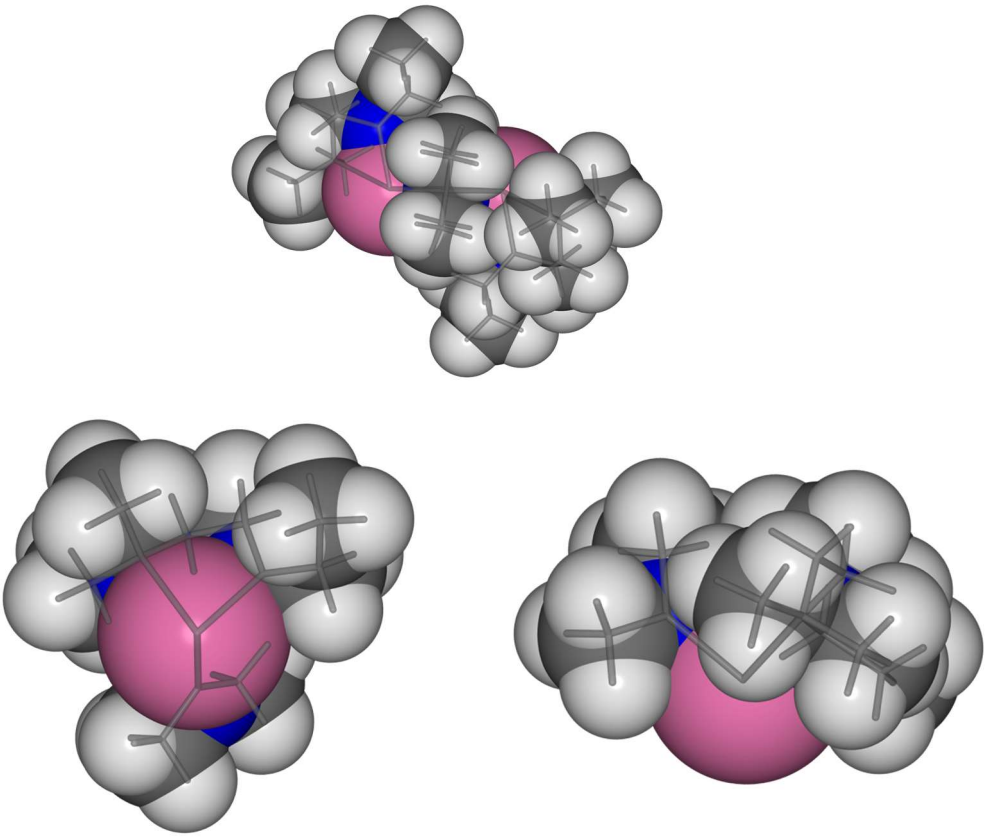

Figure 3.14 – Predicted structures and transposed VDW space-filling diagrams of dimeric (top) and monomeric (bottom left, right) Sn(deed)NMe_2 ***(15)****.*

Table 3.7 – Relevant structural data from DFT calculated gas phase structures of monomeric and dimeric [Sn(deed)NMe_2] ***(15)****.*

Distance (Å) / Angle (°)	**Monomer**	**Dimer (μ–NMe_2)**
Sn–N_{Et}	2.138 Å	2.115 Å
Sn–$NMe_{2\ (pendant)}$	2.504 Å	3.107 Å
Sn–μ-NMe_2	2.101 Å	2.315 Å
Sn–μ-$NMe_{2\ (dative\ bridge)}$	-	2.362 Å
Sn–Sn	-	3.600 Å
N_{Et}–Sn–$NMe_{2\ (Pendant)}$	74.95°	68.84°
N_{Et}–Sn–NMe_2	94.33°	-
NMe_2–Sn–$NMe_{2\ (Pendant)}$	89.46°	-
N_{Et}–Sn–μ-NMe_2 (Equatorial)	-	99.82°
μ-$NMe_{2\ (dative)}$–Sn–$NMe_{2\ (pendant)}$ (Axial)	-	159.63°
μ-NMe_2–Sn–μ-NMe_2	-	79.36°
Sn–μ-NMe_2–Sn	-	100.64°

Van der Waals space-filling depictions offer an interesting insight into the steric influences within potential precursor systems. Given the preliminary nature of tin(II) chalcogenide atomic layer deposition, no studies have yet sought to investigate the nature of surface reactions within ALD processes, and the effects of various factors, such as the presence of a stereoactive lone pair, are unknown. It is, however, reasonable to assume that the reactivity of a highly sterically shielded system is likely to be lower than that of a similarly coordinated system of lower steric bulk. Access to appropriate coordination sites on the metal atom and protonation sites of ligands is also likely to have an impact on the efficacy of a potential precursor molecule.

Qualitative visual study of monomeric [Sn(deed)NMe_2] **(15)** (Figure 3.14) reveals an exposed, three-coordinate tin centre, with a relatively low steric encumbrance from the surrounding ligands. The nitrogen environments that require protonation in order for ligand removal to take place do however seem to be largely obscured, with the possible exception of the coordinated –NMe_2 group. On comparison with the known precursor [Sn(dmamp)$_2$] **(7)** (Figure 3.15), it appears that the established precursor displays greater steric crowding, though the alkoxide protonation sites may prove more accessible. It must be remembered that on physi- and chemisorption to the substrate surface, and in any transition intermediates, geometries about the tin atom are likely to alter.

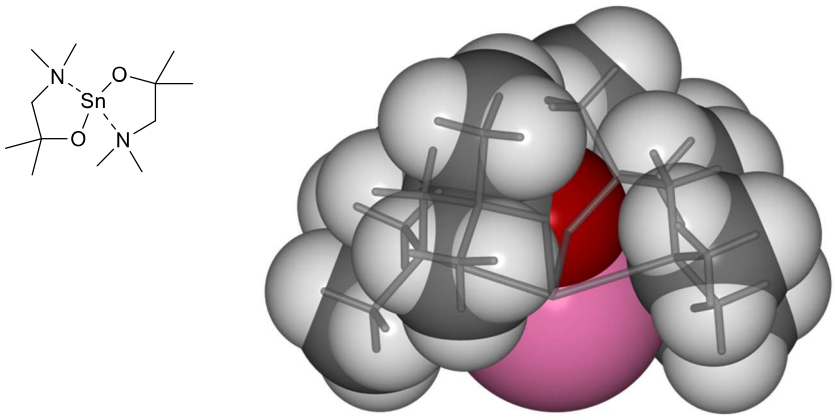

*Figure 3.15 – Molecular structure of [Sn(dmamp)$_2$] **(7)**.*

3.1.5. Further Characterisation of Sn(deed)NMe_2 (15)

With the selection of Sn(deed)NMe_2 **(15)** for further ALD trials, additional reactions were carried out to supplement the NMR data acquired for the highly reactive liquid. As such, a number of insertion reactions into the Sn–NMe_2 and Sn–deed bonds were attempted, with a view towards crystallising a “trapped” proof of the proposed system. Such a process proved to be successful, resulting in the crystallisation and characterisation of complex **21** (Figure

3.16), via insertion of the Sn–NMe_2 bond into bis(2,6-diisopropylphenyl)carbodiimide (Scheme 3.1) to form the guanidinate species **21**.

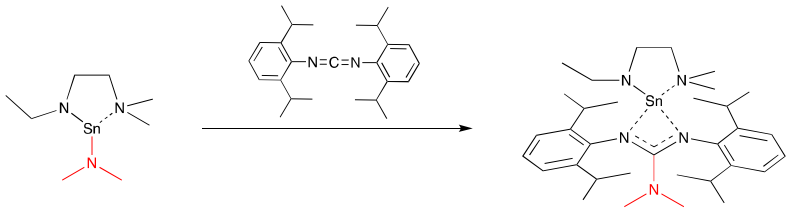

*Scheme 3.1 – [Sn(deed)NMe_2] **(15)** insertion into bis(2,6-diisopropylphenyl)carbodiimide **(21)**.*

The ^{1}H NMR spectrum of **21** displays well-defined resonances consistent with the expected structure. Peaks of note include the multiplet of the C*H*$(CH_3)_2$ (δ = 3.81-3.91 ppm), a quartet ascribed to the methylene of the free ethyl group (δ = 3.61 ppm, J = 6.90 Hz), multiplet peaks belonging to the methylene backbone groups at δ = 3.13-3.19 and 2.09-2.13 ppm (NC*H*$_2$C*H*-$_2$$NMe_2$ respectively) and the N*Me*$_2$ resonance of deed at δ = 2.16 ppm. The guanidinate N*Me*$_2$ presents at δ = 1.66 ppm, whilst two doublets at δ = 1.40 and 1.29 ppm (J = 6.80 Hz) are followed by a final upfield triplet at δ = 1.25 ppm (J = 6.9 Hz) and are assigned to the two inner and outer isopropyl C*H*$_3$ groups and C*H*$_3$ of the free ethyl chain accordingly.

The ^{13}C{^{1}H} NMR spectrum presents with no remarkable resonances, though the ^{119}Sn NMR displays a sharp signal at δ = –145 ppm. This signal is consistent with the closest heteroleptic Sn(II) guanidinate reported in the literature by Ahmet et al., [Sn{^{t}BuNC(NMe_2)N^{t}Bu}NMe_2], which was found to give ^{119}Sn resonance at δ = –121 ppm.[69] Similar ^{119}Sn NMR resonances have also been reported by Chlupatý et al., though the heteroleptic systems reported contain –N($SiMe_3$)$_2$ ligands rather than simply alkyl amines.[68] The guanidinate derivatives of tin display a wide array of ^{119}Sn resonances influenced by subtle changes in ligand sterics and electronics. This is in no small part due to the huge versatility of the guanidinate ligand itself. With a backbone capable of varying degrees of delocalisation, aromatic substituents allow for a fully delocalised ligand system, whilst steric influences may reduce the planarity and therefore π-overlap across such a system to variable extents. Even without the incorporation of aromatic substituents, the NMe_2 moiety of the backbone is itself capable of π-donation into the backbone-metal bonding when sitting in the same plane. As such, steric influences from the two substituents on either side will influence the degree of overlap displayed, and hence the ligand electronics (Figure 3.17).[68,69,72]

The solid-state structure of the monomeric heteroleptic guanidinate **21** was determined via single crystal X-ray diffraction and was found to adopt the expected pseudo trigonal bipyramidal geometry with the inferred presence of a stereochemically active lone pair. Unlike the majority of the other four-coordinate tin(II) species studied, the N–C–N backbone of the

guanidinate is capable of full delocalisation, which would theoretically result in two equal Sn–N bond distances between metal atom and guanidinate ligand. Given the pseudo trigonal bipyramidal geometry, axial bonds are still likely to comprise the 3-centre-2-electron configuration set out in Chapter 2, and hence bond lengths between tin and guanidinate ligand are found to be 2.313(3) Å and 2.287(3) Å for axial and equatorial positions respectively. These lengths lie expectedly between those observed for axial and equatorial bonds in compound **20**, consistent with the delocalised yet induced-dative behaviour of the chelating guanidinate. The bond lengths measured are marginally longer than those within the similar heteroleptic species discussed above [Sn{^{t}BuNC(NMe$_2$)N^{t}Bu}NMe$_2$], though it is important to note that the latter species lacks the pendant chelating –NMe$_2$ moiety and is instead three-coordinate.[69]

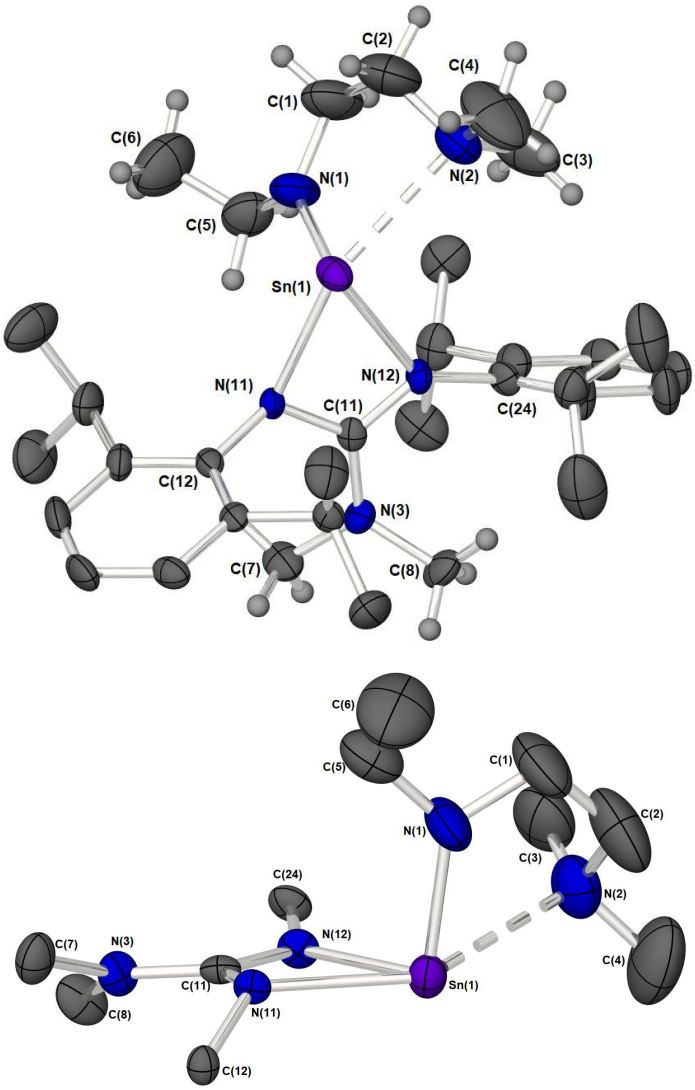

*Figure 3.16 – Molecular structure of Sn(N,N'-diisopropylphenyl dimethylamino guanidinate)deed **(21)**, [Sn(DippG)deed]. Thermal ellipsoids are shown at 50% probability. One isopropyl group, based on carbon 25 is disordered over two sites, in a 44:56 ratio and was refined with ADP restraints. The major component is shown. The lower structure depicts the core framework around the Sn centre and guanidinate distortion. 2,6-diisopropyl groups and hydrogen atoms have been omitted for clarity.*

The aforementioned bonding arrangement, in conjunction with the reduced bite angle of the chelating guanidinate, results in a significantly more distorted trigonal bipyramid than has been observed previously within this body of work. Testament to this is the ca. 73° angle between the axial and equatorial planes, which would ordinarily be expected to be around 90°. An interesting artefact of the guanidinate ligand acting more as a mixed covalent and dative chelate between its two Sn–N bonds is the fact that the equatorial, more covalent, nitrogen (N12) displays a firm planar sp^2 geometry in addition to displaying the shorter of the Sn–N bonds, whilst the axial, more dative nitrogen (N11) displays the longer Sn–N bond alongside a more pyramidal sp^3 geometry. Such geometries reflect the observations made previously wherein covalently bonded amides adopt a planar geometry, allowing potential pi-donation of the lone pair into an appropriate metal orbital. This is exemplified in the bonding within the deed ligand, where the covalently bound amide is primarily planar, with a definitively sp^3 pendant NMe_2 moiety.

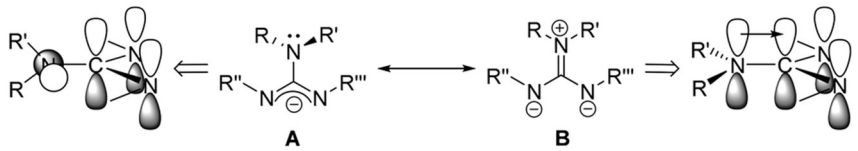

Figure 3.17 – Extremes of backbone NR_2 influence on guanidinate delocalisation. A) Out of plane NR_2 with minimal pi-overlap. B) Coplanar NR_2 with high degree of pi-overlap.[69]

The final observation worthy of note is the lack of co-planarity, and hence delocalisation, between any of the aromatic substituents and the {NCN} backbone. This is in addition to a sterically induced lack of planarity between the guanidinate {NCN} backbone and its {NMe_2} substituent. The latter, despite existing in a planar, sp^2 geometry and so able to donate effectively into the backbone, sits out of the backbone plane, resulting in any low degree of pi-donation in the direction of the metal atom being severely impaired.

*Table 3.8 – Relevant bond lengths and angles within compound **21**.*

Angle (°)		Distance (Å)	
N(11)–Sn–N(2)	148.0(1)	Sn–N(11)	2.313(3)
N(1)–Sn–N(12)	100.0(1)	Sn–N(12)	2.287(3)
∑ angles about N(1)	358.7	Sn–N(2)	2.692(4)
∑ angles about N(2)	331.9	Sn–N(1)	2.081(4)
∑ angles about N(11)	341.1		
∑ angles about N(12)	358.6		
∑ angles about N(3)	359.5		
Angle between N(2)SnN(11) (Ax) and N(1)SnN(12) (Eq) planes	73.22		
Angle between guanidinate NMe_2 plane and NCN backbone plane	25.09		

3.2. Deposition Studies and Film Characterisation

3.2.1. Deposition Parameters

The development of a reliable process for the atomic layer deposition of low-reactivity aminoalkoxide precursors allowed for the same process to be trialled using [Sn(deed)NMe_2] **(15)** as a precursor. Replication of this process provided the best chance of finding viable low-reactivity precursors and permitted subsequent comparisons with [Sn(dmamp)$_2$] depositions to be made. Trial depositions with an H_2O co-reagent were carried out at 130 °C, 150 °C and 170 °C on p-type (B-doped) Silicon substrates with a 200nm thermal oxide SiO_2 surface layer, using a precursor source temperature of 70 °C.

3.2.2. Film Characterisation

Initial depositions at temperatures of 130 °C, 150 °C and 170 °C resulted in the visible growth of uniform films determined to be tin monoxide by powder X-ray diffraction. Films grown at the two higher temperatures exhibit highly oriented crystallinity, with broad reflections of the (001, 2θ = 18.3°) and (002, 2θ = 37.1°) planes reminiscent of films deposited with the established precursor [Sn(dmamp)$_2$] (Chapter 2). Films deposited with [Sn(dmamp)$_2$] at 130 °C using the process outlined in Chapter 2 showed higher crystallinity than those deposited at higher temperatures, whereas films deposited using the novel precursor displayed a much lower degree of crystallinity at 130 °C, with low intensity reflections in the (001) and (002) planes (Figure 3.18).

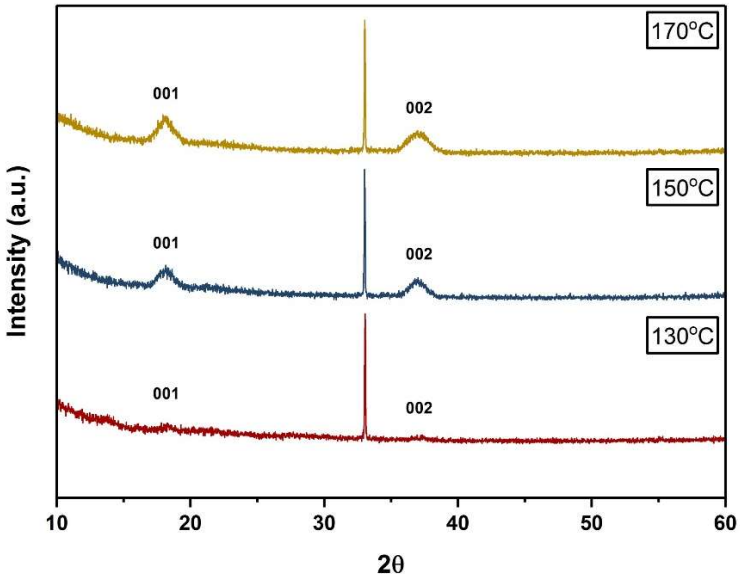

*Figure 3.18 – Powder X-Ray diffraction patterns of films deposited at 130 °C, 150 °C and 170 °C using [Sn(deed)NMe_2] **(15)**.*

All films were grown with 425 ALD cycles and were found to have thicknesses of 11.1 nm, 7.8 nm and 7.9 nm at each respective temperature, giving initial growth rate estimates of 0.26, 0.19 and 0.19 Å/cy. Simple application of the Scherrer formula on the p-XRD of films grown at 150 °C and 170 °C allows for an indication of crystallite size, as was discussed in Chapter 2. Analysis of the broadening of the (002) reflection gives values of 5.8 nm and 4.5 nm respectively, whilst the less accurate analysis of the lower angle (001) reflection affords values of 6.1 nm and 5.4 nm.

Figure 3.19 displays plots of density and sheet resistance of the as-deposited films, alongside expected growth per cycle at each respective temperature. A maximum density commensurate with that measured by Han et al. of 5.4 g/cm^{-3} is observed at 150 °C, either side of which a decrease in density is observed. Further to this, a notable decrease in sheet resistance is observed as the deposition temperature is increased from 150 °C to 170 °C, indicative of a much more conductive film. It is highly likely that the increased conductivity is as an artefact of the thermal susceptibility of the precursor at elevated temperatures, resulting in a greater proportion of metallic tin within the SnO. However, despite the observation of a decomposition point of ~145 °C for [Sn(deed)NMe$_2$] **(15)** within a sealed glass melting point tube, the formation of SnO films at higher temperatures appears to indicate that under vacuum and a flow of gas, the thermal stability is sufficient to allow successful reactions with H_2O to take place with limited decomposition to metallic tin. There are also studies that indicate that a certain degree of metallic tin within SnO films improves the electrical properties of the material for use in CMOS transistors, with an investigation by Caraveo-Frescas et al. noting an increase in hole mobility within SnO films with increasing metallic tin composition.[90]

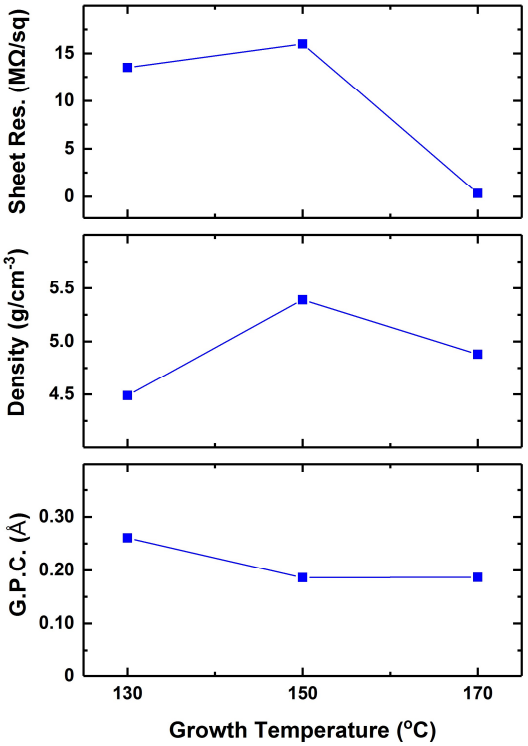

Figure 3.19 – Initial measurements of sheet resistance and density of films deposited at 130 °C, 150 °C and 170 °C, alongside estimates of potential growth per cycle at each respective temperature.

With a density of 5.4 g/cm^{-3} and a sheet resistance of 16 MΩ/sq, films deposited at 150 °C displayed the most promising properties for transistor applications. Depositions below the temperature required for the deposition of crystallinity, and at temperatures above 170 °C, where the stability of the precursor was likely to be jeopardised were not carried out. Whilst this limits the identification of an "ALD window", it is noted that as more research into low-reactivity systems is undertaken, the emphasis on steady growth rates over a defined temperature window is much diminished due to a lower understanding of the surface chemistry of low-reactivity ALD precursors. This is highlighted in not only the absence of an identifiable "ALD window" for the [Sn(dmamp)$_2$] process, but in a range of other papers which suggest physisorption of precursors plays an important role in systems with lower reactivity than traditional processes. Consequently, factors such as temperature and purge times have a large influence on growth rates for systems that rely on a high degree of physisorption.[91–93]

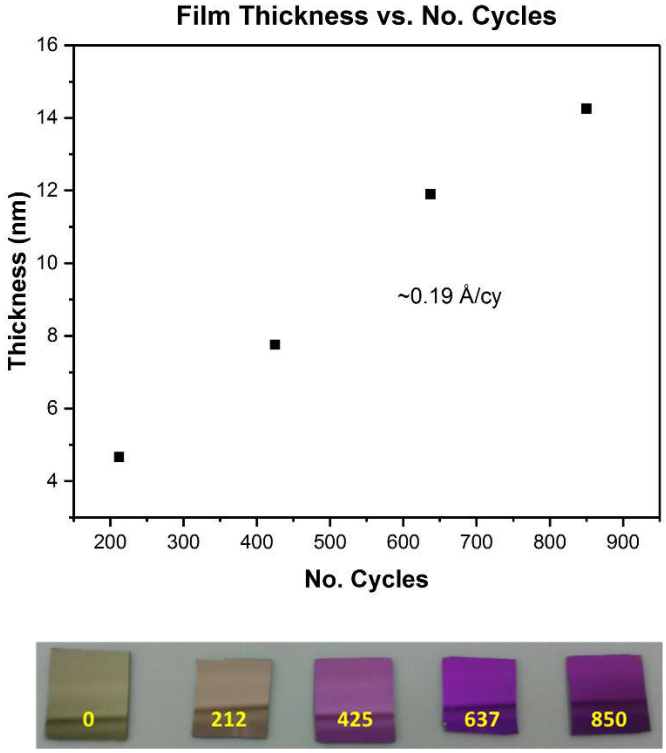

Figure 3.20 – (Top) Plot of thickness vs. number of ALD cycles at 150 °C. (Bottom) Pictures of sections of silicon/silicon dioxide wafer after increasing numbers of ALD cycles (note: reflections visible in highly reflective films).

After the selection of a deposition temperature of 150 °C for further study, a more in-depth assessment of growth rates and their linearity was undertaken (Figure 3.20), using variable-angle spectroscopic ellipsometry in conjunction with X-ray reflectivity. A largely linear relationship between the number of ALD cycles and growth rate can be seen, with an average growth rate of 0.19 Å/cy being displayed. This is consistent with expected ALD behaviour and represents a marginal improvement (~0.01 Å/cy) over the reported growth per cycle for the [Sn(dmamp)$_2$] process at the same temperature.[91] The change in film appearance as the number of cycles is increased can be seen in Figure 3.20 (bottom), though it is to be noted that as SnO is a largely transparent material, the evolution of a purple film colour is the effect of changing refractive index upon the SiO_2/Si substrate.

It is not uncommon for crystalline materials to display a high initial growth rate followed by more stable growth, as can be seen in the slight deviation at 212 cycles, due to the deposition of initially micro-crystalline or amorphous material until such a point that “annealing”-type behaviour results in a more ordered, crystalline film. This is a phenomenon that has been observed in the ALD of other metal-oxide systems, such as nickel oxide.[94,95] Corroboration of this behaviour can be seen in the p-XRD patterns of films deposited with 212, 425, 637 and 850 ALD cycles (Figure 3.21), where crystallinity on a level detectable with standard p-XRD capabilities emerged between 212 and 425 cycles (4.7–7.8 nm). It is worth noting that films of thicknesses <4.5 nm have been found to display adequate diffraction in previous studies within

the course of this research using [Sn(dmamp)$_2$] as a precursor. This would indicate that there are measurable differences between the surface reactions between the two ALD precursors, and further investigations are required to establish the cause of these. Given the steric differences between [Sn(dmamp)$_2$] and [Sn(deed)NMe$_2$], and the differences in reactivity from an inter- and intramolecular standpoint, it is entirely possible that surface coverage is different between the two systems. This is compounded by the probable differences in defect concentrations, with the inclusion of metallic tin likely to influence structural parameters.

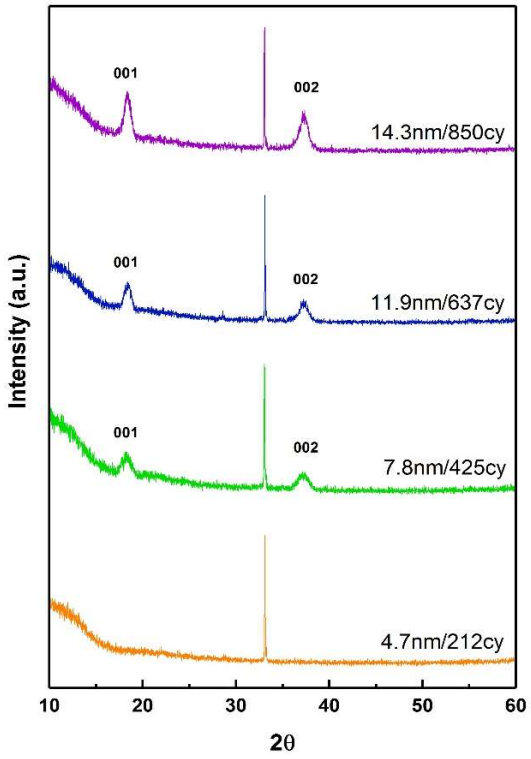

Figure 3.21 – p-XRD patterns of SnO films after 212, 425, 637 and 850 ALD cycles.

Once a sufficient quantity of material has been deposited, the powder X–ray diffraction patterns of films of different thickness display highly-oriented crystallinity in the (001) plane displayed by ALD SnO. As before, rudimentary application of the Scherrer formula to the (002, 2θ = ~37.1°) reflections gives a rough estimate of crystallite size along the *C*-axis, perpendicular to the substrate. These values are in the region of 5.6 nm, 7.0 nm and 6.9 nm for films deposited after 425, 637 and 850 cycles respectively. Interestingly, crystallite size in the (001) direction does not appear to increase past a certain size, despite films grown after 850 cycles having a thickness of 14.3 nm.

Atomic force microscopy (AFM) was carried out on films grown with 425 ALD cycles (7.8 nm) and revealed particularly flat films, with RMS values of between 0.5 and 0.8 nm. Cubic surface crystallites were observed to have diameters of between 150 and 200 nm, which are likely to extend in crystal planes not detected by p-XRD, as the only observable lattice planes were

oriented along the *C*-axis, with estimated dimensions of ~5-8 nm. With low profiles and small dimensions, conventional scanning electron microscopy was unable to detect the presence of these features; however, field-emission scanning electron microscopy was more successful. These images can be found beneath the aforementioned AFM images in Figure 3.22.

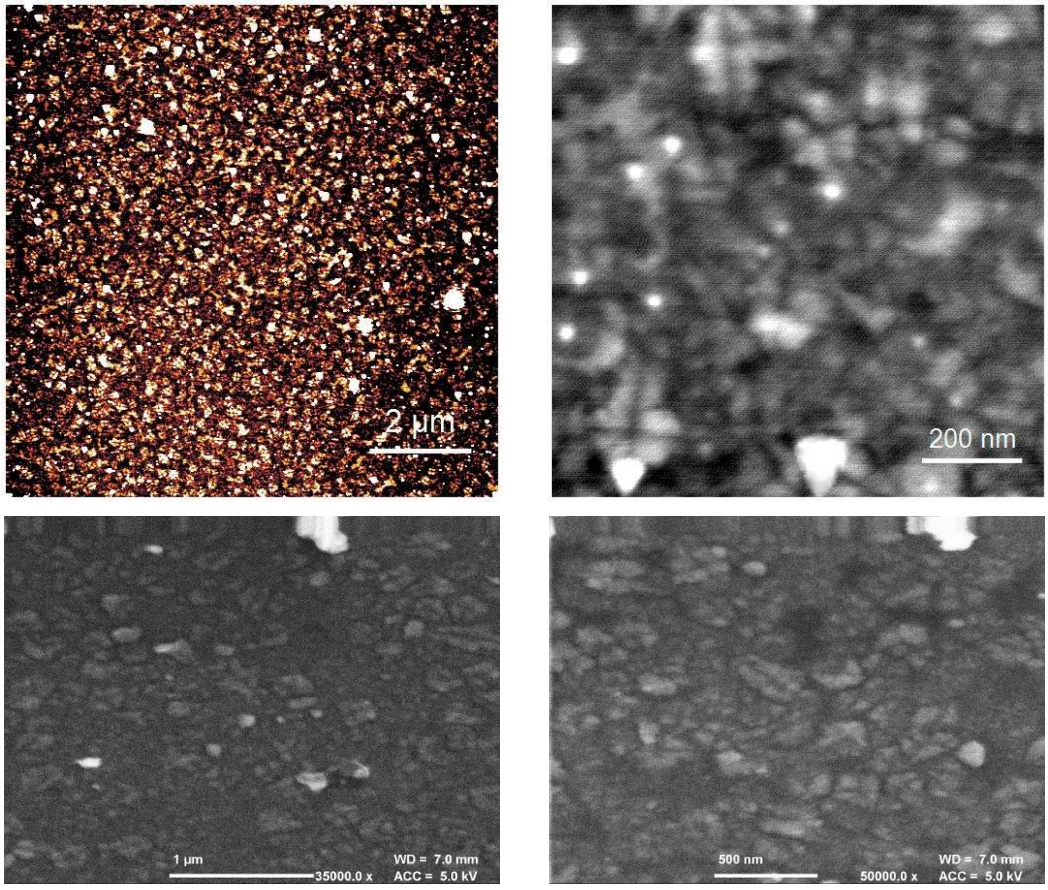

Figure 3.22 – (Top) Atomic force microscopy images of as-deposited SnO films. (Bottom) FE-SEM images of identical SnO films.

Both AFM and FE-SEM images display the presence of roughly cubic crystallite domains consisting of four segments. These could be a result of pyramidal moieties, with each face visible surrounding a central vertex, or a single nucleation point around which crystallinity has disseminated in four directions before converging. These features are consistent with those reported within the supplementary information of the [Sn(dmamp)$_2$] study by Han et al., though no further investigation is made beyond the provision of AFM images.[96]

High-resolution transmission electron microscopy (HR-TEM) is capable of providing nanometre-scale resolution by the passage and diffraction of electrons through thin layers of material. In addition to affording high-resolution images of materials down to individual lattice planes, by recording electron diffraction through the material, diffraction patterns can be generated which allows for the calculation of lattice d-spacings. This not only provides

confirmation of the crystalline material under inspection, but also gives information on the relative orientation of these planes.

For HR-TEM to be undertaken, thin films of SnO were grown on 3 mm graphene oxide (GO) holey carbon TEM grids affixed to a silicon wafer in the ALD reactor. For the images shown in Figure 3.23, 850 ALD cycles were performed at 150 °C using [Sn(deed)NMe_2]. In contrast to the hydroxylated surface present on SiO_2 substrates, the surface of graphene oxide substrates presents a considerably lower density of reactive sites. Typically, the graphene oxide consists of carbonyl, hydroxyl and carboxylic groups along the edges of graphene flakes, with hydroxy and epoxy groups on the surface of the basal plane.[97,98]

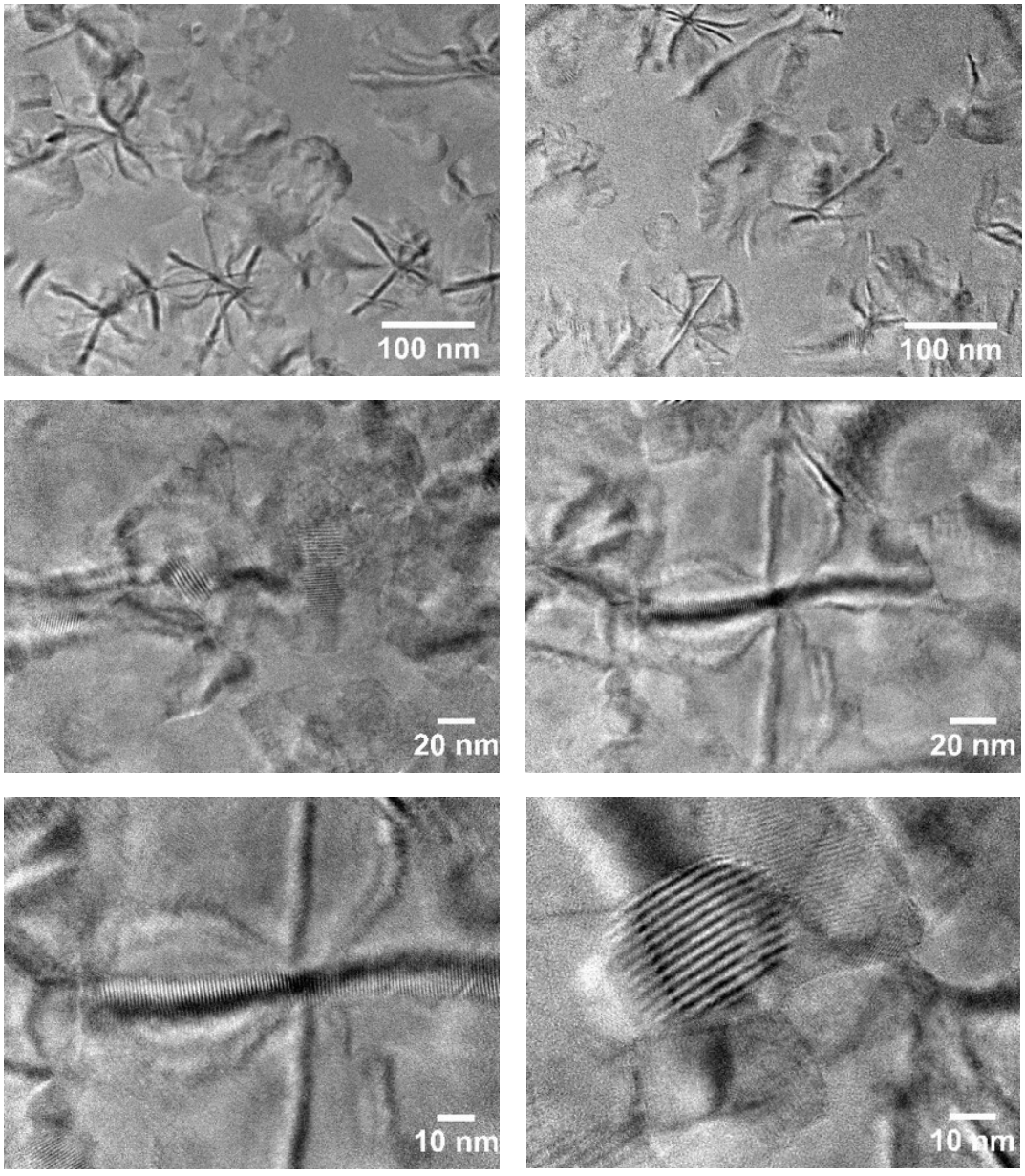

Figure 3.23 – HR-TEM images of SnO film grown on GO-Holey Carbon TEM grid at 150 °C, 850cy.

The relative paucity of hydroxyl surface groups presents a more challenging deposition environment, particularly for a low reactivity precursor such as [Sn(deed)NMe_2]. This is evident in the HR-TEM images taken on a 100 nm scale (Figure 3.23, top), where surface coverage of crystalline environments is incomplete. This is not the case with films deposited on SiO_2, as shown by AFM and FE-SEM previously.

The images of SnO on graphene oxide TEM grids show a more detailed view of what appeared to be divided square crystalline environments when visualised with AFM and FE-SEM. Under higher resolution TEM imaging, these environments are less clearly defined, though the darker ridges show high levels of constructive diffraction (Figure 3.23, Bottom Left, 10 nm), the result of two intersecting sets of lattice planes potentially attributable to the convergence of tendrils from a central nucleation point, as discussed previously. In addition to these larger features, a large number of smaller "blocks" are also visible (Figure 3.23, Top Right, 100 nm, and Bottom Right, 10 nm), which on closer inspection are found to be of identical crystallinity to the larger domains.

Figure 3.24 (Top) shows a TEM selected-area electron diffraction (SAED) pattern alongside the section of film from which it was obtained. By careful measurement of the radius of each concentric ring in reciprocal space, a value ascribed to a particular d-spacing of planes within a lattice can be determined. On submission to the Bragg equation (Equation 3.1), a corresponding 2θ value for a specific set of planes can be extracted and compared with reported diffraction patterns for the material in question. The TEM diffraction pattern gives rise to two sets of d-spacings, measured to be ~0.283 and ~0.198 nm. On submission to the Bragg equation, and with a wavelength of 2.5 pm (200kV), these correspond well to the (110) and (200) planes respectively.[99] Using HR-TEM, it is also possible to visually measure the spacing between atomic planes (Figure 3.24, Bottom). On inspection of the smallest visible set of atomic spacings, a measurement of ~0.278 nm is determined. Given the error surrounding the necessary visual measurement of both SAED patterns and HR-TEM images, this value again shows close similarity to the ~0.283 nm spacing determined from the SAED pattern, and hence the *hkl* assignment of (110).

$$n\lambda = 2d\ sin\theta \qquad \textit{Equation 3.1}$$

Interestingly, the observation of the (110) and (200) lattice planes, and the notable omission of any *l* components within the *hkl* values, supports the preferential orientation hypothesis founded on inspection of the previously discussed p-XRD patterns. Whereas the p-XRD study detected a bulk orientation perpendicular the *C* axis (001/002) and lying parallel to the substrate, the lack of any such diffraction within the HR-TEM study is indicative of a bulk diffraction parallel to the *C* axis. This is unsurprising given the fact that HR-TEM measurements are taken through the film, thereby measuring diffractions perpendicular to the substrate surface.

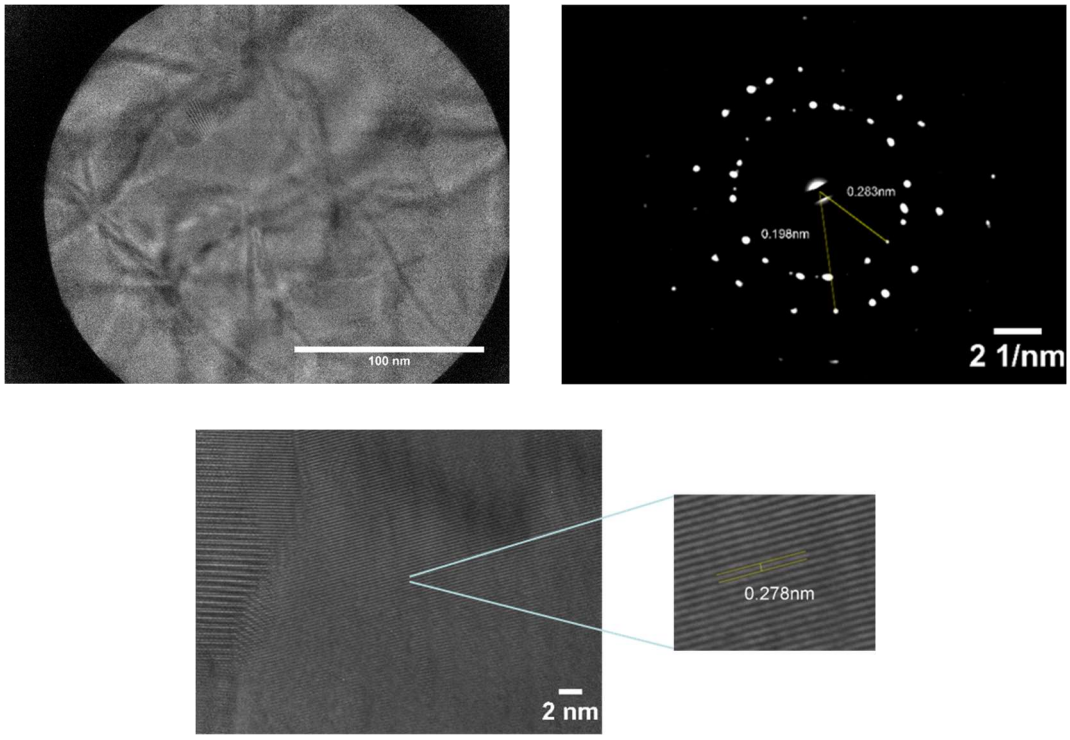

Figure 3.24 – HR-TEM images of SnO film grown on GO-Holey Carbon TEM grid at 150 °C, 637cy.

Additional confirmation of film composition was gained through the use of Raman spectroscopy (Figure 3.26). Due to the thin nature of the films (ca. 13-14 nm), only crystalline films were found to display detectable Raman signals. As was seen for the SnO films deposited with [Sn(dmamp)$_2$] (Chapter 2), the characteristic E_g and A_{1g} modes are visible at 113 cm^{-1} and 209 cm^{-1}, confirming the presence of SnO. No evidence of any SnO_2 modes is present, though given the limited volume of material and difficulty of obtaining a signal from amorphous films, this cannot necessarily be deemed definitive. The Raman vibrational modes within SnO can be seen in Figure 3.25. Despite the theoretical possibility of four Raman active vibrational modes in SnO (A_{1g}, B_{1g}, E_g, E_g"), only two have been observed within the literature (A_{1g} and E_g).

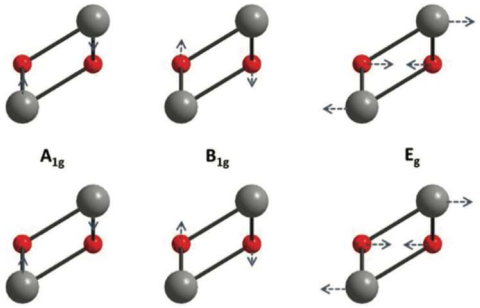

Figure 3.25 – Raman vibrational modes of SnO.[100]

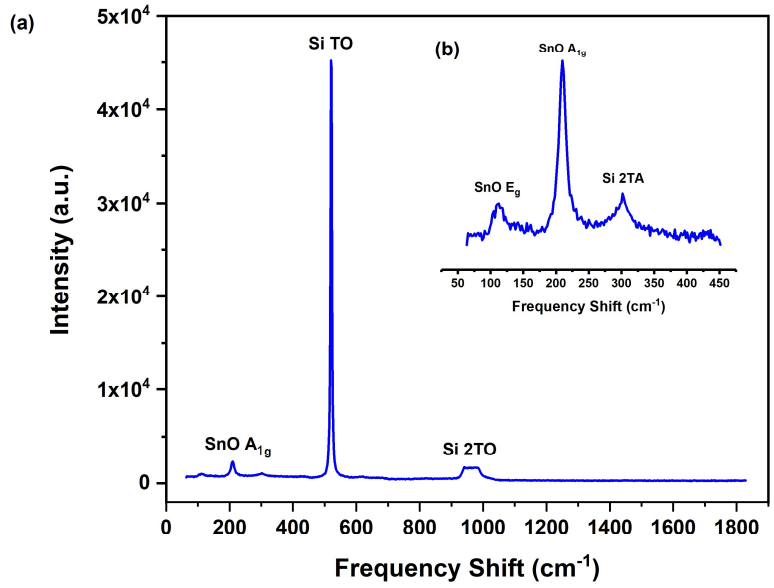

Figure 3.26 – (a) Raman spectra of crystalline SnO 150 °C, (850cy), with inset A_{1g} and E_g region (b).

X-ray photoelectron spectroscopy is a quantitative spectroscopic technique frequently used in materials analysis. The technique relies on the X-ray irradiation of a sample, with the kinetic energy and quantity of emitted electrons measured and correlated to their respective atom-specific binding energies. Despite being widely used in surface analysis, XPS is also often used in conjunction with an etching process, thereby exposing bulk areas of film, or allowing the change in sample composition with depth to be measured. Given the sensitivity of tin(II) oxide to oxidation, depth-profiling XPS is a useful technique for gaining a more accurate composition of the bulk film. XPS was undertaken on a sample of SnO deposited at 170 °C, after an Ar^+ etch of 60.9 s. The survey spectrum displays signals consistent with primarily tin and oxygen, though traces of carbon were also observed, likely due to slight decomposition of aminoamide ligands at temperatures above that of the thermal window of the precursor.

Distinction between Sn(II) and Sn(IV) through XPS is notoriously difficult to deconvolute, with an array of publications dedicated to its resolution.[101–103] This is due in part to the very limited difference in binding energies of the $3d_{5/2}$ band (ca. 0.5-0.7 eV), which is the primary source of differentiation. This is itself compounded by the fact that reported binding energies of each

tin valence vary widely. Differentiation is more troublesome in systems that contain an unknown stoichiometry of each oxidation state, and the contribution of each to the overall peak is often modelled and fitted to the data to extract relative composition. This is more easily achieved and inferred from obviously asymmetric peaks, and is considerably more difficult in peaks that are largely symmetrical but are marginally shifted from expected values, as a range of expected values are reported for each valence in the first instance. Other examples within the literature can be found detailing methods that instead rely on the relative shift in Sn $3d_{5/2}$ binding energy to denote relative quantities of Sn(II) or Sn(IV) from the ideal reported energies for SnO and SnO_2.[91,101–104] Alternative attempts are often made to characterise the presence of Sn(II) over Sn(IV) through inspection of the valence band edge. Whilst useful for bulk materials, this is also largely non-quantitative and relies on the observation of three distinct largely symmetrical peaks in Sn(II) in contrast to the three asymmetric peaks present in (IV). In practice, it is often the case that a combination of the two are observed, making any attempt at fitting incredibly difficult.[70,105–107]

A variety of binding energies for Sn(II) have been reported, ranging from 485.9 eV to 486.3 eV.[103,108] The Sn $3d_{5/2}$ peak displays a uniform shape with a maximum intensity occurring at 486.1 eV (Figure 3.27b). This is in good accordance with a range of literature values for stoichiometric SnO, and the spectra reported in the publication by Han et al. detailing the ALD of SnO using $Sn(dmamp)_2$.[103,91,108] XPS analysis was undertaken by Christopher Amey, Cavendish Laboratory, University of Cambridge.

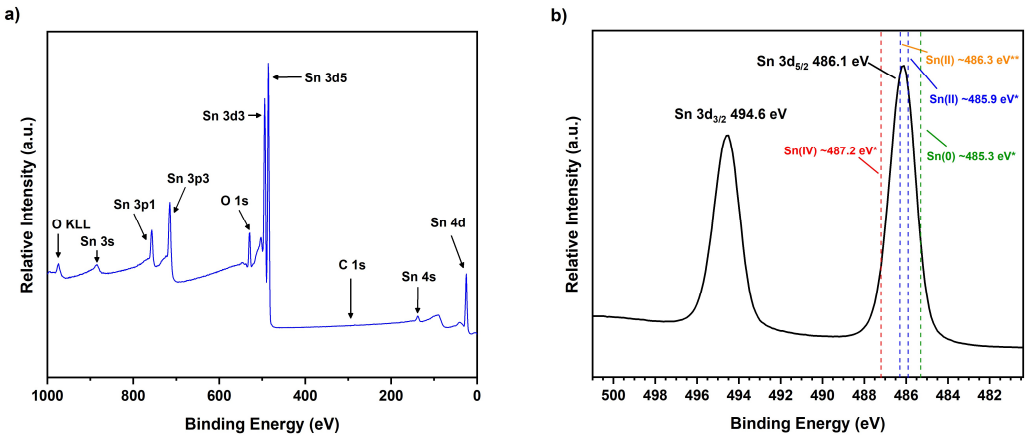

Figure 3.27 – XPS survey spectrum (a), and Sn $3d_{3/2}$ and $3d_{5/2}$ regions (b) of SnO films grown at 170 °C.[*103, **108]

With its purported use in transparent electronics, ALD of SnO was undertaken on quartz substrates in order to measure the transmission. The as-deposited films were transparent with a strong yellow tint and showed strong absorption in the 320-550 nm range, consistent with strong absorption in the near-UV end of the spectrum. This is consistent with other literature

studies on SnO.[91,109,110] Despite this, a good transparency of >60% was observed at wavelengths above ca. 550 nm.

SnO is wide band gap material with direct band gap values of between ~2.4-2.8 eV.[91,109,110] Whilst accurate determination of band gap is difficult for ultrathin films, a Tauc plot was used to give an estimation of the band gap of the as-deposited material on quartz. The extrapolated value of 2.40 eV is largely consistent with reported values. A thickness-independent calculation was used, which is responsible for the arbitrary values of the *y*-axis.

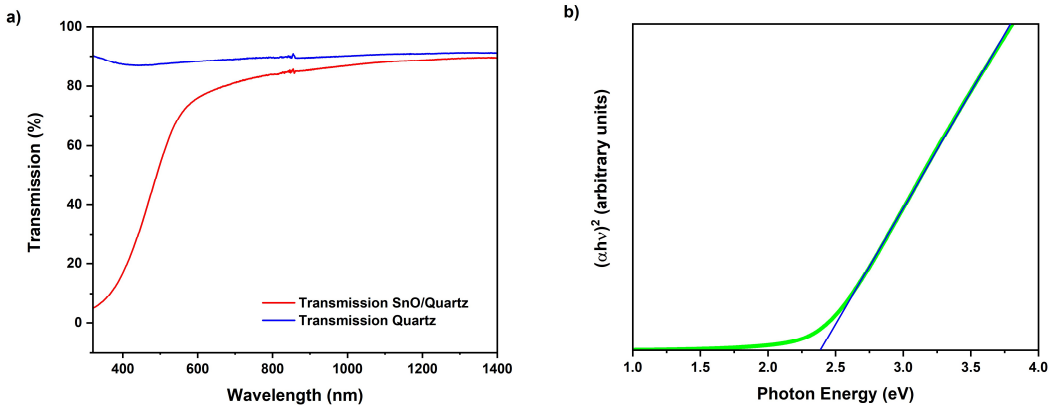

Figure 3.28 – a) Transmission spectrum for SnO films on quartz, and b) Tauc plot giving an estimation of direct band gap on quartz.

3.3. SnO/Graphene Composites

3.3.1. Precedent

In addition to their applications within CMOS circuitry, both tin(II) and tin(IV) oxides have gathered much attention in recent years over their integration into a range of sensing devices. Tin dioxide has long found uses in gas sensors,[111–113] whilst its divalent counterpart is only more recently finding increasing interest for use in electronic sensing devices. Indeed, some studies have investigated mixed Sn(II)/Sn(IV) systems, highlighting the possible benefits of SnO/SnO_2 composite sensors and devices.[114,115] Further to this, both tin mono-[116,117] and dioxide[118–120] have been reported to show promising properties for use as composite electrode materials in high-performance alkali ion batteries.

Unsurprisingly, graphitic materials have garnered huge degrees of interest as battery materials due to their low resistivity and weight in conjunction with ease of reduction and oxidation under the correct conditions.[118,121–123] Of the graphitic materials, graphene oxide (GO), reduced graphene oxide (rGO), or graphene flakes are relatively inexpensive and for many applications more preferable than monolayer graphene, and as such, a number of studies have sought to develop novel battery materials based on SnO_2/rGO composites.[120,124,125] A number of recent high impact papers have focussed on these composites, with initial investigations into the advantages of atomic layer deposition within this field, using well-established SnO_2 ALD precursors and processes.[118,125–127] Further to this, the application of atomic layer deposition for the improvement of battery materials is a growing research topic, with many battery applications employing the technique as standard practice.[128–131]

The emergence of SnO as an important 2D material has increased its attraction for uses in thin-film batteries, though limited number of publications exist as yet.[116,117,132,133] However, in addition to applications in battery materials and CMOS devices, SnO in both bulk and 2D form forms part of a rapidly expanding interest in gas sensors and other nanoscale devices.[115,134–136] With their highly tunable electronic characteristics and mechanical advantages, graphene-based materials are also suitably established within sensor applications,[137,138] but despite the overlap of these avenues of research, the integration of both SnO and graphitic materials is a relatively nascent field, with relatively few experimental SnO/graphene based studies to date. Within these studies, the SnO/graphene composites were fabricated using hydrothermal or evaporative techniques, with no literature precedent of the ALD of SnO onto graphitic materials of any nature.[114,116,139–141]

For efficient atomic layer deposition to take place, a sufficient density of surface reactive sites are required, presenting a serious limitation when depositing onto unfunctionalised surfaces

such as graphene. This fact has hampered research in the field to date, and whilst a number of publications report ALD onto graphene using highly reactive precursors such as trimethylaluminium without prior pre-treatment, deposited films lack tend to lack uniformity and nucleate from defect sites such as rips and tears on the graphene surface. As such, relatively thick films are required to overcome the initial defects caused by sparse nucleation points.[142,143]

A number of graphene pre-treatments have been studied in attempts to provide an ALD receptive surface, including deposition of seed layers, plasma or ozone damage, or wet techniques such as soaking. Functionalisation by plasma is a promising technique and allows for the entire deposition process to be undertaken *in situ*. Recent reports have indicated oxygen and hydrogen plasmas to be particularly effective in facilitating uniform atomic layer deposition.[143–146]

3.3.2. Parameters

In order to introduce oxygen-based defect sites within extended networks of pristine monolayer graphene, an exposure to a limited level of oxygen plasma was tested, and the extent of functionalisation and damage monitored with Raman spectroscopy. With some studies reporting exposure to oxygen plasma of up to 300 W,[147] a much lower dosage was trialled in this investigation. Whilst recent publications have indicated that hydrogen plasma may facilitate a certain extent of reversible damage to the graphene substrate,[143] oxygen plasma was used throughout the following study, in the first example of the ALD of SnO onto a graphitic substrate, and the first example of such deposition with a low reactivity precursor in conjunction with H_2O.

Raman spectroscopy is a useful technique for identifying defects present in samples of graphene. The Raman spectra of both monolayer graphene (MG) and graphite display two major shared features. These consist of the G band (~1580 cm^{-1}), originating from the in-plane vibration of sp^2 carbon atoms, and the 2D or G' band (~2670 cm^{-1}), which appears because of a two-phonon double resonance Raman process. For pristine MG sheets, both the G and 2D band present as sharp, symmetrical resonances.[148,149]

As intensity of the G band increases linearly with layer thickness, the relative intensity compared to the unchanging 2D band can be used to estimate the number of layers of graphene present. With an intensity of half that of the 2D band in monolayer graphene, the G band increases to reach ratios of 1:1, 2:1 and 3:1 for two, three and four-layer graphene respectively. Monitoring of this ratio ensures that the level of damage caused by oxygen plasma is kept below that which would result in the formation of multilayer graphitic flakes.[149] On the introduction of defects within a MG sheet, two additional Raman features evolve. These

consist of the D band (~1356 cm^{-1}) and D' band, which appears as a shoulder on the G band (~1620 cm^{-1}). In sp^2 graphene, the D band originates when crystal symmetry is broken by edges of graphene or point defects and is related to the "breathing modes" of carbon atoms. The D' band is ascribed to the emergence of sp^3 bonding, a necessary artefact of the disruption of graphene sheets to contain hydroxyl or other oxygen-containing moieties.[147–149]

Figure 3.29 displays Raman spectra of monolayer graphene samples exposed to differing levels of oxygen plasma. The spectrum for the pristine sample clearly displays the presence of the G and 2D modes in a 1:2 ratio. Exposure to 50 W oxygen plasma for 1 second shows a barely detectable defect D peak, with no detectable level of sp^3 functionalisation as determined by the presence of a D' mode. With a second exposure of 50 W plasma for 1 second, a considerable increase in defects are observed, in addition to a limited evolution of the D' mode. On exposure to two, 1 second pulses of 100 W plasma, an appreciable level of sp^3 functionalisation was introduced (D' = 1626 cm^{-1}), alongside a marked increase in the defect D peak (1340 cm^{-1}). The G and 2D modes presented unchanged at 1589 cm^{-1} and 2679 cm^{-1} respectively. The damage shown after this exposure was consistent with other publications detailing graphene damage using plasma-enhanced atomic layer deposition. These studies also demonstrated that damage measured by Raman appeared to evolve in a consistent manner irrespective of plasma power.[147]

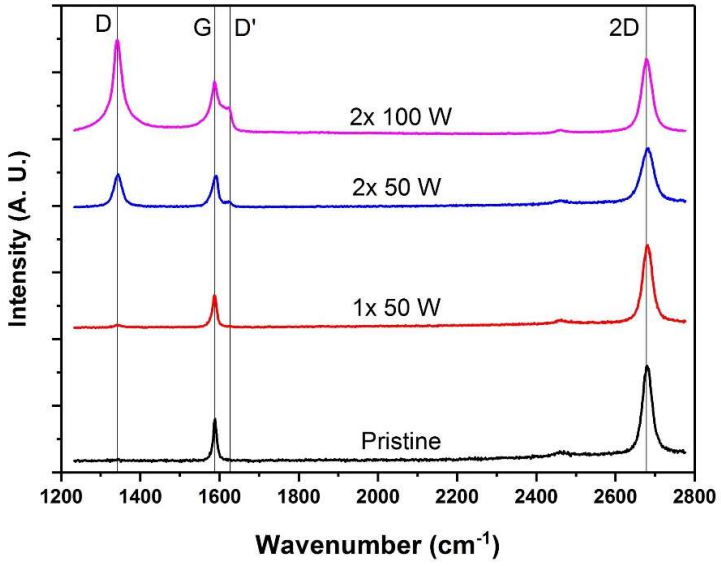

Figure 3.29 – Raman spectra of pristine MG and MG after exposure to 1 x 50 W, 2 x 50 W and 2 x 100 W oxygen plasma.

With the implementation of an adequate graphene pre-treatment, SnO deposition was trialled using the novel precursor [Sn(deed)NMe_2] **(15)** and H_2O at 150 °C in the optimised process previously described. Samples of monolayer graphene on SiO_2/Si wafers were purchased from Graphenea® and subjected to 2 x 1 s pulses of oxygen plasma at room temperature in situ, after which the plasma head was removed from the ALD tool prior to heating and deposition.

3.3.3. Film Characterisation

All depositions resulted in the silicon oxide, and monolayer graphene on silicon oxide, substrates displaying the characteristic purple hue consistent with successful deposition. Films appeared visually uniform, and those deposited on monolayer graphene were shown via p-XRD to consist of identical, preferentially oriented (001) and (002) SnO to those films deposited on blank SiO_2/Si substrates (Figure 3.30).

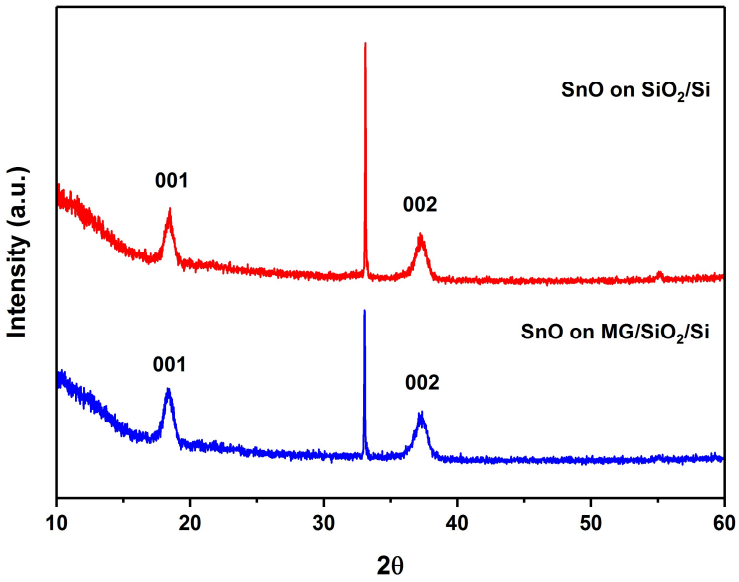

Figure 3.30 – Powder X-ray Diffraction Patterns of SnO films grown on SiO_2/Si (425 cy) and monolayer graphene/SiO_2/Si (637 cy) substrates.

Raman spectroscopy was undertaken with a 532 nm laser in order to provide further confirmation of successful SnO deposition and to ensure that the monolayer graphene had not undergone further damage or degradation (Figure 3.31). In addition to the expected silicon 2TA, TO and 2TO bands (unlabelled), the collected Raman data displays the expected SnO modes at 113 cm^{-1} and 210 cm^{-1} ascribed to the E_g and A_{1g} bands respectively. Also observed are the G (1587 cm^{-1}) and 2D (2692 cm^{-1}) modes of monolayer graphene, flanked by the same degree of defect-related D (1345 cm^{-1}) and D' (1621 cm^{-1}) peaks, which though marginally distorted by the deposition process, exhibit the same degree of damage as was observed after plasma pre-treatment.

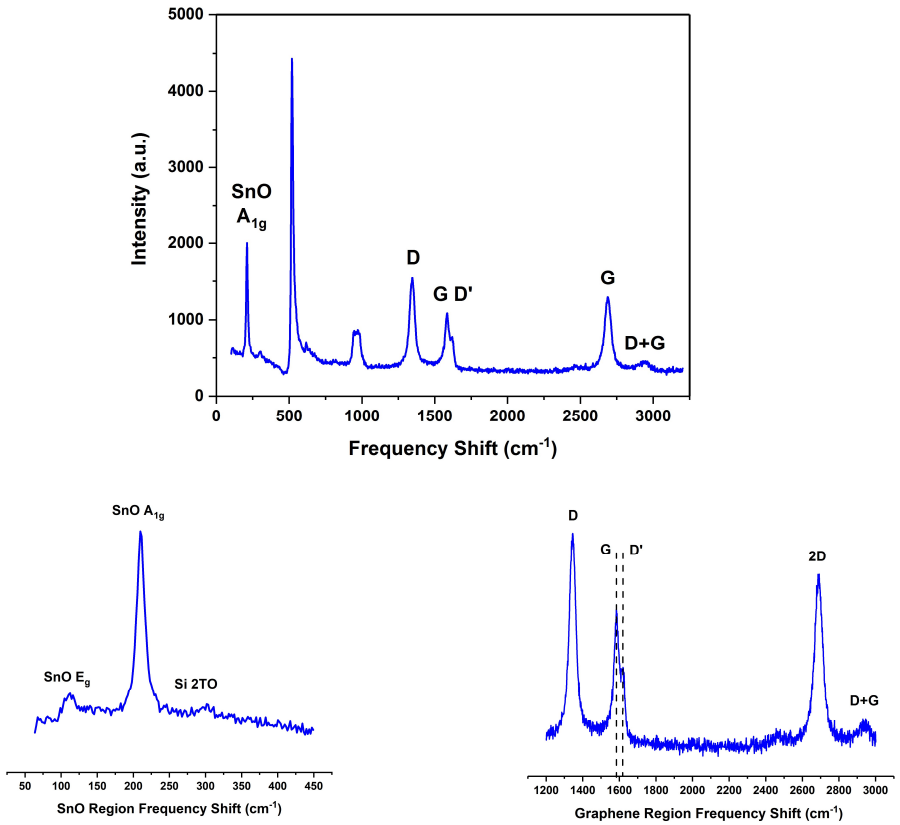

Figure 3.31 – Raman spectra of SnO on monolayer graphene/SiO_2/Si substrate, with focussed spectra of the SnO and graphitic regions below.

With initial proof of concept studies indicating that functionalisation of monolayer graphene via limited exposure to oxygen plasma was possible, and that such functionalisation had occurred to a large enough extent to allow for an H_2O based ALD process to take place, a study aiming to deposit onto unsupported monolayer graphene was devised. A transmission electron microscopy grid with a partially supported monolayer graphene surface was purchased from Graphenea®, which would add support to the hypothesis that the monolayer graphene remained intact after plasma treatment and would allow for direct observation of the nature of the SnO film post-deposition. MG-TEM grids were affixed to a SiO_2/Si wafer and subjected to the previously established plasma pre-treatment, followed by 637 ALD cycles of [Sn(deed)NMe_2]/H_2O at 150 °C. This rendered directly comparable HR-TEM images to those collected from films deposited on GO/Holey Carbon TEM grids with the same number of ALD cycles.

As is immediately evident from the HR-TEM images shown in Figure 3.32, a much higher density of material is present on the monolayer graphene substrate than was observed on the unfunctionalized graphene oxide TEM grids (Figure 3.23 and Figure 3.24). Indeed, even after 850 ALD cycles (Figure 3.23), deposition observed on GO TEM substrates was considerably less dense. The nature of the crystallites remained consistent, however, with the presence of the characteristic petal-like structures measuring 100-200 nm highlighted previously. These

can be seen to form an almost continuous sheet across the substrate, with smaller crystalline domains consisting of numerous smaller blocks (Figure 3.32, 20 nm).

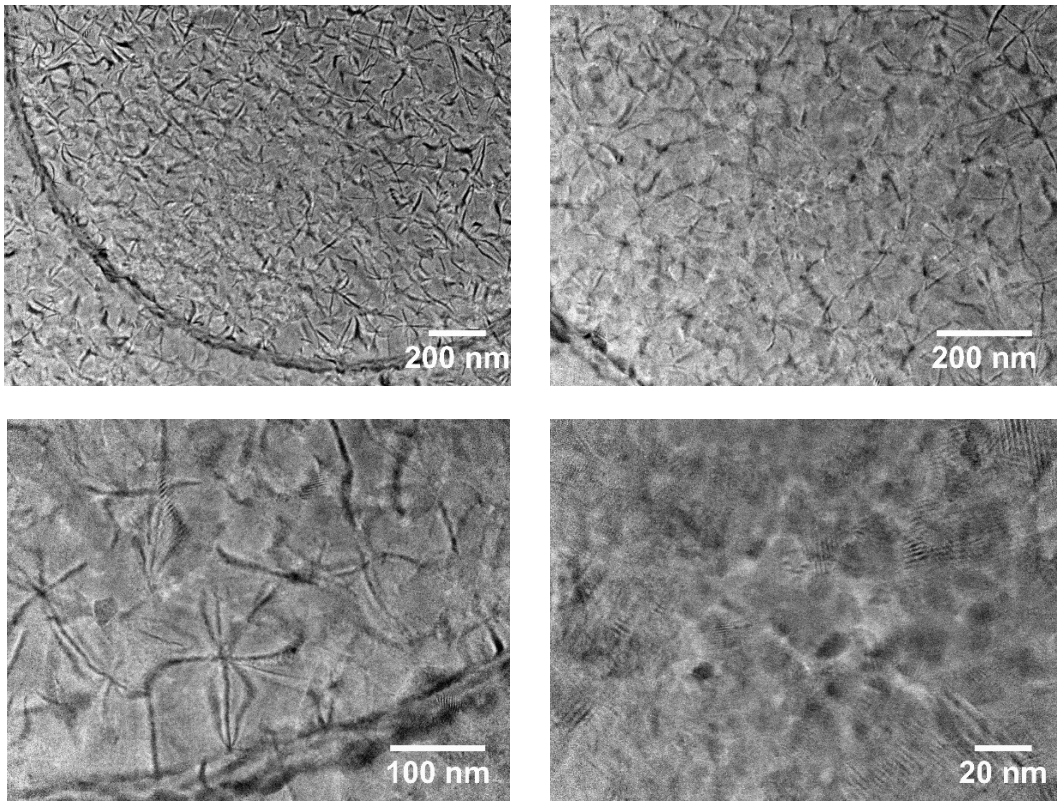

Figure 3.32 – HR-TEM images of SnO on MG/TEM grids, 637 ALD cycles.

More significantly, the SnO sheets appear to cover the entirety of the unsupported monolayer graphene regions of the TEM substrate. This is best observed in Figure 3.32, where the edge of the circular cavities in the underlying TEM grid can be seen. This adds justification to the hypothesis that the monolayer graphene substrate remains largely undamaged, though future studies using electrical data such as resistivity would be useful in further substantiating that the electrical properties of the graphene remain desirable after plasma pre-treatment.

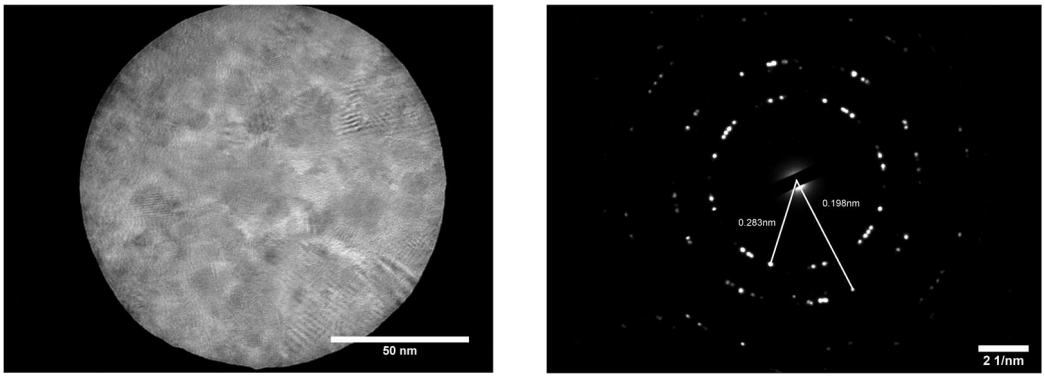

Figure 3.33 – Selected-area (left) and selected-area electron diffraction (right) images for SnO films on MG/TEM grids (637 cy).

Selected-area electron diffraction studies (Figure 3.33) again confirm the presence of highly crystalline SnO, with measured d-spacings of 0.283 nm and 0.198 nm corresponding to the (110) and (200) planes respectively. As before, this gives an indication of a bulk relative orientation of the crystalline material, with the *C* axis lying perpendicular to the substrate surface.

Deposition onto TEM grids afforded the opportunity to undertake energy-dispersive X-ray spectroscopy (EDX), a technique previously of little value for films deposited onto SiO_2/Si substrates due to the high detection of substrate oxygen through the nanometre-scale films. The technique relies on the ejection of an inner-shell electron from its ground state by a high energy electron beam, prompting the filling of this vacancy by a higher energy, outer shell electron. Upon this relaxation, excess energy is emitted in the form of X-ray photons at quantised, atom-specific energies. This allows for a largely quantitative representation of elements present within the target area.

The EDX spectrum of SnO on the MG/TEM grid is displayed in Figure 3.34. The spectrum confirms the presence of both tin and oxygen, in conjunction with a small range of impurities arising from the HR-TEM holder and chamber, in addition to a low degree of copper, likely to originate from the gaskets used in the precursor sources. The relatively high carbon content is an interesting observation, though much of this is most probably a result of the carbon TEM grid and graphene surface layer. The tin-oxgen ratio presents as roughly 1:1.2. Oxidation of SnO to SnO_2 at the surface and exposed grain boundaries was observed in previous samples and given the ambient conditions under which storage and transferral to analysis were undertaken, is likely to account for a certain degree of excess oxygen in the EDX stoichiometry. It is however worth highlighting that Sn-O ratios of 1:1.2 were observed by Han et al. in the original publication of a [$Sn(dmamp)_2$] ALD process.[91]

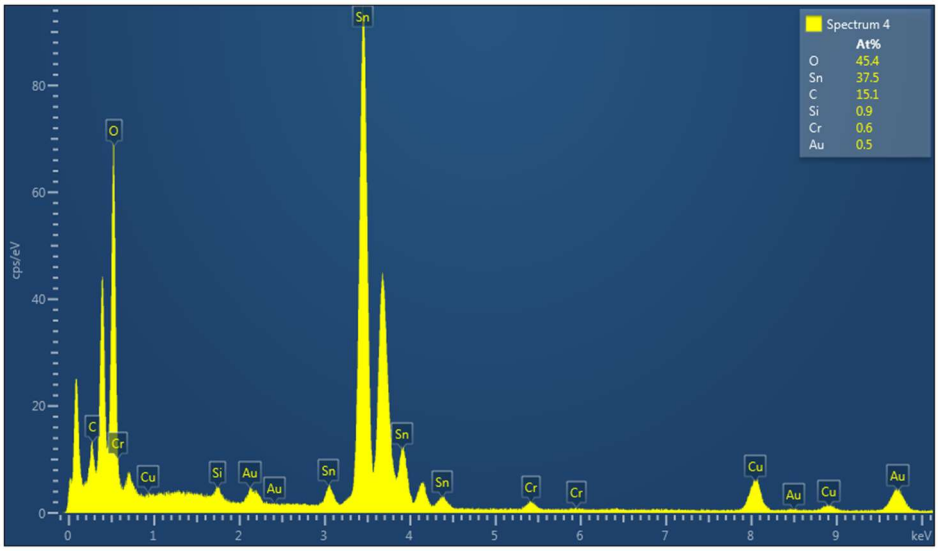

Figure 3.34 – EDX spectrum of SnO on MG graphene.

To further elucidate the composition of tin and oxygen in the SnO films on monolayer graphene, depth-profiling X-ray photoelectron spectroscopy (XPS) was undertaken (Figure 3.35). These samples were stored and transported under an inert atmosphere to minimise surface oxidation, with experiments carried out by Dr David Morgan, Cardiff University. The relative compositions of oxygen and tin are shown to be roughly equal throughout the film. After ca. 400 s of Ar^+ etching, Si–O and Si 2p signals manifest as the SiO_2 substrate begins to become detectable. This shows reasonable correlation with the tin-oxygen composition of 1:1.2 detected via EDX analysis.

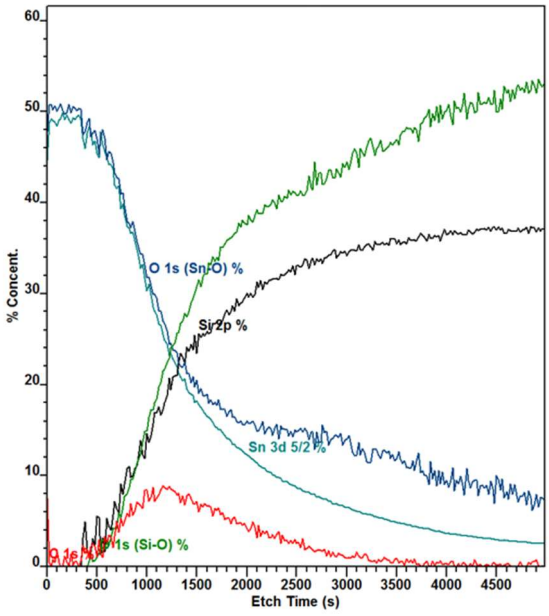

Figure 3.35 – XPS depth profile of atomic composition of SnO film on MG/SiO_2 (150 °C, 850 cy).

One of the more desirable properties of SnO, as with many metal oxides, is its relatively high transparency in the visible region. By way of a confirmation of this, UV-Visible spectroscopy was carried out on SnO films deposited onto functionalised monolayer graphene on transparent quartz substrates. As before, films were visibly transparent, with a slight yellow tint. Figure 3.36 shows a transmission spectrum for wavelengths between 320-1400 nm, confirming that as-deposited films with a thickness of ca. 14 nm display a high optical transparency at wavelengths over ca. 550 nm. Again, a thickness independent Tauc plot was used to estimate the band gap of the as deposited SnO/MG/quartz composite, giving a value marginally higher (1.48 eV) than that observed for the pure SnO/quartz sample measured previously (1.40 eV). However, as is the case for both samples, these values are consistent with literature precedent.[91,109,110]

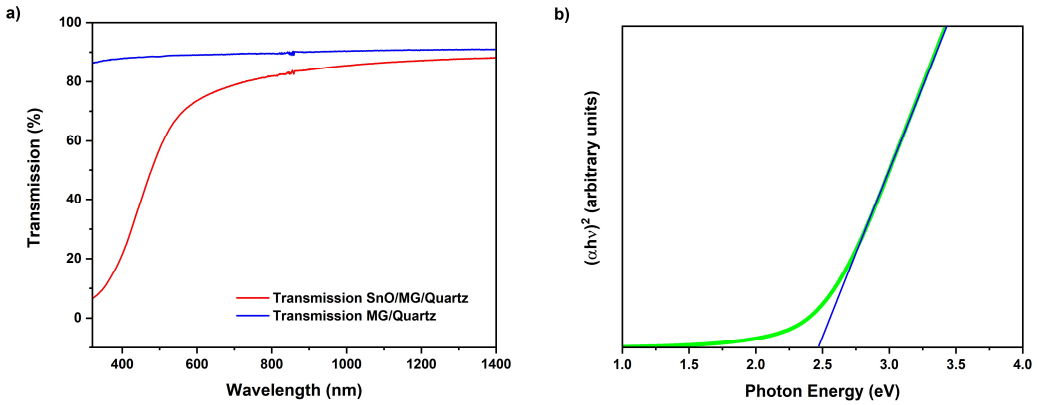

Figure 3.36 – UV-Visible transmission spectra and Tauc plot for SnO films deposited onto monolayer graphene on quartz substrates at 150 °C (850cy).

3.4. Electrical Studies

[Sn(deed)NMe$_2$] **(15)** proved capable of depositing crystalline SnO films of high uniformity over large substrate areas, and as such, material deposited at 170 °C was trialled as a p-channel in a thin film transistor fabricated and tested by Dr Kham Niang, University of Cambridge. Bottom-gate TFTs were constructed using thermally grown SiO_2 (~200 nm) and highly p-doped silicon as the gate dielectric and gate electrode respectively, on which SnO (~15 nm) was deposited. Thermally evaporated Au contacts were used as the source and drain contacts.

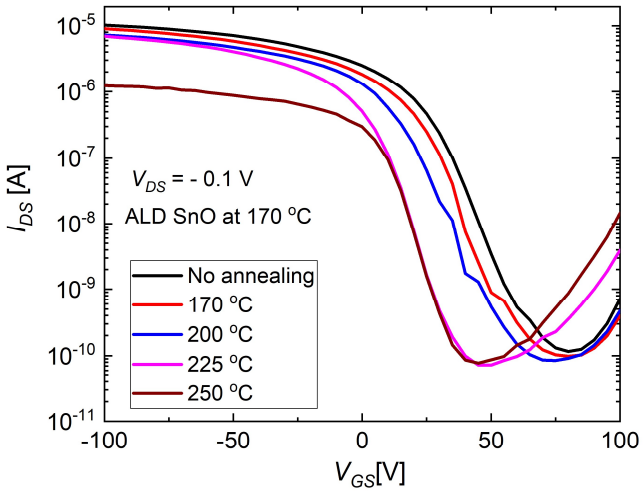

Figure 3.37 – I_{DS} vs. V_{GS} plot for passivated films with a range of annealing conditions.

Post-fabrication passivation with 20 nm Al_2O_3 deposited at 150 °C was found to significantly improve the switching characteristics of the SnO channels, as exposure to ambient oxygen at high annealing temperatures was minimised. After passivation, annealing was carried out at 170, 200, 225 and 250 °C, the results of which are displayed in Figure 3.37. The switching voltage can be seen to decrease towards 0 V as annealing temperature is increased, which is preferable for TFT applications, though mobility as reflected by switching ratio is negatively affected at annealing temperatures of 250 °C. The switching ratio for TFTs annealed at 225 °C was found to be 8 x 10^4, which is higher than that found for the device fabricated by PragmatIC Printing Ltd. discussed in Chapter 2. This ratio is also at the higher end of those reported for conventionally deposited SnO TFTs,[90,110,150–152] though is still lower than the high-performance TFTs fabricated with SnO deposited at 210 °C by Kim et al. using Sn(dmamp)$_2$, which display I_{ON}/I_{OFF} ratios of ca. 2 x 10^6.[96]

The field effect mobility as a function of gate bias for TFTs annealed at 225 °C is shown in Figure 3.38. The device showed a maximum μ_{FE} of 0.9 cm^2 V^{-1} s^{-1}, which is marginally lower than the values of ~1 cm^2 V^{-1} s^{-1} reported by Kim et al. for devices fabricated with SnO

deposited at 210 °C with [Sn(dmamp)$_2$].[96] This value is also significantly higher than that found for the devices fabricated by PragmatIC Printing Ltd. using [Sn(dmamp)$_2$] as a precursor and deposited at 170 °C (0.012 cm^2 V^{-1} s^{-1}).

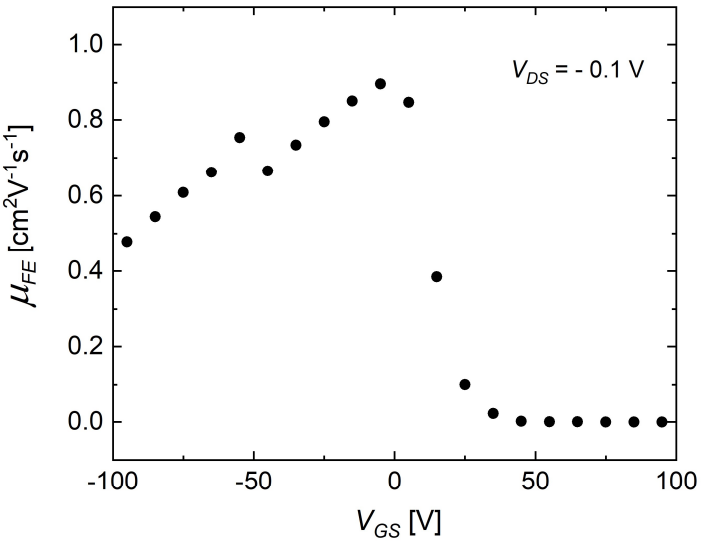

Figure 3.38 – Field effect mobility as a function of gate bias for TFTs annealed at 225 °C.

3.5. Conclusions

A series of simple and inexpensive novel aminoamide species were synthesised via facile reactions between tin(II) dimethylamide and a range of commercially available aminoamines. The series of complexes characterised scoped the fine balance between lability of Sn–N bonding and thermal stability. All alkylated aminoamide complexes **(13-18)** presented as liquids and displayed extremely high air and moisture sensitivity on any exposure to ambient conditions. High volatility was observed through the thermogravimetric analysis of thermally stable complexes **13-15**, and computational studies on heteroleptic [Sn(deed)NMe$_2$] **(15)**, which displayed the highest volatility, were undertaken as part of a collaboration with Dr. Antoine Buchard, University of Bath. These studies provided an insight into the intermolecular interactions present within complex **15**, and indicated that under expected ALD conditions the monomeric, the three-coordinate system would be the predominant species.

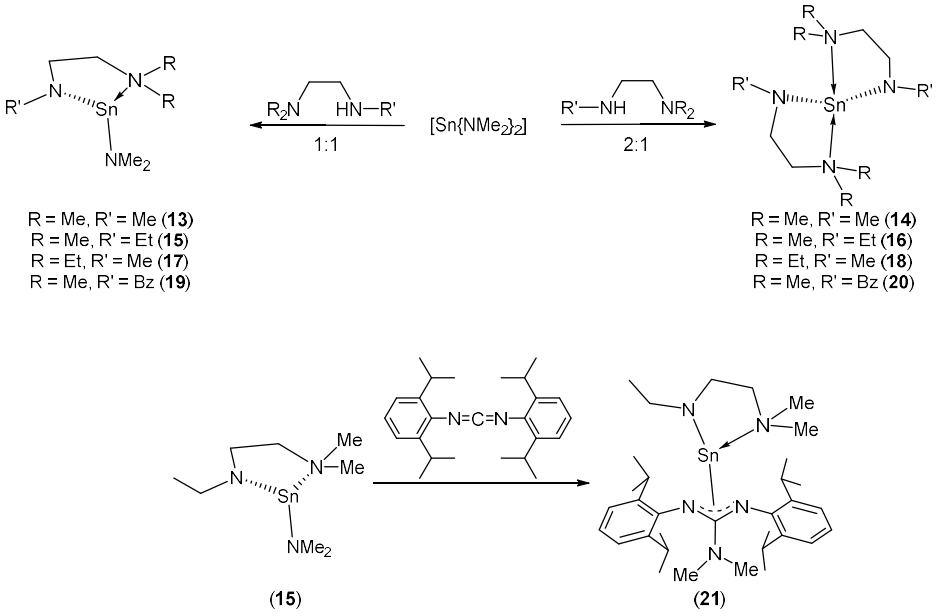

Scheme 3.2 – Summary of reactions and complexes detailed in Chapter 3.

Complex **15** was further characterised by the synthesis and structural characterisation of a guanidinato derivative via the insertion of the Sn–NMe_2 bond into 2,6-diisopropylcarbodiimide, whilst analogous hetero- and homoleptic benzylated aminoamide species **19** and **20** allowed for the structural characterisation of aryl analogues of **13-18**. The latter proved to be entirely unsuitable for deposition applications, presenting as non-volatile solids with moderate thermal stability.

Atomic layer deposition trials were undertaken using [Sn(deed)NMe_2] **(15)** and H_2O, and were shown to successfully deposit crystalline SnO between 150 and 170 °C, at marginally higher growth rates than the previously reported [Sn(dmamp)$_2$] process.[153] Films were characterised with a range of analytical techniques, and deposition on a commercially available ALD tool was shown to result in highly conformal films over entire 100 mm SiO_2/Si wafer substrates (Figure 3.39). This remains only the second example of effective tin(II) oxide atomic layer deposition to date, and was carried out with an unambiguously liquid precursor displaying neither the unexplained solid-liquid phase transitions nor hydrolytic tendencies of [Sn(dmamp)$_2$].

Thin film transistors fabricated in collaboration with the University of Cambridge showed good switching characteristics and comparable mobilities to the upper tranche of SnO TFT reports, and display significantly better properties than were found for the device fabricated in Chapter 2. This initial investigation highlighted a number of areas in which improvements to device performance could be made, which will be the subject of future research.

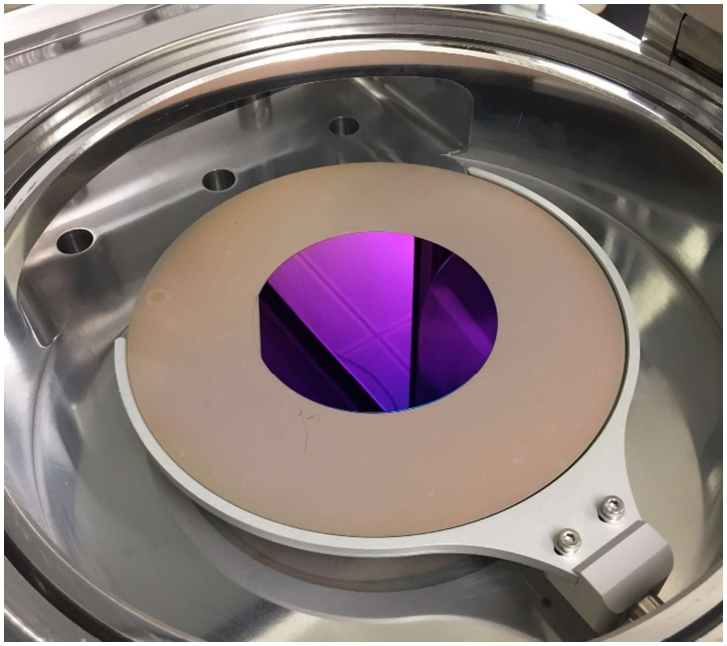

Figure 3.39 – Uniform deposition of SnO over a 100 mm SiO_2/Si wafer. (N.b. highly reflective film).

After successful atomic layer deposition trials were concluded, a short investigation into the in-situ plasma functionalisation of monolayer graphene (MG) was carried out, followed by a proof-of-concept study into the deposition of SnO onto MG substrates. Characterisation of the latter revealed the first example of the atomic layer deposition of tin(II) oxide onto monolayer graphene, or indeed any graphitic substrate. Further research will seek to explore the functional properties of this composite in battery technologies and complete electrical characterisation of the graphene substrate, before exploring potential applications in sensing.

3.6. Experimental

Generic experimental details are given in the Appendix, but it is necessary to explain that due to the highly air and moisture sensitive nature of complexes **13**-**21**, significant difficulty was encountered in obtaining sufficiently consistent elemental analysis results, despite numerous attempts for each compound. The high sensitivity is exacerbated by the liquid nature of many of the compounds in addition to the light- and time-sensitivity of others. However, the molecular structures of all novel complexes that present as solids have been confirmed with single-crystal X-ray diffraction, and all complexes have been characterised with multinuclear NMR and 2D NMR spectroscopy. Mass spectroscopy was additionally attempted, but the lack of suitable non-reactive solvents and air-sensitive equipment prevented the collection of any meaningful data.

[Sn(tmed)NMe$_2$] (13)

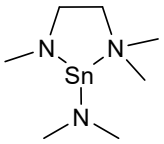

A solution of N,N,N-trimethylethylenediamine (Htmed) (0.20 g, 2 mmol) in THF (20 ml) was added to a cooled solution of [Sn(NMe$_2$)$_2$] (0.41 g, 2 mmol) in THF (20 ml) and stirred for 2 hours. The volatiles were removed *in vacuo* and the yellow oil dissolved in THF before filtration through Celite®. The solvent was removed and the yellow liquid distilled at 100 °C (10^{-2} mbar) into a receiver flask held in liquid N_2, yielding a highly air and moisture sensitive yellow liquid that displayed light sensitivity over extended periods of time. (0.40 g, 75%) Decomp. 130 °C.

^{1}H NMR (500 MHz, C_6D_6); δ_{ppm} 3.22 (2H, t, *J* = 5.6 Hz, $H_3CNC\mathit{H}_2CH_2N(CH_3)_2$), 3.02 (6H, br s, $N\mathit{Me}_2$), 2.99 (3H, s, $\mathit{H}_3CNCH_2CH_2N(CH_3)_2$), 2.28 (2H, t, *J* = 5.6 Hz, $H_3CNCH_2C\mathit{H}_2N(CH_3)_2$), 1.96 (6 H, s, $H_3CNCH_2CH_2N(C\mathit{H}_3)_2$).

^{13}C{^{1}H} NMR (125.7 MHz, C_6D_6); δ_{ppm} 60.4 (1C, $H_3CNCH_2\mathit{C}H_2N(CH_3)_2$), 55.8 (1C, $H_3CN\mathit{C}H_2CH_2N(CH_3)_2$), 45.4 (2C, $H_3CNCH_2CH_2N(\mathit{C}H_3)_2$), 44.1 (2C, $N\mathit{Me}_2$), 41.0 (s, $H_3\mathit{C}NCH_2CH_2N(CH_3)_2$).

^{119}Sn NMR (186.3 MHz, C_6D_6); δ_{ppm} 84 (br)

[Sn(tmed)$_2$] (14)

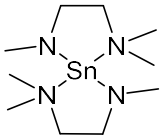

A solution of [Sn(NMe$_2$)$_2$] (0.41 g, 2 mmol) in THF (20 ml) was added to a cooled solution of N,N,N-trimethylethylenediamine (Htmed) (0.40 g, 4 mmol) in THF (20 ml) and stirred for 2 hours. The volatiles were removed *in vacuo* and the yellow oil dissolved in THF before filtration through Celite®. The solvent was removed and the yellow liquid distilled at 100 °C (10^{-2} mbar) into a receiver flask held in liquid N_2, yielding a highly air and moisture sensitive yellow liquid that displayed light sensitivity over extended periods of time. (0.51 g, 80%) Decomp. 135 °C.

^{1}H NMR (500 MHz, C_6D_6); δ_{ppm} 3.36–3.32 (4H, m, $CH_3NC\mathit{H}_2CH_2N(CH_3)_2$), 3.02 (6H, s, $C\mathit{H}_3NCH_2CH_2N(CH_3)_2$), 2.38–2.35 (4H, m, $CH_3NCH_2C\mathit{H}_2N(CH_3)_2$), 2.07 (12H, s, $CH_3NCH_2CH_2N(C\mathit{H}_3)_2$).
^{13}C{^{1}H} NMR (125.7 MHz, C_6D_6); δ_{ppm} 60.5 (2C, $CH_3NCH_2\mathit{C}H_2N(CH_3)_2$), 56.0 (2C, $CH_3N\mathit{C}H_2CH_2N(CH_3)_2$), 45.6 (4C, $CH_3NCH_2CH_2N(\mathit{C}H_3)_2$), 41.1 (2C, $\mathit{C}H_3NCH_2CH_2N(CH_3)_2$).
^{119}Sn NMR (186.3 MHz, C_6D_6); δ_{ppm} 88 (br)

[Sn(deed)NMe$_2$] (15)

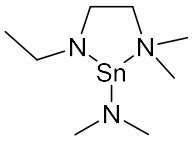

A solution of N,N-dimethyl-N-ethylethylenediamine (Hdeed) (0.23 g, 2 mmol) in THF (20 ml) was added to a cooled solution of [Sn(NMe$_2$)$_2$] (0.41 g, 2 mmol) in THF (20 ml) and stirred for 2 hours. The volatiles were removed *in vacuo* and the yellow oil dissolved in THF before filtration through Celite®. The solvent was removed and the yellow liquid distilled at 100 °C (10^{-2} mbar) into a receiver flask held in liquid N_2, yielding a highly air and moisture sensitive yellow liquid that displayed light sensitivity over extended periods of time. (0.46 g, 82%) Decomp. 145 °C.

^{1}H NMR (400 MHz, Neat); δ_{ppm} 3.50 (2H, t, J = 5.56 Hz, $CH_3CH_2NC\mathit{H}_2CH_2N(CH_3)_2$), 3.41 (2H, q, *J* = 6.88 Hz, $CH_3C\mathit{H}_2NCH_2CH_2NMe_2$), 3.10 (6H, br s, $N\mathit{Me}_2$), 2.76 (2H, t, *J* = 5.56 Hz, $CH_3CH_2NCH_2C\mathit{H}_2N(CH_3)_2$), 2.55 (6H, br s, $CH_3CH_2NCH_2CH_2N(C\mathit{H}_3)_2$), 1.41 (3H, t, *J* = 6.88 Hz, $C\mathit{H}_3CH_2NCH_2CH_2N(CH_3)_2$).

^{1}H NMR (400 MHz, C_6D_6); δ_{ppm} 3.33 (2H, q, *J* = 6.60 Hz, $CH_3CH_2NCH_2CH_2NMe_2$), 3.28–3.07 (8H, br m, (6H, NMe_2), (2H, $CH_3CH_2NCH_2CH_2N(CH_3)_2$), 2.21 (2H, br m, $CH_3CH_2NCH_2CH_2N(CH_3)_2$), 1.75 (6H, br s, ($CH_3CH_2NCH_2CH_2N(CH_3)_2$), 1.41 (3H, t, *J* = 6.60 Hz, $CH_3CH_2NCH_2CH_2N(CH_3)_2$).

^{13}C{^{1}H} NMR (125.7 MHz, C_6D_6); δ_{ppm} 61.0 (1C, $CH_3CH_2NCH_2CH_2N(CH_3)_2$), 52.7 (2C, NMe_2), 48.0 (1C, ($CH_3CH_2NCH_2CH_2N(CH_3)_2$), 43.9 (2C, ($CH_3CH_2NCH_2CH_2N(CH_3)_2$), 42.9 (1C, $CH_3CH_2NCH_2CH_2N(CH_3)_2$), 18.3 (1C, $CH_3CH_2NCH_2CH_2N(CH_3)_2$).

^{119}Sn NMR (186.3 MHz, C_6D_6); δ_{ppm} 106 (br), 124 (br, minor, $[Sn(NMe_2)_2]$)

$[Sn(deed)_2]$ (16)

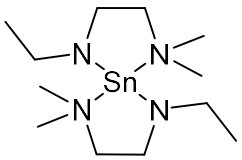

A solution of $[Sn(NMe_2)_2]$ (0.41 g, 2 mmol) in THF (20 ml) was added to a cooled solution of N,N-dimethyl-N-ethylethylenediamine (Hdeed) (0.46 g, 4 mmol) in THF (20 ml) and stirred for 2 hours. The volatiles were removed *in vacuo* and the yellow oil dissolved in THF before filtration through Celite®. The solvent was removed yielding a thermally unstable, highly air and moisture sensitive yellow liquid that displayed light sensitivity over extended periods of time. (0.52 g, 75%)

^{1}H NMR (400 MHz, C_6D_6); δ_{ppm} 3.41–3.32 (8H, m, (4H, $CH_3CH_2NCH_2CH_2NMe_2$), (4H, $CH_3CH_2NCH_2CH_2N(CH_3)_2$)), 2.39–2.31 (4H, m, $CH_3CH_2NCH_2CH_2N(CH_3)_2$), 2.05 (12H, br s, $CH_3CH_2NCH_2CH_2N(CH_3)_2$), 1.33 (6H, t, *J* = 7.0 Hz, $CH_3CH_2NCH_2CH_2N(CH_3)_2$).

^{13}C{^{1}H} NMR (125.7 MHz, C_6D_6); δ_{ppm} 61.1 (2C, $CH_3CH_2NCH_2CH_2N(CH_3)_2$), 50.7 (2C, ($CH_3CH_2NCH_2CH_2N(CH_3)_2$), 46.6 (2C, $CH_3CH_2NCH_2CH_2N(CH_3)_2$), 45.1 (4C, $CH_3CH_2NCH_2CH_2N(CH_3)_2$), 18.2 (2C, $CH_3CH_2NCH_2CH_2N(CH_3)_2$).

^{119}Sn NMR (186.3 MHz, C_6D_6); δ_{ppm} 104 (br)

[Sn(dmed)NMe$_2$] (17)

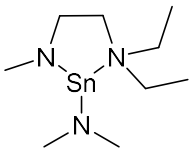

A solution of N,N-diethyl-N-methylethylenediamine (Hdmed) (0.26 g, 2 mmol) in THF (20 ml) was added to a cooled solution of [Sn(NMe$_2$)$_2$] (0.41 g, 2 mmol) in THF (20 ml) and stirred for 2 hours. The volatiles were removed *in vacuo* and the yellow oil dissolved in THF before filtration through Celite®. The solvent was removed yielding a thermally unstable, highly air and moisture sensitive yellow liquid that displayed light sensitivity over extended periods of time. The product decomposed over a period of ca. 48 h. (0.50 g, 86%)

^{1}H NMR (500 MHz, C_6D_6); δ_{ppm} 3.25 (2H, t, J = 6.0 Hz, $CH_3NC\mathit{H}_2CH_2N(CH_2CH_3)_2$), 3.04 (3H, s, $CH_3NCH_2CH_2N(CH_2CH_3)_2$), 2.99 (6H, br s, $N\mathit{Me}_2$), 2.49–2.38 (6H, m, (4H $CH_3NCH_2CH_2N(C\mathit{H}_2CH_3)_2$), (2H, $CH_3NC\mathit{H}_2C_2N(CH_2CH_3)_2$)), 0.80 (6H, t, J = 7.2 Hz, $CH_3NCH_2CH_2N(CH_2C\mathit{H}_3)_2$).

^{13}C{^{1}H} NMR (125.7 MHz, C_6D_6); δ_{ppm} 54.4 (1C, $CH_3N\mathit{C}H_2CH_2N(CH_2CH_3)_2$), 53.6 (1C, $CH_3NCH_2\mathit{C}H_2N(CH_2CH_3)$), 44.7 (2C, $CH_3NCH_2CH_2N(\mathit{C}H_2CH_3)$, 43.4 (2C, $N\mathit{Me}_2$), 40.2 (1C, $\mathit{C}H_3NCH_2CH_2N(CH_2CH_3)_2$), 9.7 (2C, $CH_3NCH_2CH_2N(CH_2\mathit{C}H_3)_2$).

^{119}Sn NMR (186.3 MHz, C_6D_6); δ_{ppm} 95 (br, with asymmetry suggestive of four coordinate mono- and bis systems), 124 (br, (Sn(NMe$_2$)$_2$).

[Sn(dmed)$_2$] (18)

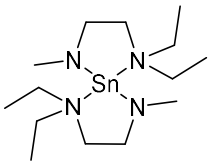

A solution of [Sn(NMe$_2$)$_2$] (0.41 g, 2 mmol) in THF (20 ml) was added to a cooled solution of N,N-diethyl-N-methylethylenediamine (Hdmed) (0.52 g, 4 mmol) in THF (20 ml) and stirred for 2 hours. The volatiles were removed *in vacuo* and the yellow oil dissolved in THF before filtration through Celite®. The solvent was removed yielding a thermally unstable, highly air and moisture sensitive yellow liquid that displayed light sensitivity over extended periods of time. The product decomposed over a period of ca. 48 h. (0.48 g, 64%)

^{1}H NMR (500 MHz, C_6D_6); δ_{ppm} 3.40 (4H, t, *J* = 6.2 Hz, $CH_3NCH_2CH_2N(CH_2CH_3)_2$), 3.12 (6H, s, $CH_3NCH_2CH_2N(CH_2CH_3)_2$), 2.57–2.47 (12H, m, (8H, $CH_3NCH_2CH_2N(CH_2CH_3)_2$), (4H, $CH_3NCH_2CH_2N(CH_2CH_3)_2$)), 0.88 (12H, t, *J* = 7.2 Hz, $CH_3NCH_2CH_2N(CH_2CH_3)_2$).

^{13}C{^{1}H} NMR (125.7 MHz, C_6D_6); δ_{ppm} 54.5 (2C, $CH_3NCH_2CH_2N(CH_2CH_3)_2$, 54.0 (2C, $CH_3NCH_2CH_2N(CH_2CH_3)_2$), 45.2 (4C, $CH_3NCH_2CH_2N(CH_2CH_3)$, 39.8 (2C, $CH_3NCH_2CH_2N(CH_2CH_3)_2$), 10.3 (4C, $CH_3NCH_2CH_2N(CH_2CH_3)_2$).

^{119}Sn NMR (186.3 MHz, C_6D_6); δ_{ppm} 102 (br)

[Sn(bded)NMe$_2$] (19)

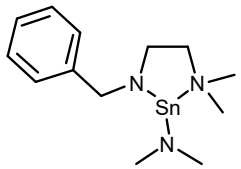

A solution of N-benzyl-N,N-dimethylethylenediamine (Hbded) (0.36 g, 2 mmol) in THF (20 ml) was added to a cooled solution of [Sn(NMe$_2$)$_2$] (0.41 g, 2 mmol) in THF (20 ml) and stirred for 2 hours. The volatiles were removed *in vacuo* and orange solid dissolved in hexane before filtration through Celite®. The solvent was reduced, affording highly air and moisture sensitive orange crystals after storage at –28 °C. (0.40 g, 60%) Decomp. 140 °C

^{1}H NMR (500 MHz, C_6D_6); δ_{ppm} (mono, bis and Sn(NMe$_2$)$_2$ present):

Mono-component **(19)**: 7.49-7.55 (m, 2H, *o*-C_6H_5), 7.23-7.31 (m, 2H, *m*-C_6H_5), 7.09-7.18 (m, 1H, *p*-C_6H_5), 4.29 (2H, s, $PhCH_2NCH_2CH_2NMe_2$), 3.15 (br m, 6H, $SnNMe_2$) 3.03 (m, 2H, $PhCH_2NCH_2CH_2NMe_2$), 2.16 (m, 2H, $PhCH_2NCH_2CH_2NMe_2$), 1.70 (6H, s, $PhCH_2NCH_2CH_2NMe_2$). *Bis-component* **(20)**: 7.54-7.56 (m, 4H, *o*-C_6H_5), 7.29-7.33 (m, 4H, *m*-C_6H_5), 7.14-7.18 (m, 2H, *p*-C_6H_5), 4.44 (4H, s, $PhCH_2NCH_2CH_2NMe_2$), 3.19 (m, 4H, $PhCH_2NCH_2CH_2NMe_2$), 2.28 (m, 4H, $PhCH_2NCH_2CH_2NMe_2$), 1.97 (12H, s, $PhCH_2NCH_2CH_2NMe_2$). Sn(NMe$_2$)$_2$: 3.16 (br m, 6H)

^{13}C{^{1}H} NMR (125.7 MHz, C_6D_6); δ_{ppm} *Mono-component* **(19)**: 145.2 (1C, *ipso*-C_6H_5), 128.9 (2C, *m*–C_6H_5), 128.4 (2C, *o*–C_6H_5), 126.7 (1C, *p*–C_6H_5), 61.0 (1C, $PhCH_2NCH_2CH_2NMe_2$), 58.2 (1C, $PhCH_2NCH_2CH_2NMe_2$), 52.4 (1C, $PhCH_2NCH_2CH_2NMe_2$), 43.7 (2C, $PhCH_2NCH_2CH_2NMe_2$), 43.2 (2C, $SnNMe_2$). *Bis-component* **(20)**: 144.6 (2C, *ipso*-C_6H_5), 128.7 (4C, *m*–C_6H_5), 128.4 (4C, *o*–C_6H_5), 126.4 (2C, *p*–C_6H_5), 60.3 (2C, $PhCH_2NCH_2CH_2NMe_2$), 56.7 (2C, $PhCH_2NCH_2CH_2NMe_2$), 50.7 (2C, $PhCH_2NCH_2CH_2NMe_2$), 45.1 (4C, $PhCH_2NCH_2CH_2NMe_2$).

^{119}Sn NMR (186.3 MHz, C_6D_6); δ_{ppm} 60 (br, bis), 88 (br, mono), 117, 124 (br, [Sn(NMe$_2$)$_2$])

[Sn(bded)$_2$] (20)

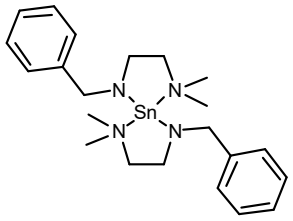

A solution of [Sn(NMe$_2$)$_2$] (0.41 g, 2 mmol) in THF (20 ml) was added to a cooled solution of N-benzyl-N,N-dimethylethylenediamine (Hbded) (0.72 g, 4 mmol) in THF (20 ml) and stirred for 2 hours. The volatiles were removed *in vacuo* and orange solid dissolved in hexane before filtration through Celite®. The solvent was reduced, affording orange crystals after storage at –28 °C. (0.63 g, 67%) Decomp. 145 °C.

^{1}H NMR (500 MHz, C_6D_6); δ_{ppm} 7.54-7.56 (m, 2H, *o*-C_6H_5), 7.29-7.33 (m, 2H, *m*-C_6H_5), 7.14-7.18 (m, 1H, *p*-C_6H_5), 4.44 (4H, s, PhC*H*$_2$NCH$_2$CH$_2$NMe$_2$), 3.19 (4H, t, *J* = 5.6 Hz, PhCH$_2$NC*H*$_2$CH$_2$NMe$_2$), 2.28 (4H, t, *J* = 5.6 Hz, PhCH$_2$NCH$_2$C*H*$_2$NMe$_2$), 1.97 (12H, s, PhCH$_2$NCH$_2$CH$_2$N*Me*$_2$).

^{13}C{^{1}H} NMR (125.7 MHz, C_6D_6); δ_{ppm} 145.3 (2C, *ipso*-C_6H_5), 128.4 (4C, *m*–C_6H_5), 128.4 (4C, *o*–C_6H_5), 126.3 (2C, *p*–C_6H_5), 60.3 (2C, PhCH$_2$NCH$_2$*C*H$_2$NMe$_2$), 56.6 (2C, Ph*C*H$_2$NCH$_2$CH$_2$NMe$_2$), 50.7 (2C, PhCH$_2$N*C*H$_2$CH$_2$NMe$_2$), 45.1 (4C, PhCH$_2$NCH$_2$CH$_2$N*Me*$_2$).

^{119}Sn NMR (186.3 MHz, C_6D_6); δ_{ppm} 60 (br)

[Sn(deed)DippG] (21)

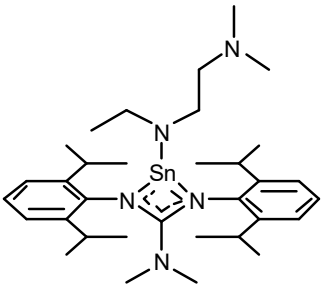

A solution of 2,6-diisopropylphenylcarbodiimide (0.36 g, 1 mmol) in THF (20 ml) was added dropwise to a cooled solution of [Sn(deed)NMe$_2$] **(15)** (0.28 g, 1 mmol) in THF (20 ml) and stirred for 8 h. The volatiles were removed *in vacuo* and orange solid dissolved in hexane before filtration through Celite®. The solvent was reduced, affording orange crystals after storage at –28 °C. (0.29 g, 46%)

^{1}H NMR (500 MHz, C_6D_6); δ_{ppm} 7.15–7.13 (4H, m, *meta*–Phenyl), 7.09–7.04 (4H, m, *para*–Phenyl), 3.91–3.81 (4H, m, –C*H*$(CH_3)_2$), 3.61 (2H, q, *J* = 6.9 Hz, $CH_3CH_2NCH_2CH_2NMe_2$), 3.19–3.13 (2H, m, $CH_3CH_2NCH_2CH_2NMe_2$), 2.16 (6H, s, $CH_3CH_2NCH_2CH_2NMe_2$), 2.13–2.09 (2H, m, $CH_3CH_2NCH_2CH_2NMe_2$), 1.66 (6H, s, *guanidinate*–NMe_2), 1.40 (12H, d, *J* = 6.8 Hz, –CH(CH_3)$_2$), 1.29 (12H, d, *J* = 6.8 Hz, –CH(CH_3)$_2$), 1.25 (3H, t, *J* = 6.9 Hz, $CH_3CH_2NCH_2CH_2NMe_2$).

^{13}C{^{1}H} NMR (125.7 MHz, C_6D_6); δ_{ppm} 161.8 (1C, NCN), 143.7 (2C, *ipso*–Phenyl), 143.4 (2C, *ortho*–Phenyl), 124.0 (2C, *para*–Phenyl), 123.9 (4C, *meta*–Phenyl), 59.5 (1C, $CH_3CH_2NCH_2CH_2NMe_2$), 49.3 (1C, $CH_3CH_2NCH_2CH_2NMe_2$), 46.9 (1C, $CH_3CH_2NCH_2CH_2NMe_2$), 44.2 (2C, *guanidinate*–NMe_2), 39.4 (2C, $CH_3CH_2NCH_2CH_2NMe_2$), 28.2 (4C, –CH(CH_3)$_2$), 26.3 (4C, br, –CH(CH_3)$_2$), 24.0 (4C, –CH(CH_3)$_2$), 17.8 (1C, $CH_3CH_2NCH_2CH_2NMe_2$).

^{119}Sn NMR (186.3 MHz, C_6D_6); δ_{ppm} –145

3.7. References

1 M. Lappert, A. Protchenko, P. Power and A. Seeber, in *Metal Amide Chemistry*, John Wiley & Sons Ltd., Chichester, 2008, 1–6.

2 Y. Yamashita, Y. Saito, T. Imaizumi and S. Kobayashi, *Chem. Sci.*, 2014, **5**, 3958–3962.

3 Y. Yamashita and S. Kobayashi, *Chem. A Eur. J.*, 2013, **19**, 9420–9427.

4 S. Hamura and H. Nagashima, *J. Synth. Org. Chem. Japan*, 1999, **57**, 698–707.

5 H. Chen, M. M. Olmstead, D. C. Pestana and P. P. Power, *Inorg. Chem.*, 1991, **30**, 1783–1787.

6 J. A. Garden and S. D. Pike, *Dalton Trans.*, 2018, **47**, 3638–3662.

7 H. Sigel and R. B. Martin, *Chem. Rev.*, 1982, **82**, 385–426.

8 J. R. Fulton, M. W. Bouwkamp and R. G. Bergman, *J. Am. Chem. Soc.*, 2000, **122**, 8799–8800.

9 H. Cao, Y. Zhang, J. Wang, Z. Xiong, G. Wu and P. Chen, *Prog. Nat. Sci. Mater. Int.*, 2012, **22**, 550–560.

10 P. Chen, Z. Xiong, J. Luo, J. Lin and K. L. Tan, *Nature*, 2002, **420**, 302.

11 M. M. Olmstead and P. P. Power, *Inorg. Chem.*, 1984, **23**, 413–415.

12 A. L. Johnson, Ph.D Thesis, Durham University, 2000.

13 H. E. Bryndza, P. J. Domaille, W. Tam, L. K. Fong, R. A. Paciello and J. E. Bercaw, *Polyhedron*, 1988, **7**, 1441–1452.

14 T. Fjeldberg, H. Hope, M. F. Lappert, P. P. Power and A. J. Thorne, *J. Chem. Soc. Chem. Comm.*, 1983, 639–641.

15 A. Devi, *Coord. Chem. Rev.*, 2013, **257**, 3332–3384.

16 T. Blanquart, J. Niinistö, M. Gavagnin, V. Longo, V. R. Pallem, C. Dussarrat, M. Ritala and M. Leskelä, *Chem. Mater.*, 2012, **24**, 3420–3424.

17 M. Reiners, K. Xu, N. Aslam, A. Devi, R. Waser and S. Hoffmann-Eifert, *Chem. Mater.*, 2013, **25**, 2934–2943.

18 M. Kaipio, T. Blanquart, M. Banerjee, K. Xu, J. Niinistö, V. Longo, K. Mizohata, A. Devi, M. Ritala and M. Leskelä, *Chem. Vap. Deposition*, 2014, **20**, 209–216.

19 M. Seo, Y.-S. Min, S. K. Kim, T. J. Park, J. H. Kim, K. D. Na and C. S. Hwang, *J. Mater. Chem.*, 2008, **18**, 4324.

20 K. Xu, A. P. Milanov, H. Parala, C. Wenger, C. Baristiran-Kaynak, K. Lakribssi, T. Toader, C. Bock, D. Rogalla, H.-W. Becker, U. Kunze and A. Devi, *Chem. Vap. Deposition*, 2012, **18**, 27–35.

21 T. Blanquart, J. Niinistö, N. Aslam, M. Banerjee, Y. Tomczak, M. Gavagnin, V. Longo, E. Puukilainen, H. D. Wanzenboeck, W. M. M. Kessels, A. Devi, S. Hoffmann-Eifert, M. Ritala and M. Leskelä, *Chem. Mater.*, 2013, **25**, 3088–3095.

22 T. Blanquart, J. Niinistö, M. Gavagnin, V. Longo, M. Heikkilä, E. Puukilainen, V. R. Pallem, C. Dussarrat, M. Ritala and M. Leskelä, *RSC Adv.*, 2013, **3**, 1179–1185.

23 G. Rampelberg, M. Schaekers, K. Martens, Q. Xie, D. Deduytsche, B. De Schutter, N. Blasco, J. Kittl and C. Detavernier, *Appl. Phys. Lett.*, 2011, **98**, 162902.

24 T. Blanquart, J. Niinistö, M. Heikkilä, T. Sajavaara, K. Kukli, E. Puukilainen, C. Xu, W. Hunks, M. Ritala and M. Leskelä, *Chem. Mater.*, 2012, **24**, 975–980.

25 D. M. Hausmann, P. de Rouffignac, A. Smith, R. Gordon and D. Monsma, *Thin Solid Films*, 2003, **443**, 1–4.

26 T. Blanquart, V. Longo, J. Niinistö, M. Heikkilä, K. Kukli, M. Ritala and M. Leskelä, *Semicond. Sci. Technol.*, 2012, **27**, 74003.

27 M. Lukas, G. Maximilian, de los A. Teresa, G. Ignacio, M. Felix, W. Manuela, P. Harish, A. Peter, G. Guido and D. Anjana, *Chem. Eur. J.*, 2017, **23**, 10768–10772.

28 D. Kim, T. Nam, J. Park, J. Gatineau and H. Kim, *Thin Solid Films*, 2015, **587**, 83–87.

29 W. Jang, H. Kim, Y. Kweon, C. Jung, H. Cho, S. Shin, H. Kim, K. Lim, H. Jeon and H. Lim, *J. Vac. Sci. Technol. A*, 2018, **36**, 031514.

30 L. Huang, B. Han, M. Fan and H. Cheng, *RSC Adv.*, 2017, **7**, 22672–22678.

31 V. Miikkulainen, M. Leskelä, M. Ritala and R. L. Puurunen, *J. Appl. Phys.*, 2013, **113**, 021301.

32 T. Hatanpää, M. Ritala and M. Leskelä, *Coord. Chem. Rev.*, 2013, **257**, 3297–3322.

33 B. Lee, K. J. Choi, A. Hande, M. J. Kim, R. M. Wallace, J. Kim, Y. Senzaki, D. Shenai, H. Li, M. Rousseau and J. Suydam, *Microelectron. Eng.*, 2009, **86**, 272–276.

34 X. Lou, H. Zhou, S. B. Kim, S. Alghamdi, X. Gong, J. Feng, X. Wang, P. D. Ye and R. G. Gordon, *Nano Lett.*, 2016, **16**, 7650–7654.

35 A. R. Sadique, M. J. Heeg and C. H. Winter, *Inorg. Chem.*, 2001, **40**, 6349–6355.

36 S. B. Kim, C. Yang, T. Powers, L. M. Davis, X. Lou and R. G. Gordon, *Angew. Chem, Int. Ed.*, 2016, **55**, 10228–10233.

37 M. S. Weimer, I. S. Kim, P. Guo, R. D. Schaller, A. B. F. Martinson and A. S. Hock, *Chem. Mater.*, 2017, **29**, 6238–6244.

38 M. S. Weimer, R. F. McCarthy, J. D. Emery, M. J. Bedzyk, F. G. Sen, A. Kinaci, M. K. Y. Chan, A. S. Hock and A. B. F. Martinson, *Chem. Mater.*, 2017, **29**, 2864–2873.

39 R. F. McCarthy, M. S. Weimer, R. T. Haasch, R. D. Schaller, A. S. Hock and A. B. F. Martinson, *Chem. Mater.*, 2016, **28**, 2033–2040.

40 A. R. Mouat, A. U. Mane, J. W. Elam, M. Delferro, T. J. Marks and P. C. Stair, *Chem. Mater.*, 2016, **28**, 1907–1919.

41 T. Jurca, A. W. Peters, A. R. Mouat, O. K. Farha, J. T. Hupp, T. L. Lohr, M. Delferro and T. J. Marks, *Dalton Trans.*, 2017, **46**, 1172–1178.

42 P. Sinsermsuksakul, J. Heo, W. Noh, A. S. Hock and R. G. Gordon, *Adv. Energy Mater.*, 2011, **1**, 1116–1125.

43 Y. Tomczak, K. Knapas, M. Leskelä and M. Ritala, *J. Vac. Sci. Technol. A*, 2014, **32**, 01A121.

44 P. de Rouffignac, A. P. Yousef, K. H. Kim and R. G. Gordon, *Electrochem. Solid-State Lett.*, 2006, **9**, F45.

45 T. Hatanpää, K. Kukli, M. Ritala and M. Leskelä, *J. Therm. Anal. Calorim.*, 2011, **105**, 61–71.

46 S. Dueñas, H. Castán, H. García, A. Gómez, L. Bailón, K. Kukli, T. Hatanpää, J. Lu, M. Ritala and M. Leskelä, *J. Electrochem. Soc.*, 2007, **154**, G207.

47 P. de Rouffignac, J.-S. Park and R. G. Gordon, *Chem. Mater.*, 2005, **17**, 4808–4814.

48 I.-S. Park, Y. Chan Jung, S. Seong, J. Ahn, J. Kang, W. Noh and C. Lansalot-Matras, *J. Mater. Chem. C*, 2014, **2**, 9240–9247.

49 S. Seppälä, J. Niinistö, T. Blanquart, M. Kaipio, K. Mizohata, J. Räisänen, C. Lansalot-Matras, W. Noh, M. Ritala and M. Leskelä, *Chem. Mater.*, 2016, **28**, 5440–5449.

50 I.-K. Oh, K. Kim, Z. Lee, K. Y. Ko, C.-W. Lee, S. J. Lee, J. M. Myung, C. Lansalot-Matras, W. Noh, C. Dussarrat, H. Kim and H.-B.-R. Lee, *Chem. Mater.*, 2015, **27**, 148–156.

51 B. S. Lim, A. Rahtu and R. G. Gordon, *Nat. Mater.*, 2003, **2**, 749–754.

52 J. Päiväsaari, C. L. Dezelah, IV, D. Back, H. M. El-Kaderi, M. J. Heeg, M. Putkonen, L. Niinistö and C. H. Winter, *J. Mater. Chem.*, 2005, **15**, 4224.

53 Z. Guo and X. Wang, *Angew. Chemie Int. Ed.*, 2018, **57**, 5898–5902.

54 Y. Çimen, A. W. Peters, J. R. Avila, W. L. Hoffeditz, S. Goswami, O. K. Farha and J. T. Hupp, *Langmuir*, 2016, **32**, 12005–12012.

55 H. Li, Y. Shao, Y. Su, Y. Gao and X. Wang, *Chem. Mater.*, 2016, **28**, 1155–1164.

56 T. D.-M. Elko-Hansen and J. G. Ekerdt, *Chem. Mater.*, 2014, **26**, 2642–2646.

57 T. D.-M. Elko-Hansen, A. Dolocan and J. G. Ekerdt, *J. Phys. Chem. Lett.*, 2014, **5**, 1091–1095.

58 H. Li, Y. Gao, Y. Shao, Y. Su and X. Wang, *Nano Lett.*, 2015, **15**, 6689–6695.

59 M. K. Wiedmann, M. C. Karunarathne, R. J. Baird and C. H. Winter, *Chem. Mater.*, 2010, **22**, 4400–4405.

60 L. Mai, N. Boysen, E. Subaşı, T. de los Arcos, D. Rogalla, G. Grundmeier, C. Bock, H.-L. Lu and A. Devi, *RSC Adv.*, 2018, **8**, 4987–4994.

61 L. Mai, Z. Giedraityte, M. Schmidt, D. Rogalla, S. Scholz, A. D. Wieck, A. Devi and M. Karppinen, *J. Mater. Sci.*, 2017, **52**, 6216–6224.

62 M. Gebhard, M. Hellwig, H. Parala, K. Xu, M. Winter and A. Devi, *Dalton Trans.*, 2014, **43**, 937–940.

63 S. Jung, D. K. Nandi, S. Yeo, H. Kim, Y. Jang, J.-S. Bae, T. E. Hong and S.-H. Kim, *Surf. Coatings Technol.*, 2018, **337**, 404–410.

64 J. P. Klesko, M. M. Kerrigan and C. H. Winter, *Chem. Mater.*, 2016, **28**, 700–703.

65 M. M. Kerrigan, J. P. Klesko, K. J. Blakeney and C. H. Winter, *ACS Appl. Mater. Interfaces*, 2018, **10**, 14200–14208.

66 K. Väyrynen, T. Hatanpää, M. Mattinen, M. Heikkilä, K. Mizohata, K. Meinander, J. Räisänen, M. Ritala and M. Leskelä, *Chem. Mater.*, 2018, **30** (10), 3499-3507.

67 T. Haenninen, I. Mutikainen, V. Saanila, M. Ritala, M. Leskelae and J. C. Hanson, *Chem. Mater.*, 1997, **9**, 1234–1240.

68 T. Chlupatý, Z. Padělková, F. DeProft, R. Willem and A. Růžička, *Organometallics*, 2012, **31**, 2203–2211.

69 I. Y. Ahmet, M. S. Hill, P. R. Raithby and A. L. Johnson, *Dalton Trans.*, 2018, **47**, 5031–5048.

70 T. Wildsmith, M. S. Hill, A. L. Johnson, A. J. Kingsley and K. C. Molloy, *Chem. Commun.*, 2013, **49**, 8773–8775.

71 I. Y. Ahmet, M. S. Hill, A. L. Johnson and L. M. Peter, *Chem. Mater.*, 2015, **27**, 7680–7688.

72 I. Y. Ahmet, J. R. Thompson and A. L. Johnson, *Eur. J. Inorg. Chem.*, 2018, **2018**, 1670–1678.

73 M. N. Mullings, C. Hägglund and S. Bent, *J. Vac. Sci. Technol. A*, 2013, **31**, 061503.

74 D. W. Choi, W. J. Maeng and J. S. Park, *Appl. Surf. Sci.*, 2014, **313**, 585–590.

75 J. Elam, D. A. Baker, A. J. Hryn, A. Martinson, M. Pellin and J. Hupp, *J. Vac. Sci. Technol. A,* 2008, **26**, 244-252

76 N. P. Dasgupta, X. Meng, J. W. Elam and A. B. F. Martinson, *Acc. Chem. Res.*, 2015, **48**, 341–348.

77 G. Ham, S. Shin, J. Park, H. Choi, J. Kim, Y.-A. Lee, H. Seo and H. Jeon, *ACS Appl. Mater. Interfaces*, 2013, **5**, 8889–8896.

78 S. B. Kim, P. Sinsermsuksakul, A. S. Hock, R. D. Pike and R. G. Gordon, *Chem. Mater.*, 2014, **26**, 3065–3073.

79 J. Heo, A. S. Hock and R. G. Gordon, *Chem. Mater.*, 2010, **22**, 4964–4973.

80 J. Heo, S. B. Kim and R. G. Gordon, *J. Mater. Chem.*, 2012, **22**, 4599–4602.

81 P. Sinsermsuksakul, J. Heo, W. Noh, A. S. Hock and R. G. Gordon, *Adv. Energy Mater.*, 2011, **1**, 1116–1125.

82 J. Tupala, M. Kemell, M. Mattinen, K. Meinander, S. Seppälä, T. Hatanpää, J. Räisänen, M. Ritala and M. Leskelä, *J. Vac. Sci. Technol. A*, 2017, **35**, 41506.

83 L. L. Crowe and L. M. Tolbert, *Langmuir*, 2008, **24**, 8541–8546.

84 I. Y. Ahmet, Ph.D. Thesis, University of Bath, 2016

85 R. O' Donoghue, D. Peeters, D. Rogalla, H.-W. Becker, J. Rechmann, S. Henke, M. Winter and A. Devi, *Dalton Trans.*, 2016, **45**, 19012–19023.

86 Z. Li, A. Rahtu and R. G. Gordon, *J. Electrochem. Soc.*, 2006, **153**, C787.

87 M. Cossi, N. Rega, G. Scalmani and V. Barone, *J. Comput. Chem.*, 2003, **24**, 669–681.

88 G. Scalmani and M. J. Frisch, *J. Chem. Phys.*, 2010, **132**, 114110.

89 D. M. York and M. Karplus, *J. Phys. Chem. A*, 1999, **103**, 11060–11079.

90 J. A. Caraveo-Frescas, P. K. Nayak, H. A. Al-Jawhari, D. B. Granato, U. Schwingenschlögl and H. N. Alshareeft, *ACS Nano*, 2013, **7**, 5160–5167.

91 J. H. Han, Y. J. Chung, B. K. Park, S. K. Kim, H. S. Kim, C. G. Kim and T. M. Chung, *Chem. Mater.*, 2014, **26**, 6088–6091.

92 T. Eom, T. Gwon, S. Yoo, B. J. Choi, M.-S. Kim, I. Buchanan, M. Xiao and C. S. Hwang,

Chem. Mater., 2014, **26**, 1583–1591.

93 R. Timm, A. R. Head, S. Yngman, J. V Knutsson, M. Hjort, S. R. McKibbin, A. Troian, O. Persson, S. Urpelainen, J. Knudsen, J. Schnadt and A. Mikkelsen, *Nat. Commun.*, 2018, **9**, 1412.

94 E. Lindahl, M. Ottosson and J.-O. Carlsson, *Chem. Vap. Deposition*, 2009, **15**, 186–191.

95 S. J. Song, S. W. Lee, G. H. Kim, J. Y. Seok, K. J. Yoon, J. H. Yoon, C. S. Hwang, J. Gatineau and C. Ko, *Chem. Mater.*, 2012, **24**, 4675–4685.

96 S. H. Kim, I.-H. Baek, D. H. Kim, J. J. Pyeon, T.-M. Chung, S.-H. Baek, J.-S. Kim, J. H. Han and S. K. Kim, *J. Mater. Chem. C*, 2017, **5**, 3139–3145.

97 D. R. Dreyer, S. Park, C. W. Bielawski and R. S. Ruoff, *Chem. Soc. Rev.*, 2010, **39**, 228–240.

98 Z. Liu, J. Liu, D. Li, P. S. Francis, N. W. Barnett, C. J. Barrow and W. Yang, *Chem. Commun.*, 2015, **51**, 10969–10972.

99 S.-C. Wang and M. Shaikh, *Sensors*, 2015, **15**, 14286–14297.

100 K. J. Saji, K. Tian, M. Snure and A. Tiwari, *Adv. Electron. Mater.*, 2016, **2**, 1500453.

101 J.-M. Themlin, M. Chtaïb, L. Henrard, P. Lambin, J. Darville and J.-M. Gilles, *Phys. Rev. B*, 1992, **46**, 2460–2466.

102 L. Kövér, Z. Kovács, R. Sanjinés, G. Moretti, I. Cserny, G. Margaritondo, J. Pálinkás and H. Adachi, *Surf. Interface Anal.*, 2018, **23**, 461–466.

103 S. Axnanda, W.-P. Zhou and M. G. White, *Phys. Chem. Chem. Phys.*, 2012, **14**, 10207.

104 J. Szuber, G. Czempik, R. Larciprete, D. Koziej and B. Adamowicz, *Thin Solid Films*, 2001, **391**, 198–203.

105 U. Berg, T. Chassé and O. Brümmer, *Phys. Status Solidi*, 2018, **108**, 507–510.

106 P. Hanyš, P. Janeček, V. Matolı´n, G. Korotcenkov and V. Nehasil, *Surf. Sci.*, 2006, **600**, 4233–4238.

107 M. Fujishima, Q. Jin, H. Yamamoto, H. Tada and M. Nolan, *Phys. Chem. Chem. Phys.*, 2012, **14**, 705–711.

108 M. Chen, D. Chao, J. Liu, J. Yan, B. Zhang, Y. Huang, J. Lin and Z. X. Shen, *Adv. Funct. Mater.*, 2017, **27**, 1606232.

109 L. Y. Liang, Z. M. Liu, H. T. Cao and X. Q. Pan, *ACS Appl. Mater. Interfaces*, 2010, **2**, 1060–1065.

110 Y. Ogo, H. Hiramatsu, K. Nomura, H. Yanagi, T. Kamiya, M. Hirano and H. Hosono, *Appl. Phys. Lett.*, 2008, **93**, 32113.

111 J. Watson, *Sensors and Actuators*, 1984, **5**, 29–42.

112 D. V Nazarov, N. P. Bobrysheva, O. M. Osmolovskaya, M. G. Osmolovsky and V. M. Smirnov, *Rev. Adv. Mater. Sci.*, 2015, **40**, 262–275.

113 Y. Yuan, Y. Wang, M. Wang, J. Liu, C. Pei, B. Liu, H. Zhao, S. Liu and H. Yang, *Sci. Rep.*, 2017, **7**, 1231.

114 X. Chu, X. Zhu, Y. Dong, W. Zhang and L. Bai, *J. Mater. Sci. Technol.*, 2015, **31**, 913–

917.
115 L. Li, C. Zhang and W. Chen, *Nanoscale*, 2015, **7**, 12133–12142.
116 F. Zhang, J. Zhu, D. Zhang, U. Schwingenschlögl and H. N. Alshareef, *Nano Lett.*, 2017, **7** (2), 1302-1311.
117 J. H. Shin and J. Y. Song, *Nano Converg.*, 2016, **3**, 9.
118 X. Li, X. Meng, J. Liu, D. Geng, Y. Zhang, M. N. Banis, Y. Li, J. Yang, R. Li, X. Sun, M. Cai and M. W. Verbrugge, *Adv. Funct. Mater.*, 2012, **22**, 1646–1646.
119 J. S. Chen and X. W. Lou, *Mater. Today*, 2012, **15**, 246–254.
120 Y. Wang, J. Ding, Y. Liu, Y. Liu, Q. Cai and J. Zhang, *Ceram. Int.*, 2015, **41**, 15145–15152.
121 S. Kim, S.-K. Kim, P. Sun, N. Oh and P. V Braun, *Nano Lett.*, 2017, **17**, 6893–6899.
122 C. Zhao, H. Gao, C. Chen and H. Wu, *J. Mater. Chem. A*, 2015, **3**, 18360–18364.
123 Z. Yao, X. Xia, Y. Zhong, Y. Wang, B. Zhang, D. Xie, X. Wang, J. Tu and Y. Huang, *J. Mater. Chem. A*, 2017, **5**, 8916–8921.
124 X. Wang, X. Zhou, K. Yao, J. Zhang and Z. Liu, *Carbon N. Y.*, 2011, **49**, 133–139.
125 C. Zhu, Z. Chen, S. Zhu, Y. Li, H. Pan, X. Meng, M. Imtiaz and D. Zhang, *Sci. Rep.*, 2017, **7**, 3276.
126 M. Xie, X. Sun, S. M. George, C. Zhou, J. Lian and Y. Zhou, *ACS Appl. Mater. Interfaces*, 2015, **7**, 27735–27742.
127 L. Liu, M. An, P. Yang and J. Zhang, *Sci. Rep.*, 2015, **5**, 9055.
128 X. Li, J. Liu, M. N. Banis, A. Lushington, R. Li, M. Cai and X. Sun, *Energy Environ. Sci.*, 2014, **7**, 768–778.
129 B. Wang, J. Liu, M. Norouzi Banis, Q. Sun, Y. Zhao, R. Li, T.-K. Sham and X. Sun, *ACS Appl. Mater. Interfaces*, 2017, **9**, 31786–31793.
130 E. Kessels, H. Knoops, M. Weber, A. Mackus and M. Creatore, *Mater. Matters*, 2013, **8**, 117–120.
131 J. W. Elam, N. P. Dasgupta and F. B. Prinz, *MRS Bull.*, 2011, **36**, 899–906.
132 Q. G. and G. W. and A. K. and R. Pandey, *Nanotechnology*, 2017, **28**, 475708.
133 Y. Cheng, J. Huang, J. Li, L. Cao and H. Qi, *Micro Nano Lett.*, 2018, **13**, 257–260.
134 P. H. Suman, A. A. Felix, H. L. Tuller, J. A. Varela and M. O. Orlandi, *Sensors Actuators B Chem.*, 2015, **208**, 122–127.
135 S. Seal and S. Shukla, *JOM*, 2002, **54**, 35–38.
136 M. S. Barbosa, P. H. Suman, J. J. Kim, H. L. Tuller, J. A. Varela and M. O. Orlandi, *Sensors Actuators B*, 2017, **239**, 253–261.
137 A. Nag, A. Mitra and S. C. Mukhopadhyay, *Sensors Actuators A*, 2018, **270**, 177–194.
138 R. Bogue, *Sens. Rev.*, 2014, **34**, 233–238.
139 H. Mu, K. Wang, Z. Zhang and H. Xie, *J. Phys. Chem. C.*, 2015, **119**, 10102–10108.
140 H. Mu, K. Wang and H. Xie, *J. Mater. Res.*, 2016, **31**, 1993–2003.
141 Q. Guo, G. Wang, R. Pandey and S. P. Karna, *Phys. Chem. Chem. Phys.*, 2018, **20**, 17983–17989.

142 R. H. J. Vervuurt, W. M. M. Kessels and A. A. Bol, *Adv. Mater. Interfaces*, 2017, **4**, 1700232.

143 R. H. J. Vervuurt, B. Karasulu, M. A. Verheijen, W. M. M. Kessels and A. A. Bol, *Chem. Mater.*, 2017, **29**, 2090–2100.

144 R. Rammula, L. Aarik, A. Kasikov, J. Kozlova, T. Kahro, L. Matisen, A. Niilisk, H. Alles and J. Aarik, *IOP Conf. Ser. Mater. Sci. Eng.*, 2013, **49**, 012014.

145 L. Zheng, X. Cheng, D. Cao, G. Wang, Z. Wang, D. Xu, C. Xia, L. Shen, Y. Yu and D. Shen, *ACS Appl. Mater. Interfaces*, 2014, **6**, 7014–7019.

146 N. Y. Garces, V. D. Wheeler, J. K. Hite, G. G. Jernigan, J. L. Tedesco, N. Nepal, C. R. Eddy and D. K. Gaskill, *J. Appl. Phys.*, 2011, **109**, 124304.

147 X. Tang, N. Reckinger, O. Poncelet, P. Louette, F. Ureña, H. Idrissi, S. Turner, D. Cabosart, J.-F. Colomer, J.-P. Raskin, B. Hackens and L. A. Francis, *Sci. Rep.*, 2015, **5**, 13523.

148 A. C. Ferrari and D. M. Basko, *Nat. Nanotechnol.*, 2013, **8**, 235.

149 A. C. Ferrari, *Solid State Commun.*, 2007, **143**, 47–57.

150 H. Yabuta, N. Kaji, R. Hayashi, H. Kumomi, K. Nomura, T. Kamiya, M. Hirano and H. Hosono, *Appl. Phys. Lett.*, 2010, **97**, 72111.

151 P.-C. Hsu, C.-J. Hsu, C.-H. Chang, S.-P. Tsai, W.-C. Chen, H.-H. Hsieh and C.-C. Wu, *ACS Appl. Mater. Interfaces*, 2014, **6**, 13724–13729.

152 E. Fortunato, R. Barros, P. Barquinha, V. Figueiredo, S.-H. K. Park, C.-S. Hwang and R. Martins, *Appl. Phys. Lett.*, 2010, **97**, 52105.

153 J. H. Han, Y. J. Chung, B. K. Park, S. K. Kim, H.-S. Kim, C. G. Kim and T.-M. Chung, *Chem. Mater.*, 2014, **26**, 6088–6091.

Chapter 4

Chapter 4: Tin(II) Alkoxides

4.1. Introduction

4.1.1. Background

A more comprehensive overview of alkoxide chemistry can be found in Chapter 2, where relevant discussion of alkoxide bonding, synthesis and reactivity was given, with direct relevance to the amino-functionalised alkoxides discussed therein. After identification of the limitations within alkoxide systems, focus was directed towards the incorporation of a range of substituents to alter various properties, such as reactivity, volatility and tendency towards oligomerisation.

This short chapter seeks to give a brief overview of an avenue of research hitherto overlooked in the field of atomic layer deposition, despite extensive work having been undertaken on the underpinning chemistry.

A great deal of attention was drawn in Chapter 2 to the oligomeric tendencies of alkoxide species, whereby electropositive metal centres and electron-dense oxygen atoms were thermodynamically driven to form oxygen bridged structures.[1–4] Work by Bradley in 1958 postulated that metal alkoxide compounds adopt the smallest possible structural unit in which all metal atoms have assumed a higher coordination number than in the base unit.[5] This donation of electron density by the coordinated oxygen atoms is thought to be largely responsible for the lower than expected polarity observed in M–O bonding.[6] Nevertheless, the electropositivity of the metal atom leaves it highly susceptible to nucleophilic attack, leading a range of potential reactions.[3]

Of these reactions, alcoholysis is commonplace and indeed a useful method of alkoxide synthesis, whereby alcohols of a higher acidity displace those less acidic. It is thought that this process proceeds via a four-membered transition state, with the more acidic alcohol coordinating to the metal centre whilst protonating the already-bound alkoxide ligand.[6]

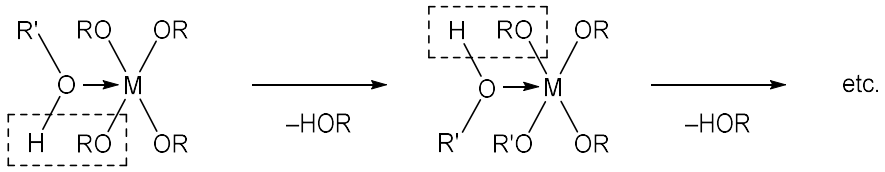

Scheme 4.1 – Alcoholysis of metal alkoxide species.[6]

The thermodynamic drive for higher coordination within the chemistry of alkoxides leads inevitably to the ready formation of cluster species. The latter have become so ubiquitous that their wealth of chemistry rivals that of the base alkoxides.[1,7] Applications are almost as broad as those of metal alkoxides themselves, including materials deposition[8–10], ceramics[11,12] and catalysis.[4,13–15] The facile formation of cluster species poses a considerable challenge when considering the use of metal alkoxides in many fields. Metal alkoxide complexes are susceptible to a number of decomposition pathways, many of which result in the formation of higher nuclearity clusters or metal oxide precipitates.[1–3,16]

Given the lability of alkoxide ligands in the presence of alcoholic groups of greater acidity, hydrolysis of metal alkoxides by latent H_2O or exposure to moisture results in the displacement and protonation of alcohol in favour of the metal hydroxide (Scheme 4.2a). This likely occurs through the same four-membered transition state depicted in Scheme 4.1. After initial hydrolysis, subsequent dehydration or dealkoxylation reactions have been shown to occur, with the former in particular driving further hydrolysis due to the elimination of H_2O (Scheme 4.2b and c). Both reactions follow a similar pathway, with the metal hydroxide protonating and eliminating either a second hydroxide (in the case of dehydration), or an alkoxide ligand (in the case of dealkoxylation). In both cases, a M–O–M bond is formed, alongside the formation of H_2O or HOR respectively.[2,6]

a) Hydrolysis: $M(OR)_n + HOH \rightleftharpoons M(OR)_{n-1}(OH) + ROH$

b) Dehydration: $(RO)_{n-1}MOH + HOM(OR)_{n-1} \rightleftharpoons (RO)_{n-1}M{-}O{-}M(OR)_{n-1} + H_2O$

c) Dealkoxylation: $(RO)_{n-1}MOH + (RO)M(OR)_{n-1} \rightleftharpoons (RO)_{n-1}M{-}O{-}M(OR)_{n-1} + ROH$

Scheme 4.2 – Hydrolysis (a), dehydration (b) and dealkoxylation (c) of alkoxides.

It has also been demonstrated that even under the most anhydrous conditions, metal alkoxides are capable of the self-formation of oxo-species by the elimination of ether (Scheme 4.3a).[2] Of particular relevance to this research, alkoxide-based ALD precursors such as $[Nb(OEt)_5]$ have also been shown to self-eliminate ether. Similarly, ß-hydride elimination has also been observed within metal alkoxide species, leading to the elimination of alcohol and alkene species (Scheme 4.3b).[17,18] The longevity of many alkoxide species has also been proven to be limited, with many displaying signs of "ageing". This has been shown in $[Al(O^iPr)_3]$ species, which exists as a dimer in the vapour phase, before distilling as a trimeric liquid before aggregating over time into stable tetrameric form.[6,19,20]

a) Ether elimination: $2\ M{-}OR \longrightarrow M{-}O{-}M + R_2O$

b) Alkene elimination: $M(OR)_2 \longrightarrow MO + ROH + R'$

(where R' = alkene formed from R via β–hydride elimination)

Scheme 4.3 – a) Self-elimination of ether within alkoxide compounds, and b) alkene formation via ß-hydride elimination.

4.1.2. Simple Alkoxides as Precursors

Alkoxide compounds have long been adopted as low-pressure and aerosol-assisted chemical vapour deposition precursors, exhibiting generally good volatility and solubility in a number of organic solvents. The thermal decomposition of the alkoxide ligand in many cases yields M–O bonds, leading to a wealth of literature on the deposition of metal oxide films from alkoxide precursors.[21,22]

The application of metal alkoxide compounds as single-source precursors for CVD has been shown for a range of metal oxide materials, from simple binary systems such as CeO_2,[23] HfO_2[24,25] and ZrO_2,[26,27] to multinary oxides such as $SrTaNbO_x$.[28] Much less commonly, decomposition of metal alkoxide compounds has been shown to yield metallic films, as seen in the case of the copper(I) tetramer $[Cu(O^tBu)]_4$. Judicious control over H_2O concentration was shown to result in either Cu(0) or CuO films by Jeffries and Girolami via an LP-CVD process.[29,30]

Similarly well-established is the use of alkoxide species in atomic layer deposition. Aside from the plethora of multidentate alkoxide species catalogued, the simple alkoxides play a significant part in industrial ALD processes for metal oxide materials. H_2O-based ALD processes for a large number of metal alkoxides have been reported, including Ti,[31,32] V,[33,34] Al,[35] B,[36,37] Ga,[38] Si[39,40] and Zr,[41] and extend to many of the rare earth elements as well, forming oxides of yttrium, gadolinium, lanthanum and praseodymium.[42,43]

Interestingly, ALD has also been reported for a number of the alkali metals using alkoxide precursors. With the predictably oligomeric structures associated with highly ionic, monovalent alkoxide species, it is surprising that adequate volatility is achieved with compounds such as lithium tert-butoxide, which exists as a hexamer in the solid state.[44,45] Deposition has been reported with the tertiary butoxides of lithium, sodium, potassium and rubidium by a number of studies.[46–50]

4.1.3. Tin(II) Alkoxides

The chemistry of tin(II) alkoxides is, to a large degree, interwoven with that of the related hydrolysis products. The high susceptibility to hydrolysis has led to a wealth of studies into the use of tin(II) alkoxides as routes towards cluster species, of a similar form to those mentioned in Chapter 2.[51,52] The presence of oxo-cluster side-products after synthesis of tin(II) alkoxides is similarly well-documented, with many cage-like clusters of the form $[Sn_6(\mu\text{-}O)_4(\mu\text{-}OR)_4]$ formed during and after synthesis of simple alkoxides.[9,53,54]

Though presenting as a compound of reasonable volatility despite its polymeric nature, $[Sn(O^iPr)_2]_\infty$ is limited in its application to thermal materials chemistry. A prior observation[55] of a tendency to self-degrade through ß-hydride transfer to eliminate acetone and isopropanol, was supported by an LP-CVD study by Caulton et al,[56] which found films of tin metal were deposited at temperatures of 295 °C, with only acetone and HO^iPr observed as volatile by-products.

Precedent was however set for the use of simple tin(II) alkoxides in the deposition of SnO by Hill and co-workers, in a publication that characterised a series of homoleptic alkoxide species of the form $[Sn(OR)_2]$ (where R = ^{i}Pr, ^{t}Bu, $C(CH_3)CH_2CH_3$, $CHPh_2$ and CPh_3). Subsequent AA-CVD studies were undertaken, with films of SnO successfully deposited at temperatures >250 °C and >350 °C with $[Sn(O^iPr)_2]$ and $[Sn(O^tBu)_2]$ respectively.[57] A previous LP-CVD study by Boyle et al. applied the polymeric $[Sn(OCH_2CMe_3)_2]_\infty$ to the deposition of tin oxide, instead forming a mixed phase material comprising SnO, Sn_2O_3, SnO_2 and Sn(0).[58]

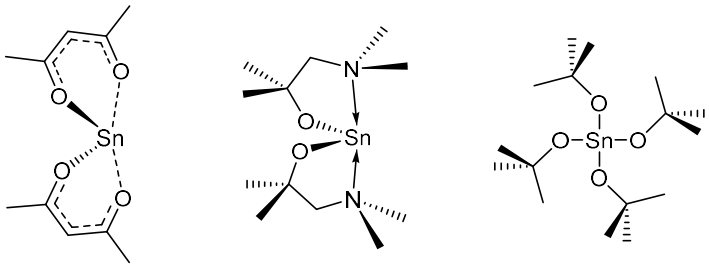

Figure 4.1 – ALD precursors containing Sn–O bonds.

Whilst a substantial range of simple tin(II) alkoxide species are known and characterised, the application of these species to atomic layer deposition has surprisingly been overlooked to date. Whilst the only example of a successful tin(II) oxide ALD precursor, $[Sn(dmamp)_2]$, has been extensively covered throughout this work, two additional compounds are worthy of a brief note during a discussion on tin alkoxide ALD precursors.

Serving merely as an example of the importance of astute ligand selection amongst oxygen-based systems, $[Sn\{OC(Me)CHC(Me)=O\}_2]$, or $[Sn(acac)_2]$, provides an interesting case study. As only the second example of an M–O based precursor comprising a tin(II) centre, its complete lack of reactivity towards H_2O and oxygen is in complete contrast to the successful H_2O-based ALD achieved using $[Sn(dmamp)_2]$. Consequently, only Sn(IV) oxide films were produced through reaction of $[Sn(acac)_2]$ and ozone, despite the initial tin(II) oxidation state within the precursor.[59]

The only example of a simple tin alkoxide species having been applied to ALD is found in the form of tin(IV) tert-butoxide, which has been shown to deposit SnO_2 films at temperatures as low as 70 °C when reacted in an ALD adaption of a sol-gel route using acetic acid as the

oxygen source.[60] Reactions in this manner proceed through the elimination of alcohol by carboxylic acid in the first step, followed by elimination of an ester on the second pulse of alkoxide complex (Scheme 4.4). These non-hydrolytic routes avoid any –O–H terminations and eliminate the interaction of H_2O with the substrate and film, whilst additionally negating the necessity for harsher oxidants. Similar routes have also been shown to be successful for titanium, hafnium and vanadium oxides.[61,62]

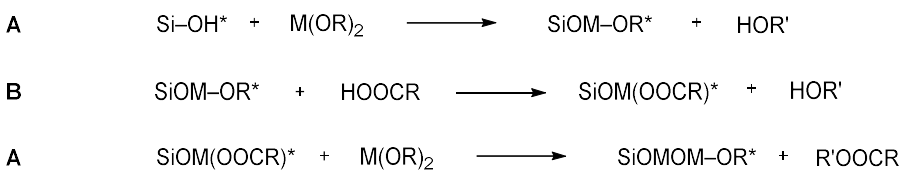

*Scheme 4.4 – Carboxylic acid-based ALD half reactions. Sequential pulses of A – M(OR) and B – HOOCR. *Denotes surface bound species.*

4.1.4. Target Compounds

A range of known and novel tin(II) alkoxides were targeted in order to attempt to discover a precursor of suitable reactivity, stability and volatility to be taken forward to ALD trials. Simple species based on the alkoxide derivatives of isopropanol, tert-butanol, sec-butanol, 3-methyl-2-butanol and 2-methyl-2-butanol were investigated due to their high likelihood of volatility and reactivity. In addition to their respective properties and tendency towards oligomerisation, the ALD efficacy of these series was of interest, with particular focus on the nature of the C(1) environment of the alcohol and its effect, if any, on reactivity and ALD activity.

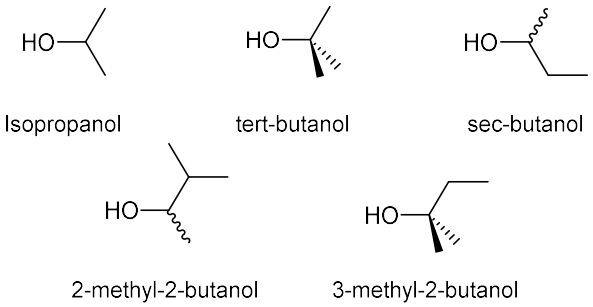

Figure 4.2 – Target alcoholic pro-ligands

4.2. Sn(II) Alkoxides: Synthesis and Characterisation

4.2.1. Synthesis of Simple Alkoxides

Given the enhanced stability of the Sn–O bond over that of the Sn–N, tin(II) alkoxides are readily synthesised through direct amide ligand displacement reactions. Such procedures were adopted in this investigation, though a number of other more cost-effective routes exist, should a larger scale production of material become necessary. One such technique is the elimination of existing alkoxide ligands by more acidic alcohols. The equilibrium formed between the two alcohols can be driven by distillation of the displaced alcohol. Additional routes include the direct salt metathesis using a lithiated alkoxide and a tin(II) halide. Schematics for these methods of synthesis can be found in Chapter 2, Scheme 2.1.[3,16]

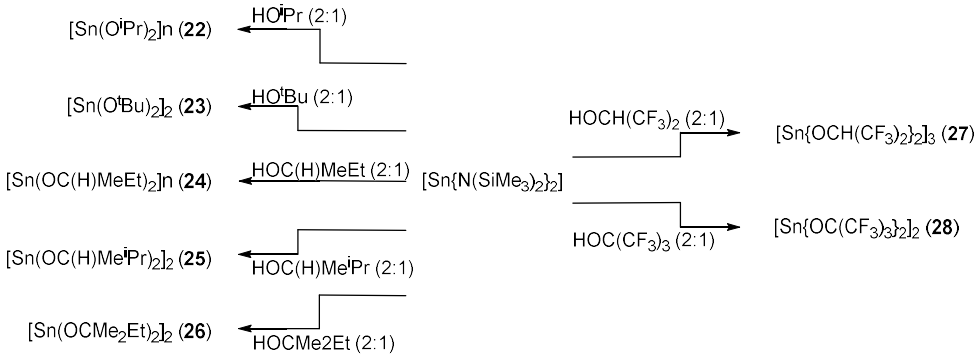

*Scheme 4.5 – Synthetic routes to complexes **22-28**.*

All complexes were synthesised in good yields, though as expected, the formation of cluster-species was a significant challenge, particularly in complexes that proved difficult to purify by distillation, namely [Sn(O^{i}Pr)$_2$] **(22)** and [Sn(O^{t}Bu)$_2$] **(23)**. Despite the use of dry reagents, trace clusters identified by sharp ^{119}Sn NMR resonances ca. –160 ppm were found to be present in all samples, despite numerous purification steps.

As mentioned previously, the synthesis and characterisation of fluorinated derivatives of simple alkoxides **(27)** and **(28)** was of great interest, allowing for comparisons between non-fluorinated species and the donor-functionalised systems discussed in Chapter 2 to be drawn. Synthesis of these systems proved challenging, with a number of attempts resulting in adducts of the displaced ligand, presumably due to the greater desire to electronically satisfy the electron-deficient tin(II) centre.[63] Greater detail on the challenges and electronic considerations of the fluorinated systems is given within their individual characterisations.

4.2.2. Characterisation

Tin(II) isopropoxide **(22)** has been previously characterised and has been determined to adopt a polymeric, μ-O^{i}Pr structure consisting of orthogonal, planar {Sn_2O_2} rings at approximately 90° to each other.[64] This structure is an expected manifestation of the coordinative unsaturation of Sn(II) centres with simple monodentate ligands, in conjunction with available lone pairs and excess electron density on many alkoxide ligands. The polymeric structure adopted by [Sn(O^{i}Pr)$_2$] is consistent with those observed for the similarly sterically undemanding [Sn(OCH$_2$CMe$_3$)$_2$], as reported by Boyle and co-workers.[53,58] It also thought that, though structurally uncharacterised, both [Sn(OMe)$_2$] and [Sn(OEt)$_2$] exist as polymeric in the solid state, with unintended hydrolysis products well-characterised for the latter.[9,57]

The ^{1}H, ^{13}C{^{1}H} and ^{119}Sn NMR gathered for **(22)** are consistent with those reported in the literature, with the ^{1}H NMR displaying the expected septet and doublet of the isopropyl at δ = 4.62 and 1.34 ppm, with ^{13}C{^{1}H} NMR shifts of δ = 65.6 and 28.2 ppm for their respective carbon environments. Similarly, the ^{119}Sn NMR is observed at δ = –211 ppm in C_6D_6.[64] A 2013 study by Wang et al.[65] carried out diffusion-ordered NMR spectroscopy on [Sn(O^{i}Pr)$_2$], which determined that it existed as dimeric in solution. For this reason, complex **22** was included in the screening of simple alkoxides for atomic layer deposition, on the hypothesis that at elevated temperatures, breakdown of the polymeric chains may allow for greater volatility than would otherwise be expected for a polymeric tin(II) system.

With previous characterisation in place for the dimeric [Sn(O^{t}Bu)$_2$] **(23)**, and its deposition potential having been already established within thermal AA-CVD, samples were synthesised and characterised in an analogous manner to **22**. ^{1}H, ^{13}C{^{1}H} and ^{119}Sn NMR were again consistent with the reported data, exhibiting a singular ^{1}H NMR environment at δ = 1.45 ppm, alongside ^{13}C{^{1}H} NMR resonances at δ = 72.8 and 32.4 ppm. Interestingly, the carbon environment adjacent to the alkoxide appears marginally more deshielded than that of complex **22**. As expected, the ^{119}Sn NMR resonance, which appeared at δ = –91 ppm is consistent with those reported previously.[66,67]

In an attempt to disrupt the structure and improve the volatility of the polymeric tin(II) isopropoxide system, the chiral alcohol sec-butanol [HOCH(CH$_3$)CH$_2$CH$_3$] was reacted with [Sn{N(SiMe$_3$)$_2$}$_2$] to afford the complex [Sn(O^{s}Bu)$_2$] **(24)**. The compound presented as a clear, non-viscous liquid, showing initial promise for ALD applications. After distillation at 150 °C (10^{-2} mbar), ^{1}H NMR displayed a well-defined spectrum consistent with the expected complex and sufficiently distinct from that of the free alcohol. This comprised a broad indistinct multiplet (OC*H*) at δ = 4.26-4.33 ppm followed by two well-defined but complex multiplets ascribed to each of the methylene protons (δ = 1.70-1.80 and 1.50-1.60 ppm). Further upfield the doublet associated with the OCH(C*H*$_3$) moiety is seen at δ = 1.36 ppm before a final triplet at δ = 0.98

ppm completes the spectrum for the termination of the ethyl chain. The $^{13}C\{^{1}H\}$ spectrum presents as expected, with four clear resonances at δ = 71.4, 35.1, 26.1 and 11.0 ppm. These correspond to the alkoxide 2° carbon, the methylene environment, the OCH(*C*H_3) and ethyl termination respectively. A broad ^{119}Sn resonance at δ = –141 ppm was observed in C_6D_6.

In order to maintain the secondary carbon environments at the alkoxide carbon seen in **22** and **24**, but improve the steric bulk of the alkoxide systems, 3-methyl-2-butanol was reacted with [Sn{N(SiMe$_3$)$_2$}$_2$] to afford complex **25**, [Sn{OCH(CH$_3$)CH(CH$_3$)$_2$}$_2$]. Complex **25** presented in a similar manner to **24**, as a clear, marginally more viscous liquid distilling at 170 °C (10^{-2} mbar). Again the ^{1}H NMR spectrum displays the expected multiplet resonances for the protons of both secondary carbon environments [OC*H*(CH$_3$)C*H*(CH$_3$)$_2$] at δ = 4.0-4.08 and 1.66-1.76 ppm respectively, in addition to three doublet resonances at δ = 1.29 (J = 5.6 Hz), 1.03 (J = 6.2 Hz) and 0.98 (J = 6.2 Hz) ppm. The latter three resonances are attributed to the methyl group of the alkoxide 2° carbon and the two methyl groups of the CH(C*H*$_3$)$_2$ termination respectively. The $^{13}C\{^{1}H\}$ NMR spectrum largely emulates the proton assignations, with $^{13}C\{^{1}H\}$ resonances observed at δ = 74.1, 36.8, 22.6, 18.8 and 18.0 ppm. These environments correspond to the 2° alkoxide carbon, OCH(*C*H_3), *C*H(CH$_3$)$_2$, and both CH(*C*H$_3$)$_2$ groups respectively. A similar broad resonance to that observed for **25** was observed in the ^{119}Sn spectrum, appearing at δ = –154 ppm.

The final simple alkoxide species in the series was the complex [Sn{OC(CH$_3$)$_2$CH$_2$CH$_3$}$_2$] **(26)**, previously characterised within a doctoral thesis by T. Wildsmith.[64] This was of interest due to the marginal difference to [Sn(O^{t}Bu)$_2$] **(23)**, comprising the same tertiary alkoxide carbon environment, but with a free ethyl chain in an attempt to aid volatility. Disruption of the crystal packing was indeed evident, as exhibiting higher volatility than both liquid compounds **24** and **25**, [Sn{OC(CH$_3$)$_2$CH$_2$CH$_3$}$_2$] was found to distil as a clear, colourless liquid at 120 °C (10^{-2} mbar), in stark contrast to the solid [Sn(O^{t}Bu)$_2$] **(23)**. The ^{1}H NMR was found to be consistent with that reported, displaying a quartet resonance ascribed to the methylene CH$_2$ at δ = 1.71 ppm (J = 7.5 Hz), followed by a singlet and triplet resonances at δ = 1.41 and 1.05 (J = 7.5 Hz) ppm. The latter two correspond to the two methyl groups of the 3° alkoxide carbon and the terminal ethyl C*H*$_3$ respectively. The $^{13}C\{^{1}H\}$ NMR spectrum was again consistent with that reported, and the ^{119}Sn NMR spectrum displayed a well-defined resonance at δ = –98 ppm, very close to that observed for dimeric [Sn(O^{t}Bu)$_2$] **(23)**.

Though a number of attempts have been made to discern trends in the ^{119}Sn NMR of tin(II) complexes with particular focus on alkoxide derivatives, differences of ~50-100 ppm in a spectral window which for tin spans over 3000 ppm are often problematic when used in attempts to elucidate structural conformations.[53,68,69] A 2015 study by Wang et al.[70] sought to correlate structure with ^{119}Sn chemical shift with a mixture of experimental and DFT

experiments with some success, though it was expressed that such correlations are at best estimations.

Table 4.1 – ^{119}Sn chemical shifts observed for a range of simple tin(II) complexes.

Compound	^{119}Sn Chemical Shift (ppm) C_6D_6/d_8-tol*	Expected nuclearity in solution
$Sn(O^iPr)_2$ **(22)**	–211 (–200*)[70]	3
$Sn(O^tBu)_2$ **(23)**	–91 (–94*)[70]	3
$Sn(O^sBu)_2$ **(24)**	–141	Unknown
$Sn[OCH(CH_3)_2CH(CH_3)_2]_2$ **(25)**	–154	Unknown
$Sn[OC(CH_3)_2CH_2CH_3]_2$ **(26)**	–98	Unknown
$Sn[(OCH_2CH_3)_2]_\infty$	(–361, –394, –197)**[53]	Unknown
$Sn[(OCHPh_2)_2]_2$	[–181 (min.), –263 (maj.)]**[57]	3
$Sn[(OCPh_3)_2]_2$	(–244, –328)**[57]	3

*Recorded in d_8-toluene, ** Recorded in d_8-THF

As can be seen from Table 4.1, no discernible trend can be derived from the ^{119}Sn NMR shifts of the simple tin(II) alkoxides studied. It would appear that when compared to the higher nuclearity pendant aminoalkoxides discussed in Chapter 2, simple alkyl alkoxides **(22-26)** display lower ^{119}Sn resonances, with $[Sn(dmae)_2]$ **(1)**, $[Sn(dmap)_2]$ **(4)** and $[Sn(dmamp)_2]$ **(7)** exhibiting ^{119}Sn chemical shifts of δ = –279, –231 and –259, and –218 ppm respectively.

As alkoxide species begin to incorporate aromatic substituents, a general shift of ^{119}Sn NMR resonances to higher field is observed.[57,69] Though not directly relevant to the alkyl alkoxides under scrutiny in this investigation, a brief ^{119}Sn study of a series of polymeric, dimeric and monomeric aromatic alkoxides was undertaken by Boyle et al., and the reader is directed towards this for any further elaboration on the predicted ^{119}Sn NMR shifts of three- coordinate tin(II) species.[69]

4.2.3. Thermogravimetric Analysis of Compounds 22-26

Mass Loss-Temperature Thermogravimetric Analysis

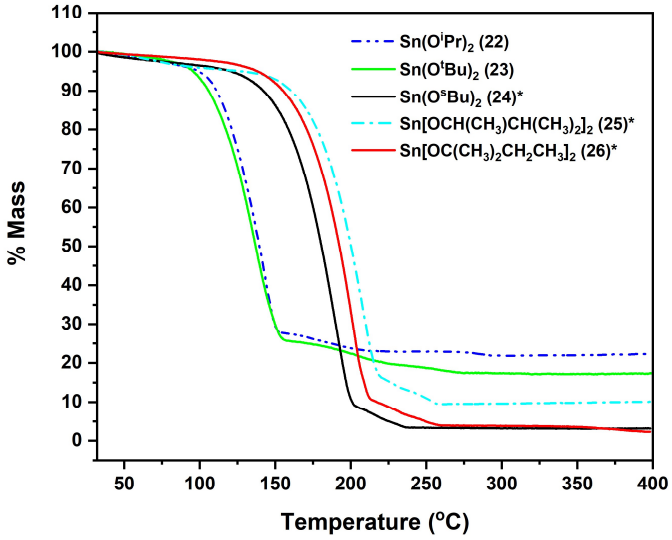

*Figure 4.3 – Mass loss/temperature TGA plots for Sn(II) alkoxides **22-26**. *Liquid compounds.*

The mass loss/temperature plots for complexes **22-26** is shown in Figure 4.3. Despite complexes **22**, **23** and **26** having been previously characterised,[57] measurements were repeated to ensure a level of consistency with the reported data. All complexes display a loss of mass greater than expected for the decomposition to any of metallic tin, tin(II) oxide or tin(IV) oxide (Table 4.2). At first observations, the degree of volatility appears to be higher in the isopropoxide and tert-butoxide systems **22** and **23** than is evident for the remainder of the series.

All complexes display similar TGA traces, with a sharp loss of mass to ca. 90-95% of the entire mass loss, after which a second smaller loss of mass occurs. There are a number of possible explanations for this phenomenon. It is possible that decomposition of the complexes begins to occur at elevated temperatures, before the entire sample has had time to volatilise. This may be particularly relevant for the polymeric [Sn(O^{i}Pr)$_2$] **(22)**, with reported self-elimination reactions occurring at elevated temperatures.[55,56] It is also probable that each of the simple alkoxide species contains a degree of cluster species as a result of the synthetic routes used, which would display differing volatility and stability to the bulk complexes within each sample. This does not limit their potential for ALD applications, but would require more stringent purification methods to be used for high quality film growth.

It would appear that with the exception of **22** and its reported instability, all complexes display promising stabilities and volatilities for ALD applications, with the latter confirmed more quantitively through subsequent isothermal thermogravimetric analysis.

*Table 4.2 – Residual masses from the TGA of **22-26**, with expected masses of decomposition products.*

		Expected Residual Mass (%)		
Compound	Residual Mass (%)	SnO	SnO_2	Sn
22	22.5	56.9	63.6	50.1
23	17.1	50.8	56.9	44.8
24	3.7	50.8	56.9	44.8
25	9.8	46.0	51.4	40.5
26	2.6	46.0	51.4	40.5

Isothermal Thermogravimetric Analysis

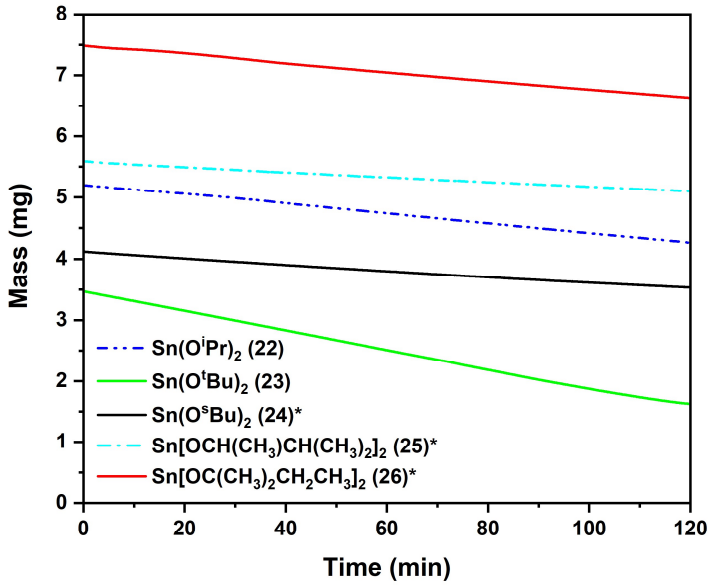

*Figure 4.4 – Isothermal TGA plots (70 °C/*100 °C) for Sn(II) alkoxides **22-26**. Ar flow 20 ml min^{-1}.*

Due to the higher observed volatilities of [Sn(O^{i}Pr)$_2$] **(22)** and [Sn(O^{t}Bu)$_2$] **(23)**, isothermal analyses were undertaken at temperatures of 70 °C, consistent with the precursor source temperatures for [Sn(dmamp)$_2$] (**7**, Chapter 2) and [Sn(deed)NMe$_2$] (**15**, Chapter 3). For the remaining three complexes, **24**, **25** and **26**, isothermal experiments were undertaken at temperatures of 100 °C.

As is evident from the isothermal plots (Figure 4.4) and evaporation rates (Table 4.3) for the five simple alkoxide complexes, despite a lower "source" temperature, $[Sn(O^iPr)_2]$ **(22)** and $[Sn(O^tBu)_2]$ **(23)** displayed the highest volatility, the latter by a large margin. With an evaporation rate of 128.4 μg min^{-1} cm^{-1}, dimeric **23** exhibits almost twice as much volatility as the next in the series (**22**, 65.0 μg min^{-1} cm^{-1}). After a change in temperature to 100 °C, the three liquid complexes display decreasing evaporation rates in the order $[Sn\{OC(CH_3)_2CH_2CH_3\}_2]$ **(26)** > $[Sn(O^sBu)_2]$ **(24)** > $[Sn\{OCH(CH_3)CH(CH_3)_2\}_2]$ **(25)**, with evaporation rates of 60.8, 40.4 and 32.4 μg min^{-1} cm^{-1} respectively.

*Table 4.3 – Evaporation rates of compounds **22-26** at 70 °C and 100 °C.*

Compound	Evaporation rate (μg min^{-1} cm^{-2})
22	65.0
23	128.4
24	40.4*
25	32.4*
26	60.8*

*Isothermal carried out at 100 °C

Given the reported instability[55,56] of $[Sn(O^iPr)_2]$ **(22)**, three complexes emerge as worthy of deposition trials. $[Sn(O^tBu)_2]$ **(23)** and $[Sn\{OC(CH_3)_2CH_2CH_3\}_2]$ **(26)** both contain 3° alkoxide carbon atoms, whilst $[Sn(O^sBu)_2]$, with the lowest volatility of the three, is in possession of a 2° chiral centre. The low relative volatility of the latter is surprising given its liquid nature and molecular structure, which contains not only oily alkyl chains but a carbon centre capable of introducing asymmetry into the system. This low volatility is even more surprising given its identical molecular weight to the highly volatile $[Sn(O^tBu)_2]$ complex **(23)**.

4.2.4. Synthesis and Characterisation of Fluorinated Alkoxides 27 and 28

*$[Sn(O^{Fi}Pr)_2]$ **(27)***

In an attempt to investigate the effects of alkoxide electronics on structure, $[Sn\{N(SiMe_3)_2\}_2]$ was reacted with two equivalents of the fluorinated alcohols 1,1,1,3,3,3-hexafluoro-2-propanol ($HO^{Fi}Pr$) and 1,1,1,3,3,3-hexafluoro-2-trifluoromethyl-2-propanol ($HO^{Ft}Bu$), to form Sn(II) analogues of $[Sn(O^iPr)_2]$ **(22)** and $[Sn(O^tBu)_2]$ **(23)**. Previous attempts at the synthesis of the former had not been structurally characterised, and molecular structures obtained from the reaction of $[Sn(NMe_2)_2]$ with $HO^{Fi}Pr$ had afforded the $HO^{Fi}Pr$-adduct of the desired complex due to the hugely electron deficient alkoxide ligand and its inability to form the effective Sn–O–Sn bridges observed in the non-fluorinated analogue **(22)**.[63]

Reaction of $[Sn\{N(SiMe_3)_2\}_2]$ with two equivalents of $HO^{Fi}Pr$ in Et_2O at –78 °C afforded a clear, colourless solution, after which the volatiles were removed *in vacuo* to leave a white, low melting powder. This was washed several times with cold hexane, which was successively removed *in vacuo*. A final solution in hexane was reduced and stored at –28 °C to yield extremely low-melting and highly reactive clear and colourless needles suitable for single-crystal X-ray diffraction.

The ^{1}H and $^{13}C\{^{1}H\}$ NMR spectra of **27** display largely consistent resonances with those reported for the structurally uncharacterised system described by Suh and Hoffman.[63] An ill-defined multiplet in the proton ascribed to the C*H* at δ = 4.45-4.55 was reported as a fluorine-coupled septet by Suh, whilst the $^{13}C\{^{1}H\}$ NMR spectrum displayed the identical quartet (δ = 123 ppm, $^{1}J_{CF}$ = 285 Hz) and septet (δ = 70.6, $^{2}J_{CF}$ = 33 Hz) ascribed to the *C*H and *C*F_3 environments respectively. A single resonance was observed in the ^{19}F NMR at δ = –75.2 ppm. The previously unreported ^{119}Sn NMR spectrum consists of two distinct resonances in a 3:2 ratio at δ = –441 and –498 ppm. On inspection of the molecular structure of **27** (Figure 4.5 and Figure 4.6), the reason for the two differing ^{119}Sn environments becomes evident.

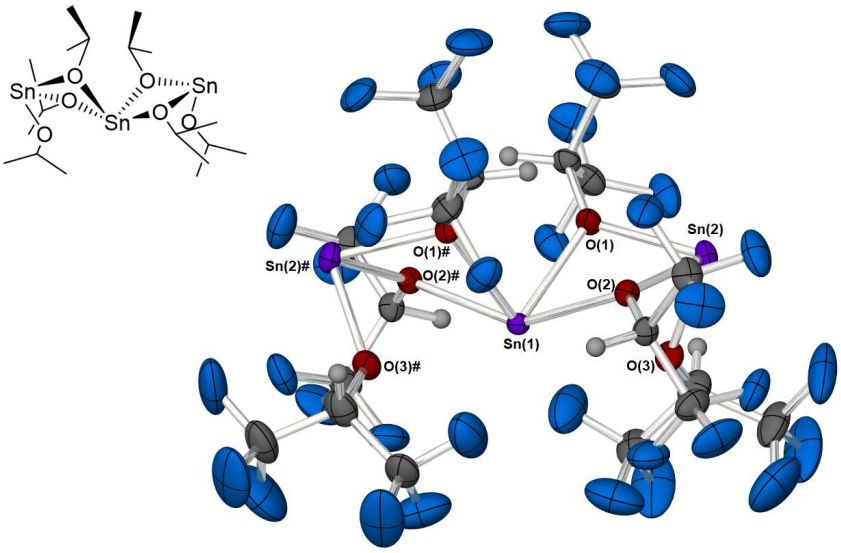

*Figure 4.5 – Side-on views of the molecular structure of trimeric $[Sn(O^{Fi}Pr)_2]_3$ **(27)**. Thermal ellipsoids shown at 50% probability. Symmetry equivalent atoms are generated by the symmetry operator: # 1–X, Y, 3/2–Z.*

$[Sn(O^{Fi}Pr)_2]_3$ **(27)** was found to exist as trimeric in the solid state, comprising two distinctly different tin environments. The molecule is symmetrical, with a C_2-axis about the central four coordinate tin atom, which is flanked by two other tin atoms, each three coordinate, with μ_2-$O^{Fi}Pr$ bridges to the central tin. The presence of four μ_2-$O^{Fi}Pr$ bridges across three tin centres leads to two non-planar $\{Sn_2O_2\}$ heterocycles originating from the central tin environment. Terminal $O^{Fi}Pr$ ligands on each of the two outer tin atoms adopt a cisoid orientation, projecting

on the same side of the bent row of Sn atoms. These terminal $O^{Fi}Pr$ moieties appear to fold inwards, creating an angle below the expected 90° at each outer tin when measured from the plane of the other two bridging ligands. This is unusual for what is essentially a three-coordinate tin(II) species, where larger angles approaching ~107° between coordination sites would be expected taking into account the likely presence of a stereoactive lone pair on the tin driving a pseudo-tetrahedral geometry. With Sn–O distances of 2.859 Å between the terminal ligand oxygen atom and central tin, it is likely that the distortion of ligands inwards is an attempt to impart additional electron density on the still electron-deficient central tin atom. Distances of 2.859 Å, whilst weak, are still worthy of note, with distances of up to and above 3 Å having been reported for dative O→Sn interactions.[71] This would imply that the central tin atom can be considered six-coordinate or if the presence of a stereoactive lone pair is considered, as pseudo seven-coordinate.

If the weak donation from the two terminal alkoxides is momentarily omitted, the central tin atom can be seen to adopt the same pseudo trigonal bipyramidal geometry seen for the majority of the four-coordinate tin(II) systems discussed throughout this report. Shorter Sn–O(1) bonds (2.259 Å) are observed in a roughly equatorial position, with longer Sn–O(2) bonds (2.404 Å) lying in axial positions. The planes of the axial and equatorial O–Sn–O environments do not sit at the expected ~90°, but instead are found at a 71° offset. On inclusion of the weak Sn---O(3) interactions between the tin and terminal alkoxides, a tilted ring around the central tin is observed, with the sum of the O(1)–Sn–O(1), O(3)---Sn---O(3) and two O(1)–Sn---O(3) angles equating ca. 363°.

The two tilted and bent $\{Sn_2O_2\}$ heterocycles which originate from the central tin atom are initially at odds to each other, with planes defined by O(1)–Sn(1)–O(2) atoms sitting at an angle of ~82° at the central tin. A kink in each of these heterocycles at the bridging oxygen atoms leads to each half of the heterocycle lying at a ca. 136° offset (as defined by O(1)–Sn(1)–O(2) and O(1)–Sn(2)–O(2) planes).

The three-coordinate nature and constrained geometry of the two flanking tin atoms leaves the tin centres ostensibly considerably exposed. Given the poor coordinative and electronic saturation offered by the electron deficient fluorinated alkoxides, the thermodynamic drive to form polymeric chains as observed in the non-fluorinated tin(II) isopropoxide species must be relatively high. This is obviously offset by a greater preference for the terminal alkoxides to donate electron density to the central tin atom, despite its four-coordinate geometry, as is evidenced by the inward inclination of the terminal alkoxides towards this central tin. This is manifested in angles of ~79.9° and ~82.2° between the bridging oxygens (O(1) and O(2)) and the terminal (O(3)) about the outer tin atoms. These angles, in conjunction with the heterocyclic angle O(1)–Sn(2)–O(2) (~71.5°), are considerably lower than either the 90°

expected for an sp^2 tin centre with a dative coordination into a vacant p_z orbital, or the ~107° that would be expected for an sp^3-type geometry with a stereoactive lone pair on the tin.

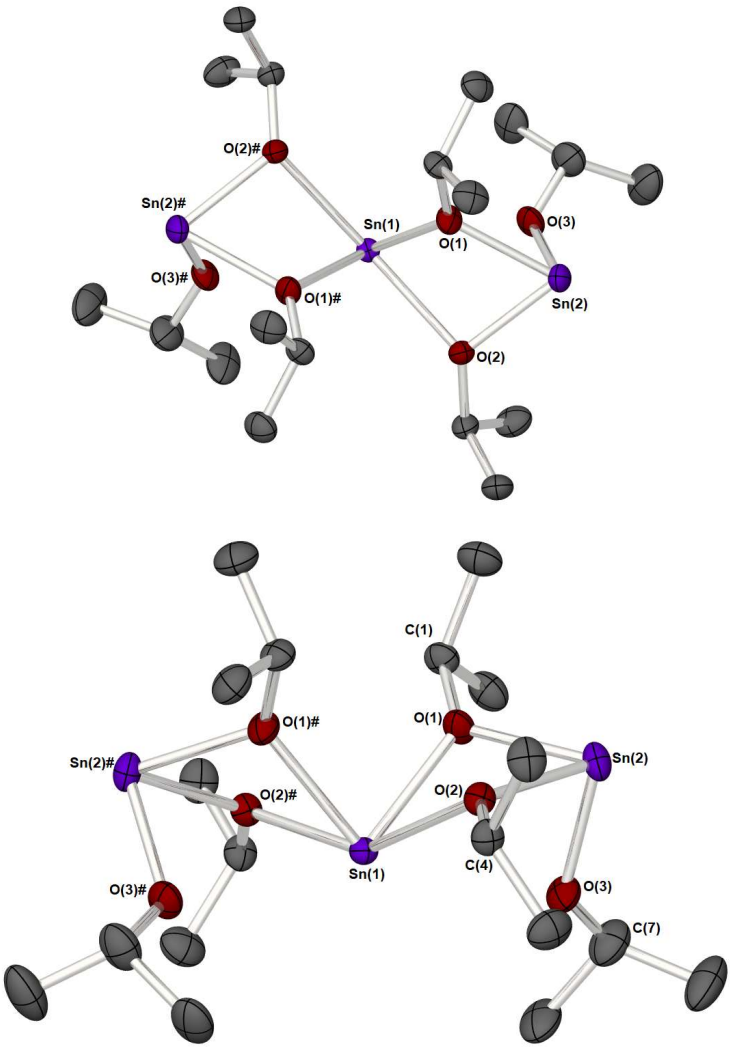

*Figure 4.6 – Molecular structure of [Sn(O^{Fi}Pr)$_2$] **(27)**. Thermal ellipsoids shown at 50% probability. Fluorine and hydrogen atoms have been omitted for clarity. Symmetry equivalent atoms are generated by the symmetry operator: # 1–X, Y, 3/2–Z.*

The bonding distances between oxygen atoms and tin centres give an indication of the distinct [Sn(O^{Fi}Pr)$_2$] units. Bonding across bridging alkoxides is not completely equal and is indicative of an O–Sn bond with more covalent character, and an O–Sn bond with more dative character. The terminal Sn(2)–O(3) bond is of a commensurate length (2.053(2) Å) with those observed in the monomeric [Sn{OC(RR')CH$_2$NMe$_2$}$_2$] complexes detailed in Chapter 2 (**1**, **4**, **7** and **10**). Interestingly, all Sn–O bonds around the four-coordinate central tin atom are longer than those observed from the same oxygen atoms to the outer tin centres (2.259 Å, 2.404 Å cf. 2.193(2) Å and 2.157(2) Å). Even the shorter of these bonds are notably longer than those observed in polymeric [Sn(O^{i}Pr)$_2$]$_\infty$ **(22)** and [Sn(OCH$_2$CH$_3$)$_2$]$_\infty$, with lengths of 2.1156(19) Å and 2.108(2) Å, and 2.114(3) Å and 2.122(3) Å respectively.[53,64,65] Comparison with the monomeric HNMe$_2$ adduct of [Sn(O^{Fi}Pr)$_2$], which consists of a three-coordinate tin atom with terminal O^{Fi}Pr

ligands, reveals Sn–O bond lengths of 2.061(5) Å and 2.107(4) Å, one of which is comparable to the 2.053(2) Å found for the terminal alkoxide bond in **27**. The three angles present between ligands in the $HNMe_2$ adduct are considerably more in line with the expected 90°, as opposed to the inwardly deflecting terminal alkoxides observed in trimeric **27**.[63]

The structure of **27** bears a great degree of similarity to the polymeric structure of $[Sn(O^iPr)_2]_\infty$ **(22)**, with "zig-zag" chains of tin and oxygen atoms forming bent, offset heterocycles. Whereas the terminal alkoxide ligands were shown to deflect inwards towards the central tin atom in **27**, the equivalent alkoxide groups are less compressed in the non-fluorinated polymer, forming angles of ~93.6° and ~94.1° to the O–Sn–O half of the adjacent $\{Sn_2O_2\}$ heterocycle.[65] One of the most interesting comparisons is that the $\{Sn_2O_2\}$ heterocycles in the non-fluorinated polymer are largely planar, whilst a large degree of bending is observed in the fluorinated system as discussed above.

*Table 4.4 – Relevant bond lengths and angles within compound **27**.*

Angle (°)		**Distance (Å)**	
O(2)–Sn(1)–O(2)	148.95(9)	Sn(1)–Sn(2)	3.453(2)
O(1)–Sn(1)–O(1)	82.14(10)	Sn(1)–O(1)	2.2587(19)
Angle between O(2)–Sn(1)–O(2) plane and O(1)–Sn(1)–O(1) plane	71.1	Sn(1)–O(2)	2.4044(18)
		Sn(1)---O(3)	2.860(2)
O(3)---Sn(1)---O(3)	154.26(17)	Sn(2)–O(1)	2.193(2)
		Sn(2)–O(2)	2.157(2)
O(1)–Sn(2)–O(2)	71.50(7)	Sn(2)–O(3)	2.053(2)
O(1)–Sn(2)–O(3)	79.86(8)		
O(2)–Sn(2)–O(3)	82.17(8)	O(1)–C(1)	1.392(3)
		O(2)–C(4)	1.396(3)
Sn(1)–O(1)–Sn(2)	101.73(8)	O(3)–C(7)	1.376(4)
∑ angles about O(1)	358.7		
Sn(1)–O(2)–Sn(2)	98.26(7)		
∑ angles about O(2)	350.3		
Sn(1)---O(3)–Sn(2)	87.73(8)		
∑ angles about O(3)	348.8		

*$[Sn(O^{Ft}Bu)_2]_2$ **(28)***

Ligand metathesis towards $[Sn(O^{Ft}Bu)_2]$ **(28)** presented fewer challenges than those encountered in the synthesis of **27**, largely due to the bulkier $HO^{Ft}Bu$. The slightly orange crystals obtained were however highly air- and moisture-sensitive and thus required careful manipulation to afford the solid-state structure depicted in Figure 4.7, determined by single crystal X-ray diffraction.

The ^{19}F NMR spectrum displays a single resonance at δ = –74.5 ppm, whilst the $^{13}C\{^{1}H\}$ NMR spectrum consists of a quartet at δ = 122.2 ($^{1}J_{CF}$ = 292.8 Hz). Unfortunately, no resonance for the expected multiplet of the tertiary carbon was detected, nor could an adequate ^{119}Sn signal be obtained despite numerous attempts.

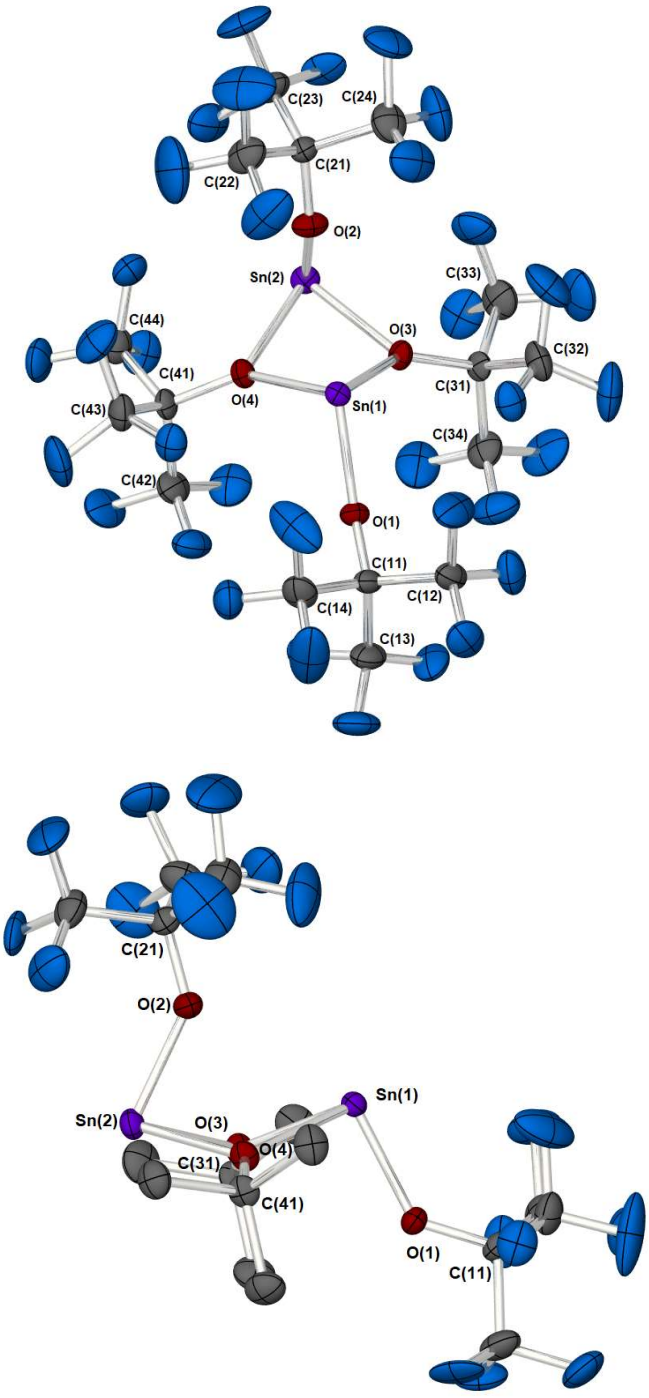

*Figure 4.7 – Molecular structure of [Sn(O^{Et}Bu)$_2$] **(28)**. Thermal ellipsoids shown at 50% probability. The lower structure gives a side-on view where fluorine atoms from bridging {OC(CF$_3$)$_3$)} groups have been omitted for clarity.*

There are a number of similarities between the molecular structures of **27** and **28**, though rather than forming the symmetrical trimer observed in **27**, an asymmetric dimer is instead formed. $[Sn(O^{Ft}Bu)_2]_2$ **(28)** adopts a largely comparable structure to its non-fluorinated counterpart $[Sn(O^tBu)_2]_2$ **(23)**, with two identical three-coordinate tin centres bound within a central $\{Sn_2O_2\}$ ring. Two different tin environments can be seen within dimeric **28**, though in much the same heterocyclic manner as in **23**, the structure retains one ring to bind them together. Whereas in the simple $[Sn(O^tBu)_2]_2$ dimer, the central $\{Sn_2O_2\}$ heterocycle is completely planar, as was seen for the $[Sn(O^iPr)_2]_\infty$ polymer, the central $\{Sn_2O_2\}$ ring in **28** adopts the bent configuration reminiscent with that observed in the fluorinated isopropoxide trimer **27** (angle between O(3)–Sn(1)–O(4) plane and O(3)–Sn(2)–O(4) plane = 142.21°).

In both fluorinated and non-fluorinated tert-butoxide complexes, the structure consists of two bridging alkoxide ligands and two terminal alkoxides, the latter projecting trans to each other on either side of the $\{Sn_2O_2\}$ heterocycle. Angles of ~90.5° and ~93.2° are observed between terminal alkoxides and the O–Sn heterocycle within the $[Sn(O^tBu)_2]_2$ dimer, whilst within the fluorinated system only one terminal alkoxide adopts an angle approaching 90° (O(1)–Sn(1)–O(3), 92.11(8)° and O(1)–Sn(1)–O(4), 94.78(8)°). The other terminal alkoxide ligand is angled across the top of the $\{Sn_2O_2\}$ ring in what would appear to be a degree of electron donation to its neighbouring tin atom, in much the same way as was seen in the trimeric **27** discussed previously. This leads to compressed angles between the terminal alkoxide and the $\{Sn_2O_2\}$ heterocycle (O(2)–Sn(2)–O(3), 81.34(8)° and O(2)–Sn(2)–O(4), 81.54(8)°), in addition to a long O(2)---Sn(1) distance of 3.030(2) Å, nearing the upper reported limits for O→Sn interactions.[71]

*Table 4.5 – Relevant bond lengths and angles within compound **28**.*

Angle (°)		Distance (Å)	
O(1)–Sn(1)---O(2)	148.13(7)	Sn(1)–Sn(2)	3.4915(3)
O(3)–Sn(1)–O(4)	69.42(8)	Sn(1)–O(1)	2.059(2)
Angle between O(1)–Sn(1)–O(2) plane and O(3)–Sn(1)–O(4) plane	87.47	Sn(1)–O(3)	2.305(2)
		Sn(1)–O(4)	2.341(2)
		Sn(1)---O(2)	3.030(2)
O(2)–Sn(2)–O(3)	81.34(8)	Sn(2)–O(2)	2.052(2)
O(2)–Sn(2)–O(4)	81.54(9)	Sn(2)–O(3)	2.223(2)
O(3)–Sn(2)–O(4)	73.22(8)	Sn(2)–O(4)	2.213(2)
Sn(1)–O(3)–Sn(2)	100.89(8)	O(1)–C(11)	1.369(4)
∑ angles about O(3)	359.7	O(2)–C(21)	1.372(4)
Sn(1)–O(4)–Sn(2)	100.08(8)	O(3)–C(31)	1.400(4)
∑ angles about O(4)	359.9	O(4)–C(41)	1.395(4)
Sn(1)---O(2)–Sn(2)	84.46(7)		
∑ angles about O(2)	360.0		

The Sn–O bond lengths of the terminal alkoxide species are identical to the values observed throughout the investigation (2.059(2) Å and 2.052(2) Å), though are notably shorter than those observed within the trimeric system described previously. This is presumably due to the loss of electron density on donation to the central tin atom in compound **27**.

With the weak 3.030(2) Å interaction between the "terminal" alkoxide and Sn(1) taken into account, the tin environment to which this coordination is directed (Sn(1)) can be considered to be loosely four-coordinate. This would give the same pseudo trigonal pyramidal arrangement commonly found in four-coordinate tin(II), with O–Sn–O planes existing at an angle of 87.47°. The second tin environment (Sn(2)) is undoubtedly three-coordinate, with constrained angles of 81.34(8)° and 81.54(9)° between the "terminal" alkoxide which loosely coordinates to Sn(1) and each of the heterocyclic Sn–O bonds respectively. Both heterocyclic bridging oxygen atoms, alongside the "terminal" donating alkoxide adopt planar sp^2 arrangements, with the sum of bonding angles about each totalling ca. 360°.

4.3. Deposition Trials

Depositions with $[Sn(O^tBu)_2]_2$ ***(24)***

Interestingly, $[Sn(O^tBu)_2]_2$ **(23)** displayed the highest volatility out of all simple alkoxide species characterised **(22-26)**, with an evaporation rate of 128.4 μg min^{-1} cm^{-2} at 70 °C. Whilst dimeric species are often avoided for use in atomic layer deposition, a comparable volatility to $[Sn(dmamp)_2]$ **(7)**, alongside the presence of a similar 3° alkoxide environment, were encouraging factors in attempting deposition. Proof-of-concept ALD experiments were undertaken at 130 °C, 150 °C, 170 °C, 210 °C and 250 °C, and confirmed that successful deposition of material was taking place. The resultant films were characterised by p-XRD, Raman spectroscopy and variable-angle spectroscopic ellipsometry. The thicknesses of each film determined by variable-angle spectroscopic ellipsometry were found to decrease with increasing temperature with values of 25.19, 15.78, 12.95, 6.75 and 5.01 nm respectively.

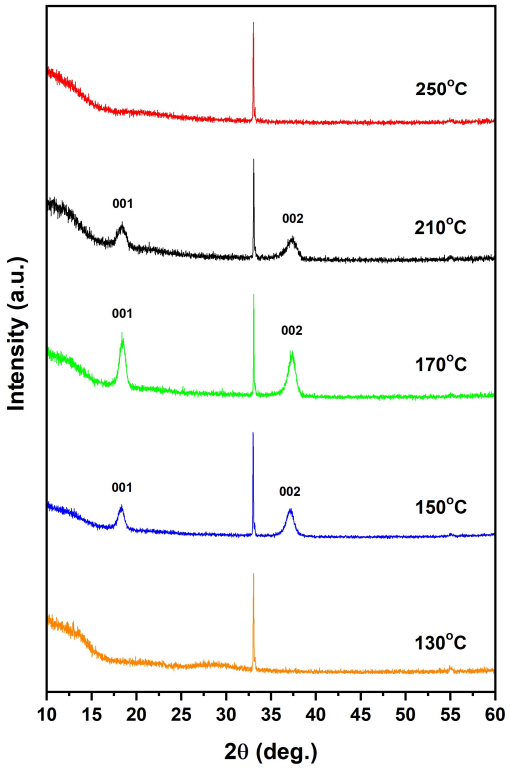

Figure 4.8 – p-XRD patterns of [Sn(O^{t}Bu)$_2$] depositions at 130-250 °C.

Powder X-ray diffraction patterns of films deposited at temperatures between 130 °C and 250 °C confirm that crystalline SnO was deposited at 150 °C, 170 °C and 210 °C. All crystalline films displayed highly oriented SnO, with the (001) and (002) reflections present at 2θ values of ~18.3° and ~37.1°. Basic analysis of the peak broadening within the patterns indicate rough estimates of ca. 7.5, 8.0 and 5.8 nm for the mean crystallite dimensions along the *C*-axes at each temperature. Interestingly, the crystallites seem to reach the maximum value of ca. 8 nm in a similar way to those observed in films grown with [Sn(deed)NMe$_2$] and [Sn(dmamp)$_2$]. Whilst the values determined through Scherrer analysis in this way cannot be thought of as entirely accurate, it would seem that there is a generally favourable dimension for SnO crystallites grown via ALD processes.

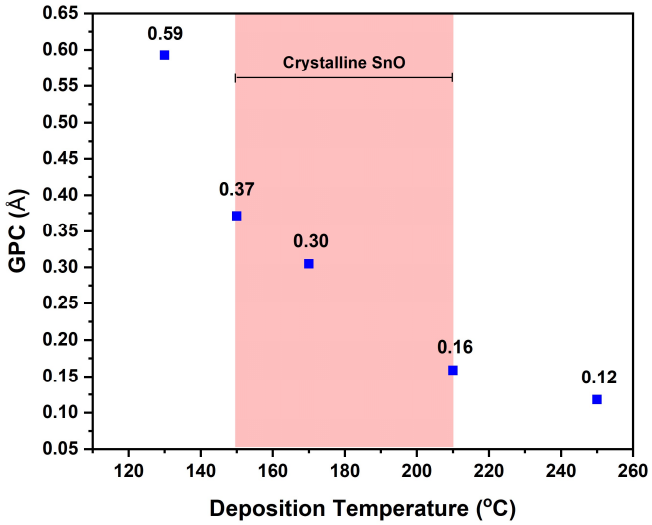

Figure 4.9 – Estimated GPC and region of crystallinity for [Sn(O^{t}Bu)$_2$]. Depositions after 425 ALD cycles at 130 °C, 150 °C, 170 °C, 210 °C and 250 °C.

The thicknesses of all films were shown to be consistently higher than those reported by Han et al. for the published precursor [Sn(dmamp)$_2$].[72] Indeed, even after the reactivity optimisation for [Sn(dmamp)$_2$] undertaken earlier in this research, growth rates appear to be significantly higher at each respective temperature. Though the presence of a distinct "ALD window" is lacking, the growth follows a similar decrease with increased temperature to that observed for [Sn(dmamp)$_2$].

Raman spectroscopy (Figure 4.10) was also undertaken on crystalline films grown at 170 °C and 210 °C, confirming the presence of SnO and lack of appreciable quantities of crystalline SnO_2. Given the thin films deposited after 425 cycles, the intensity is lower than was observed for films deposited after 850 cycles, as seen elsewhere in this research. The presence of the SnO A_{1g} stretch can clearly be observed at 210 cm^{-1}, consistent with SnO films previously characterised.

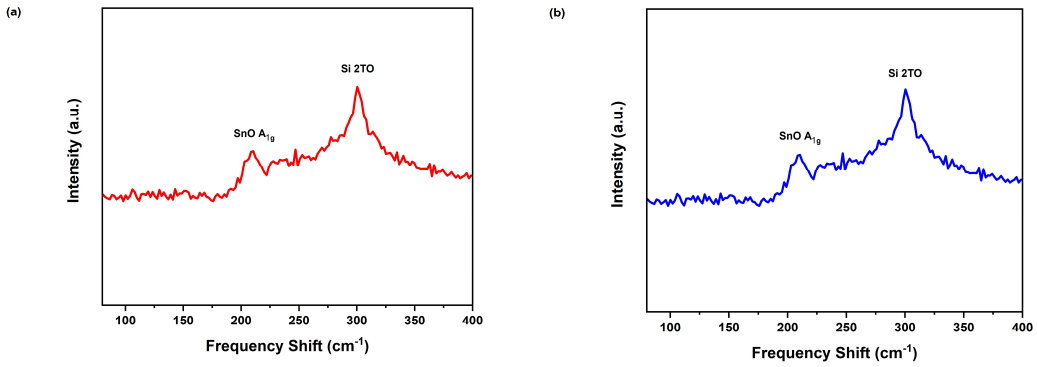

Figure 4.10 – Raman spectra of SnO films deposited from [Sn(O^{t}Bu)$_2$] at 170 °C (a) and 210 °C (b).

A study to determine an accurate growth rate and extent of ALD behaviour was undertaken at 170 °C (Figure 4.11). Growth was found to follow a largely linear trajectory consistent with a self-limiting ALD process. The growth per cycle was confirmed to considerably exceed that observed for $Sn(dmamp)_2$ at the same deposition temperature, using the same deposition parameters. Whereas growth rates were reported to be ca. 0.16 Å/cy at 170 °C, and increased to 0.18 Å/cy through optimisation undertaken throughout this research, growth at the same temperature using $Sn(O^tBu)_2$ was found to occur at a rate of 0.32 Å.

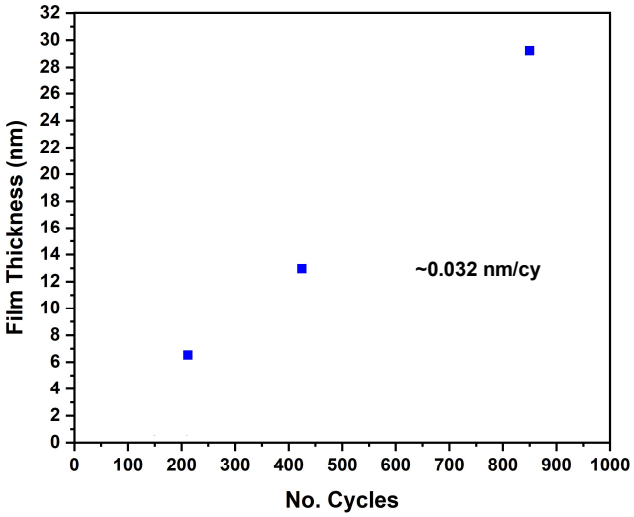

Figure 4.11 – Plot of film thickness vs. no. ALD cycles for $Sn(O^tBu)_2$ depositions at 170 °C.

$Sn(O^tBu)_2$ (23) was the first oxygen-based novel precursor trialled in this research, and as such, it was important to determine whether or not true atomic layer deposition was indeed occurring, or whether a CVD-style process was responsible for material growth. Whilst no material deposition was reported by Hill et al.[57] with the same precursor at temperatures under 350 °C in the CVD furnace used in the report, it was necessary to eliminate this growth as a possibility. Furthermore, it was of additional interest to confirm that no precursor self-elimination of the form observed within $Sn(O^iPr)_2$ occurred at elevated temperatures, resulting in deposition of tin metal.

As such a standard ALD process was undertaken at 170 °C, though with the H_2O pulse removed. No deposition was observed on the substrate, and spectroscopic ellipsometry confirmed only a marginal <1 nm change to the surface of the SiO_2, most likely due to a monolayer of adsorbed precursor affecting the refractive index of the substrate.

There has been some speculation within the ALD community as to the nature of the surface chemistry of ALD processes utilising lower-reactivity precursors, and to what extent the conventional stepwise process is likely to be consistent with the actual processes on the film.[73–76] To this end, it was of interest to attempt deposition with an excessively long purge length

in gain an indication of to what extent precursor adsorption on the surface was a reversible process.

Accounting for this, a standard ALD process was undertaken at 170 °C with the standard 10 second purge length between cycles replaced by a 30 second purge. It was found that whilst crystalline material was still deposited, the growth per cycle decreased from the 0.32 Å/cy observed for the standard process, to 0.21 Å/cy. This would imply that physisorption of precursor to the substrate surface in addition to chemisorption plays an important role in the effectiveness of a low-reactivity precursor. This is supported by the lack of visible "ALD windows" within many novel precursors, whereby lower growth rates are observed at elevated temperatures due to an increased desorption of precursor and hydroxyl groups. Testament to this is the growth profile reported by Han et al. for $[Sn(dmamp)_2]$, which bears a great deal of resemblance to that displayed in Figure 4.9, previously.[72] The effect of precursor physisorption and decreasing growth rate with purge times and temperature has also been described in other reports by a number of authors.[73–76]

Depositions with $[Sn(O^sBu)_2]$ ***(24)***

Presenting as a liquid with an evaporation rate of ~40 μg min^{-1} cm^{-2} at 100 °C, $[Sn(O^sBu)_2]$ **(24)** displayed the highest volatility of the alkoxide precursors containing 2° alkoxide carbon environment, after the elimination of $[Sn(O^iPr)_2]$ **(22)** as a viable option. Its volatility was lower than that of polymeric $[Sn(O^iPr)_2]$ and the two 3° alkoxide species, but given the differences in deposition between analogous $[Sn(dmap)_2]$ **(4)** (inefficient, amorphous) and $[Sn(dmamp)_2]$ **(7)** (consistent, crystalline), which contain 2° and 3° alkoxide ligands respectively, it was of interest to see if similar effects were replicated within non-chelating 2° and 3° alkoxides.

The precursor was heated to 100 °C and deposition was attempted on to SiO_2/Si wafers at both 150 °C and 170 °C, using the optimised process applied throughout this investigation. Whilst precursor was successfully volatilised and delivered to the reaction chamber, no deposition was found to have occurred on any occasion.

Depositions with $[Sn\{OC(CH_3)_2CH_2CH_3\}_2]$ ***(26)***

Given the difference in efficacy between 3° alkoxide species $[Sn(O^tBu)_2]$ **(23)** and 2° alkoxide species $[Sn(O^sBu)_2]$ **(24)**, it was of interest to determine if any other simple alkoxide systems were of use as ALD precursors. The most attractive remaining system in this regard was the volatile liquid $[Sn\{OC(CH_3)_2CH_2CH_3\}_2]$ **(26)**, which displayed an evaporation rate of 60.8 μg min^{-1} cm^{-2} at 100 °C.

Trial depositions were undertaken at reactor temperatures of 170 °C and 210 °C. Unlike trials involving [Sn(O^{s}Bu)$_2$] **(24)**, successful deposition was observed at both temperatures. However, whereas films grown with [Sn(O^{t}Bu)$_2$] **(23)** were shown to exhibit crystallinity at temperatures as low as 150 °C, only films deposited at the higher temperature of 210 °C displayed detectable crystallinity (Figure 4.12).

As in all crystalline atomic layer deposited SnO films throughout this investigation, highly oriented material was observed, clearly displaying peaks consistent with the (001) and (002) planes of SnO. The amorphous films were determined to have a thickness of 20.7 nm after 425 ALD cycles, giving an estimated growth per cycle of 0.49 Å, whilst the crystalline films determined to consist of SnO by p-XRD were shown to have a thickness of 11.3 nm, with a growth rate of 0.27 Å/cy. Estimations of crystallite dimensions in the *C*-axis for the crystalline film were found to be ca. 7.7 nm, consistent with results outlined previously.

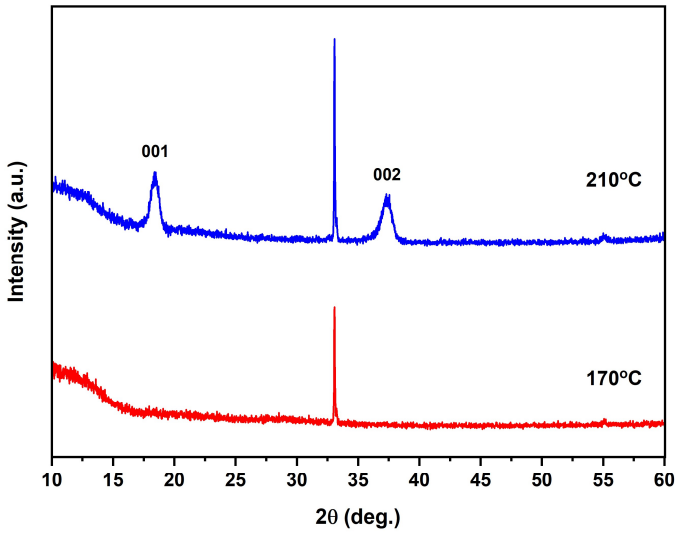

*Figure 4.12 – p-XRD patterns of [Sn{OC(CH$_3$)$_2$CH$_2$CH$_3$}$_2$] **(26)** depositions at 170 °C and 210 °C.*

Intended as an initial proof-of-concept study, no further depositions or analyses were undertaken, though research is ongoing in this regard. Whilst crystalline material was deposited only at higher temperatures, the successful deposition highlighted some interesting observations. It would appear that only minor alterations in alkoxide environment have substantial impact on deposition capabilities, with 2° alkoxide [Sn(O^{s}Bu)$_2$] **(24)** displaying no deposition at all. This is indicative that it is not influenced by steric bulk of substituents, as the bulkier system [Sn{OC(CH$_3$)$_2$CH$_2$CH$_3$}$_2$ **(26)** was shown successfully deposit SnO thin films.

Also highlighted, is the importance of precursor choice, with [Sn{OC(CH$_3$)$_2$CH$_2$CH$_3$}$_2$] **(26)** displaying a markedly higher estimated growth per cycle at elevated temperature than [Sn(O^{t}Bu)$_2$] **(23)**. Conversely, the latter system is capable of crystalline deposition at considerably lower temperatures than complex **26**. These factors are independent of any electrical and stoichiometric differences yet to be determined that may arise out of precursor selection.

4.4. Sn(II) Alkoxyethers

4.4.1. Alkoxyethers in ALD

An in-depth overview of alkoxyether chemistry can be found in Chapter 2, section 2.1.1. Therein a more comprehensive discussion over bonding modes and applications within CVD and ALD is given. To date, a vast array of alkoxyether complexes have been characterised and used in the chemical vapour deposition of a number of elements including Al, Bi, Hf, Sc, Zr, Ti, Ga, In and a number of lanthanides.[22,77–87]

Uses within ALD are somewhat more constrained. With relatively low volatility and facile formation of higher nuclearity species many processes are constrained to a solvent-based approach, such as the liquid-injection ALD of the 1-methoxy-2-methylpropan-2-oxide (mmp) complexes of aluminium, bismuth, titanium, praseodymium and gadolinium in solvents such as ethylcyclohexane or tetraglyme.[88,80,82,89] Conventional ALD has thus far been confined to a low number of elements, such as the ALD of $CeHfO_2$ composites with $[Ce(mmp)_4]$, requiring precursor source temperatures of 130 °C.[90,91]

Despite these disadvantages, the analogous tin(II) complexes have not been characterised in this regard, and due to the obvious similarities between the complexes of 1-methoxy-2-propanol (mp) and 1-methoxy-2-methylpropan-2-ol (mmp), and the aminoalkoxide systems characterised in Chapter 2, a brief investigation into their respective properties was undertaken.

4.4.2. Synthesis and Characterisation

Reactions of two equivalents of the alkoxyethers 1-methoxy-2-propanol and 1-methoxy-2-methyl-2-propanol with $[Sn\{N(SiMe_3)_2\}_2]$ afforded the complexes $[Sn\{OC(CH_3)CH_2OMe\}_2]$ **(29)** and $[Sn\{OC(CH_3)_2CH_2OMe\}_2]$ **(30)** in good yield. After distillation under static vacuum at 150 °C (10^{-2} mbar), compound **29** presented as a viscous liquid. Contrastingly, after storage at –28 °C, compound **30** was collected as colourless needles of suitable quality for single crystal X-ray diffraction.

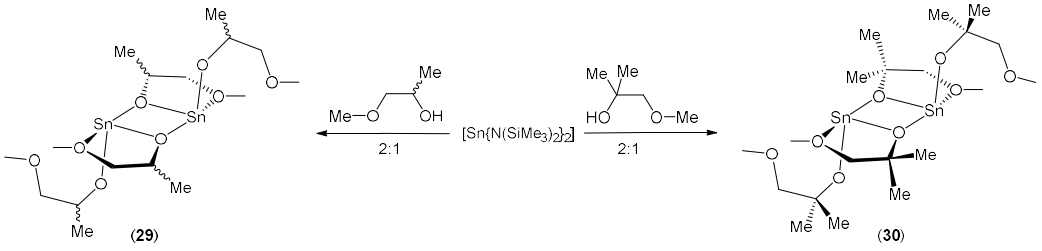

*Scheme 4.6 – Synthetic route to complexes **29** and **30**.*

The ^{1}H NMR spectrum of **29** displayed the expected resonances, suitably distinct from those of the free pro-ligand, consisting of two multiplet signals at δ = 4.47-4.53 ppm (C*H*(CH$_3$)) and δ = 3.24-3.31 ppm (C*H*$_2$), followed by singlet and doublet resonances at δ = 3.17 and 1.36 (J = 6.3 Hz) ppm, ascribed to the methoxy and backbone CHC*H*$_3$ respectively. Similarly, the ^{13}C{^{1}H} NMR spectrum displays well-defined signals at δ = 80.5, 67.6, 57.9 and 22.4 ppm, corresponding to the methylene, alkoxide 2° carbon, methoxy and chiral CH*C*H$_3$ environments respectively. The ^{119}Sn NMR spectrum shows a broad resonance at δ = –298 ppm.

The NMR analysis of **30** presents in a similar fashion, with the ^{1}H NMR spectrum displaying three singlet resonances in a 2:3:6 ratio at δ = 3.27, 3.28 and 1.54 ppm, with each ascribed to the methylene, methoxy and dimethyl groups respectively. The ^{13}C{^{1}H} NMR spectrum also displays the expected signals at δ = 83.9, 58.1 and 29.9 ppm and correlate to the same progression of environments seen in the ^{1}H NMR spectrum. Finally, the ^{119}Sn NMR displays a signal at δ = –246 ppm downfield of that observed for **29**.

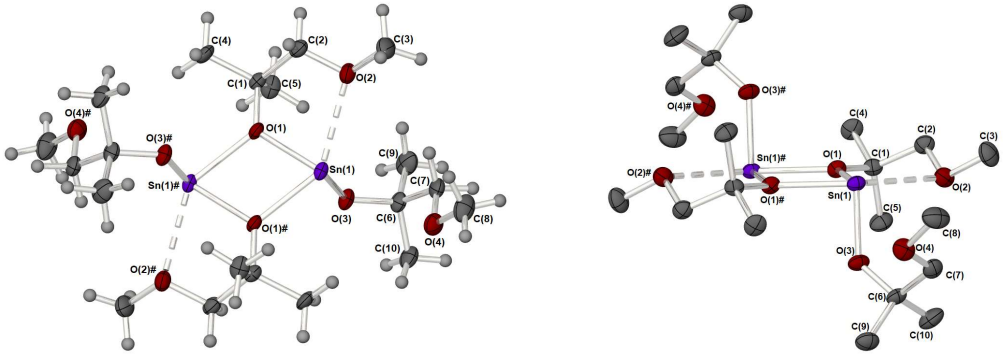

*Figure 4.13 – Molecular structure of [Sn{OC(CH$_3$)$_2$CH$_2$OMe}$_2$] **30**. Thermal ellipsoids shown at 50% probability. Symmetry equivalent atoms are generated by the symmetry operator: # –X, 1–Y, –Z.*

The molecular structure differs significantly from that observed for the analogous aminoalkoxide [Sn(dmamp)$_2$] **(7)**, Chapter 2. Whereas all homoleptic chelating aminoalkoxide complexes synthesised in this investigation (**1**, **4**, **7** and **10**) crystallised in monomeric form, alkoxyether **30** exists as a dimer comprising two identical halves bridged by μ_2-alkoxoether ligands.

The structure of **30** is directly comparable to that of the [Sn(O^{t}Bu)$_2$]$_2$ dimer, with a central planar {Sn$_2$O$_2$} heterocycle and terminal alkoxide ligands adopting a trans configuration across the {Sn$_2$O$_2$} ring. These terminal alkoxide bonds sit at almost 90° to the central heterocycle, with angles of 94.1° and 89.9° (O(1)–Sn–O(3)$_t$ and O(1)$_1$–Sn–O(3)$_t$ respectively, where $_1$ denotes the symmetrical other half of the complex, and $_t$ denotes terminally-bound alkoxide).

If no consideration were given to the extraordinarily long Sn–O distance between tin centre and the pendant ether of the terminal alkoxide (3.203(3) Å), the tin(II) centres can be seen to adopt the pseudo trigonal-pyramidal geometry so often observed in four-coordinate tin(II) systems. This geometry gives rise to an angle of 138.3(1)° between axially coordinated oxygens $O(1)_1$ and $O(2)_E$ ($_E$ denoting datively bound ether group), and an equatorial angle of 94.1(1)° between terminal alkoxide $O(3)_t$ and heterocyclic O(1). The angle between equatorial and axial planes presents as 89.11°.

*Table 4.6 – Relevant bond lengths and angles within compound **28**.*

Angle (°)		**Distance (Å)**	
O(1)#–Sn–O(2)	138.3(1)	Sn–Sn	3.5302(3)
O(1)–Sn–O(3)	94.1(1)	Sn–O(1)	2.144(3)
Angle between O(1)#–Sn–O(2) plane and O(3)–Sn–O(1) plane	89.11	Sn–O(1)#	2.185(3)
		Sn–O(2)	2.752(3)
		Sn–O(3)	2.030(3)
O(1)–Sn–O(3)	94.1(1)	Sn---O(4)	3.203(3)
O(1)#–Sn–O(3)	89.9(1)		
O(1)–Sn–O(1)#	70.8(1)	O(1)–C(1)	1.432(5)
		O(3)–C(6)	1.410(4)
Sn–O(1)–Sn	109.2(1)		
∑ angles about O(1)	359.2		
C(2)–O(2)–Sn	99.6(2)		
∑ angles about O(2)	324.9		

The alkoxide oxygen atoms forming the $\{Sn_2O_2\}$ heterocycle exhibit a planar sp^2 hybridisation, with Sn–O–Sn angles of 109.2° and the sum of bonding angles at each oxygen totalling 359.2°. Conversely, the coordinated ether pendant moieties possess total bonding angles of 324.9°, indicating an sp^3 oxygen environment consistent with the dative coordination of a single lone pair to the tin centre.

Bond lengths across the molecule are on the whole unremarkable, with bridging μ_2-O–Sn lengths and terminal lengths commensurate with the other alkoxide complexes studied. Elongated O→Sn bonds (2.752(3) Å) are however observed for the ether moieties adjoining the heterocyclic alkoxides, whilst a long-range interaction between the pendant ether of the terminal ligands and tin centres is tentatively suggested with a distance of 3.203(3) Å.

The structural characterisation of alkoxyether complex **30** provides an interesting contrast with the aminoalkoxide complexes characterised in Chapter 2. With the alkoxide environment remaining unchanged between the aminoalkoxide and alkoxoether systems, it is perhaps

surprising that μ_2-alkoxide bridges form. It therefore seems likely that the influence of the pendant group change from -NMe_2 to -OMe has a greater effect than was first expected. Either the additional steric bulk of the second methyl substituent on the -NMe_2 moiety exerts a steric influence large enough to encourage the formation of the monomer over the dimer, or the orientation and degree of dative donation is greater with an sp^3 nitrogen than oxygen.

It is likely that with a ^{119}Sn chemical shift very similar to that of dimeric [Sn{$OC(CH_3)_2CH_2OMe$}$_2$] **(30)**, the complex [Sn{$OCH(CH_3)CH_2OMe$}$_2$] **(29)** also exists in dimeric form and as such these species would prove to be an interesting class of molecules for further characterisation. It is unlikely that such dimers would rival the volatility and reactivity demonstrated by their aminoalkoxide counterparts, though applications in lower-volatility deposition methods and catalysis may prove fruitful. To elucidate the volatility of complexes **29** and **30**, thermogravimetric analyses were undertaken.

4.4.3. Thermogravimetric Analysis

Mass Loss-Temperature Thermogravimetric Analysis

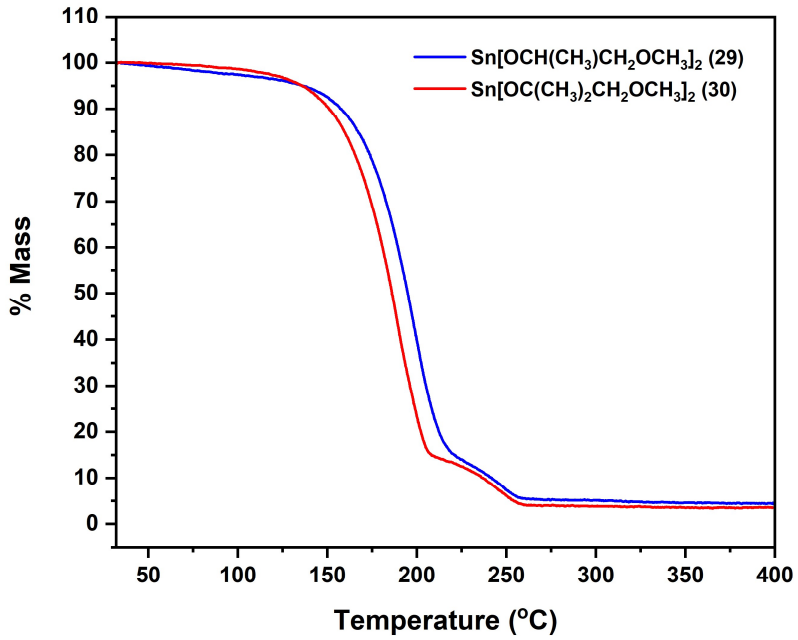

*Figure 4.14 – Mass loss/temperature TGA plots for Sn(II) alkoxyethers **29** and **30**. Ramp rate of 5 °C min^{-1} and Ar flow of 20 ml min^{-1}.*

With residual masses of 4.5% and 3.7% respectively, alkoxyether complexes **29** and **30** display similar and almost complete volatilities. The TGA traces display the second mass loss feature that was observed in the thermal profiles of the simple alkoxide compounds, indicative

of either decomposition at higher temperatures, or the presence of cluster species. The two complexes appeared to exhibit similar volatility, showing largely identical thermal traces.

*Table 4.7 – Residual masses from the TGA of **29** and **30**, with expected masses of decomposition products.*

		Expected Residual Mass (%)		
Compound	Residual Mass (%)	SnO	SnO_2	Sn
29	4.5	45.4	50.8	40.1
30	3.7	41.5	46.4	36.5

Isothermal Thermogravimetric Analysis

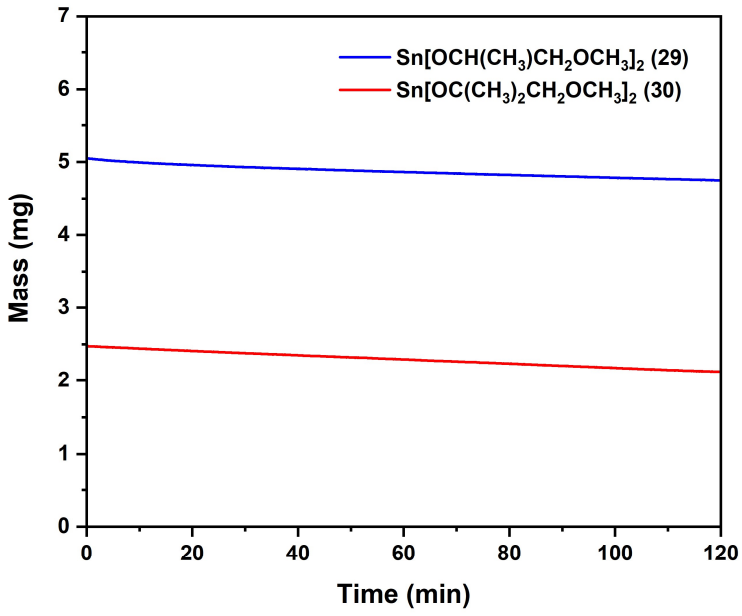

*Figure 4.15 – Isothermal TGA plots for Sn(II) alkoxyethers **29** and **30**. Ar flow of 20 ml min^{-1}.*

The similarity between volatilities of complexes 29 and 30 was confirmed via isothermal experiments held at 70 °C. The bulkier alkoxyether $[Sn\{OC(CH_3)_2CH_2OMe\}_2]$ **(30)** displayed an evaporation rate of 22.8 μg min^{-1} cm^{-1}, whilst complex **29** was shown to evaporate at a rate of 17.6 μg min^{-1} cm^{-1}. The low volatility exhibited by the two systems when compared to that of other compounds characterised throughout this study is unsurprising given their dimeric nature and larger molecular weight.

More interesting, however, is the similarity between the two species when compared to the monomeric aminoalkoxide species catalogued in Chapter 2. There proved to be a remarkable disparity between the analogous species to **29**, [Sn(dmap)$_2$] **(4)**, and the analogous species to **30**, [Sn(dmamp)$_2$] **(7)**, a difference which is not observed in the alkoxyether complexes. [Sn(dmamp)$_2$] was shown to display a considerably higher volatility (118.7 μg min^{-1} cm^{-1}) than [Sn(dmap)$_2$] (55.0 μg min^{-1} cm^{-1}) at the same temperature. The reason for this disparity is not immediately evident.

*Table 4.8 – Evaporation rates of compounds **29** and **30** at 70 °C.*

Compound	Evaporation rate (μg min^{-1} cm^{-2})
29	17.6
30	22.8

Despite the low volatilities and dimeric nature, the alkoxyether complexes **29** and **30** provide interesting contrast to the other species characterised throughout the course of this research. With volatilities not best suited to conventional ALD processes, their application in techniques such as liquid-injection atomic layer deposition would be worthwhile investigating, particularly given the prior demonstration of such systems within these techniques.[81,92,93]

4.5. Conclusion

The work contained within this chapter entailed a brief investigation of an overlooked application of tin(II) alkoxides. With the chemistry of many simple alkoxide species well-explored, a range of simple complexes were synthesised and their properties as potential atomic layer deposition precursors characterised.

Unexpectedly successful deposition was demonstrated with an H_2O ALD process wtih the tertiary alkoxide species [Sn(O^{t}Bu)$_2$] **(23)** and [Sn{OC(CH$_3$)$_2$CH$_2$CH$_3$}$_2$] **(26)**, whilst no deposition was observed for the closely related secondary alkoxide [Sn(O^{s}Bu)$_2$] **(24)**. Though initially envisaged as a proof-of-concept study, estimated growth rates across a wide temperature region of 130-250 °C were established for [Sn(O^{t}Bu)$_2$] **(23)**, along with a temperature window in which crystalline, highly oriented SnO was obtained (150-210 °C). A maximum growth per cycle for crystalline material of 0.37 Å was observed at 150 °C, which represents a significant improvement when compared to the maximum growth rate for crystalline films reported by Han et al. for the [Sn(dmamp)$_2$]/H_2O process, which also was found to be at 150 °C.

Similarly, a smaller study into the deposition capabilities of [Sn{OC(CH$_3$)$_2$CH$_2$CH$_3$}$_2$] **(26)** was undertaken, showing the deposition of amorphous films at temperatures of 170 °C, and

crystalline SnO films at 210 °C, the latter with a growth per cycle of 0.27 Å. This in itself is an interesting observation, as this growth rate is significantly higher than that reported for [Sn(dmamp)$_2$] at the same temperature (0.08 Å/cy),[94] and is higher also than that found within this study for [Sn(O^{t}Bu)$_2$] **(24)** (0.16 Å/cy). These observations are important, as it has been reported that the most promising electrical characteristics for TFT applications were obtained for films grown from [Sn(dmamp)$_2$] at 210 °C[95] and with current precursor technology, growth rates of 0.08 Å/cy are not suitable for fabrication in a commercial setting.

In order to explore the electronic influences within simple tin(II) alkoxides, the fluorinated derivatives of [Sn(O^{i}Pr)$_2$]$_\infty$ and [Sn(O^{t}Bu)$_2$]$_2$ were synthesised and structurally characterised. The resultant complexes, [Sn(O^{Fi}Pr)$_2$]$_3$ **(27)** and [Sn(O^{Ft}Bu)$_2$]$_2$ **(28)**, were found to exhibit interesting structural differences to their non-fluorinated analogues, with **27** presenting as a trimeric complex consisting of a central four-coordinate tin(II) flanked by two three-coordinate tin(II) atoms, in contrast to polymeric [Sn(O^{i}Pr)$_2$]$_\infty$. Whilst presenting as a dimer in a similar manner to [Sn(O^{t}Bu)$_2$]$_2$, **28** was observed to show significant asymmetry and distortion in an attempt to satisfy the electronically unsaturated tin centres. Whilst no deposition was undertaken using these complexes, atomic layer deposition using H_2O, H_2O_2 and O_2-plasma would prove very interesting, providing potential routes to tin(II) oxide for the H_2O process, and to the highly desirable fluorine-doped tin(IV) oxide (FTO) with the plasma and peroxide processes.

Furthermore, the two final complexes characterised in this Chapter, liquid [Sn{OCH(CH$_3$)$_2$CH$_2$OMe}$_2$] **(29)** and solid [Sn{OCH(CH$_3$)$_2$CH$_2$OMe}$_2$] **(30)**, were synthesised and their thermal properties characterised. Complex **(30)** was shown to be dimeric in the solid-state and similar ^{119}Sn NMR between the two complexes indicates that this is also likely to be the case for liquid **29**. This could account for the low volatilities observed for the two species when compared to the aminoalkoxide analogues [Sn(dmap)$_2$] **(4)** and [Sn(dmamp)$_2$] **(7)**, characterised in Chapter 2. Despite the low volatility, the ligand system has proved effective in the liquid-injected atomic layer deposition of a number of other metal oxides,[80,96] and as such would prove an interesting area for further study.

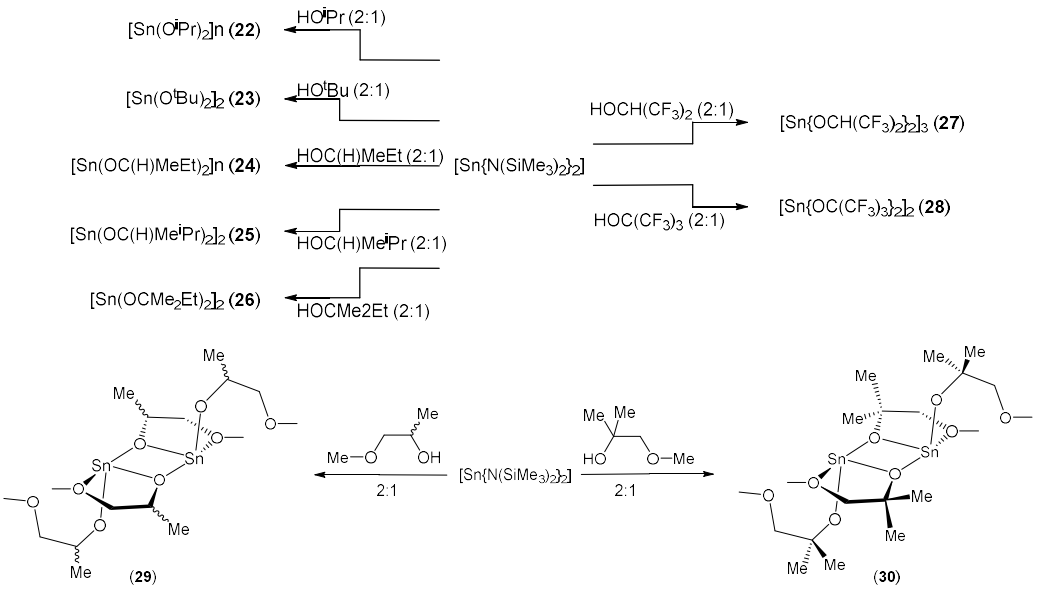

Figure 4.16 – Summary of reactions and complexes presented within Chapter 4.

4.6. Experimental

Generic experimental details are given in the Appendix, but it is necessary to explain that due to the highly air and moisture sensitive nature of complexes **22**-**30**, significant difficulty was encountered in obtaining sufficiently consistent elemental analysis results, despite numerous attempts for each novel compound. The high sensitivity of these systems is exacerbated by the liquid nature of many of the compounds. However, the molecular structures of all novel complexes that present as solids have been confirmed with single-crystal X-ray diffraction, and all complexes have been characterised with multinuclear NMR and 2D NMR spectroscopy. Mass spectroscopy was additionally attempted, but the lack of suitable non-reactive solvents and air-sensitive equipment prevented the collection of any meaningful data.

$[Sn(O^iPr)_2]_\infty$ (22)

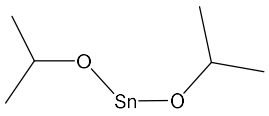

Compound **22** was prepared via adaptation of published procedures.[57,64]

A stirring solution of $[Sn\{N(SiMe_3)_2\}_2]$ (0.88 g, 2 mmol) in hexane (50 mL) was cooled and added to a –78 °C solution of 2-propanol (0.24 g, 4 mmol) in hexane (20 mL) affording a colourless solution. After removal of the volatiles, the white powder was redissolved in hexane, filtered through Celite® and the volume reduced. Colourless crystals were afforded at –28 °C. (0.37 g, 80 %).

^{1}H NMR (500 MHz, C_6D_6); 4.62 (sept, 2H, C*H*$(CH_3)_2$, 1.34 (d, 12H, C*H*$_3$).
^{13}C{^{1}H} NMR (75.5 MHz, C_6D_6); 65.6 (2C, *C*H$(CH_3)_2$), 28.2 (4C, CH(*C*H$_3)_2$).
^{119}Sn NMR (111.8 MHz, C_6D_6); –211

$[Sn(O^tBu)_2]_2$ (23)

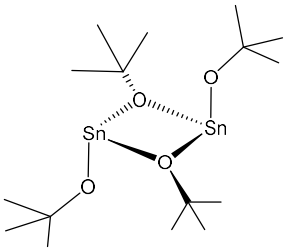

Compound **23** was prepared via adaptation of a published procedures.[57,64]

A stirring solution of [Sn{N(SiMe$_3$)$_2$}$_2$] (0.88 g, 2 mmol) in hexane (50 mL) was cooled and added to a –78 °C solution of tert-butanol (0.30 g, 4 mmol) in hexane (20 mL) affording a colourless solution. After removal of the volatiles, the white powder was redissolved in hexane, filtered through Celite® and the volume reduced. Colourless crystals were afforded at –28 °C. (0.48 g, 91 %).

^{1}H NMR (500 MHz, C_6D_6); 1.45 (s, 18H, C*H*$_3$).
^{13}C{^{1}H} NMR (75.5 MHz, C_6D_6); 72.8 (2C, *C*(CH$_3$)$_3$), 32.4 (6C, C(*C*H$_3$)$_2$).
^{119}Sn NMR (111.8 MHz, C_6D_6); –91

[Sn(O^{s}Bu)$_2$] (24)

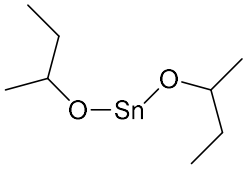

A stirring solution of [Sn{N(SiMe$_3$)$_2$}$_2$] (0.88 g, 2 mmol) in hexane (50 mL) was cooled and added to a –78 °C solution of sec-butanol (0.30 g, 4 mmol) in hexane (20 mL) affording a colourless solution. After removal of the volatiles, the viscous clear liquid was redissolved in hexane, filtered through Celite® and the solvent removed. Distillation at 150 °C into liquid N_2 (10^{-2} mbar) afforded a colourless liquid. (0.37 g, 70 %)

^{1}H NMR (500 MHz, C_6D_6); 4.26-4.33 (m, 2H, C*H*(CH$_3$), 1.70-1.80 (br m, 2H, C*H*$_2$), 1.50-1.60 (br m, 2H, C*H*$_2$), 1.36 (d, J = 6.2 Hz, 6H, OCH(C*H*$_3$)), 0.98 (t, 7.6 Hz, 6H, CH$_2$C*H*$_3$).
^{13}C{^{1}H} NMR (75.5 MHz, C_6D_6); 71.4 (2C, *C*H(CH$_3$)), 35.1 (2C, CH$_2$), 26.1 (OCH(*C*H$_3$)), 11.0 (2C, CH$_2$*C*H$_3$).
^{119}Sn NMR (111.8 MHz, C_6D_6); –141

[Sn{OCH(CH$_3$)CH(CH$_3$)$_2$}$_2$] (25)

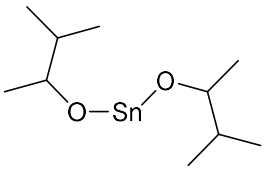

A stirring solution of [Sn{N(SiMe$_3$)$_2$}$_2$] (0.88 g, 2 mmol) in hexane (50 mL) was cooled and added to a –78 °C solution of 3-methyl-2-butanol (0.35 g, 4 mmol) in hexane (20 mL) affording a colourless solution. After removal of the volatiles, the viscous clear liquid was redissolved in

hexane, filtered through Celite® and the solvent removed. Distillation at 170 °C into liquid N_2 (10^{-2} mbar) afforded a viscous colourless liquid. (0.38 g, 64 %)

^{1}H NMR (500 MHz, C_6D_6); 4.0-4.08 (m, 2H, OC*H*(CH_3)), 1.66-1.76 (m, 2H, C*H*(CH_3)$_2$), 1.29 (d, J = 5.6 Hz, 6H, OCH(C*H*$_3$)), 1.03 (d, J = 6.2 Hz, 6H, CH(C*H*$_3$)), 0.98 (d, J = 6.2 Hz, 6H, CH(C*H*$_3$)).
^{13}C{^{1}H} NMR (75.5 MHz, C_6D_6); 74.1 (2C, O*C*H), 36.8 (2C, OCH(*C*H$_3$)), 22.6 (2C, *C*H(CH_3)$_2$), 18.8 (2C, CH(*C*H$_3$)$_2$), 18.0 (2C, CH(*C*H$_3$)$_2$).
^{119}Sn NMR (111.8 MHz, C_6D_6); –154

[Sn{OC(CH_3)$_2$$CH_2$$CH_3$}$_2$] (26)

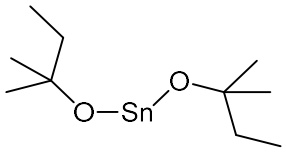

Compound **26** was prepared via an adaptation of a published procedure.[64]

A stirring solution of [Sn{N($SiMe_3$)$_2$}$_2$] (0.88 g, 2 mmol) in hexane (50 mL) was cooled and added to a –78 °C solution of 2-methyl-2-butanol (0.35 g, 4 mmol) in hexane (20 mL) affording a colourless solution. After removal of the volatiles, the viscous clear liquid was redissolved in hexane, filtered through Celite® and the solvent removed. Distillation at 120 °C into liquid N_2 (10^{-2} mbar) afforded a colourless liquid. (0.39 g, 67 %)

^{1}H NMR (500 MHz, C_6D_6); 1.71 (q, J = 7.5 Hz, 4H, C*H*$_2$), 1.41 (s, 12H, C(C*H*$_3$)$_2$), 1.05 (t, J = 7.5 Hz, 6H, CH_2C*H*$_3$).
^{13}C{^{1}H} NMR (75.5 MHz, C_6D_6); 39.7 (2C, *C*H$_2$), 32.0 (br, 4C, C(*C*H$_3$)$_2$), 9.74 (2C, CH_2*C*H$_3$)
^{119}Sn NMR (111.8 MHz, C_6D_6); –98

[Sn(O^{Fi}Pr)$_2$]$_3$ (27)

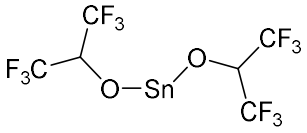

A stirring solution of [Sn{N($SiMe_3$)$_2$}$_2$] (0.88 g, 2 mmol) in Et_2O (50 mL) was cooled and added to a –78 °C solution of 1,1,1,3,3,3-hexafluoro-2-propanol (0.67 g, 4 mmol) in Et_2O (20 mL) affording a colourless solution. After removal of the volatiles, the white powder was redissolved in hexane and filtered through Celite®, before subsequent removal of volatiles.

Further dissolutions were undertaken (5 x 10 mL), with the volatiles removed after each dissolution. Low-melting crystals were collected from 5 mL of hexane at –28 °C. (0.64 g, 71 %).

^{1}H NMR (500 MHz, C_6D_6); 4.45-4.55 (m, 2H, C*H*)
^{19}F NMR (470.6 MHz, C_6D_6); –75.2
^{13}C{^{1}H} NMR (75.5 MHz, C_6D_6); 123.0 (q, $^{1}J_{CF}$ = 285 Hz, 4C), 70.6 (sept, $^{2}J_{CF}$ = 33 Hz, 2C, C*H*).
^{119}Sn NMR (111.8 MHz, C_6D_6); –498, –441

[Sn(O^{Ft}Bu)$_2$]$_2$ (28)

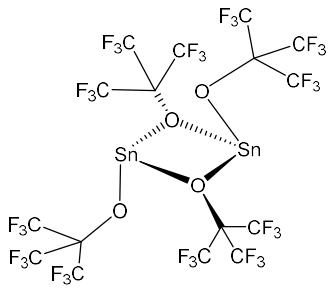

A stirring solution of [Sn{N(SiMe$_3$)$_2$}$_2$] (0.88 g, 2 mmol) in Et$_2$O (50 mL) was cooled and added to a –78 °C solution of 1,1,1,3,3,3-hexafluoro-2-trifluoromethyl-2-propanol (0.94 g, 4 mmol) in Et$_2$O (20 mL) affording a colourless solution. After removal of the volatiles, the pale orange powder was redissolved in hexane and filtered through Celite®, before subsequent removal of volatiles. Further dissolutions were undertaken (5 x 10 mL), with the volatiles removed after each dissolution. Orange crystals were collected from 5 mL of hexane at –28 °C. (0.75 g, 64 %).

^{19}F NMR (470.6 MHz, C_6D_6); –74.5
^{13}C{^{1}H} NMR (75.5 MHz, C_6D_6); 122.2 (q, $^{1}J_{CF}$ = 292.8 Hz, 6C, *C*F$_3$)

[Sn{OCH(CH$_3$)CH$_2$OMe}$_2$] (29)

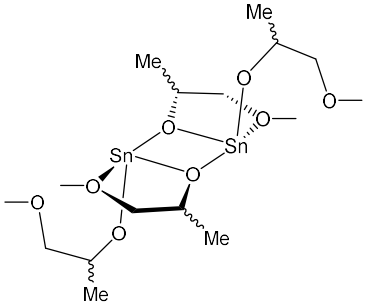

A stirring solution of [Sn{N(SiMe$_3$)$_2$}$_2$] (0.88 g, 2 mmol) in hexane (50 mL) was cooled and added to a –78 °C solution of 1-methoxy-2-propanol (0.36 g, 4 mmol) in hexane (20 mL) affording a colourless solution. After removal of the volatiles, the viscous clear liquid was redissolved in hexane, filtered through Celite® and the solvent removed. Distillation at 120 °C into liquid N_2 (10^{-2} mbar) afforded a viscous colourless liquid. (0.43 g, 72 %)

^{1}H NMR (500 MHz, C_6D_6); 4.47-4.53 (m, 2H, C*H*(CH$_3$)), 3.24-3.31 (m, 4H, C*H*$_2$), 3.17 (s, 6H, O*Me*), 1.36 (d, J = 6.3 Hz, 6H, CH(C*H*$_3$)).
^{13}C{^{1}H} NMR (75.5 MHz, C_6D_6); 80.5 (2C, *C*H$_2$), 67.6 (2H, O*C*), 57.9 (2C, O*Me*), 22.4 (2C, CH*C*H$_3$).
^{119}Sn NMR (111.8 MHz, C_6D_6); –298

[Sn{OC(CH$_3$)$_2$CH$_2$OMe}$_2$] (30)

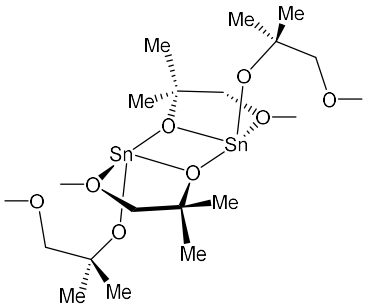

A stirring solution of [Sn{N(SiMe$_3$)$_2$}$_2$] (0.88 g, 2 mmol) in hexane (50 mL) was cooled and added to a –78 °C solution of 1-methoxy-2-methyl-2-propanol (0.42 g, 4 mmol) in hexane (20 mL) affording a colourless solution. After removal of the volatiles, the white powder was redissolved in hexane, filtered through Celite® and the volume reduced. Colourless crystals were afforded at –28 °C. (0.51 g, 80 %)

^{1}H NMR (500 MHz, C_6D_6); 3.27 (s, 4H, C*H*$_2$), 3.28 (s, 6H, O*Me*), 1.54 (s, 12H, (C*H*$_3$)$_2$).
^{13}C{^{1}H} NMR (75.5 MHz, C_6D_6); 83.9 (2C, *C*H$_2$), 58.1 (2C, O*Me*), 29.9 (4C, (*C*H$_3$)$_2$).
^{119}Sn NMR (111.8 MHz, C_6D_6); –246

4.7. References

1 V. G. Kessler, in *Comprehensive Inorganic Chemistry II*, Eds. J. Reedijk and K. Poeppelmeier, Elsevier, Amsterdam, 2013, 455–470.

2 R. C. Mehrotra and A. Singh, *Chem. Soc. Rev.*, 1996, **25**, 1–13.

3 D. C. Bradley, in *Metal-Organic Compounds*, ACS Publishing, New York, 1959, **23**, 2–10.

4 M. H. Chisholm, *J. Solid State Chem.*, 1985, **57**, 120–133.

5 D. C. Bradley, *Nature*, 1958, **182**, 1211.

6 R. C. Mehrotra, *J. Non. Cryst. Solids*, 1988, **100**, 1–15.

7 J. A. Garden and S. D. Pike, *Dalton Trans.*, 2018, **47**, 3638–3662.

8 S. L. Cumberland, K. M. Hanif, A. Javier, G. A. Khitrov, G. F. Strouse, S. M. Woessner and C. S. Yun, *Chem. Mater.*, 2002, **14**, 1576–1584.

9 N. Hollingsworth, G. A. Horley, M. Mazhar, M. F. Mahon, K. C. Molloy, P. W. Haycock, C. P. Myers and G. W. Critchlow, *Appl. Organomet. Chem.*, 2006, **20**, 687–695.

10 G. V Kunte, S. A. Shivashankar and A. M. Umarji, *Thermochim. Acta*, 2008, **474**, 12–15.

11 D. C. Bradley, *Chem. Rev.*, 1989, **89**, 1317–1322.

12 N. Steunou, G. Kickelbick and C. Sanchez, *J. Chem. Soc., Dalton Trans.,*1999, 3653–3655.

13 M. G. Stanton, C. B. Allen, R. M. Kissling, A. L. Lincoln and M. R. Gagné, *J. Am. Chem. Soc.*, 1998, **120**, 24, 5981-5989.

14 R. M. Kissling and M. R. Gagné, *J. Org. Chem.*, 1999, **64**, 1585–1590.

15 M. G. Stanton and M. R. Gagné, *J. Am. Chem. Soc.*, 1997, **119**, 5075–5076.

16 W. A. Herrmann, N. W. Huber and O. Runte, *Angew. Chemie Int. Ed. Engl.*, 1995, **34**, 2187–2206.

17 A. Rahtu, K. Kukli and M. Ritala, *Chem. Mater.*, 2001, **13**, 817–823.

18 K. Knapas and M. Ritala, *Crit. Rev. Solid State Mater. Sci.*, 2013, **38**, 167–202.

19 O. Kříž, B. Čásenský, A. Lyčka, J. Fusek and S. Heřmánek, *J. Magn. Reson.*, 1984, **60**, 375–381.

20 W. Fieggen and H. Gerding, *Recl. des Trav. Chim. des Pays-Bas*, 1970, **89**, 175–185.

21 Y. Kuzminykh, A. Dabirian, M. O. Reinke and P. Hoffmann, *Surf. & Coatings Technol.*, **230**, 13–21.

22 P. Marchand and C. J. Carmalt, *Coord. Chem. Rev.*, 2013, **257**, 3202–3221.

23 S. Suh, J. Guan, L. A. Mîinea, J.-S. M. Lehn and D. M. Hoffman, *Chem. Mater.*, 2004, **16**, 1667–1673.

24 A. Baunemann, R. Thomas, R. Becker, M. Winter, R. A Fischer, P. Ehrhart, R. Waser and A. Devi, *Chem. Commun.*, 2004, 1610-1611.

25 T. S. Yang, K.-S. An, E.-J. Lee, W. Cho, H. S. Jang, S. K. Park, Y. K. Lee, T.-M. Chung, C. G. Kim, S. Kim, J.-H. Hwang, C. Lee, N.-S. Lee and Y. Kim, *Chem. Mater.*, 2005,

17, 6713–6718.

26 P. A. Williams, J. L. Roberts, A. C. Jones, P. R. Chalker, N. L. Tobin, J. F. Bickley, H. O. Davies, L. M. Smith and T. J. Leedham, *Chem. Vap. Deposition*, 2002, **8**, 163–170.

27 H. Yoshioka, T. Ishihara and M. Motoyama, *Adv. Mater. '93*, 1994, 735–738.

28 H. Kadokura, Y. Okuhara, M. Mitsuya and H. Funakubo, *Chem. Vap. Deposition,* 2000, **6**, 225–227.

29 P. M. Jeffries and G. S. Girolami, *Chem. Mater.*, 1989, **1**, 8–10.

30 M. J. Hampden-Smith and T. T. Kodas, *Chem. Vap. Deposition*, 2018, **1**, 8–23.

31 S. K. Kim, S. Hoffmann-Eifert, S. Mi and R. Waser, *J. Electrochem. Soc.*, 2009, **156**, D296.

32 T. Blanquart, J. Niinistö, M. Gavagnin, V. Longo, V. R. Pallem, C. Dussarrat, M. Ritala and M. Leskelä, *Chem. Mater.*, 2012, **24**, 3420–3424.

33 X. Chen, E. Pomerantseva, P. Banerjee, K. Gregorczyk, R. Ghodssi and G. Rubloff, *Chem. Mater.*, 2012, **24**, 1255–1261.

34 J. Musschoot, D. Deduytsche, R. L. Van Meirhaeghe and C. Detavernier, *ECS Trans.*, 2009, 29–37.

35 W. Cho, K. Sung, K.-S. An, S. Sook Lee, T.-M. Chung and Y. Kim, *J. Vac. Sci. Technol. A*, 2003, **21**, 1366–1370.

36 H. A. Gatz, D. Koushik, J. K. Rath, W. M. M. Kessels and R. E. I. Schropp, *Energy Procedia*, 2016, **92**, 624–632.

37 D. Garcia-Alonso, S. E. Potts, C. A. A. van Helvoirt, M. A. Verheijen and W. M. M. Kessels, *J. Mater. Chem. C*, 2015, **3**, 3095–3107.

38 H. Lee, K. Kim, J.-J. Woo, D.-J. Jun, Y. Park, Y. Kim, H. W. Lee, Y. J. Cho and H. M. Cho, *Chem. Vap. Deposition*, 2011, **17**, 191–197.

39 J. D. Ferguson, E. R. Smith, A. W. Weimer and S. M. George, *J. Electrochem. Soc.*, 2004, **151**, G528.

40 K. A. Miller, C. John, K. Z. Zhang, K. T. Nicholson, F. R. McFeely and M. M. Banaszak Holl, *Thin Solid Films*, 2001, **397**, 78–82.

41 C. Nistorica, J.-F. Liu, I. Gory, G. D. Skidmore, F. M. Mantiziba, B. E. Gnade and J. Kim, *J. Vac. Sci. Technol. A*, 2005, **23**, 836–840.

42 T. Hatanpää, K. Kukli, M. Ritala and M. Leskelä, *J. Therm. Anal. Calorim.*, 2011, **105**, 61–71.

43 S. Dueñas, H. Castán, H. García, A. Gómez, L. Bailón, K. Kukli, T. Hatanpää, J. Lu, M. Ritala and M. Leskelä, *J. Electrochem. Soc.*, 2007, **154**, G207.

44 G. T. DeLong, D. K. Pannell, M. T. Clarke and R. D. Thomas, *J. Am. Chem. Soc.*, 1993, **115**, 7013–7014.

45 J. D. Kahn, A. Haag and P. v. R. Schleyer, *J. Phys. Chem.*, 1988, **92**, 212–220.

46 M. Putkonen, T. Aaltonen, M. Alnes, T. Sajavaara, O. Nilsen and H. Fjellvag, *J. Mater. Chem.*, 2009, **19**, 8767–8771.

47 M. Nisula, Y. Shindo, H. Koga and M. Karppinen, *Chem. Mater.*, 2015, **27**, 6987–6993.

48 A. C. Kozen, A. J. Pearse, C.-F. Lin, M. Noked and G. W. Rubloff, *Chem. Mater.*, 2015, **27**, 5324–5331.

49 H. H. Sønsteby, O. Nilsen and H. Fjellvåg, *J. Vac. Sci. Technol. A*, 2016, **34**, 041508.

50 E. Østreng, H. H. Sønsteby, S. Øien, O. Nilsen and H. Fjellvåg, *Dalton Trans.*, 2014, **43**, 16666–16672.

51 F. Salvatore, D. Ferri, M. Trifuoggi, C. Manfredi and E. Vasca, *Ann. Chim. 1997, **87** (7), 477-481.*

52 E. V Suslova, N. Y. Turova, V. G. Kessler and A. I. Belokon', *Russ. J. Inorg. Chem.*, 2007, **52**, 1682–1686.

53 T. J. Boyle, T. M. Alam, M. A. Rodriguez and C. A. Zechmann, *Inorg. Chem.*, 2002, **41**, 2574–2582.

54 N. Y. Turova, *Russ. Chem. Rev.*, 2004, **73**, 1041–1064.

55 L. G. Hubert-Pfalzgraf, *J. Mater. Chem.*, 2004, **14**, 3113–3123.

56 D. J. Teff, C. D. Minear, D. V Baxter and K. G. Caulton, *Inorg. Chem.*, 1998, **37**, 2547–2553.

57 M. S. Hill, A. L. Johnson, J. P. Lowe, K. C. Molloy, J. D. Parish, T. Wildsmith and A. L. Kingsley, *Dalton Trans.*, 2016, **45**, 18252–18258.

58 T. J. Boyle, T. L. Ward, S. M. De'Angeli, H. Xu and W. F. Hammetter, *Chem. Mater.*, 2003, **15**, 765–775.

59 S. Kannan Selvaraj, A. Feinerman and C. G. Takoudis, *J. Vac. Sci. Technol. A*, 2014, **32**, 01A112/1-01A112/6.

60 C. Marichy, N. Donato, M.-G. Willinger, M. Latino, D. Karpinsky, S.-H. Yu, G. Neri and N. Pinna, *Adv. Funct. Mater.*, 2010, **21**, 658–666.

61 E. Rauwel, G. Clavel, M.-G. Willinger, P. Rauwel and N. Pinna, *Angew. Chemie Int. Ed.*, 2008, **47**, 3592–3595.

62 E. Rauwel, M.-G. Willinger, F. Ducroquet, P. Rauwel, I. Matko, D. Kiselev and N. Pinna, *J. Phys. Chem. C*, 2008, **112**, 12754–12759.

63 S. Suh and D. M. Hoffman, *Inorg. Chem.*, 1996, **35**, 6164–6169.

64 T. Wildsmith, Ph.D. Thesis, University of Bath, 2014.

65 L. Wang, M. Bochmann, R. D. Cannon, J.-F. Carpentier, T. Roisnel and Y. Sarazin, *Eur. J. Inorg. Chem.*, 2013, **2013**, 5896–5905.

66 T. Fjeldberg, P. B. Hitchcock, M. F. Lappert, S. J. Smith and A. J. Thorne, *J. Chem. Soc. Chem. Commun.*, 1985, 939–941.

67 T. Wildsmith, M. S. Hill, A. L. Johnson, A. J. Kingsley and K. C. Molloy, *Chem. Commun.*, 2013, **49**, 8773–8775.

68 R. Hani and R. A. Geanangel, *Coord. Chem. Rev.*, 1982, **44**, 229–246.

69 T. J. Boyle, T. Q. Doan, L. A. M. Steele, C. Apblett, S. M. Hoppe, K. Hawthorne, R. M. Kalinich and W. M. Sigmund, *Dalton Trans.*, 2012, **41**, 9349–9364.

70 L. Wang, C. E. Kefalidis, T. Roisnel, S. Sinbandhit, L. Maron, J.-F. Carpentier and Y. Sarazin, *Organometallics*, 2015, **34**, 2139–2150.

71 I. Haiduc, F. T. Edelmann and J.-M. Lehn, *Supramolecular Organometallic Chemistry*, Wiley-VCH, Weinheim, 1999.

72 J. H. Han, Y. J. Chung, B. K. Park, S. K. Kim, H. S. Kim, C. G. Kim and T. M. Chung, *Chem. Mater.*, 2014, **26**, 6088–6091.

73 T. Eom, S. Choi, B. J. Choi, M. H. Lee, T. Gwon, S. H. Rha, W. Lee, M.-S. Kim, M. Xiao, I. Buchanan, D.-Y. Cho and C. S. Hwang, *Chem. Mater.*, 2012, **24**, 2099–2110.

74 T. Gwon, T. Eom, S. Yoo, H.-K. Lee, D.-Y. Cho, M.-S. Kim, I. Buchanan, M. Xiao, S. Ivanov and C. S. Hwang, *Chem. Mater.*, 2016, **28**, 7158–7166.

75 T. Gwon, T. Eom, S. Yoo, C. Yoo, E. Park, S. Kim, M.-S. Kim, I. Buchanan, M. Xiao, S. Ivanov and C. S. Hwang, *Chem. Mater.*, 2017, **29**, 8065–8072.

76 R. Timm, A. R. Head, S. Yngman, J. V Knutsson, M. Hjort, S. R. McKibbin, A. Troian, O. Persson, S. Urpelainen, J. Knudsen, J. Schnadt and A. Mikkelsen, *Nat. Commun.*, 2018, **9**, 1412.

77 M. A. Matchett, M. Y. Chiang and W. E. Buhro, *Inorg. Chem.*, 1990, **29**, 358–360.

78 H. C. Aspinall, J. F. Bickley, J. M. Gaskell, A. C. Jones, G. Labat, P. R. Chalker and P. A. Williams, *Inorg. Chem.*, 2007, **46**, 5852–5860.

79 H. C. Aspinall, J. Bacsa, A. C. Jones, J. S. Wrench, K. Black, P. R. Chalker, P. J. King, P. Marshall, M. Werner, H. O. Davies and R. Odedra, *Inorg. Chem.*, 2011, **50**, 11644–11652.

80 R. O'Kane, J. Gaskell, A. C. Jones, P. R. Chalker, K. Black, M. Werner, P. Taechakumput, S. Taylor, P. N. Heys and R. Odedra, *Chem. Vap. Depos.*, 2007, **13**, 609–617.

81 J. Thery, C. Dubourdieu, T. Baron, C. Ternon, H. Roussel and F. Pierre, *Chem. Vap. Deposition*, 2007, **13**, 232–238.

82 Y.-S. Min, Y. J. Cho and C. S. Hwang, *Chem. Mater.*, 2005, **17**, 626–631.

83 S. Van Elshocht, P. Lehnen, B. Seitzinger, A. Abrutis, C. Adelmann, B. Brijs, M. Caymax, T. Conard, S. De Gendt, A. Franquet, C. Lohe, M. Lukosius, A. Moussa, O. Richard, P. Williams, T. Witters, P. Zimmerman and M. Heyns, *J. Electrochem. Soc.*, 2006, **153**, F219–F224.

84 Y. Otani, K. Uchiyama, S. Okamura and T. Shiosaki, *Integr. Ferroelectr.*, 2006, **81**, 261–270.

85 C. Dubourdieu, E. Rauwel, C. Millon, P. Chaudouet, F. Ducroquet, N. Rochat, S. Rushworth and V. Cosnier, *Chem. Vap. Deposition*, 2006, **12**, 187–192.

86 R. J. Potter, P. A. Marshall, P. R. Chalker, S. Taylor, A. C. Jones, T. C. Q. Noakes and P. Bailey, *Appl. Phys. Lett.*, 2004, **84**, 4119–4121.

87 J. S. Zhao, D.-Y. Park, M. J. Seo, C. S. Hwang, Y. K. Han, C. H. Yang and K. Y. Oh, *J. Electrochem. Soc.*, 2004, **151**, C283–C291.

88 R. J. Potter, P. R. Chalker, T. D. Manning, H. C. Aspinall, Y. F. Loo, A. C. Jones, L. M. Smith, G. W. Critchlow and M. Schumacher, *Chem. Vap. Deposition*, 2005, **11**, 159–169.

89 J. Thery, T. Baron, C. Dubourdieu, C. Ternon, B. Pelissier, H. Roussel, S. Coindeau and I.-L. Prejbeanu, *Proc. Electrochem. Soc.*, 2005, **2005-01**, 498–509.

90 W.-H. Kim, M.-K. Kim, I.-K. Oh, W. J. Maeng, T. Cheon, S.-H. Kim, A. Noori, D. Thompson, S. Chu and H. Kim, *J. Am. Ceram. Soc.*, 2014, **97**, 1164–1169.

91 P. J. King, N. Sedghi, S. Hall, I. Z. Mitrovic, P. R. Chalker, M. Werner and S. Hindley, *J. Vac. Sci. Technol. B*, 2014, **32**, 03D103/1-03D103/5.

92 R. J. Potter, P. A. Marshall, J. L. Roberts, A. C. Jones, P. R. Chalker, M. Vehkamaeki, M. Ritala, M. Leskelae, P. A. Williams, H. O. Davies, N. L. Tobin and L. M. Smith, *Mater. Res. Soc. Symp. Proc.*, 2004, **784**, 97–108.

93 Y. S. Min, Y. J. Cho and C. S. Hwang, *Chem. Mater.*, 2005, **17**, 626–631.

94 J. H. Han, Y. J. Chung, B. K. Park, S. K. Kim, H.-S. Kim, C. G. Kim and T.-M. Chung, *Chem. Mater.*, 2014, **26**, 6088–6091.

95 S. H. Kim, I.-H. Baek, D. H. Kim, J. J. Pyeon, T.-M. Chung, S.-H. Baek, J.-S. Kim, J. H. Han and S. K. Kim, *J. Mater. Chem. C*, 2017, **5**, 3139–3145.

96 Y. S. Min, Y. J. Cho, I. P. Asanov, J. H. Han, W. D. Kim and C. S. Hwang, *Chem. Vap. Deposition*, 2005, **11**, 38–43.

Chapter 5

Chapter 5: Sn(II) Pyrrolide Complexes

5.1. Preface

This chapter is presented in the Alternative Format, with the entirety of the self-contained results having been accepted for publication within the RSC Journal Dalton Transactions. (J. D. Parish, M. W. Snook, A. L. Johnson and G. Kociok-Köhn, *Dalton Trans.*, 2018, **47**, 7721–7729).[1]

The publication is presented as accepted, with changes made to formatting. Additionally, side-on views of the molecular structures presented have been added, and the compound numbers amended with bracketed values to conform with the numbering used throughout this thesis. Whilst the introduction and brief review given within the publication are sufficient for the format in which the article was submitted, an overview of the background, scope and relevance of the work is first given. A final conclusion is also added to complete the integration of the publication into the work as whole.

5.2. Introduction

5.2.1. Further Aspects of Metal–Nitrogen Bonding

An overview of simple metal–nitrogen bonding has previously been given (Chapters 2 and 3). Focus within this overview was directed at bonding within systems directly relevant to those contained therein, omitting a number of alternative systems and pathways, the more relevant of which are discussed hereafter.

Much attention was previously drawn to bonding within systems comprising nitrogen in an sp^3 hybridisation, with either covalent nitrogen–metal interactions, or dative interactions between the nitrogen-based lone pair and a relevant metal acceptor orbital. Coverage was also given to systems that displayed an sp^2-nitrogen or planar geometry, which was usually encountered within μ_2–bridging nitrogen atoms and many terminal metal amides. This is exemplified within systems such as $[Sn\{N(SiMe_3)_2\}_2]$, where it is postulated that a degree of lone pair–metal interaction reinforces covalent bonding already in place.[2] The chemistry and precedent of N-heterocyclic ligand systems was not however covered, nor that of coordinating imine-based systems.

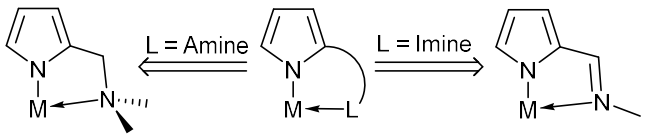

Figure 5.1 – General schematic of sp^2 and sp^3–hybridised nitrogen lariats appended to a pyrrole group.

N-heterocyclic ligands cover a broad range of systems, and focus is drawn within this chapter towards those of the pyrrole derivatives. Pyrrole as a ligand offers a number of interesting features and can be viewed to some extent as a more versatile cyclopentadienyl analogue, capable of η^5 coordination to a metal centre in addition to the conventional κ^1 N–M covalent bonding mode. With facile functionalisation possible, it is unsurprising that the chemistry of pyrrolide derivatives is well explored, with a range of functionalisation added and leveraged across widespread coordination chemistry to encompass simple monodentate systems, to crown and pincer-type arrays.[3–6]

As a pseudo aromatic system comprising an sp^2 nitrogen, limited donor ability exists on behalf of the delocalised nitrogen lone pair, limiting pyrrolide ligands to purely covalent nitrogen–metal interactions. With a relatively high acidity (N–H pK_a ~16.5), the bonding to the metal atom is unlikely to be overtly strong, enhancing one aspect of ALD precursor viability. Conversely, the protonation of the pyrrolide ligand on reaction with hydroxylated surfaces is likely to be less of a driving force with such high relative acidity. There is also precedent that by constraining heteroatoms within a carbocycle, tendency for pendant groups to rotate and bridge to other metal centres is minimised and as such, heterocyclic systems have found application in a number of CVD applications.[7–9]

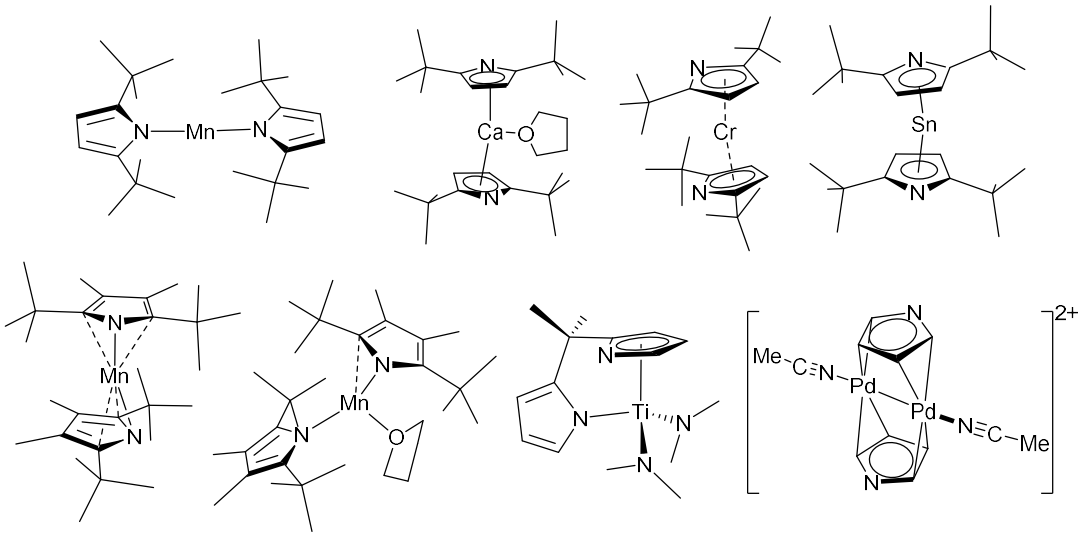

Figure 5.2 – Pyrrolide bonding modes.

Whilst nowhere near as developed as the chemistry of metallocenes, the η^5 coordination of sterically hindered pyrroles is well-documented. Pyrrole-based metallocene analogues of Ca, Sr, Cr, Zr, Pb and Sn have been characterised[10–13] (Figure 5.2), whilst interesting coordination modes are displayed by constrained dipyrrolide ligand systems complexed with titanium, wherein one η^5 pyrrolide-Ti bond is observed alongside an η^1 from a second pyrrolide fragment. (Figure 5.2).[14] The η^1 bonding mode is also found within di-substituted manganese complexes with sterically demanding pyrrolide ligands.[15] η^2 bridging has additionally been observed within multidentate pyrrole-derived systems of Mo and W with pendant imidazole groups (Figure 5.2). This η^2 bridging behaviour has also been found within unsubstituted pyrrolide dimers of palladium.[16] Within sterically demanding systems, ring slippage to an η^3 coordination has been found to occur within the THF adduct of $[Mn(Pyr^tBu_2{}^tMe_2)_2]$, which ordinarily displays κN coordination in the non-adducted complex.[15]

Of particular relevance to the work contained within this chapter is the functionalisation of pyrrole with simple pendant donor groups to form bidentate ligand systems (Figure 5.1). These systems comprise either the sp^3 donor nitrogen of an amine, or the sp^2 donation of an imine. The latter exhibits aromaticity across the entire backbone of the ligand, and results in a much more rigid ligand structure. In addition to providing an interesting comparison of amine and imine coordination environments, it has additionally been shown that via the introduction of double-bond moieties within the core structure of ligands, bridging of a single ligand between multiple metal centres can be avoided.[7]

These imine-substituted pyrrolide ligands primarily display κ N coordination to the metal from the pyrrolide fragment, and dative coordination from the imine, as observed for complexes such as $[Ca(C_4H_3N\text{-}CH{=}NAr)(HMDS).THF_2]$ (where Ar = 2,6-^{i}Pr$_2$-C$_6$H$_3$). Interestingly, the bis-substituted complex of the latter displays a dimeric structure with η^4 bridging from an κN pyrrolide (Figure 5.3).[17] Other abnormal modes have been observed within imine substituted pyrrolides, such as those observed within the species $[M(C_4H_3N\text{-}CH{=}N^iPr)^tBu]$ (M = Mg, Zn). Within the magnesium analogue, the bidentate ligand is bound as expected, but with bridging interactions from the pyrrolide lone pair resulting in a dimeric species. This observation is in contrast to the zinc analogue, in which conventional bidenticity is also observed, but a dimer is formed through an η^1–Zn bridging interaction from the C4 position on the pyrrolide (Figure 5.3).[18] When complexed to copper(I), the pyrrolylaldimine ligand was found to bridge between two copper centres, with only a single bond per ligand to its respective copper centre.[19]

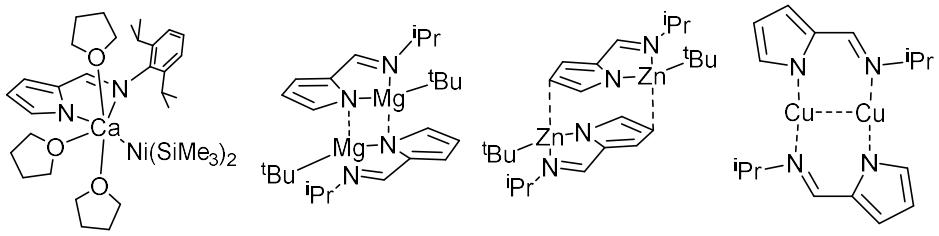

Figure 5.3 – Pyrrolylaldimine bonding modes.

5.2.2. N-Heterocyclic and Imine Systems Within ALD

An interesting series of imino-based precursors of the form [M[OC(Me)^{t}BuCHN^{t}Bu]$_2$] (Figure 5.4) have been developed within the research group of Prof. Charles Winter, Wayne State University, and have been successfully applied to the metallic ALD of iron, cobalt, nickel, chromium and manganese through reductive processes.[20,21] Whilst strictly a metal-alkoxide ligand system, a pendant imine group differentiates the ligand from the structurally similar aminoalkoxide ligands discussed in Chapter 2.

A limited number of examples of N-heterocyclic ALD precursors are reported within the literature. Within these limited examples, a variety of configurations exist. Amongst these systems is the structurally uncharacterised, proprietary barium pyrrole system, [py-Ba], which has been shown by Acharya et al.[22] to afford films of BaO when used in conjunction with H_2O. The precursor remains undisclosed after development by BASF (Ludwigshafen, Germany), however BaO was deposited at a uniform growth rate of ca. 0.45 Å/cy at temperatures of 180-210°C.

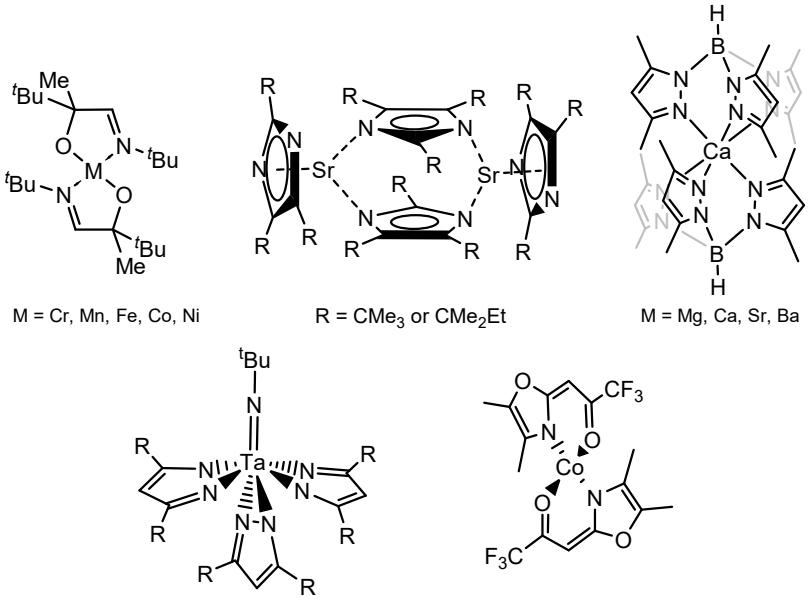

Figure 5.4 – Examples of N-heterocyclic and iminie-containing ALD precursors.

More useful from a structural perspective are the publications applying dimeric precursor systems of the form [M(2-tert-butyl-4,5-ditert-amylimidazolate)$_2$]$_2$ (where M = Sr and Ba) to the ALD of alkaline earth oxide materials using O_3 as an oxidant.[23] The dimeric species (Figure 5.4) were suggested to dissociate at evaporation temperatures, exhibiting volatilities matching those of previously determined monomeric Sr and Ba precursors. This was corroborated with GCMS and computational studies and consequently afforded novel routes into the ALD of large, ionic metals by using imidazolate precursors in coordination modes of up to η^5 in order to satisfy demanding coordination spheres.[23]

Similar research into Group 2 atomic layer deposition was undertaken by Winter et al., developing a series of calcium, strontium and barium bis(tris(pyrazolyl)borate systems (Figure 5.4). These thermally stable systems were found to deposit alkaline earth metal borates (MB_2O_4) on reaction with H_2O and are a rare example of a "single source" ALD precursor approach utilising a precursor containing two desired elements. Growth per cycle ranged from ~0.23 Å (Ba, 250-375^{o}C) and ~0.35 Å (Ca, 300-375^{o}C) to 0.47 Å (Sr, 300-375^{o}C).[24–26] Researchers from within the same group developed a similar a boron-free tantalum pyrazolate precursor (Figure 5.4) which was used to successfully deposit thin films of Ta_2O_5 with an ozone oxidant. A growth rate of ca. 0.30 Å/cy was observed for temperatures between 300^{o}C and 450^{o}C.

An interesting heterocyclic precursor, [Co(DMOCHCOCF$_3$)$_2$] (where DMOCHCOHCF$_3$ = 1-(dimethyl-1,3-oxazol-2-yl)-3,3,3-trifluor-prop-1-en-2-ol), was recently reported by Büyükyazi and co-workers (Figure 5.4).[27] Though displaying no reactivity with water, the complex was found to deposit Co_3O_4 on reaction with ozone at a growth rate of 0.2 Å/cy (150-200^o).

Despite the presence of a number of patents[28–30] attesting to the efficacy of imine-substituted pyrrolide precursors for the atomic layer deposition of copper and manganese films, the only published precedent is set for the deposition of copper metal with pyrrolide precursors including the pyrrolide aldimines NC$_4$H$_3$CHNR, where R = Et or ^{i}Pr. Deposition was undertaken with alternating pulses of copper precursor and either [ZnEt$_2$], [AlMe$_3$] or [BEt$_3$] in an ALD adaptation of a previously described solution-based process.[19,31,32]

Further advances within N-heterocyclic ALD precursors have seen a number of cobalt and copper complexes containing N-heterocyclic carbene ligands applied to reductive ALD processes aiming to deposit metallic films. As M–C systems, discussion of these systems is beyond the scope of this overview, though a number of publications can be found on the subject matter.[33,34]

5.2.3. Sn(II) Pyrrolide Systems

With facile functionalisation possible, it is unsurprising that the chemistry of pyrrolide and chelating-pendant pyrrolide systems extends to a vast array of multidentate systems and crown-type chelates, with no appreciable relevance to precursor chemistry. However, a number of relevant systems have been reported, containing either Sn(II) or pyrrolide ligands of the type contained within this body of work.

Research into tin(II) pyrrolide complexes is thus far stunted, with the only significant reported species being the stannocene [Sn(η^5-2,5-$NC_4{}^tBu_2H_2)_2$] and the pyrrolide complex [Sn{κ^2-*N*,*O*-$NC_4H_3CH(O)R\}_2$] (R = NMe_2 or Me).[35,36]

5.2.4. Target Compounds

A range of simple pyrrolide ligands were synthesised and their tin(II) derivatives targeted (Figure 5.5). All pyrrolide ligands comprised a pendant-nitrogen chelating arm consisting of either a CH_2NMe_2 moiety or an aldimine CHNR group (where R = Me, Et, ^{n}Bu, ^{s}Bu, ^{t}Bu, Dipp). Reactions of each ligand in a 1:1 and 2:1 ratio with [Sn{$N(SiMe_3)_2\}_2$] were attempted in order to yield both hetero- and homoleptic species.

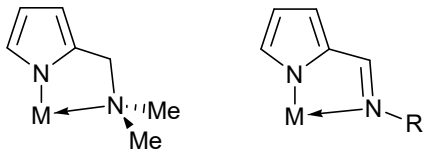

R = Me (**3**) (**33***)
R = Et (**4**) (**34***)
R = ^{t}Bu (**5**) (**35***)
R = ^{s}Bu (**6**) (**36***)
R = ^{n}Bu (**7**) (**37***)
R = 2,6-^{i}Pr-C_6H_3 (**8**) (**38***)

Figure 5.5 – Pyrrolide ligands exploited in this Chapter.

This declaration concerns the article entitled									
Synthesis, characterisation and thermal properties of Sn(II) pyrrolide complexes									
Publication status (tick one)									
Draft manuscript		**Submitted**		**In review**		**Accepted**		**Published**	X
Publication details (reference)	J. D. Parish, M. W. Snook, A. L. Johnson and G. Kociok-Köhn, *Dalton Trans*., 2018, 47, 7721–7729								
Candidate's contribution to the paper (detailed, and also given as a percentage)	The candidate contributed to/ considerably contributed to/predominantly executed the: **Formulation of ideas (70%):** Ideas conceived in discussions between JDP and ALJ (30%), building on Sn(II) aminoamide research previously undertaken by JDP **Design of methodology (90%)**: Synthetic procedures researched and designed by JDP with input from ALJ (10%) **Experimental work (70%)**: JDP carried out the majority of the experimental work and analysis, with assistance from MWS (25%). GKK provided the crystallography (5%) **Presentation of data in journal format (70%)**: JDP wrote the majority of the paper for publication. ALJ assisted with discussion of crystallographic components and corrections (30%).								
Statement from Candidate	This paper reports on original research I conducted during my Ph.D. candidature and formed part of a summer student project undertaken by MWS.								
Signed	James D. Parish						**Date**	20/09/2018	

5.3. Synthesis, Characterisation and Thermal Properties of Sn(II) Pyrrolide Complexes

SnO is a rare example of a stable p-type semiconductor material. Here, we describe the synthesis and characterisation of a family of Sn(II) pyrrolide complexes for future application in the MOCVD and ALD of tin containing thin films. Reaction of the Sn(II) amide complex, $[Sn\{N(SiMe_3)_2\}_2]$, with a N,N-bidentate pyrrole pro-ligand, L^1H, forms the hetero- and homoleptic complexes $[\{L^1\}Sn\{N(SiMe_3)_2\}]$, (**1**) (**31***) and $[\{L^1\}_2Sn]$ (**2**) (**32***) respectively, bearing the 2-dimethylaminomethyl-pyrrolide ligand (L^1). Reaction of $[Sn\{N(SiMe_3)_2\}_2]$ with the pyrrole-aldimine pro-ligands, L^2H-L^7H, results in the exclusive formation of the homoleptic bis-pyrrolide complexes $[\{L^{2-7}\}_2Sn]$ (**3**-**8**) (**33-38***). All complexes have been characterised by elemental analysis, NMR spectroscopy, and the molecular structures of complexes **1**-**5** (**31-35***) and **8** (**38***) determined by single crystal X-ray diffraction. TG analysis and isothermal TG analysis have been used to evaluate the utility of these systems as potential MOCVD and ALD precursors.

5.3.1. Introduction

Transparent semiconducting oxide (TSO) thin films have attracted considerable interest due to their omnipresence in modern technology, finding wide-spread application in solar cells, light emitting diodes, flat panel displays, optical communicators, gas sensors and thin film transistors.[37–42] The majority of commercially available semiconducting oxides are *n*-type, e.g. ZnO, many potential applications of TSOs are still limited by the scarcity of *p*-type counterparts.[43] The development of high performance *p*-type TSOs would leverage the inordinate potential of oxides for transparent electronics and optoelectronics by combining then with *n*-type TSOs into *p*–*n* heterojunctions.[44] The recent rapid development of both photovoltaics and solar water splitting also calls for *p*-type electrodes for more efficient hole collection.[45] However, the most significant challenge to the realisation of this goal is the paucity of suitable *p*-type TSOs. To this end, a great deal of experimental work has focused on the development of *p*-type semiconducting materials such as SnO, Cu_2O and N-doped ZnO.[43,45,46] Unfortunately, these metastable materials all suffer from an intrinsic instability towards oxidation. Despite this, SnO which possess a layered PbO-like Litharge structure has received considerable attention as a *p*-type semiconductor.[39,43,46,47] Interest was initially sparked by SnO grown on Yittria stabilised ZrO_2 (YSZ) reportedly displaying a Hall mobility of 2.4 $cm^2\ V^{-1}\ s^{-1}$ and with a field effect mobility of 1.3 $cm^2\ V^{-1}\ s^{-1}$, when used as a *p*-channel thin film transistor (TFT).[48] More recently, Hall mobility values as high as ~18.71 $cm^2\ V^{-1}\ s^{-1}$ and field effect mobilities of 6.75 $cm^2\ V^{-1}\ s^{-1}$ have been reported.[49]

Physical vapour deposition (PVD)[48–53] and chemical vapour deposition (CVD)[54–61] have both been used to produce thin films of SnO with varying degrees of success. Since modern devices are topographically diverse structures, a vapor phase technique capable of producing thin films with exceptional conformality is required. Atomic layer deposition (ALD), and to a lesser extent metalorganic chemical vapor deposition (MOCVD), offer such a solution. However, SnO is intrinsically reactive towards oxygen, and formation of both Sn_2O_3 and SnO_2 as phase impurities results in thin films with undesirable properties.[60] Therefore, precise control over the oxidation state of the metal is paramount. Whilst a number of Sn-precursor/reactant combinations have been surveyed for the growth of SnO, the majority have focused of the utility of Sn(IV) precursor combinations, e.g. $SnCl_4/H_2O$,[62] $/H_2O_2$[63,64] SnI_4/O_2,[65] $[Sn(NMe_2)_4]/H_2O/H_2O_2$,[66,67] $[SnEt_4]/H_2O_2/O_2/O_3$-plasma and $[Bu_3SnOEt]/O_3$.[68] Of the precursor/reactant combinations investigated, only three have utilised Sn(II) precursors (Figure 5.6): In the case of the stannylene complex (**A**), reaction with H_2O failed to produce SnO, and reaction with either H_2O_2[69,70] or NO[71] resulted in the formation of a mixed phase of SnO/SnO_2 (i.e. SnO_x). Similarly, $Sn(HMDS)_2$ (**B**) has also been used in conjunction with either H_2O or O_3 in an ALD process, to deposit Sn(II) and Sn(IV) oxides and SiO_2 mixes between 80 and 250 °C.[72] To date, only the Sn(II) aminoalkoxide complex (**C**) has been found to produce phase pure SnO in an ALD process, with H_2O, between 90 °C and 210 °C, with crystallinity occurring above 150 °C.[73]

This dearth of suitable precursors for SnO production has prompted us, and others,[74] to investigate new Sn(II)-ligand combinations. In an attempt to optimise precursor reactivity and thermal stability, we chose to investigate the utility of the amino-pyrrolide (L^1) and pyrrolyaldiminato ligands (L^2-L^6) shown in Scheme 5.1.[6,32,75] The ligands (L^1-L^6) can be tuned by substitution of the R groups to limit oligomerisation and tune the volatility. The bidentate chelating effect should increase the thermal stability of resulting metal compounds. Whilst numerous metal compounds with pyrrole ligands can be found in the literature, their application as CVD or ALD precursors is limited to selected titanium,[76] barium[22] and copper(I)[19,31] complexes. To date, Sn(II)-pyrrolide systems are limited to the stannocene complex $[Sn\{\eta^5\text{-}2,5\text{-}NC_4{}^tBu_2H_2\}_2]$,[35] and the carbonyl-substituted pyrrolide complexes, $[Sn\{\kappa^2\text{-}N,O\text{-}NC_4H_3CH(O)R\}_2]$ (R = NMe_2 or Me).[36] Here we describe details for the synthesis and structure of a series of bidentate pyrrolide based Sn(II) complexes, including investigations into their thermal properties.

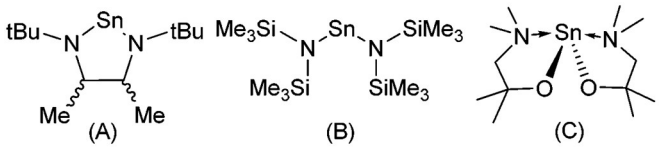

Figure 5.6 – Molecular structures of the three reported Sn(II) ALD precursors which have been used to produce tin oxide thin films.

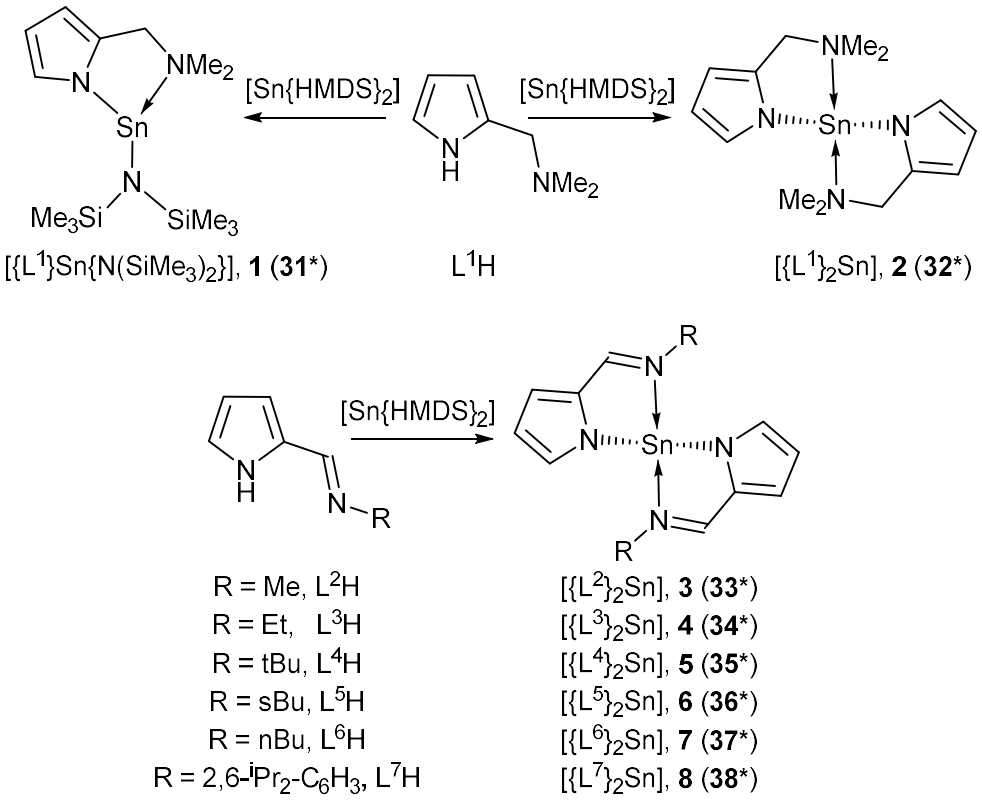

Scheme 5.1 – General schematic showing the general methodology and complexes synthesised in this work.

5.3.2. Results and Discussion

Synthesis of Sn(II) complexes

In all cases, isolated products were characterised by solution state NMR (^{1}H, ^{13}C{^{1}H} and ^{119}Sn) spectroscopy and elemental analysis. Initial attempts to prepare the mono(dimethylamido) Sn(II) compounds by direct stoichiometric (1:1) reaction of bis(dimethylamido)tin(II) with the pyrrole ligands, L^{1}H-L^{7}H, in both hexane and THF respectively, were unsuccessful. However, reactions did result in the formation of bis(pyrrolide) compounds **2**-**8** (**32**-**38***). We attribute this failure to prepare the dimethylamido-tin(II) species to the stronger acidity of the pyrrole {N-H} relative to that of the dimethylamine hydrogen, combined with the enhanced basicity of dimethylamide group in the monoamide intermediate, [{pyrrolide}Sn-NMe$_2$], relative to [Sn{NMe$_2$}$_2$].

In contrast, reaction of the bulkier and less basic amide system [Sn{N(SiMe$_3$)$_2$}$_2$], with ligand L^{1}H in a stoichiometric 1:1 reaction results in the formation, and isolation after recrystallisation, of the mono-pyrrolide complex **1** (**31***). The ^{1}H NMR spectrum of **1** (**38***) clearly shows the presence of a singlet resonance at δ = 0.25 ppm representative of the presence of a {HMDS}

group, in a 18H:3H ratio with the dimethylamine group, {NMe_2}, associated with {L^1} (δ = 1.76 ppm), indicative of the presence of {L^1} and {HMDS} ligands in a 1:1 ratio. Comparable reaction of [Sn{HMDS}$_2$] in an equimolar reaction with L^2H-L^8H, results in the formation of the bis-pyrrolide complexes, **2**-**8** (**32**-**38***), in yields <50%, suggestive of a Schlenk equilibrium in which the putative mono-amide intermediates are unstable with respect to disproportionation, and formation of the bis pyrrole complex. The ^{1}H NMR spectra of **2**-**8** (**32-38***), clearly show the absence of resonances associated with the {HMDS} ligands, and are consistent with the formation of the bis-pyrrole complexes. In the case of the sec-Bu derivative complex, **6** (**36***), racemic (±)sec-butyl amine was used for the synthesis of the proligand L^5H, resulting in the ^{1}H and ^{13}C NMR spectra containing two sets of resonances corresponding to the presence of the associated (R,R/S,S and R,S/S,R) stereoisomers in solution. Elemental analysis confirms the formation of the bis-pyrrole complexes. The intrinsic C_2 symmetry of complexes **2**-**7** (**32-37***) is negated somewhat in solution by a rapid, so-called, “flip-flop” equilibrium process in which the N→Sn coordination bonds repeatedly open and close. In compound **8** (**38***) however, the methyl and methine groups of the isopropyl substituents display a series of convoluted multiplets (δ = 0.89-1.36 ppm, 12H), alongside two broad resonances respectively (δ = 3.00 ppm, 1H; and 3.43 ppm, 1H) suggestive of a slow rotation, on the NMR timescale, about the N-C(phenyl) bond. Stoichiometric reaction (2:1) of the pro-ligands, L^1H-L^7H, with [Sn{HMDS}$_2$] produce the expected complexes cleanly in moderate to high yields (64-87%).

Solid-state structures

X-ray diffraction studies on single crystals of complexes **1** (**31***), **2** (**32***), **3** (**33***), **4** (**34***), **5** (**35***) and **8** (**38***) unambiguously established their solid-state structures. The structure of the heteroleptic, and the homoleptic complexes [Sn{κ^2-N,N-$NC_4H_3CH_2NMe_2$}{$N(SiMe_3)_2$}] (**1**) (**31***) and [Sn{κ^2-N,N-$NC_4H_3CH_2NMe_2$}$_2$}] (**2**) (**32***) are shown in Figure 5.7. While compounds **1** (**31***) and **2** (**32***) are both chiral, the enantiomers co-crystallise in noncentrosymmetric space groups.

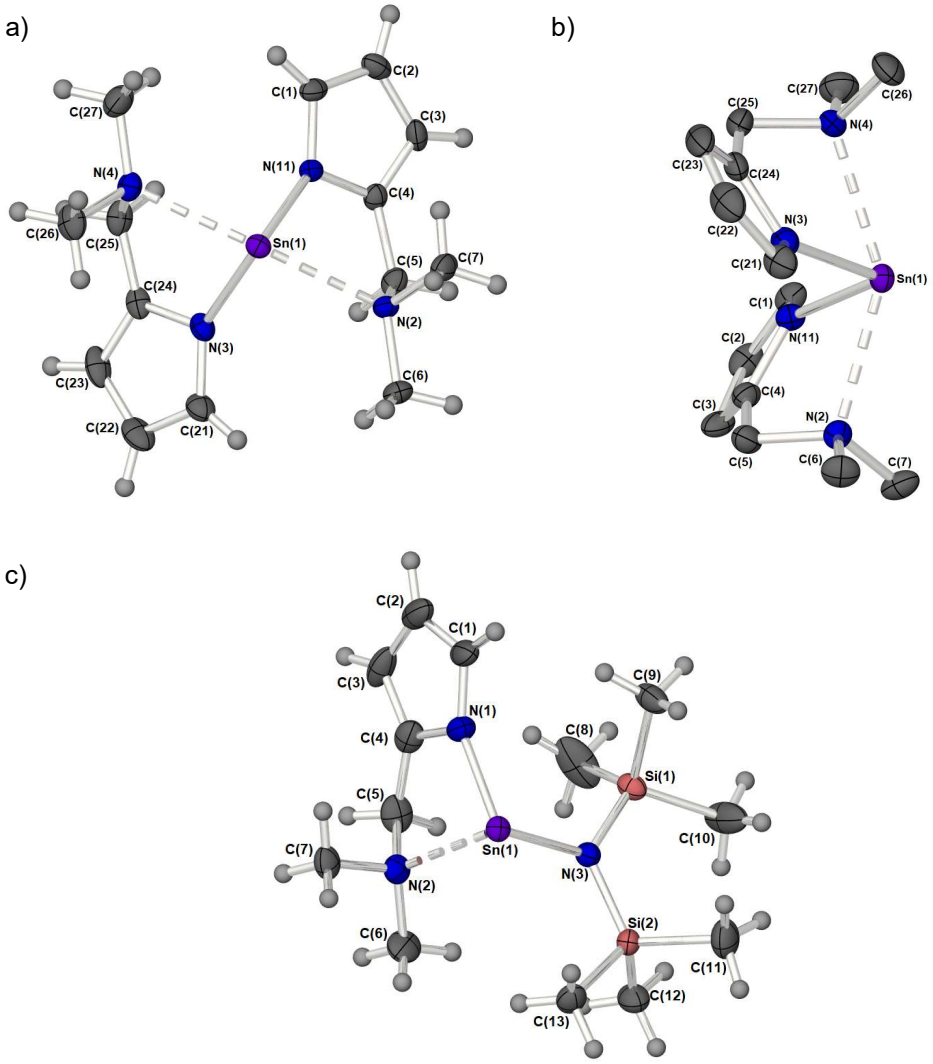

*Figure 5.7 – The molecular structures of complex **1** (**31***) (left) and **2** (**32***) (right) (50% probability ellipsoids).*

In the solid state, **1** (**31***) crystallises in the monoclinic space group $P2_1/c$. The asymmetric unit cell contains a single monomeric complex with a three coordinate, pseudo trigonal-pyramidal geometry about the Sn(II) centre, with the {L^1}- ligand coordinated in a κ^2 fashion via the pyrrolide nitrogen and the pendant {NMe_2} group, as well as the nitrogen of the {HMDS} ligand, in a terminal bonding mode (Figure 5.7).

The Sn(1)-N(1) (2.152) and Sn(1)–N(3) (2.127) bond lengths are comparable to those already reported for Sn-amide compounds,[2,77–80] whereas the dative Sn(II)←NMe_2 bond [Sn(1)–N(2) (2.418)] is expectedly longer. Despite a constrained bite angle for the {L^1}- ligand [N(1)-Sn(1)-N(2) (74.52°)], the N-Sn-N bond angles in **1** [N(1)-Sn(1)-N(3) (96.36°), and N(2)-Sn(1)-N(3) (96.84°)] suggest the absence of *sp*-hybridisation at the Sn(II) centre and that the tin–ligand bonds almost exclusively involve the *p*-orbitals; the nature of the electron lone pair in compound **1** (**31***) can therefore be considered as essentially a $5s^2$ configuration and therefore non-directional.

Complex **2** (**32***), which has intrinsic C_2 symmetry, crystallises in the monoclinic space group $P2_1/c$ and is shown in Figure 5.9. Here the asymmetric unit cell contains a single molecule of the complex with a four coordinate, pseudo trigonal bipyramidal geometry ($\kappa = 0.83$)[81] in which the two {L^1}- ligands are coordinated in the same κ^2 fashion observed in **1** (**31***), with the N-atoms of the pyrrolide ligands occupying two equatorial, and the pendant {NMe_2} groups occupying the axial positions. A cursory analysis of the bond angles about the Sn(II) centre in 2 [N(1)-Sn(1)-N(3) (97.44°) & N(2)-Sn(1)-N(3) (147.21°)] again suggest that tin–ligand bonds almost exclusively involve the *p*-orbitals on Sn, and that the lone pair of electrons in **2** (**32***) is therefore again essentially $5s^2$ based. The Sn-N_{py} [Sn(1)-N(1) (2.179°) & Sn(1)–N(3) (2.165°)] and Sn←NMe_2 [Sn(1)-N(2) (2.516°) & Sn(1)–N(4) (2.528°)] bond lengths in **2** (**32***) are commensurate with **1** (**31***) and comparable complexes.

For the imine complexes **3** (**33***), **4** (**34***) and **5** (**35***), which are structurally related to **2** (**32***), the molecular structures are shown in Figure 5.8. For complexes **3** (**33***) and **5** (**35***), which crystallise in the centrosymmetric space group $P2_1/n$, the asymmetric unit cell contains one full molecule of the bis-(pyrrolyaldiminate) Sn(II) complex. Complexes **3** (**33***) and **5** (**35***) are disordered such that all ligand atoms, with the exception of Sn(1), N(1) and N(3), exhibit (67:33) and (80:20) disorder, respectively, via a pseudo mirror plane containing the three non-affected atoms. Complex **4** (**34***), crystallises in the polar space group $P2_1$ with only one enantiomer of the chiral complex in the crystals. While in all three cases, the central Sn(II) atoms are four-coordinate, analysis of the bond angles about the tin centre suggest a trigonal bipyramidal geometry[81] [3: $\tau = 0.92$, 4: $\tau = 0.82$, 5: $\tau = 1.06$] with the imine nitrogen atoms occupy the axial coordination sites and the pyrrole nitrogen atoms the equatorial positions. While the $N_{(imine)}$-Sn-$N_{(imine)}$ bond angles increase from ~143° to 152° as the imine substituent changes from methyl, to ethyl and ^{t}Butyl, respectively, the N_{py}-Sn-N_{py} angles [3: 92.17(10)°, 4: 95.64(19)°, 5: 88.33(15)°] are all around 90°, suggesting the Sn–N_{py} bonds involve mostly the Sn(II) p-orbitals. The Sn-N_{py} and Sn←NR bond lengths (displayed in Table 5.1) are all similar, *vide supra*.

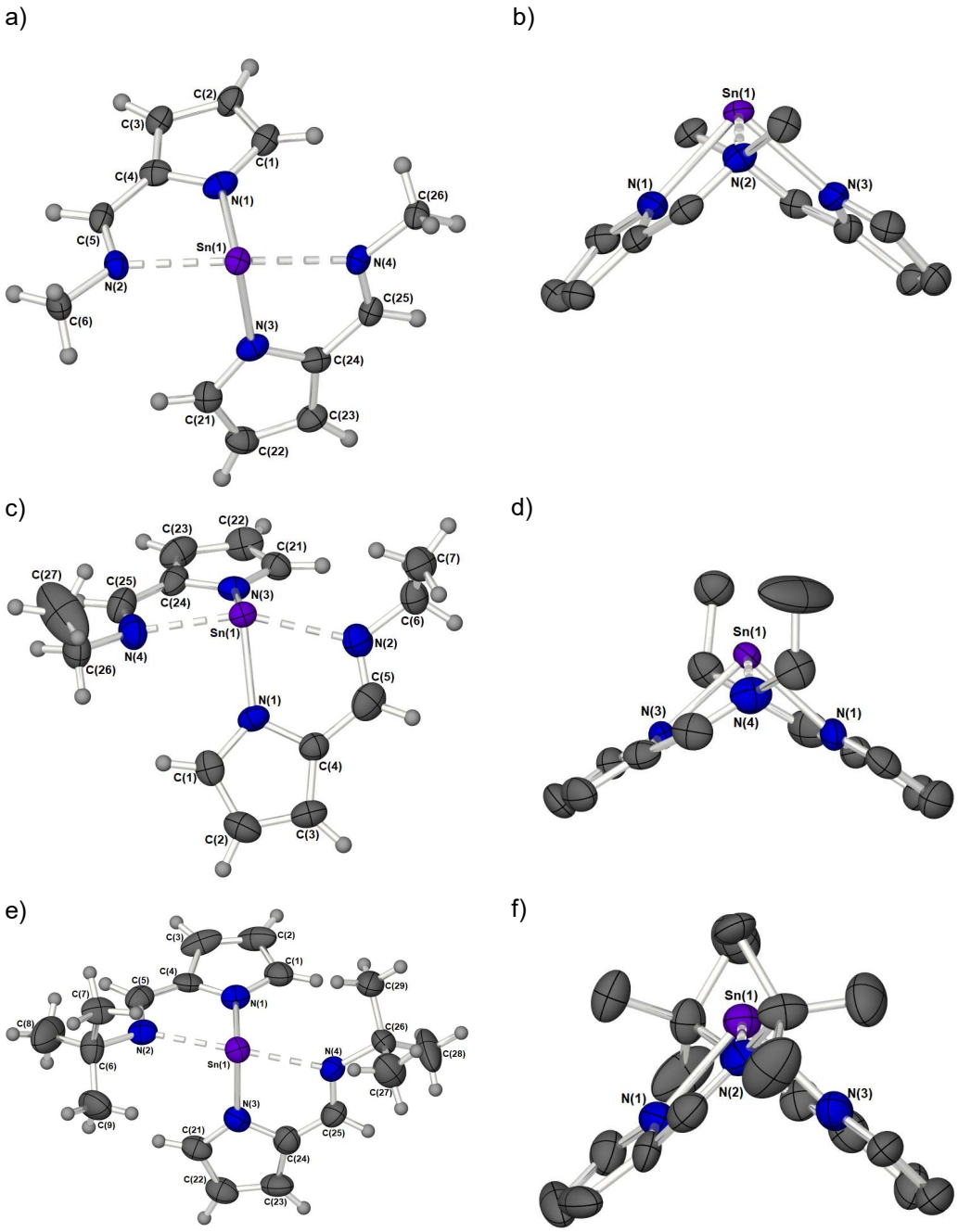

*Figure 5.8 – The molecular structures of complex **3** (**33***) (40% probability ellipsoids), **4** (**34***) (50% probability ellipsoids) and **5** (**35***) (50% probability ellipsoids). Complexes **3** (**33***) and **5** (**35***) are disordered such that all ligand atoms, with the exception of Sn(1), N(1) and N(3), exhibited 67 : 33 and 80 : 20 disorder, respectively, via a pseudo-mirror plane containing the three non-affected atoms. The major component only is depicted for clarity.*

*Table 5.1 – Selected bond lengths (Å) and bond angles (°) for complexes **1-5** (**31-35***) and **8** (**38***).*

	1 (**31***)	**2** (**32***)	**3**† (**33***)	**4** (**34***)	**5**† (**35***)	**8** (**36***)
	Selected bond lengths (Å)					
Sn(1)-N(1)	2.152(2)	2.179(2)	2.181(3)	2.171(5)	2.185(4)	2.3138(16)
Sn(1)-N(2)	2.418(2)	2.516(2)	2.409(3)	2.470(8)	2.462(5)	2.3308(16)
Sn(1)-N(3)	2.127(2)	2.165(2)	2.186(3)	2.167(5)	2.165(4)	2.2871(16)
Sn(1)-N(4)	-	2.528(2)	2.439(3)	2.375(7)	2.442(5)	2.3127(15)
N=C	-	-	1.294(6) 1.280(5)	1.279(12) 1.302(11)	1.300(10) 1.273(10)	1.297(2) 1.304(2)
	Selected bond angles (°)					
N(1)-Sn(1)-N(2)	74.52(8)	72.14(8)	70.13(11)	70.0(2)	69.99(18)	71.26(6)
N(2)-Sn(1)-N(3)	96.84(8)	86.71(8)	84.73(10)	86.3(2)	88.31(17)	81.34(5)
N(3)-Sn(1)-N(4)	-	72.16(8)	70.26(11)	72.1(2)	73.54(17)	71.84(6)
N(1)-Sn(1)-N(3)	96.36(8)	97.44(8)	92.17(10)	95.64(19)	88.33(15)	127.03(6)
N(2)-Sn(1)-N(4)	-	147.21(7)	142.69(11)	144.9(2)	151.8(2)	117.62(5)

† Complexes **3 (33*)** and **5 (35*)** are disordered such that all ligand atoms, with the exception of Sn(1), N(1) and N(3), exhibited (67:33) and (80:20) disorder respectively, via a pseudo mirror plane containing the three non-affected atoms. Only the major component is shown here, for clarity.

Similarly to complexes **2**-**5** (**32**-**35***), compound **8** (**38***) is chiral (Figure 5.9), possessing molecular C_2 symmetry; the other enantiomer is also formed in the product, with **8** (**38***) crystallising in the centrosymmetric monoclinic space group $P2_1/n$. Exhibiting a 4-coordinate Sn(II) centre, the geometry about the Sn(II) atom is best described as square based pyramidal [$\tau = 0.15$]. Interestingly, the Sn-N_{py} bonds in **8** (**38***) [Sn(1)-N(1) = 2.3138(16) Å, Sn(1)-N(3) = 2.2871(16) Å], are significantly longer than those reported for **1**-**5** (**34**-**35***). Similarly, the Sn←NR bond are also significantly longer [Sn(1)-N(2) = 2.3308(16) Å, Sn(1)-N(4) = 2.3127(15) Å] than those observed in **3**-**5** (**33**-**35***). Consistent with this observation the N_{py}-Sn-N_{py} and $N_{(imine)}$-Sn-$N_{(imine)}$ angles observed in **8** (**38***) are both close to 120° [127.03(6)° and 117.62(5)° respectively], suggesting that tin-ligand bonds almost exclusively involve sp^2 hybridised orbitals on the tin, with the lone pair in **8** (**38***) considered to be essentially based in a directional sp^2 orbital.

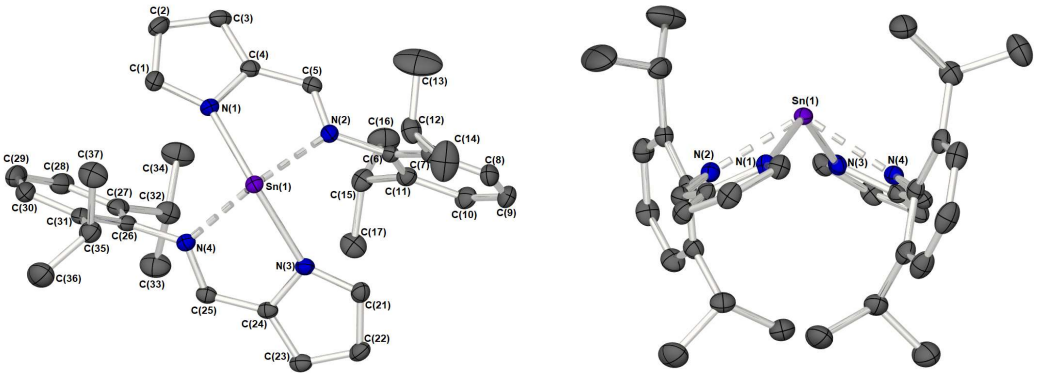

*Figure 5.9 – The molecular structures of complex **8** (**38***) (50% probability ellipsoids), showing a view from above the Sn atom (left), and a view from the side (b), showing the relative ligand arrangement about the Sn atom. Hydrogen atoms have been omitted for clarity.*

Thermal Profiles

Two of the main precursor requirements for MOCVD and ALD applications are the need for volatility and thermal stability.[82,83] As the primary goal of synthesising compounds **1**-**8** (**31**-**38***) was driven by our interest in their application as precursors for the MOCVD and ALD of Sn(II) oxide films, melting point analysis, thermogravimetric analysis (TGA) and isothermal studies were employed to investigate the volatility and thermal stability of complexes **1**-**8** (**31**-**38***). The melting points and analysis of compounds **1**-**8** (**31**-**38***) were recorded with instruments housed in an argon filled glove-box in order to minimise reaction with atmospheric moisture/air. For the amino-pyrrolide complexes **1** (**31***) and **2** (**32***), results suggest these materials are unsuitable for application as ALD precursors. Table 5.1 shows the melting and decomposition points for these complexes. Complex **1** (**31***) displays a rather low decomposition temperature (100 °C) quite close to its melting point (95 °C). Similarly for **2** (**32***), a relatively low decomposition (50 °C) was observed before any phase transition could be detected, suggesting the possible lack of utility of these systems as ALD precursors. Despite this observation TGA of the Sn(II)bis-(pyrrolide) **2**-**8** (**32**-**38***) were performed, in order to gain greater insight into the relative volatilities and thermal stabilities of the compounds.

*Table 5.2 - Physical properties of the Sn(II) pyrrolide complexes **1–8** (**31-38***)*

Compound R=	Melting Point (°)	Decomp^{n}. Point (°)	Evaporation rate (μg min^{-1} cm^{-2})‡
(**1**) (**31***)	95	~100	-
(**2**) (**32***)	-	~50	-
-Me (**3**) (**33***)	-	140	6.409(8)
-Et (**4**) (**34***)	130	137	19.894(1)
-^{t}Bu (**5**) (**35***)	-	141	19.974(7)
-^{n}Bu (**6**) (**36***)	85	100	14.085(8)
-^{s}Bu (**7**) (**37***)	Viscous oil	94	5.611(6)
-Dipp (**8**) (**38***)	153	290	2.357(5)
-Dipp (**8**)† (**38***)			12.653(9)

‡ Isothermal TGA recorded at 130 °C, † Isothermal TGA recorded at 160 °C

As seen in Figure 5.10, compounds **3-8** (**33-38***) exhibit very similar thermal behaviour, consistent with single step evaporation. For all precursors, the onset of volatilisation (~100 °C) and the temperature at which the evaporation is completed (between 220 and 255 for **3-7** (**33-37***) and by 286 °C for **8** (**38***) are similar.

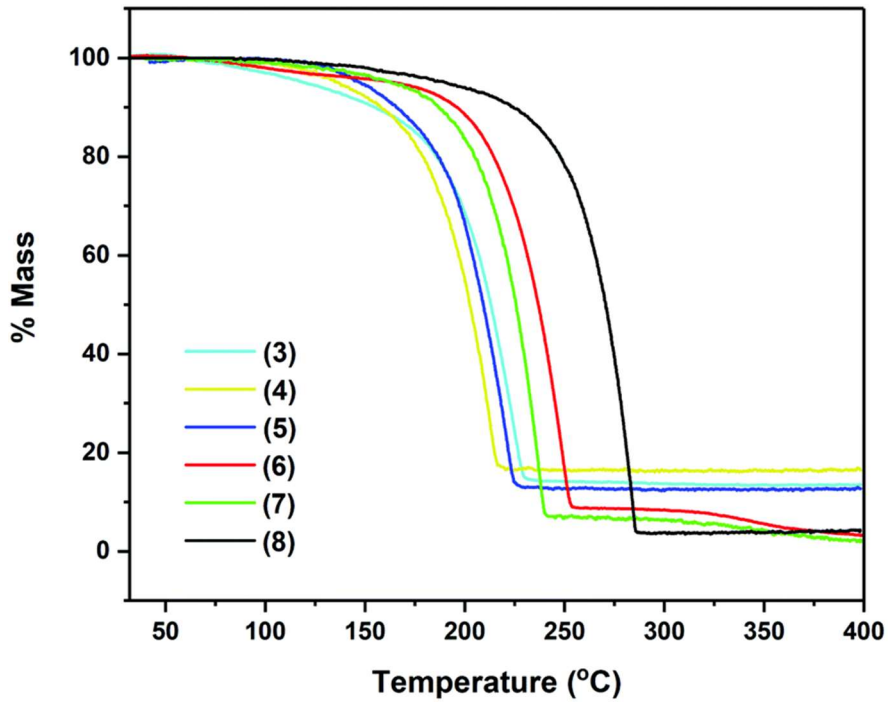

*Figure 5.10 – Thermogravimetric analysis data for complexes **3–8** (**33-38***).*

Table 5.2 gathers germane data, relating to the TG analysis of compounds **3**-**8** (**33**-**38***), i.e. % Residual mass and %wt of Sn in complexes. Figure 5.10 clearly shows that compounds **3**-**8** (**33**-**38***) exhibit very similar thermal behaviour, undergoing a clear, single mass loss event over a small temperature window to yield stable residues of between 4-16.5%, consistent with a single step evaporation process. In the case of complexes **6**-**8** (**36**-**38***) the final mass residues are considerably lower than the mass residue expected for the production of Sn metal, strongly suggestive of a high degree of volatility within these systems. For complexes **3**-**5** (**35**-**38***), the mass residues are proportionately higher although still below the % mass residue expected if decomposition resulted in the formation of Sn metal. Compound **2** (**32***), which was also analysed, showed a complicated and shallow decomposition profile with mass loss starting at 36 °C. At 400 °C the residual mass is ~67%, indicative of a non-volatile material with incomplete thermal decomposition (Figure 5.12, ESI).

*Table 5.3 - % Residual mass, wt% of Sn and onset of mass loss for complexes **3–8** (**33-38***)*

Compound R=	Residual Mass	%Sn by wt.	Onset of mass loss‡ (°C)
-Me (**3**) (**33***)	13.5	35.7	85
-Et (**4**) (**34***)	16.5	32.9	125
-^{t}Bu (**5**) (**35***)	12.7	28.5	132
-^{n}Bu (**6**) (**36***)	7.1 (2.0)*	28.5	95
-^{s}Bu (**7**) (**37***)	8.7 (3.3)*	28.5	126
-Dipp (**8**) (**38***)	4.0	19.0	147

* Residual mass after second mass loss event in TGA.

‡ Temperature at 2% mass loss.

Given the nature of the ligand systems involved in **3**-**8** (**33**-**38***), it is unlikely that the TGA residues contain oxide products (i.e. SnO_x), and is instead are more likely to be metallic Sn (with possible carbon impurities). This is consistent with the observation of metallic deposits (of Sn) in the TGA crucibles after decomposition studies, suggesting the possible application of these systems in the deposition of metallic tin under a non-oxidative atmosphere.

While TGA data provide an indication of the volatility of the complexes, decomposition characteristics are less easy to discern for complexes with significant volatility. However, no stepwise decomposition processes are observed in the TGA profiles of **3**-**8** (**33**-**38***), corresponding to the systematic breakdown of the pyrrolide ring systems, as postulated in other studies.[84] More relevant investigations have suggested that pyrrolide complexes are susceptible to ß-hydride elimination processes,[76] in these cases most likely arising from hydride abstraction from the aldimine substituents. This is in contrast to complex **2** (**32***), which possesses pendant {CH_2NMe_2} groups, and as such as such does not share the same

electronic delocalisation observed for the aldimine systems **3**-**8** (**33**-**38***). Consequently, the thermal analysis of **2** (**32***) (ESI) shows a stepwise decomposition over a broad temperature range, consistent with the aforementioned decomposition pathway.

Remarkably, no discernible trends are observed between pyrrolide-aldimine substituents and volatilities/stabilities, with the ethyl (**3**) (**33***) and t-butyl (**4**) (**34***) substituted complexes showing highest volatility followed by the 2,6-diisopropyl-phenyl complex (**8**) (**38***). However, it is noteworthy that the aryl containing system, **8** (**38***), displays a strikingly high thermal stability, in contrast to the other systems investigated here.

We suggest that this high degree of thermal stability is in part due to the absence of a suitable hydride abstraction process, as discussed previously. This observation is the focus of further studies to enhance thermal stability of selected precursor systems, and to expand the ALD window of selected compounds, whilst inhibiting CVD processes.

The thermal behaviour of complexes **3**-**8** (**33**-**38***) were further investigated using isothermal TGA-studies (Figure 5.11). At the fixed temperature of 130 °C, the mass loss for each compound was measured over a period of 120 min (2 h). In all measurements, an approximate linear weight loss was observed, which could be indicative of sublimation, with limited signs of decomposition. However, for complexes **6** (**36***) and **7** (**37***), visual (m.p. studies) decomposition appears to begin at below 100 °C (Table 5.1). From the gradient of the corresponding plots, the evaporation rates at a set temperature of 130 °C were determined (Table 5.1). The evaporation rates were found to be in the range 2.4−20 μg min^{-1} cm^{-2}. From the thermal studies, one can conclude that among the Sn(II) pyrrolide complexes reported here, the ethyl and tert-butyl substituted complex **4** (**34***) and **5** (**35***) show the greatest promise for MOCVD and ALD applications with comparable evaporation rates of ca. 20 μg $min^{-1}cm^{-2}$. These values are within a range previously determined suitable for vapour based deposition process. The difference in evaporation rate between the sec-Bu, n-Bu and t-Bu derivatives **5** (**35***), **6** (**36***) and **7** (**37***) respectively is noticeable, and indicates clearly, that not only the molecular mass of a compound, but factors such as steric crowding, electronic saturation, crystal packing, intermolecular interactions, and so forth, strongly influence thermal behaviour, highlighting the importance of precursor screening. In the case of compound **8** (**38***), which produced the lowest % residue in the TG analysis (4%) and demonstrated an unusually high thermal stability *Cf*. **1**-**7** (**31**-**37***) in this series, isothermal analyses were performed at both 130 °C and 160 °C respectively, where a significantly higher volatility was observed above the recorded melting point of 153 °C.

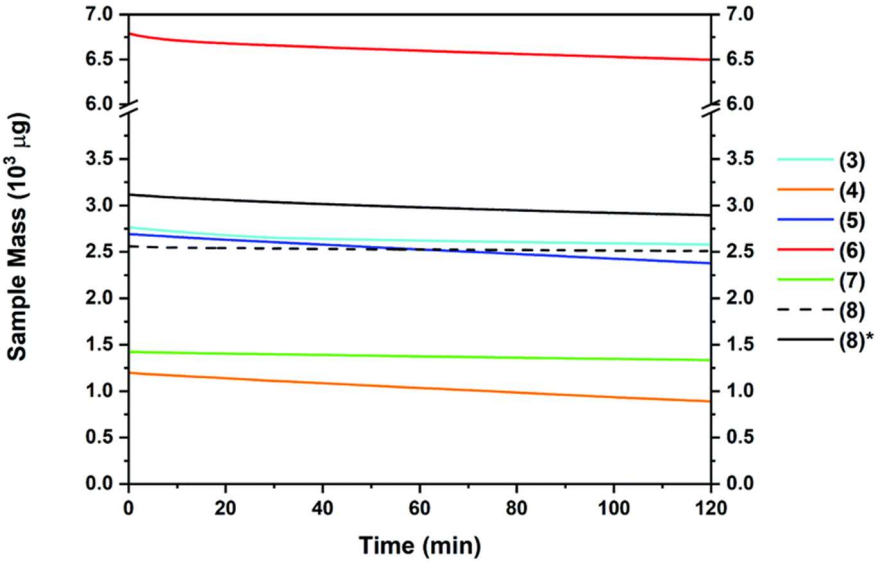

*Figure 5.11 – Mass loss (mg) for complexes **3–8** (**31-38***) over 120 min at 120 °C and 160 °C*.*

It should be noted that these differences would not have been recognised from a standard plot of % mass loss verses time commonly found elsewhere in the literature, which fails to take into account the differences in mass between samples, and instead reports the change in mass as a percentage of sample size, which is rarely consistent on scales such as these.

5.3.3. Conclusions

With the use of amine and aldimine substituted pyrroles as chelating ligands, a series of novel homoleptic Sn(II) complexes have been developed. All the compounds are monomeric and volatile, showing variable sublimation behaviour. Given the limited choice of precursors available for MOCVD and ALD of Sn(II) oxide thin films, the ethyl, t-butyl and 2,6-di-isopropylphenyl complexes of **4** (**34***), **5** (**35***) and **8** (**38***), reported here, are promising precursor candidates for vapour deposition processes. Work presented here primarily concerns precursor development and molecular characterisation. Detailed studies into the MOCVD and ALD of Sn(II) oxides using these precursors, and subsequent thin film characterisation, will be published separately.

5.3.4. Experimental

General Procedures: Elemental analyses were performed using an Exeter Analytical CE 440 analyser. ^{1}H, ^{13}C and ^{119}Sn NMR spectra were recorded on Bruker Advance 300 or 500 MHz FT–NMR spectrometers, as appropriate, as saturated solutions at room temperature. Chemical shifts are in ppm with respect to Me_4Si (^{1}H, ^{13}C{^{1}H}). TGA and PXRD were performed using a Perkin Elmer TGA7 and Bruker D8 instrument (Cu-kα radiation), respectively.

All reactions were carried out under an inert atmosphere using standard Schlenk techniques. Solvents were dried and degassed under an argon atmosphere over activated alumina columns using an Innovative Technology solvent purification system (SPS). The Sn(II) amides, [Sn{NMe_2}$_2$] and [Sn{$N(SiMe_3)_2$}$_2$], were prepared by literature methods;[2,85,86] The pro-ligands L^1H-L^7H were synthesized using literature methods.[6,32,75]

Synthesis of [Sn{κ^2-N,N'-$NC_4H_3CH_2NMe_2$}{$N(SiMe_3)_2$}] (**1**) (**31***)

A solution of L^1H (0.62g, 5 mmol) in hexane (30 mL) was added to a cooled solution of $Sn(HMDS)_2$ (2.20 g, 5 mmol) in hexane (30 mL). The resultant clear, pale yellow solution was stirred for 3 h before in vacuo removal of the volatiles and dissolution in fresh hexane. The solution was filtered through Celite® and the volume reduced before storage at –28 °C afforded colourless crystals. Yield: 1.13 g, 56%. Elemental analysis for $C_{13}H_{29}N_3Si_2Sn$ (expected): C 38.92 (38.81); H, 7.26 (7.27); N, 10.48 (10.45). ^{1}H NMR (500 MHz, C_6D_6); 6.96-7.04 (m, 1H, Pyr, C4-H), 6.54-6.61 (m, 1H, Pyr, C3-H), 6.32-6.38 (m, 1H, Pyr, C2-H), 3.35 (br s, 1H, CH_2), 1.76 (br s, 6H, NMe_2), 0.25 (s, 18H, $SiMe_3$): ^{13}C{^{1}H} NMR (125.7 MHz, C_6D_6); 135.5 (1C, Pyr, C1), 125.5, 111.3, 107.5, 60.8 (1C, CH_2), 45.3 (2C, NMe_2), 6.7 (6C, $SiMe_3$) ^{119}Sn NMR (186.4 MHz, C_6D_6); 49.9.

Synthesis of [Sn{κ^2-N,N'-$NC_4H_3CH_2NMe_2$}$_2$] (**2**) (**32***)

A solution of L^1H (1.25g, 10mmol) in hexane (30 mL) was added to a cooled solution of $Sn(HMDS)_2$ (2.20 g, 5 mmol) in hexane (30 mL). The resultant clear, pale yellow solution was stirred for 3 h before in vacuo removal of the volatiles and dissolution in fresh hexane. The solution was filtered through Celite® and the volume reduced before storage at −28 °C afforded colourless crystals. Yield: 1.22 g, 67%. Elemental analysis for $C_{14}H_{22}N_4Sn$ (expected): C 45.94 (46.06) %, H 5.93 (6.07) %, N 15.22 (15.33) %. ^{1}H NMR (300 MHz, C_6D_6); 6.99-7.01 (m, 1H, Pyr, C4-H), 6.59-6.61 (m, 1H, Pyr, C3-H), 6.36-6.39 (m, 1H, Pyr, C2-H), 3.35 (s, 1H, CH_2), 1.86 (s, 6H, NMe_2). ^{13}C{^{1}H} NMR (75.5 MHz, C_6D_6); 137.0 (1C, Pyr, C1), 125.5 (1C, Pyr, C4), 109.5 (1C, Pyr, C3), 108.0 (1C, Pyr, C2), 59.3 (1C, CH_2), 44.8 (2C, NMe_2). ^{119}Sn NMR (111.8 MHz, C_6D_6); −275.0

Synthesis of [Sn{κ^2-N,N'-$NC_4H_3C(H)NMe$}$_2$] (**3**) (**33***)

A solution of L^2H (1.1 g, 10 mmol) in hexane (30 mL) was added to a cooled solution of $Sn(HMDS)_2$ (2.20 g, 5 mmol) in hexane (30 mL) The resultant clear, pale yellow solution was stirred for 3 h before in vacuo removal of the volatiles and dissolution in fresh hexane. The solution was filtered through Celite® and the volume reduced before storage at −28 °C afforded colourless crystals. Yield: 1.45 g, 87%. Elemental analysis for $C_{12}H_{14}N_4Sn$ (expected): C 42.96 (43.29) %, H 4.07 (4.24) %, N 16.63 (16.83) %. ^{1}H NMR (500 MHz, C_6D_6);

7.35-7.41 (m, 1H, PyrC*H*NMe), 6.97-7.02 (m, 1H, Pyr, C4-H), 6.69-6.74 (m, 1H, Pyr, C3-H), 6.48-6.53 (m, 1H, Pyr, C2-H), 2.83 (s, 3H, CH_3). $^{13}C\{^1H\}$ NMR (75.5 MHz, C_6D_6); 159.3 (1C, PyrCHNMe), 137.5 (1C, Pyr, C1), 133.3 (1C, Pyr, C4), 117.5 (1C, Pyr, C3), 112.9 (1C, Pyr, C2), 42.4 (1C, CH_3). ^{119}Sn NMR (111.8 MHz, C_6D_6); −401.0

Synthesis of [Sn{κ^2-N,N'-$NC_4H_3C(H)NEt$}$_2$] (**4**) (**34***), [Sn{κ^2-N,N'-$NC_4H_3C(H)NtBu$}$_2$] (**5**) (**35***), [Sn{κ^2-N,N'-$NC_4H_3C(H)N^sBu$}$_2$] (**6**) (**36***) [Sn{κ^2-N,N'-$NC_4H_3C(H)N^nBu$}$_2$] (**7**) (**37***)and [Sn{κ^2-N,N'-$NC_4H_3C(H)N(2,6\text{-}^iPr_2C_6H_3)$}$_2$] (**8**) (**38***).

Complexes **4** (**34***), **5** (**35***), **6** (**36***), **7** (**37***) and **8** (**38***) were made in an analogous manner to **3** (**33***) using of 1.22 g (10 mmol) of L^3H, 1.50g (10 mmol) L^4H, L^5H L^6H and 2.54g (10 mmol) of L^7H, respectively.

(**4**) (**34***): Storage at −28 °C afforded colourless crystals. Yield: 1.16g, 64%. Elemental analysis for $C_{14}H_{18}N_4Sn$ (expected): C 46.46 (46.58) %, H 4.87 (5.03) %, N 15.61 (15.52) %. ^1H NMR (500 MHz, C_6D_6); 7.49-7.56 (m, 1H, PyrC*H*NEt), 7.04-7.07 (m, 1H, Pyr, C4-*H*), 6.73-6.77(m, 1H, Pyr, C3-*H*), 6.50-6.53 (m, 1H, Pyr, C2-*H*), 3.18-3.25 (s, 2H, CH_2), 1.03 (t, 3H, CH_3). $^{13}C\{^1H\}$ NMR (75.5 MHz, C_6D_6); 156.9 (1C, Pyr*C*HNEt), 137.3 (1C, Pyr, *C*1), 133.1 (1C, Pyr, *C*4), 117.4 (1C, Pyr, *C*3), 112.5 (1C, Pyr, *C*2), 51.2 (1C, *C*H_2), 17.3 (1C, *C*H_3). ^{119}Sn NMR (111.8 MHz, C_6D_6); -402.3.

(**5**) (**35***): Storage at −28 °C afforded colourless crystals. Yield: 1.69 g, 81%. Elemental analysis for $C_{18}H_{26}N_4Sn$ (expected): C 51.93 (51.83) %, H 6.15 (6.28) %, N 13.86 (13.43) % ^1H NMR (500 MHz, C_6D_6); 7.97-8.02 (m, 1H, PyrrC*H*N^{t}Bu), 7.19-7.21 (m, 1H, Pyrr, C4-*H*), 6.76-6.79 (m, 1H, Pyrr, C3-*H*), 6.46-6.48 (m, 1H, Pyrr, C2-*H*), 1.19 (s, 9H, CH_3). $^{13}C\{^1H\}$ NMR (75.5 MHz, C_6D_6); 154.0 (1C, Pyrr*C*HN^{t}Bu), 138.5 (1C, Pyrr, *C*1), 133.7 (1C, Pyrr, *C*4), 118.3 (1C, Pyrr, *C*3), 112.6 (1C, Pyrr, *C*2), 57.5 (1C, *C*$(CH_3)_3$), 31.3 (3C, C(*C*$H_3)_3$). ^{119}Sn NMR (111.8 MHz, C_6D_6); −384.1.

(**6**) (**36***): Storage at −28 °C afforded colourless crystals. Yield: 1.50g, 72%. Elemental analysis for $C_{18}H_{26}N_4Sn$ (expected): C 52.13 (51.83) %, H 6.37 (6.28) %, N 13.28 (13.43) %. ^1H NMR (500 MHz, C_6D_6); 7.70-7.77 (m, 1H, PyrrC*H*N^{s}Bu), 7.15-7.19 (m, 1H, Pyrr, C4-*H*), 6.77-6.80 (m, 1H, Pyrr, C3-*H*), 6.47-6.50 (m, 1H, Pyrr, C2-*H*), 3.10-3.20 (m, 1H, -NC*H*$(CH_3)CH_2CH_3$), 1.54-1.66 (m, 1H, NCH(CH_3)CH_2CH_3), 1.36-1.47 (m, 1H, NCH(CH_3)CH_2CH_3) 1.14-1.19 (m, 3H, NCH(C$H_3)CH_2CH_3$), 0.70-0.75 (m, 3H, NCH$(CH_3)CH_2$CH_3).$^{13}C\{^1H\}$ NMR (125.7 MHz, C_6D_6); 156.0 (1C, Pyrr*C*HN^{s}Bu), 137.6 (1C, Pyrr, *C*1), 133.7 (1C, Pyrr, *C*4), 118.2 (1C, Pyrr, *C*3), 112.7 (1C, Pyrr, *C*2), 64.3 (br, d, 1C, N*C*$(CH_3)CH_2CH_3$), 32.3 (d, 1C, NC(CH_3)*C*H_2CH_3), 22.6 (d, 1C, NC(*C*$H_3)CH_2CH_3$), 11.5 (d, 1C, NC$(CH_3)CH_2$*C*H_3). ^{119}Sn NMR (186.4 MHz, C_6D_6); -385.7

(**7**) (**37***): Storage at −28 °C afforded colourless crystals. Yield: 1.56g,75%. Elemental analysis for $C_{18}H_{26}N_4Sn$ (expected):C 51.55 (51.83) %, H 6.20 (6.28) %, N 13.12 (13.43) %. ^{1}H NMR (500 MHz, C6D6); 7.55-7.61 (m, 1H, PyrrC*H*NnBu), 7.09-7.12 (m, 1H, Pyrr, C4-*H*), 6.76-6.79 (m, 1H, Pyrr, C3-*H*), 6.53-6.55 (m, 1H, Pyrr, C2-*H*), 3.26-3.31 (t, J=6.85Hz, 2H, NC*H*$_2$CH$_2$CH$_2$CH$_3$), 1.47-1.54 (m, 2H, PyrrCHNCH$_2$C*H*$_2$CH$_2$C*H*$_3$), 1.12-1.20 (m, 2H, -NCH$_2$CH$_2$C*H*$_2$C*H*$_3$), 0.79 (t, J=7.34Hz 3H, NCH$_2$CH$_2$CH$_2$C*H*$_3$). ^{13}C{^{1}H} NMR (125.7 MHz, C_6D_6); 157.82 (s, 1C, Pyrr*C*HN^{n}Bu), 137.6 (1C, Pyrr, *C*1), 133.5 (1C, Pyrr, *C*4), 117.8 (1C, Pyrr, *C*3), 112.9 (1C, Pyrr, *C*2), 57.4 (1C, N*C*H$_2$ CH$_2$CH$_2$CH$_3$), 34.6 (1C, NCH$_2$*C*H$_2$CH$_2$CH$_3$), 21.1 (1C, NCH$_2$CH$_2$*C*H$_2$CH$_3$) 14.3 (1C, NCH$_2$CH$_2$CH$_2$*C*H$_3$).^{119}Sn NMR (186.4 MHz, C_6D_6); -401.5.

(**8**) (**38***): Storage at −28 °C afforded colourless crystals. Yield: 2.63g, 84%. Elemental analysis for $C_{34}H_{42}N_4Sn$ (expected): C 65.37 (65.29) %, H 6.83 (6.77) %, N 8.91 (8.96) %. ^{1}H NMR (500 MHz, C_6D_6); 7.85-7.86 (m, 1H, PyrrC*H*NDipp), 7.13-7.23 (m, 3H, *ortho, meta*-Dipp), 6.84-6.86 (m, 1H, Pyrr, C4-*H*), 6.62-6.64 (m, 1H, Pyrr, C3-*H*), 6.35-6.37 (m, 1H, Pyrr, C2-*H*), 3.43 (br s, 1H, C*H*Me$_2$), 3.00 (br s, 1H, C*H*Me$_2$), 0.89-1.36 (br, m, 12H, CH*Me$_2$*). ^{13}C{^{1}H} NMR (125.7 MHz, C_6D_6); 158.6 (1C, Pyrr*C*HNDipp), 149.8 (1C, *ipso-Dipp*), 145.6 (1C, Pyrr, *C*1), 142.8 (1C, *ortho-Dipp*), 142.3 (1C, *ortho-Dipp*), 137.0 (s, 1C, Pyrr, *C*3), 126.7 (br, 2C, *meta-Dipp*), 124.6 (br, 1C, *para-Dipp*), 121.0 (1C, Pyrr, *C*4), 114.5 (1C, Pyrr, *C*2), 29.1 (br, 1C, *C*HMe$_2$), 28.7 (br, 1C, *C*HMe$_2$), 26.4 (br, CH*Me$_2$*), 24.9 (br, CH*Me$_2$*), 24.6 (br, CH*Me$_2$*), 23.1 (br, CH*Me$_2$*).^{119}Sn NMR (111.8 MHz, C_6D_6); −419.0.

Single crystal X-ray diffraction

Experimental details relating to the single-crystal X-ray crystallographic studies for compounds 1-5 and 8 are summarised in Table 5.4. All crystallographic data were collected at 150(2) K either on a SuperNova, Dual, EosS2 diffractometer using radiation Cu-Kα (λ= 1.54184 Å) or Mo-Kα (λ= 0.71073 Å). All structures were solved by direct methods followed by full-matrix least squares refinement on F2 using the WINGX-2014 suite of programs[87] or OLEX2.[88] All hydrogen atoms were included in idealised positions and refined using the riding model. Crystals were isolated from an argon filled Schlenk flask and immersed under oil before being mounted onto the diffractometer.

*Table 5.4 - X-ray crystallographic data for compounds 1–5 (**31-35***) and 8 (**38***)*

Compound Number	**1** (**31***)	**2** (**32***)	**3** (**33***)	**4** (**34***)	**5** (**35***)	**8** (**38***)
Chemical formula	$C_{13}H_{29}N_3Si_2Sn$	$C_{14}H_{22}N_4Sn$	$C_{12}H_{14}N_4Sn$	$C_{14}H_{18}N_4Sn$	$C_{18}H_{26}N_4Sn$	$C_{34}H_{42}N_4Sn$
Formula Mass	402.26	365.04	332.96	361.01	417.12	625.40
Crystal System	Monoclinic	Monoclinic	Monoclinic	Monoclinic	Monoclinic	Monoclinic
Space group	*P*121/*c*1	*P*121/*c*1	*P*21/*n*	*P*21	*P*21/*n*	*P*121/*n*1
a/Å	11.8512(4)	9.3277(3)	13.7265(4)	8.5561(3)	12.1057(3)	15.0740(1)
b/Å	10.4036(3)	11.3766(4)	5.93000(10)	8.8998(3)	9.7711(2)	11.8067(1)
c/Å	15.6557(5)	14.9148(6)	16.1287(4)	10.0193(3)	16.0995(4)	18.2296(2)
α/°	90	90	90	90	90	90
β/°	96.431(3)	98.662(4)	104.195(3)	93.866(3)	95.487(2)	106.666(1)
γ/°	90	90	90	90	90	90
Unit cell volume/Å^3	1918.13(11)	1564.67(10)	1272.76(6)	761.21(4)	1895.62(8)	3108.11(5)
Crystal Size (mm)	0.403 × 0.37 × 0.293	0.516 × 0.378 × 0.266	0.372 x 0.040 x 0.028	0.320 x 0.150 x 0.030	0.389 x 0.251 x 0.037	0.277 × 0.238 × 0.196
Temperature/K	150.00(10)	150.00(10)	150(2)	150(2)	150(2)	150.00(10)
Z	4	4	4	2	4	4
Radiation type	MoKα	MoKα	Cu Kα	Cu Kα	Cu Kα	CuKα
Theta range (°)	6.54 to 54.958	6.586 to 54.958	3.797 to 72.307	4.423 to 73.010	4.375 to 73.438	6.732 to 145.674
Absorption coefficient, μ/mm^{-1}	1.451	1.627	15.833	13.285	10.746	6.741
No. of reflections measured	15655	13218	13015	5956	12882	26377
No. of independent reflections	4329	3586	2487	2288	3772	6142
R_{int}	0.0354	0.0361	0.0405	0.0279	0.0598	0.0393
Final R_1 values ($I > 2\sigma(I)$)	0.0295	0.0291	0.0260	0.0336	0.0495	0.0258
Final $wR(F^2)$ values ($I > 2\sigma(I)$)	0.0561	0.0563	0.0631	0.0894	0.1407	0.0697
Final R_1 values (all data)	0.0372	0.0381	0.0291	0.0338	0.0536	0.0265
Final $wR(F^2)$ values (all data)	0.0596	0.0607	0.0646	0.0896	0.1453	0.0702
Goodness of fit on F^2	1.068	1.061	1.128	1.077	1.090	1.062
Largest diff. peak and hole (e.Å^{-3})	0.42 and -0.35	0.33 and -0.51	1.008 and -0.401	1.203 and -0.788	1.728 and -0.965	0.73 and -0.70
CCDC Number	1820592	1820591	1820595	1820596	1820594	1820593

The asymmetric unit cell of **3** (**33***) comprises of one molecule of the complex in which all ligand atoms, with the exception of Sn1, N3 and N1, exhibited 80:20 disorder via a pseudo mirror plane containing the three non-affected atoms. Bond length restraints were included (for chemically equivalent bonds in both the major/minor components), in addition to ADP restraints.

Complex **5** (**35***) suffers from similar disorder to that observed in 3, i.e. asymmetric unit cell the comprises of one molecule of the complex in which all ligand atoms, with the exception of N3 and N1, exhibited 67:33 disorder via a pseudo mirror plane containing the three non-affected atoms. Distance-similarity restraints were included (for chemically equivalent bonds in both the major/minor components), in addition to ADP restraints, to assist convergence. The Sn centre is disordered over two sites in 9:1 ratio.

Thermogravimetric analysis (TGA)

TGA was collected using a TGA 4000 Perkin Elmer system, housed in an argon filled glovebox. Samples were prepared air sensitively, and TGAs were performed under a flow of Ar at 20 mL min^{-1} and heated from 30 °C to 400 °C at a ramp rate of 5 °C min^{-1}.

5.3.5. Conflicts of Interest

There are no conflicts to declare.

5.3.6. Acknowledgements

We acknowledge the financial support of the University of Bath (PhD studentships to J.D.P.), and the Department of Chemistry (Masters Studentship to M.W.S.).

5.4. Supporting Information

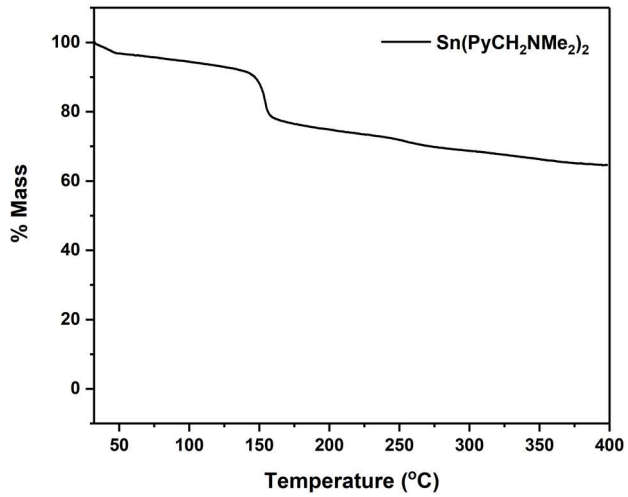

*Figure 5.12 - Thermogravimetric analysis data for complex 2 (**32***).*

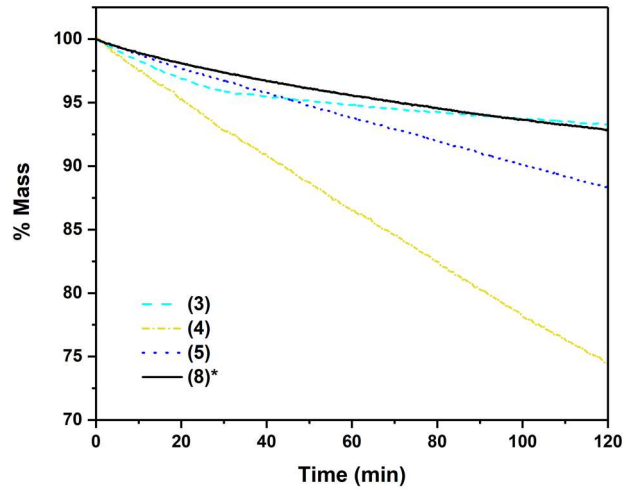

*Figure 5.13 - Plot of %Mass loss over time for complexes 3 (**33***), 4 (**34***), 5 (**35***) and 8(**38***).*

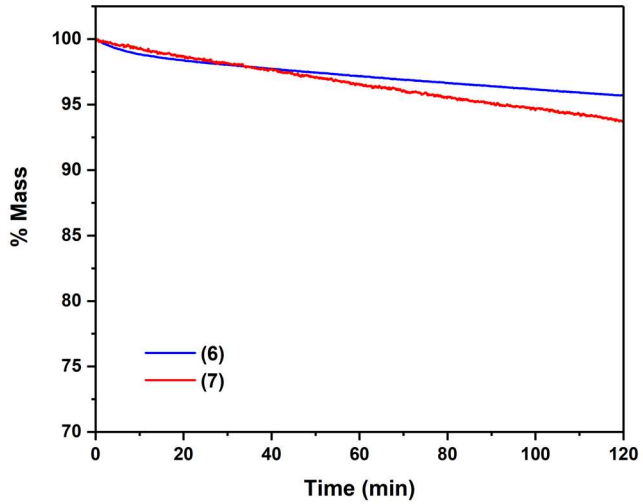

*Figure 5.14 - Plot of %Mass loss over time for complexes 6 (**36***) and 7 (**37***).*

5.5. Conclusions

With the proven efficacy of tin(II) amide systems in the ALD of tin(II) oxide established within Chapter 3, attempts to improve the stability of tin(II) amides, whilst retaining high reactivity resulted in the synthesis and characterisation of a range of Sn(II)-pyrrolide systems. These systems contained either a pendant sp^3 nitrogen moiety within the amino (NMe_2) fragment, or an sp^2-based system comprising an imino (C=NR) group. These alterations resulted in markedly different thermal behaviours, with the amine-based groups proving entirely unsuitable for any thermal process.

Whilst the pyrrolyl-imine derived systems displayed volatility, this was found to be considerably lower than the other complexes characterised throughout this research as a whole. Where melting points were observed, these proved to lie incredibly close to decomposition temperatures, which were also found to be largely lower than desirable for ALD applications. The only exception to these observations was found within the aryl-imine system [Sn(py-CH=Ndipp)$_2$] (**8**) (**38***), which displayed a melting point of 153 °C and thermal stability up to 290°C. This is highly unusual within tin(II) amide species and warrants further investigation. It is likely that the lack of available hydrogen elimination pathways is responsible for the heightened stability compared to the alkylated species,[76] which could be utilised in the design of thermally robust tin(II) systems in future research.

5.6. References

1 J. D. Parish, M. W. Snook, A. L. Johnson and G. Kociok-Köhn, *Dalton Trans.*, 2018, **47**, 7721–7729.

2 T. Fjeldberg, H. Hope, M. F. Lappert, P. P. Power and A. J. Thorne, *J. Chem. Soc. Chem. Comm.*, 1983, 639–641.

3 A. P. Sadimenko, *Adv. Heterocyclic Chem.*, 2001, **79**, 115–197.

4 E. Baltazzi and L. I. Krimen, *Chem. Rev.*, 1963, **63**, 511–556.

5 C. Maaß, D. M. Andrada, R. A. Mata, R. Herbst-Irmer and D. Stalke, *Inorg. Chem.*, 2013, **52**, 9539–9548.

6 Y. Yang, D. Cui and X. Chen, *Dalton Trans.*, 2010, **39**, 3959–3967.

7 A. C. Jones, H. C. Aspinall, P. R. Chalker, R. J. Potter, T. D. Manning, Y. F. Loo, R. O'Kane, J. M. Gaskell and L. M. Smith, *Chem. Vap. Deposition*, 2006, 12, 83–98.

8 P. A. Williams, J. L. Roberts, A. C. Jones, P. R. Chalker, N. L. Tobin, J. F. Bickley, H. O. Davies, L. M. Smith and T. J. Leedham, *Chem. Vap. Deposition*, 2002, **8**, 163–170.

9 K. A. Fleeting, P. O'Brien, A. C. Jones, D. J. Otway, A. J. P. White and D. J. Williams, *J. Chem. Soc., Dalton Trans.*, 1999, 2853–2859.

10 N. Kuhn, G. Henkel and S. Stubenrauch, *Angew. Chemie Int. Ed. Engl.*, 2018, **31**, 778–779.

11 M. Kreye, C. G. Daniliuc, M. Freytag, P. G. Jones and M. D. Walter, *Dalton Trans.*, 2014, **43**, 9052–9060.

12 H. Schumann, J. Gottfriedsen and J. Demtschuk, *Chem. Commun.*, 1999, 2091–2092.

13 M. Kreye, A. Glöckner, C. G. Daniliuc, M. Freytag, P. G. Jones, M. Tamm and M. D. Walter, *Dalton Trans.*, 2013, **42**, 2192–2200.

14 A. Novak, A. J. Blake, C. Wilson and J. B. Love, *Chem. Commun.*, 2002, 2796–2797.

15 M. Kreye, M. Freytag, C. G. Daniliuc, P. G. Jones and M. D. Walter, *Z. Anorg. Allg. Chem.*, 2015, **641**, 2109–2114.

16 T. Murahashi, S. Kimura, K. Takase, S. Ogoshi and K. Yamamoto, *Chem. Commun.*, 2013, **49**, 4310–4312.

17 T. K. Panda, K. Yamamoto, K. Yamamoto, H. Kaneko, Y. Yang, H. Tsurugi and K. Mashima, *Organometallics*, 2012, **31**, 2268–2274.

18 J. Lewiński, M. Dranka, I. Kraszewska, W. Śliwiński and I. Justyniak, *Chem. Commun.*, 2005, 4935–4937.

19 B. Vidjayacoumar, D. J. H. Emslie, J. M. Blackwell, S. B. Clendenning and J. F. Britten, *Chem. Mater.*, 2010, **22**, 4854–4866.

20 L. C. Kalutarage, P. D. Martin, M. J. Heeg and C. H. Winter, *J. Am. Chem. Soc.*, 2013, **135**, 12588–12591.

21 L. C. Kalutarage, S. B. Clendenning and C. H. Winter, *ECS Trans.*, 2014, **64**, 147–157.

22 S. Acharya, J. Torgersen, Y. Kim, J. Park, P. Schindler, A. L. Dadlani, M. Winterkorn, S. Xu, S. P. Walch, T. Usui, C. Schildknecht and F. B. Prinz, *J. Mater. Chem. C*, 2016, **4**, 1945–1952.

23 J. A. T. Norman, M. Perez, M. S. Kim, X. Lei, S. Ivanov, A. Derecskei-Kovacs, L. Matz, I. Buchanan and A. L. Rheingold, *Inorg. Chem.*, 2011, **50**, 12396–12398.

24 M. J. Saly, F. Munnik, R. J. Baird and C. H. Winter, *Chem. Mater.*, 2009, **21**, 3742–3744.

25 M. J. Saly, F. Munnik and C. H. Winter, *J. Mater. Chem.*, 2010, **20**, 9995–10000.

26 M. J. Saly, F. Munnik and C. H. Winter, *Chem. Vap. Deposition*, 2011, **17**, 128–134.

27 M. Bueyuekyazi, T. Fischer, P. Yu, M. Coll and S. Mathur, *Dalton Trans.*, 2017, **46**, 12996–13001.

28 V. Grushin, E.I. Du Pont De Nemours and Company, PCT Int. Appl., WO2004015164A1 2002.

29 C. Lansalot-Matras, L'Air Liquide, *PCT Int. Appl.*, WO2012059881A1, 2012.

30 A. Koralev and C. Lansalot-Matras, L'Air Liquide, *PCT Int. Appl.*, WO2013101303A1, 2013.

31 B. Vidjayacoumar, D. J. H. Emslie, S. B. Clendenning, J. M. Blackwell, J. F. Britten and A. Rheingold, *Chem. Mater.*, 2010, **22**, 4844–4853.

32 V. V Grushin and W. J. Marshall, *Adv. Synth. Catal.*, 2004, **346**, 1457–1460.

33 K. Lubitz, V. Sharma, S. Shukla, J. H. J. Berthel, H. Schneider, C. Hoßbach and U. Radius, *Organometallics*, 2018, **37**, 1181–1191.

34 J. P. Coyle, G. Dey, E. R. Sirianni, M. L. Kemell, G. P. A. Yap, M. Ritala, M. Leskelä, S. D. Elliott and S. T. Barry, *Chem. Mater.*, 2013, **25**, 1132–1138.

35 N. Kuhn, G. Henkel and S. Stubenrauch, *J. Chem. Soc. Chem. Commun.*, 1992, 760–761.

36 K. Hübler and U. Hübler, *Z. Anorg. Allg. Chem.*, 2000, **626**, 1224–1236.

37 P. P. Edwards, A. Porch, M. O. Jones, D. V Morgan and R. M. Perks, *Dalton Trans.*, 2004, 2995–3002.

38 J. Robertson, R. Gillen and S. J. Clark, *Thin Solid Films*, 2012, **520**, 3714–3720.

39 E. Fortunato, P. Barquinha and R. Martins, *Adv. Mater.*, 2012, **24**, 2945–2986.

40 M. Yan, Q. Zhang, Y. Zhao, J. Yang, T. Yang, J. Zhang and X. Li, *J. Nanosci. Nanotechnol.*, 2015, **15**, 6279–6294.

41 X. Yu, T. J. Marks and A. Facchetti, *Nat. Mater.*, 2016, **15**, 383.

42 S. A. Miller, P. Gorai, U. Aydemir, T. O. Mason, V. Stevanović, E. S. Toberer and G. J. Snyder, *J. Mater. Chem. C*, 2017, **5**, 8854–8861.

43 K. H. L. Z. and K. X. and M. G. B. and R. G. Egdell, *J. Phys. Condens. Matter*, 2016, **28**, 383002.

44 A. N. Banerjee and K. K. Chattopadhyay, *Prog. Cryst. Growth Charact. Mater.*, 2005, **50**, 52–105.

45 L. Chen, J. Yang, S. Klaus, L. J. Lee, R. Woods-Robinson, J. Ma, Y. Lum, J. K. Cooper,

F. M. Toma, L.-W. Wang, I. D. Sharp, A. T. Bell and J. W. Ager, *J. Am. Chem. Soc.*, 2015, **137**, 9595–9603.

46 Z. Wang, P. K. Nayak, J. A. Caraveo-Frescas and H. N. Alshareef, *Adv. Mater.*, 2016, **28** (20), 3831-3892.

47 K. J. Saji, K. Tian, M. Snure and A. Tiwari, *Adv. Electron. Mater.*, 2016, **2**, 1500453.

48 Y. Ogo, H. Hiramatsu, K. Nomura, H. Yanagi, T. Kamiya, M. Kimura, M. Hirano and H. Hosono, *Phys. Status Solidi A*, 2009, **206**, 2187–2191.

49 J. A. Caraveo-Frescas, P. K. Nayak, H. A. Al-Jawhari, D. B. Granato, U. Schwingenschlögl and H. N. Alshareeft, *ACS Nano*, 2013, **7**, 5160–5167.

50 D. Das and R. Banerjee, *Thin Solid Films*, 1987, **147**, 321–331.

51 Y. Ogo, H. Hiramatsu, K. Nomura, H. Yanagi, T. Kamiya, M. Hirano and H. Hosono, *Appl. Phys. Lett.*, 2008, **93**, 32113.

52 H. Mu, K. Wang, Z. Zhang and H. Xie, *J. Phys. Chem. C.*, 2015, **119**, 10102–10108.

53 B. Kumar, D.-H. Lee, S.-H. Kim, B. Yang, S. Maeng and S.-W. Kim, *J. Phys. Chem. C*, 2010, **114**, 11050–11055.

54 N. Hollingsworth, G. A. Horley, M. Mazhar, M. F. Mahon, K. C. Molloy, P. W. Haycock, C. P. Myers and G. W. Critchlow, *Appl. Organomet. Chem.*, 2006, **20**, 687–695.

55 H. Uchiyama and H. Imai, *Langmuir*, 2008, **24**, 9038–9042.

56 J. Ning, T. Jiang, K. Men, Q. Dai, D. Li, Y. Wei, B. Liu, G. Chen, B. Zou and G. Zou, *J. Phys. Chem. C*, 2009, **113**, 14140–14144.

57 T. J. Boyle, T. Q. Doan, L. A. M. Steele, C. Apblett, S. M. Hoppe, K. Hawthorne, R. M. Kalinich and W. M. Sigmund, *Dalton Trans.*, 2012, **41**, 9349–9364.

58 K. Okamura, B. Nasr, R. A. Brand and H. Hahn, *J. Mater. Chem.*, 2012, **22**, 4607–4610.

59 I. Barbul, A. L. Johnson, G. Kociok-Köhn, K. C. Molloy, C. Silvestru and A. L. Sudlow, *Chempluschem*, 2013, **78**, 866–874.

60 T. Wildsmith, M. S. Hill, A. L. Johnson, A. J. Kingsley and K. C. Molloy, *Chem. Commun.*, 2013, **49**, 8773–8775.

61 M. S. Hill, A. L. Johnson, J. P. Lowe, K. C. Molloy, J. D. Parish, T. Wildsmith and A. L. Kingsley, *Dalton Trans.*, 2016, **45**, 18252–18258.

62 H. Viirola and L. Niinistö, *Thin Solid Films*, 1994, **249**, 144–149.

63 X. Du, Y. Du and S. M. George, *J. Phys. Chem. A*, 2008, **112**, 9211–9219.

64 X. Du, Y. Du and S. M. George, *J. Vac. Sci. Technol. A*, 2005, **23**, 581–588.

65 J. Sundqvist, J. Lu, M. Ottosson and A. Hårsta, *Thin Solid Films*, 2006, **514**, 63–68.

66 H.-E. Cheng, D.-C. Tian and K.-C. Huang, *Procedia Eng.*, 2012, **36**, 510–515.

67 J. Elam, D. A. Baker, A. J. Hryn, A. Martinson, M. Pellin and J. Hupp, *J. Vac. Sci. Technol. A.*, 2008, 26, 244-252.

68 C. E. Nanayakkara, G. Liu, A. Vega, C. L. Dezelah, R. K. Kanjolia and Y. J. Chabal, *Langmuir*, 2017, **33**, 5998–6004.

69 J. Heo, A. S. Hock and R. G. Gordon, *Chem. Mater.*, 2010, **22**, 4964–4973.

70 M. S. Weimer, B. Hu, S. J. Kraft, R. G. Gordon, C. U. Segre and A. S. Hock, *Organometallics*, 2016, **35**, 1202–1208.

71 J. Heo, S. B. Kim and R. G. Gordon, *J. Mater. Chem.*, 2012, **22**, 4599–4602.

72 J. Tupala, M. Kemell, M. Mattinen, K. Meinander, S. Seppälä, T. Hatanpää, J. Räisänen, M. Ritala and M. Leskelä, *J. Vac. Sci. Technol. A*, 2017, **35**, 41506.

73 J. H. Han, Y. J. Chung, B. K. Park, S. K. Kim, H. S. Kim, C. G. Kim and T. M. Chung, *Chem. Mater.*, 2014, **26**, 6088–6091.

74 G. S. Mary, N. J. Hyeun, L. G. Yeon, H. J. Hwan, P. B. Keun, K. C. Gyoun, J. D. Ju and C. Taek-Mo, *Eur. J. Inorg. Chem.*, 2016, **2016**, 5539–5546.

75 B.-C. Xu, T. Hu, J.-Q. Wu, N.-H. Hu and Y.-S. Li, *Dalt. Trans.*, 2009, 8854–8863.

76 K. Black, A. C. Jones, J. Bacsa, P. R. Chalker, P. A. Marshall, H. O. Davies, P. N. Heys, P. O'Brien, M. Afzaal, J. Raftery and G. W. Critchlow, *Chem. Vap. Depos.*, 2010, **16**, 93–99.

77 G. L. Fondong, E. Y. Njua, A. Steiner, C. F. Campana and L. Stahl, *Polyhedron*, 2011, **30**, 2856–2862.

78 W.-P. Leung, C.-W. So, Y.-S. Wu, H.-W. Li and T. C. W. Mak, *Eur. J. Inorg. Chem.*, 2004, **2005**, 513–521.

79 M. Westerhausen, J. Greul, H.-D. Hausen and W. Schwarz, *Zeitschrift für Anorg. und Allg. Chemie*, 2018, **622**, 1295–1305.

80 J. R. Babcock, L. Liable-Sands, A. L. Rheingold and L. R. Sita, *Organometallics*, 1999, **18**, 4437–4441.

81 A. W. Addison, T. N. Rao, J. Reedijk, J. van Rijn and G. C. Verschoor, *J. Chem. Soc. Dalt. Trans.*, 1984, 1349–1356.

82 A. Devi, *Coord. Chem. Rev.*, 2013, **257**, 3332–3384.

83 C. Dussarrat, *ECS Trans.* , 2014, **64**, 233–241.

84 G. B. Bacskay, M. Martoprawiro and J. C. Mackie, *Chem. Phys. Lett.*, 1999, **300**, 321–330.

85 P. Foley and M. Zeldin, *Inorg. Chem.*, 1975, **14**, 2264–2267.

86 M. M. Olmstead and P. P. Power, *Inorg. Chem.*, 1984, **23**, 413–415.

87 L. J. Farrugia, *J. Appl. Crystallogr.*, 1999, **32**, 837–838.

88 O. V Dolomanov, L. J. Bourhis, R. J. Gildea, J. A. K. Howard and H. Puschmann, *J. Appl. Crystallogr.*, 2009, **42**, 339–341.

Chapter 6

Chapter 6: Conclusions and Future Directions

6.1. Conclusions

Research undertaken within Chapter 2 sought to replicate, understand and optimise the only effective reported ALD process for tin(II) oxide to date.[1] Resultant study demonstrated an optimised process on a commercial ALD tool that allowed for comparative study of novel ALD precursors. With a developed understanding of the limitations of the process, the temperature window of crystalline deposition was significantly extended, and displayed high growth rates (0.36 Å/cy) for crystalline SnO at 130 °C.

Furthermore, the molecular structure of the reported [Sn(dmamp)$_2$] precursor was obtained, and a range of related complexes synthesised and characterised in attempts to deconstruct the various steric and electronic influences within a proven tin(II) oxide precursor. A series of interesting molecular structures were elucidated, displaying unexpected bridging preferences as a result of subtle steric and electronic changes.

Work detailed in Chapter 3 attempted to leverage the high reactivity of Sn–N bonds in the design of a novel ALD precursor. The led to the development of a range of novel simple tin(II) amide systems, a number of which proved to be highly reactive and volatile liquids that displayed neither unexplained solid-liquid phase changes nor propensity to form cluster species, as observed in the aminoalkoxide systems detailed in Chapter 2. Subsequent deposition trials succeeded in depositing highly oriented, crystalline SnO making [Sn(deed)NMe$_2$] **(15)** the second reported ALD precursor for the oxidative control of tin(II) oxide deposition. Further study successfully deposited crystalline SnO onto *in situ* functionalised monolayer graphene, an important novel composite in sensing and battery research, for the first time.

With a greater understanding of the chemistry behind SnO deposition, a brief investigation was undertaken into the potential application of simple tin(II) alkoxides within ALD. This hitherto overlooked avenue proved to be highly successful and identified a number of areas for further research *ibid*. Significantly improved growth rates over previously encountered processes (up to 0.37 Å/cy) were observed for the deposition of crystalline SnO films between 150 °C and 210 °C for the precursor [Sn(O^{t}Bu)$_2$] **(24)**, whilst a second alkoxide precursor, [Sn{O(CH$_3$)$_2$CH$_2$CH$_3$}$_2$] **(26)** showed successful deposition of crystalline material at higher temperatures with improved high-temperature growth rates over all other precursors. Additionally, two fluorinated simple alkoxide complexes were structurally characterised, elucidating further electronic considerations within effective ligand design, whilst two final alkoxyether systems gave interesting contrast to similar systems characterised in Chapter 2.

Finally, a chapter presented in the Alternative Format detailed a published article containing a series of pyrrolide-based tin(II) systems and their assessment of structural and precursor properties. Whilst these systems were found to be less promising than those others detailed within the work as a whole, a number of considerations were brought to discussion, including the unusually high stability >290 °C of the aromatic pyrrolylaldimine [Sn(py-CH=Ndipp)$_2$], where dipp = 2,6-diisopropylphenyl, which was in sharp contrast to the stability of all tin(II) amides detailed in this work as a whole.

A number of thin film transistors using material deposited at the University of Bath were fabricated as part of ongoing collaborations with PragmatIC Printing Ltd. and the University of Cambridge. All devices showed successful p-type enhancement mode TFT behaviour, and it was determined throughout the course of the research that encapsulation of devices prior to post-deposition annealing significantly improved performance. The highest performing devices showed switching ratios of 8 x 10^4 and field-effect mobilities of 0.9 $cm^2\ V^{-1}\ s^{-1}$. These initial studies proved highly promising, with devices demonstrating above average performance compared with the majority of PVD deposited SnO devices in the literature.[2–6] More iterations are however needed before the switching ratios can achieve parity with those reported by Kim et al. fabricated using [Sn(dmamp)$_2$] deposited at 210 °C.[7]

6.2. Future Directions

Throughout the course of this work, a number of avenues for further elaboration and research have been identified. Though previously reported, there is further scope within the [Sn(dmamp)$_2$]/H_2O ALD process that would allow for a greater understanding of the mechanisms of SnO deposition. A facet of this is an observation made within the deposition of [Sn(O^{t}Bu)$_2$] **(24)** in Chapter 4, where growth rates decreased on exposure to longer purge cycles. The extent of this effect within the [Sn(dmamp)$_2$] process would be interesting and if similar, would indicate the important role precursor physisorption plays in the deposition of low reactivity precursor systems. Similar experiments could also be undertaken with the aminoamide precursors detailed in Chapter 3.

Though Chapter 3 saw the development of the highly effective simple tin(II) amide species [Sn(deed)NMe$_2$] **(15)**, an increase in the thermal robustness of the precursor allowing for higher temperature depositions would be desirable. It is possible that by applying the knowledge gained from the thermally robust pyrrolide system [Sn(py-CH=Ndipp)$_2$], a less thermally sensitive system could be developed. The proof-of-concept ALD of SnO onto monolayer graphene provides a topical direction of research. The testing of the composite as a battery material, or within sensing applications could prove highly effective, with other more simply deposited composites having been shown to have high potential. The high

transparency of SnO/graphene composites could also direct research down a number of thin film transparent electronics applications.

A body of work that holds the largest promise for expansion, is that of the atomic layer deposition of simple Sn(II) alkoxides. Aside from the previously discussed physisorption investigation, a number of avenues for research were identified. Of the precursors identified that resulted in successful atomic layer deposition, a more in-depth investigation is needed into the mechanisms and stabilities with respect to hydrolysis reactions and whether self-elimination occurs for all alkoxide species characterised.

Further research is required into the thermal deposition window and effectiveness of precursors that have, as yet, only been demonstrated to work in proof-of-concept trial depositions, such as [Sn{O(CH_3)$_2$$CH_2$$CH_3$}$_2$] **(26)**. There is merit in confirming categorically that no simple secondary alkoxide precursors are effective SnO precursors, and whether any other tertiary systems display ALD activity. Furthermore, TFT characterisation is highly desirable on films deposited at a range of temperatures, though in particular those deposited at 210 °C, which have been previously proven to be most effective in published reports,[7] as the much improved growth rates displayed by the simple alkoxides at this temperature could prove highly beneficial. Additionally, the possibility of a liquid-injection ALD process using the alkoxyether complexes **29** and **30** should be explored in future study,[8,9] whilst the H_2O/H_2O_2 and O_2-plasma enhanced ALD of the fluorinated alkoxide systems **27** and **28** could prove to be a viable method towards the atomic layer deposition of fluorine-doped tin oxide (FTO).

An avenue that provides perhaps the most interest from a chemical perspective, is the possibility of a non-aqueous ALD route to SnO using the alkoxide systems developed in Chapter 4. Such a method has been shown to work with titanium, hafnium and vanadium oxides, whereby a carboxylic acid precursor is introduced as a second precursor in place of H_2O. Processes therefore proceed via ligand displacement of alcohol by carboxylic acid after the second precursor pulse, and by elimination of an ester on the next pulse of alkoxide precursor.[10,11] This route could prove to be invaluable in the deposition of low-reactivity precursors and could substantially improve reaction rates across the ALD process.

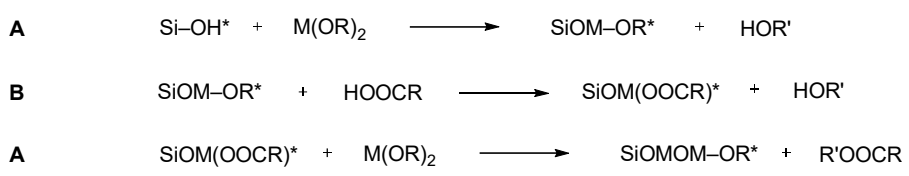

*Scheme 6.1 – Alkoxide-carboxylic acid ALD process. Sequential pulses of A – M(OR) and B – HOOCR. *Denotes surface bound species.*[10,11]

With extensive applications in microelectronics, sensing, and battery and optical technologies, the demand for advances in p-type oxide materials and advanced methods of deposition is burgeoning. The research outlined within this thesis encompasses significant developments within the field of atomic layer deposition, in addition to the identification of a number of avenues for further exploration. The application of p-type oxides in “true” CMOS devices could see an inflection point in the dissemination of low-power, low-cost and disposable devices across the globe, and with increasing desire for miniaturised and highly complex devices, atomic layer deposition and precursor development is set to become of increasing importance in coming years. To these ends, and further to the more fundamental aspects of the investigations contained herein, this research has identified and successfully trialled three viable Sn(II) precursor systems for the deposition of SnO, and has additionally described the synthesis and characterisation of a large number of other prospective systems whose efficacy is yet to be established.

6.3. References

1 J. H. Han, Y. J. Chung, B. K. Park, S. K. Kim, H.-S. Kim, C. G. Kim and T.-M. Chung, *Chem. Mater.*, 2014, **26**, 6088–6091.

2 H. Yabuta, N. Kaji, R. Hayashi, H. Kumomi, K. Nomura, T. Kamiya, M. Hirano and H. Hosono, *Appl. Phys. Lett.*, 2010, **97**, 72111.

3 P.-C. Hsu, C.-J. Hsu, C.-H. Chang, S.-P. Tsai, W.-C. Chen, H.-H. Hsieh and C.-C. Wu, *ACS Appl. Mater. Interfaces*, 2014, **6**, 13724–13729.

4 J. A. Caraveo-Frescas, P. K. Nayak, H. A. Al-Jawhari, D. B. Granato, U. Schwingenschlögl and H. N. Alshareeft, *ACS Nano*, 2013, **7**, 5160–5167.

5 E. Fortunato, R. Barros, P. Barquinha, V. Figueiredo, S.-H. K. Park, C.-S. Hwang and R. Martins, *Appl. Phys. Lett.*, 2010, **97**, 52105.

6 Y. Ogo, H. Hiramatsu, K. Nomura, H. Yanagi, T. Kamiya, M. Hirano and H. Hosono, *Appl. Phys. Lett.*, 2008, **93**, 32113.

7 S. H. Kim, I.-H. Baek, D. H. Kim, J. J. Pyeon, T.-M. Chung, S.-H. Baek, J.-S. Kim, J. H. Han and S. K. Kim, *J. Mater. Chem. C*, 2017, **5**, 3139–3145.

8 M. Fanciulli, S. Spiga, G. Scarel, G. Tallarida, C. Wiemer and G. Seguini, *Mater. Res. Soc. Symp. Proc.*, 2004, **786**, 341–346.

9 Y. S. Min, Y. J. Cho, I. P. Asanov, J. H. Han, W. D. Kim and C. S. Hwang, *Chem. Vap. Deposition*, 2005, **11**, 38–43.

10 E. Rauwel, G. Clavel, M.-G. Willinger, P. Rauwel and N. Pinna, *Angew. Chemie Int. Ed.*, 2008, **47**, 3592–3595.

11 E. Rauwel, M.-G. Willinger, F. Ducroquet, P. Rauwel, I. Matko, D. Kiselev and N. Pinna, *J. Phys. Chem. C*, 2008, **112**, 12754–12759.

Appendix

7.1. General Experimental Details

All reactions were performed under inert conditions, unless otherwise stated, using standard Schlenk line and glove box techniques under either argon or nitrogen atmospheres. All starting chemicals were provided by Sigma-Aldrich, Fisher Scientific, Alfa Aesar or Acros. All solvents were dried under argon using an Innovative Technologies solvent purification system, then degassed once (twice for THF and diethyl ether) using cold vacuum degassing (77 K) and argon. Solvents were stored in J Youngs ampules over molecular sieves. Deuterated benzene (C_6D_6) and toluene (D_8-tol) NMR solvents were purchased from Sigma-Aldrich and dried by refluxing over potassium before isolating by vacuum distillation.

NMR experiments were carried out using J Youngs valve NMR tubes prepared in a glove box. NMR data was collected at 25 °C unless otherwise stated using either a Bruker Avance AV-300, Avance AV-400 or Avance II+ AV-500 spectrometer.

UV-Visible spectra were recorded on a PerkinElmer Lambda 750 S UV/VIS/NIR Spectrometer. Ellipsometry measurements were performed on a J. A. Woollam Variable-Angle α-SE Spectroscopic Ellipsometer and modelled using the CompleteEASE software suite. Elemental analysis was performed under inert conditions by the elemental analysis service at the Science Centre, London Metropolitan University, UK.

Single crystal X-ray diffraction data were collected at 150 K using either a Nonius Kappa CCD, an Agilent Xcalibur or an Agilent SuperNova Dual diffractometer with either Mo-Kα (λ = 0.71073 Å) or Cu-Kα (λ = 1.5418 Å) radiation. The data collected by the diffractometers were processed using the proprietary Nonius or Agilent software. Structures were solved by full-matrix least squares refinement using either the WinGX-170 suite of programs or the programme suite X-SEED. All structural data were obtained by Dr Andrew Johnson with structure refinement performed by Dr Andrew Johnson or Dr Gabriele Kociok-Köhn.

TGA was performed under nitrogen (20 ml/min) at a ramp rate of 5 °C/min between 50 and 600 °C on a PerkinElmer TGA4000 with autosampler; samples were contained in either crimped aluminium pans (closed pans) or in alumina crucibles (open pans).

PXRD patterns were collected on either a Siemens Kristalloflex D5000 (Cu-Kα radiation, λ = 1.54056 Å) or Bruker AXS D8 Advance (Cu-Kα radiation, λ = 1.5418 Å) diffractometer in flat plate mode at 298 K. Results were analysed in EVA and Excel.

SEM images were collected on either a JEOL FESEM6301F. Samples were mounted on stainless steel stubs or clamps using carbon tape and stored under vacuum. TEM analysis was performed using a JEOL JEM-2100Plus system. SEM and TEM images were analysed

using ImageJ software. Raman spectra were recorded on a Renishaw inVia system using a 532 nm laser and analysed using the programs Wire and Excel. AFM was performed in contact mode on either a Veeco Multimode Nanoscope III using Bruker SNL-10 tips or a Nanosurf Flex-Axiom using Budget Sensors Contact-G tips. Images were processed in Gwyddion. XPS was carried out either at the University of Cambridge, Microelectronics Research Centre (MRC) using an Escalab 250Xi, or at Cardiff University, using a Kratos Axis Ultra-DLD system. Data was analysed using CasaXPS.

7.2. Selected NMR Spectra

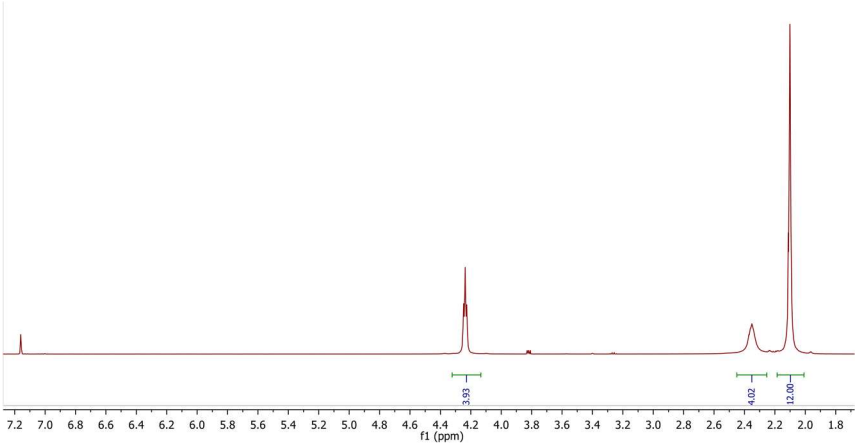

^{1}H NMR spectrum of [Sn(dmae)$_2$] **(1)**. C_6D_6, 298 K, 500 MHz.

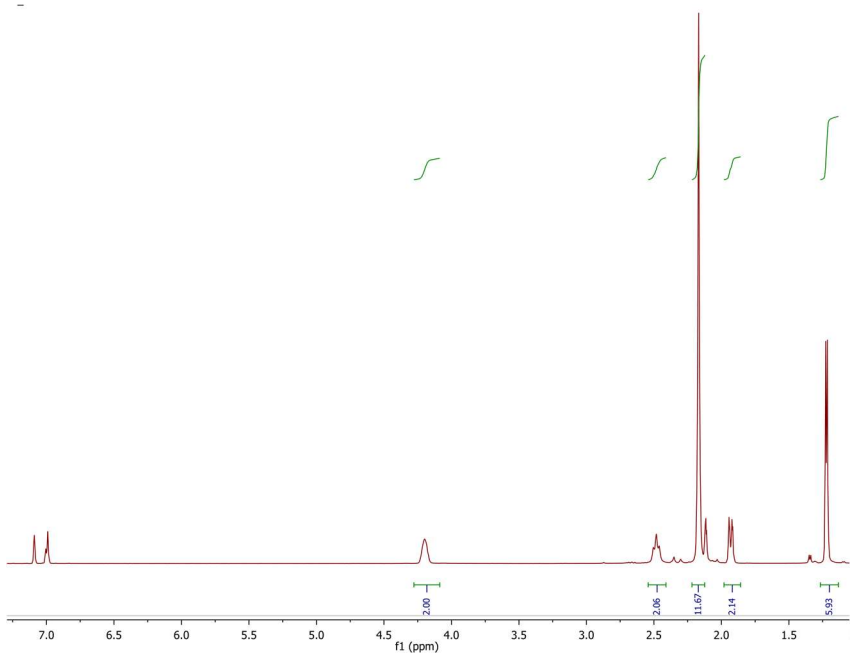

^{1}H NMR spectrum of [Sn(dmap)$_2$] **(4)**. D_8-tol, 363 K, 500 MHz.

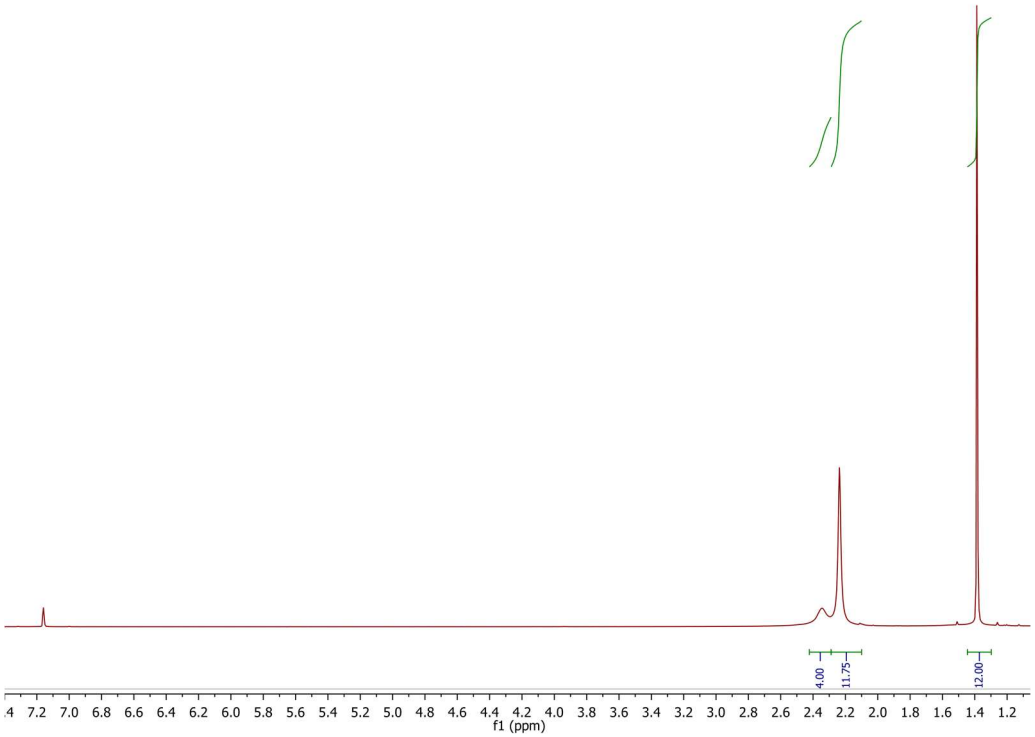

^{1}H NMR spectrum of [Sn(dmamp)$_2$] **(7)**. C_6D_6, 298 K, 500 MHz.

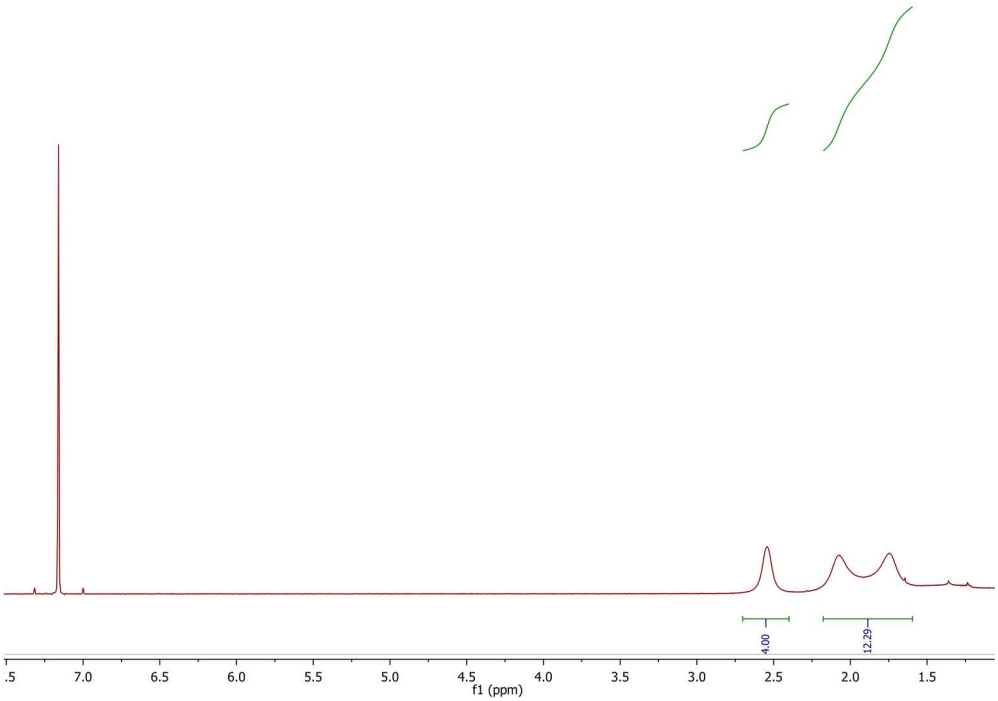

^{1}H NMR spectrum of [Sn(Fdmamp)$_2$] **(10)**. C_6D_6, 298 K, 500 MHz.

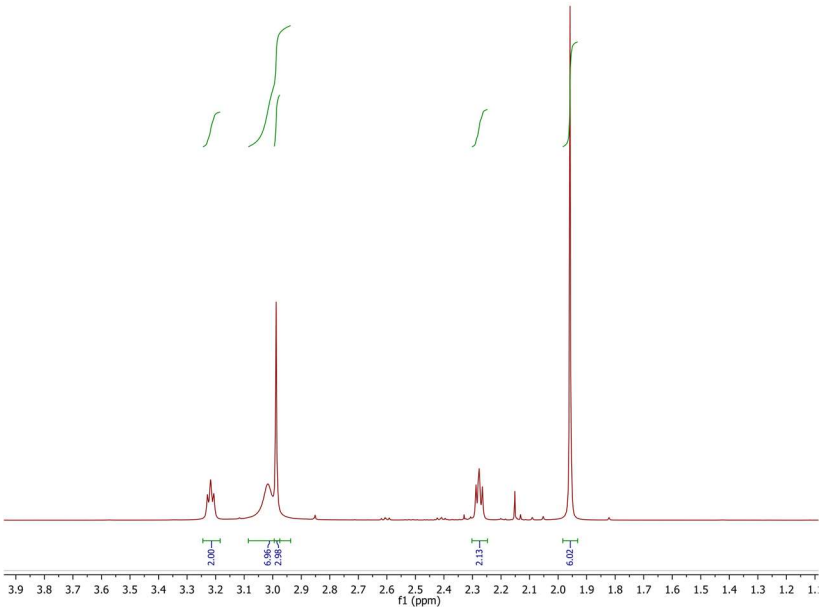

^{1}H NMR spectrum of [Sn(tmed)NMe$_2$] **(13)**. C_6D_6, 298 K, 500 MHz.

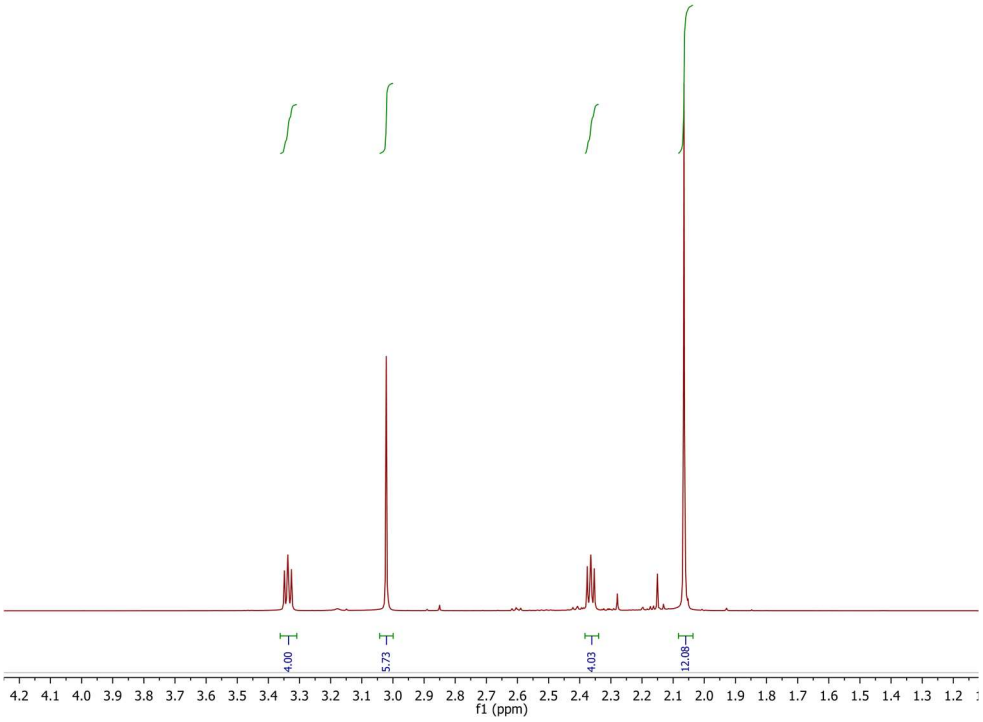

^{1}H NMR spectrum of [Sn(tmed)$_2$] **(14)**. C_6D_6, 298 K, 500 MHz.

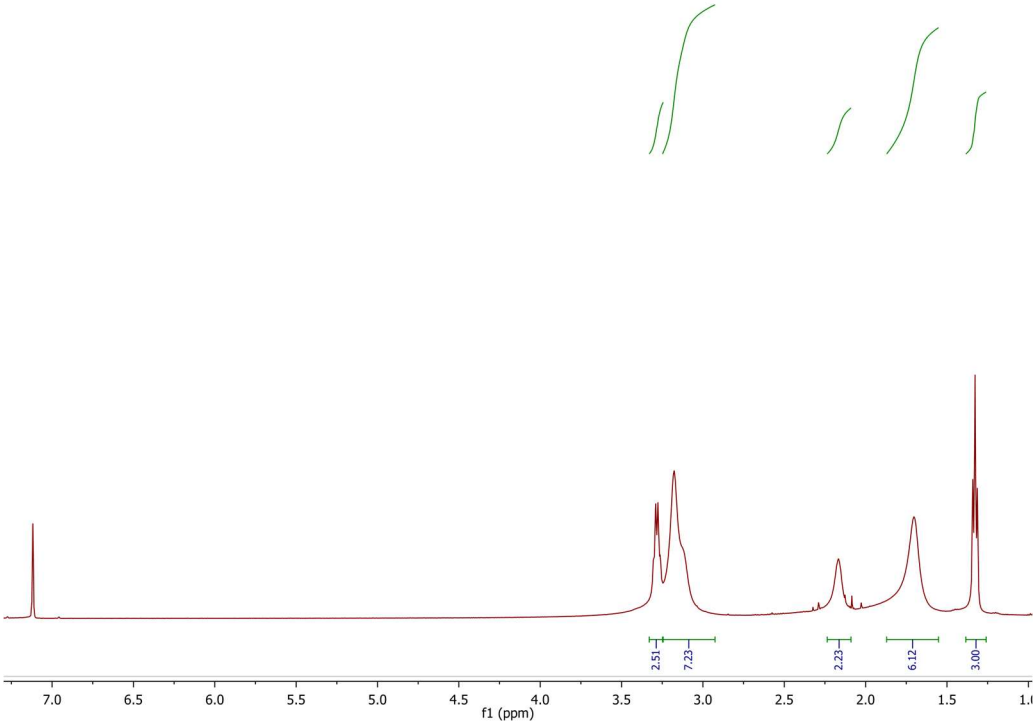

^{1}H NMR spectrum of [Sn(deed)NMe$_2$] **(15)**. C_6D_6, 298 K, 500 MHz.

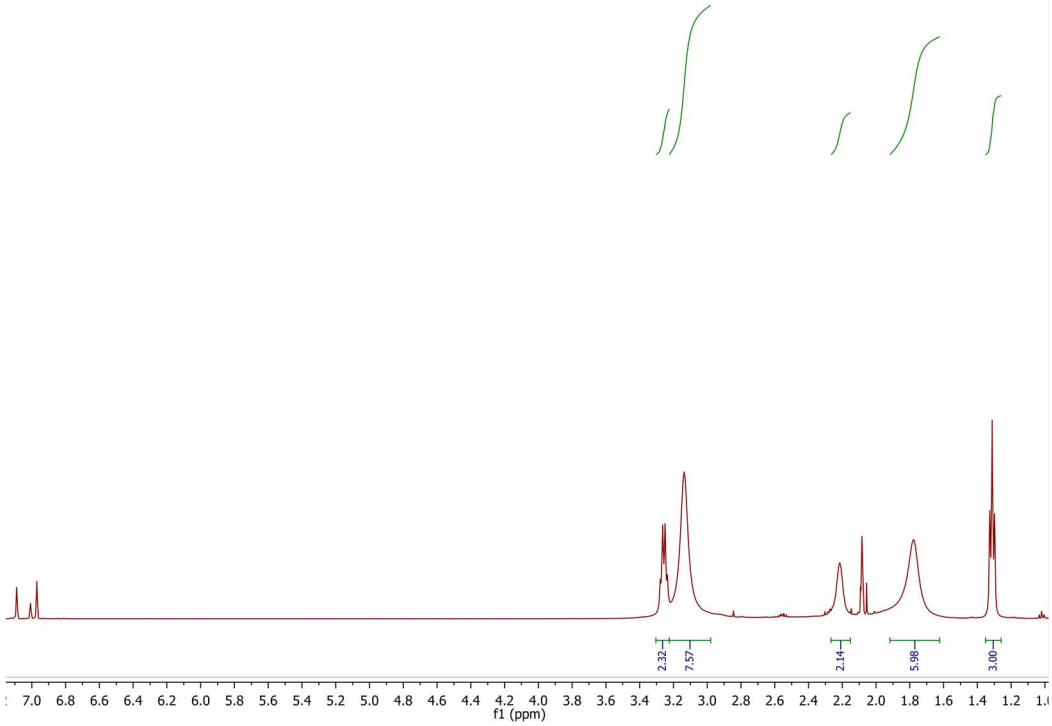

^{1}H NMR spectrum of [Sn(deed)NMe$_2$] **(15)**. D_8-tol, 363 K, 500 MHz.

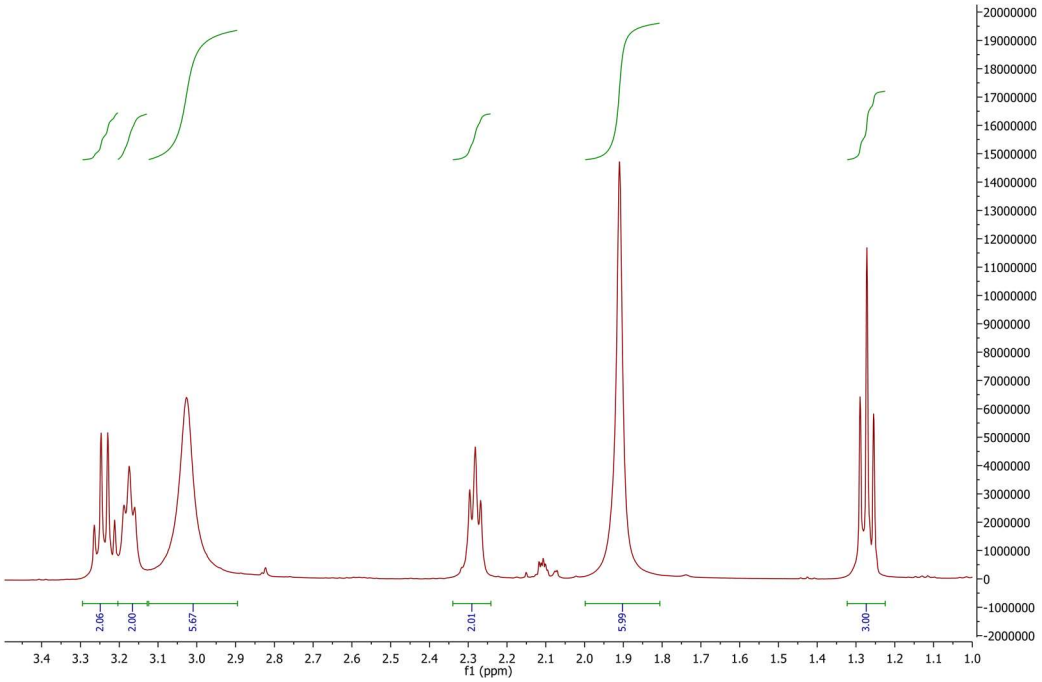

^{1}H NMR spectrum of [Sn(deed)NMe$_2$] **(15)**. D$_8$-tol, 321 K, 400 MHz.

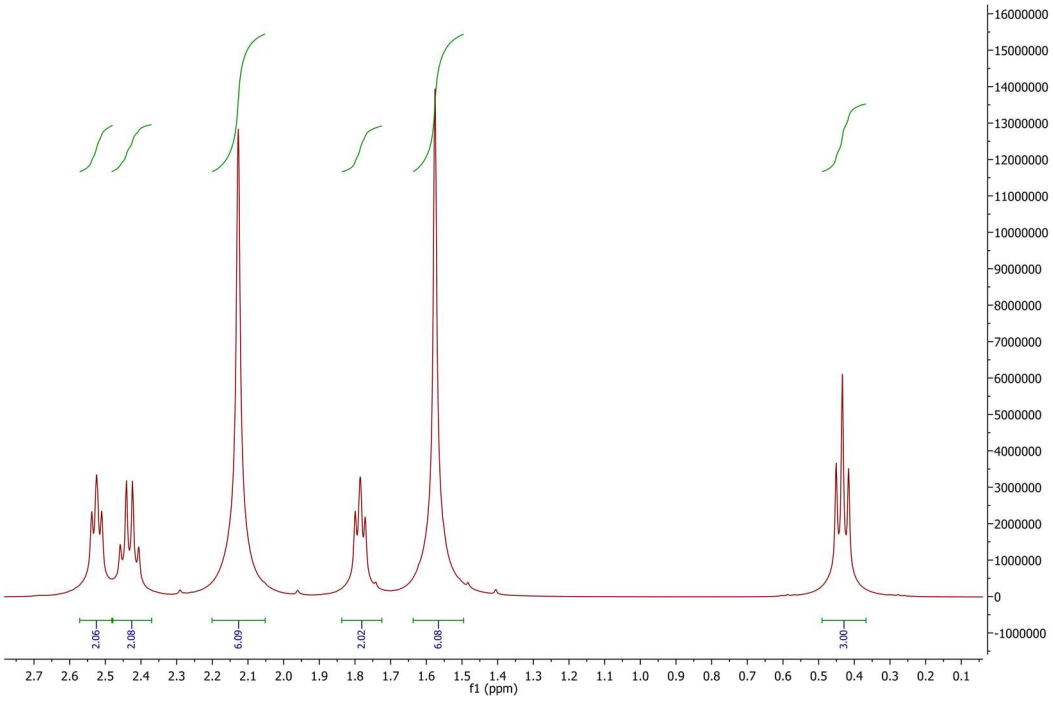

Neat, unsolvated and unreferenced ^{1}H NMR spectrum of [Sn(deed)NMe$_2$] **(15)**. 298 K, 400 MHz.

7.3. Crystal Data and Structural Refinement Tables

Table 7.1 – Crystal data and structure refinement for Complex 1.

Identification code	e18alj12	
Empirical formula	$C_8H_{20}N_2O_2Sn$	
Formula weight	294.95	
Temperature	150.00(10) K	
Wavelength	0.71073 Å	
Crystal system	Orthorhombic	
Space group	Aba2	
Unit cell dimensions	a = 11.8081(2) Å	α= 90°.
	b = 10.1306(2) Å	β= 90°.
	c = 10.0735(2) Å	γ = 90°.
Volume	1205.02(4) $Å^3$	
Z	4	
Density (calculated)	1.626 Mg/m^3	
Absorption coefficient	2.097 mm^{-1}	
F(000)	592	
Crystal size	0.457 x 0.365 x 0.312 mm^3	
Theta range for data collection	3.333 to 28.120°.	
Index ranges	-15<=h<=15, -13<=k<=13, -12<=l<=13	
Reflections collected	32894	
Independent reflections	1410 [R(int) = 0.0673]	
Completeness to theta = 25.242°	100.0 %	
Absorption correction	Analytical	
Max. and min. transmission	0.789 and 0.715	
Refinement method	Full-matrix least-squares on F^2	
Data / restraints / parameters	1410 / 1 / 63	
Goodness-of-fit on F^2	1.211	
Final R indices [I>2sigma(I)]	R1 = 0.0255, wR2 = 0.0509	
R indices (all data)	R1 = 0.0287, wR2 = 0.0521	
Absolute structure parameter	0.47(8)	
Extinction coefficient	n/a	
Largest diff. peak and hole	0.473 and -0.394 $e.Å^{-3}$	

Table 7.2 – Crystal data and structure refinement for Complex 2.

Identification code	e18alj11	
Empirical formula	$C_{20}H_{56}N_4O_2Si_4Sn_2$	
Formula weight	734.42	
Temperature	150.01(10) K	
Wavelength	0.71073 Å	
Crystal system	Triclinic	
Space group	P-1	
Unit cell dimensions	a = 8.7579(4) Å	α= 80.516(5)°.
	b = 8.9319(4) Å	β= 86.651(5)°.
	c = 23.8923(19) Å	γ = 68.460(4)°.
Volume	1714.68(18) $Å^3$	
Z	2	
Density (calculated)	1.422 Mg/m^3	
Absorption coefficient	1.618 mm^{-1}	
F(000)	752	
Crystal size	0.371 x 0.187 x 0.097 mm^3	
Theta range for data collection	3.458 to 27.515°.	
Index ranges	-11<=h<=11, -11<=k<=11, -29<=l<=30	
Reflections collected	7177	
Independent reflections	7177 [R(int) = ?]	
Completeness to theta = 25.242°	99.1 %	
Absorption correction	Semi-empirical from equivalents	
Max. and min. transmission	1.00000 and 0.86963	
Refinement method	Full-matrix least-squares on F^2	
Data / restraints / parameters	7177 / 6 / 306	
Goodness-of-fit on F^2	1.085	
Final R indices [I>2sigma(I)]	R1 = 0.0443, wR2 = 0.0877	
R indices (all data)	R1 = 0.0538, wR2 = 0.0894	
Extinction coefficient	n/a	
Largest diff. peak and hole	1.222 and -1.488 $e.Å^{-3}$	

Table 7.3 – Crystal data and structure refinement for Complex 3.

Identification code	s18alj30	
Empirical formula	$C_{12}H_{32}N_4O_2Sn_2$	
Formula weight	501.79	
Temperature	150.0(3) K	
Wavelength	1.54184 Å	
Crystal system	Monoclinic	
Space group	$P2_1/n$	
Unit cell dimensions	a = 6.78330(10) Å	α= 90°.
	b = 17.20280(10) Å	β= 95.9880(10)°.
	c = 8.14230(10) Å	γ = 90°.
Volume	944.955(19) $Å^3$	
Z	2	
Density (calculated)	1.764 Mg/m^3	
Absorption coefficient	21.080 mm^{-1}	
F(000)	496	
Crystal size	0.120 x 0.100 x 0.050 mm^3	
Theta range for data collection	5.142 to 72.982°.	
Index ranges	-8<=h<=8, -21<=k<=21, -10<=l<=10	
Reflections collected	18198	
Independent reflections	1884 [R(int) = 0.0404]	
Completeness to theta = 67.684°	100.0 %	
Absorption correction	Semi-empirical from equivalents	
Max. and min. transmission	1.00000 and 0.20494	
Refinement method	Full-matrix least-squares on F^2	
Data / restraints / parameters	1884 / 0 / 95	
Goodness-of-fit on F^2	1.048	
Final R indices [I>2sigma(I)]	R1 = 0.0173, wR2 = 0.0431	
R indices (all data)	R1 = 0.0183, wR2 = 0.0437	
Extinction coefficient	n/a	
Largest diff. peak and hole	0.712 and -0.623 $e.Å^{-3}$	

Table 7.4 – Crystal data and structure refinement for Complex 4.

Identification code	s15alj23	
Empirical formula	$C_{10}H_{24}N_2O_2Sn$	
Formula weight	323.00	
Temperature	150.00(10) K	
Wavelength	0.71073 Å	
Crystal system	Monoclinic	
Space group	C2/c	
Unit cell dimensions	a = 11.7352(4) Å	α= 90°.
	b = 10.3182(3) Å	β= 95.166(3)°.
	c = 12.0111(4) Å	γ = 90°.
Volume	1448.47(8) $Å^3$	
Z	4	
Density (calculated)	1.481 Mg/m^3	
Absorption coefficient	1.752 mm^{-1}	
F(000)	656	
Crystal size	0.241 x 0.087 x 0.072 mm^3	
Theta range for data collection	3.406 to 27.502°.	
Index ranges	-15<=h<=15, -13<=k<=12, -15<=l<=15	
Reflections collected	6274	
Independent reflections	1660 [R(int) = 0.0303]	
Completeness to theta = 25.242°	99.8 %	
Absorption correction	Gaussian	
Max. and min. transmission	1.000 and 0.588	
Refinement method	Full-matrix least-squares on F^2	
Data / restraints / parameters	1660 / 0 / 72	
Goodness-of-fit on F^2	1.072	
Final R indices [I>2sigma(I)]	R1 = 0.0195, wR2 = 0.0418	
R indices (all data)	R1 = 0.0212, wR2 = 0.0424	
Extinction coefficient	n/a	
Largest diff. peak and hole	0.366 and -0.357 $e.Å^{-3}$	

Table 7.5 – Crystal data and structure refinement for Complex 5.

Identification code	s17alj24	
Empirical formula	$C_{22}H_{60}N_4O_2Si_4Sn_2$	
Formula weight	762.48	
Temperature	150.00(10) K	
Wavelength	1.54184 Å	
Crystal system	Orthorhombic	
Space group	$Pca2_1$	
Unit cell dimensions	a = 20.53720(10) Å	α= 90°.
	b = 12.18560(10) Å	β= 90°.
	c = 14.37850(10) Å	γ = 90°.
Volume	3598.34(4) $Å^3$	
Z	4	
Density (calculated)	1.415 Mg/m^3	
Absorption coefficient	12.523 mm^{-1}	
F(000)	1576	
Crystal size	0.267 x 0.218 x 0.188 mm^3	
Theta range for data collection	3.627 to 73.116°.	
Index ranges	-23<=h<=25, -15<=k<=15, -17<=l<=16	
Reflections collected	35425	
Independent reflections	6731 [R(int) = 0.0390]	
Completeness to theta = 67.684°	100.0 %	
Absorption correction	Gaussian	
Max. and min. transmission	0.299 and 0.045	
Refinement method	Full-matrix least-squares on F^2	
Data / restraints / parameters	6731 / 26 / 415	
Goodness-of-fit on F^2	1.065	
Final R indices [I>2sigma(I)]	R1 = 0.0426, wR2 = 0.1115	
R indices (all data)	R1 = 0.0430, wR2 = 0.1119	
Absolute structure parameter	0.034(12)	
Extinction coefficient	n/a	
Largest diff. peak and hole	1.261 and -1.120 $e.Å^{-3}$	

Table 7.6 – Crystal data and structure refinement for Complex 6.

Identification code	s17alj25	
Empirical formula	$C_{14}H_{36}N_4O_2Sn_2$	
Formula weight	529.85	
Temperature	150.00(10) K	
Wavelength	1.54184 Å	
Crystal system	Triclinic	
Space group	P-1	
Unit cell dimensions	a = 7.5712(4) Å	α= 73.154(5)°.
	b = 8.6744(5) Å	β= 74.104(5)°.
	c = 9.2638(4) Å	γ = 68.138(5)°.
Volume	530.90(5) $Å^3$	
Z	1	
Density (calculated)	1.657 Mg/m^3	
Absorption coefficient	18.795 mm^{-1}	
F(000)	264	
Crystal size	0.320 x 0.171 x 0.141 mm^3	
Theta range for data collection	5.078 to 72.931°.	
Index ranges	-8<=h<=9, -8<=k<=10, -11<=l<=11	
Reflections collected	3776	
Independent reflections	2104 [R(int) = 0.0224]	
Completeness to theta = 67.684°	99.9 %	
Absorption correction	Gaussian	
Max. and min. transmission	0.534 and 0.192	
Refinement method	Full-matrix least-squares on F^2	
Data / restraints / parameters	2104 / 0 / 105	
Goodness-of-fit on F^2	1.103	
Final R indices [I>2sigma(I)]	R1 = 0.0297, wR2 = 0.0792	
R indices (all data)	R1 = 0.0304, wR2 = 0.0799	
Extinction coefficient	n/a	
Largest diff. peak and hole	1.180 and -0.999 $e.Å^{-3}$	

Table 7.7 – Crystal data and structure refinement for Complex 7.

Identification code	s15alj21	
Empirical formula	$C_{12}H_{28}N_2O_2Sn$	
Formula weight	351.05	
Temperature	150.00(10) K	
Wavelength	0.71073 Å	
Crystal system	Orthorhombic	
Space group	$P2_12_12_1$	
Unit cell dimensions	a = 8.1592(3) Å	α= 90°.
	b = 13.8664(5) Å	β= 90°.
	c = 14.1626(5) Å	γ = 90°.
Volume	1602.34(10) $Å^3$	
Z	4	
Density (calculated)	1.455 Mg/m^3	
Absorption coefficient	1.590 mm^{-1}	
F(000)	720	
Crystal size	0.400 x 0.250 x 0.100 mm^3	
Theta range for data collection	3.234 to 29.403°.	
Index ranges	-11<=h<=10, -17<=k<=18, -18<=l<=17	
Reflections collected	13388	
Independent reflections	3800 [R(int) = 0.0348]	
Completeness to theta = 25.242°	99.6 %	
Absorption correction	Semi-empirical from equivalents	
Max. and min. transmission	1.00000 and 0.61849	
Refinement method	Full-matrix least-squares on F^2	
Data / restraints / parameters	3800 / 0 / 163	
Goodness-of-fit on F^2	1.051	
Final R indices [I>2sigma(I)]	R1 = 0.0252, wR2 = 0.0422	
R indices (all data)	R1 = 0.0283, wR2 = 0.0430	
Absolute structure parameter	0.16(3)	
Extinction coefficient	n/a	
Largest diff. peak and hole	0.313 and -0.498 $e.Å^{-3}$	

Table 7.8 – Crystal data and structure refinement for Complex 8.

Identification code	e17alj08	
Empirical formula	$C_{24}H_{64}N_4O_2Si_4Sn_2$	
Formula weight	790.53	
Temperature	150(2) K	
Wavelength	0.71073 Å	
Crystal system	Monoclinic	
Space group	$P2_1/n$	
Unit cell dimensions	a = 8.6975(5) Å	α= 90°.
	b = 14.292(3) Å	β= 93.032(11)°.
	c = 15.194(3) Å	γ = 90°.
Volume	1886.0(5) $Å^3$	
Z	2	
Density (calculated)	1.392 Mg/m^3	
Absorption coefficient	1.476 mm^{-1}	
F(000)	816	
Crystal size	0.388 x 0.263 x 0.239 mm^3	
Theta range for data collection	3.692 to 28.555°.	
Index ranges	-11<=h<=9, -19<=k<=15, -20<=l<=20	
Reflections collected	21534	
Independent reflections	4216 [R(int) = 0.0347]	
Completeness to theta = 25.242°	99.7 %	
Absorption correction	Semi-empirical from equivalents	
Max. and min. transmission	1.00000 and 0.85159	
Refinement method	Full-matrix least-squares on F^2	
Data / restraints / parameters	4216 / 0 / 173	
Goodness-of-fit on F^2	1.067	
Final R indices [I>2sigma(I)]	R1 = 0.0238, wR2 = 0.0456	
R indices (all data)	R1 = 0.0288, wR2 = 0.0473	
Extinction coefficient	n/a	
Largest diff. peak and hole	0.362 and -0.352 $e.Å^{-3}$	

Table 7.9 – Crystal data and structure refinement for Complex 9.

Identification code	e15alj02	
Empirical formula	$C_{16}H_{40}N_4O_2Sn_2$	
Formula weight	557.90	
Temperature	150.0(3) K	
Wavelength	0.71073 Å	
Crystal system	Monoclinic	
Space group	$P2_1/n$	
Unit cell dimensions	a = 9.2945(3) Å	α= 90°.
	b = 11.9266(4) Å	β= 100.737(4)°.
	c = 10.7094(4) Å	γ = 90°.
Volume	1166.37(7) $Å^3$	
Z	2	
Density (calculated)	1.589 Mg/m^3	
Absorption coefficient	2.156 mm^{-1}	
F(000)	560	
Crystal size	0.250 x 0.200 x 0.140 mm^3	
Theta range for data collection	3.416 to 26.020°.	
Index ranges	-11<=h<=11, -10<=k<=14, -12<=l<=13	
Reflections collected	7109	
Independent reflections	2261 [R(int) = 0.0542]	
Completeness to theta = 25.242°	99.7 %	
Absorption correction	Semi-empirical from equivalents	
Max. and min. transmission	1.00000 and 0.97230	
Refinement method	Full-matrix least-squares on F^2	
Data / restraints / parameters	2261 / 0 / 115	
Goodness-of-fit on F^2	1.036	
Final R indices [I>2sigma(I)]	R1 = 0.0339, wR2 = 0.0538	
R indices (all data)	R1 = 0.0462, wR2 = 0.0606	
Extinction coefficient	n/a	
Largest diff. peak and hole	0.529 and -0.446 $e.Å^{-3}$	

Table 7.10 – Crystal data and structure refinement for Complex 10.

Identification code	s16alj17	
Empirical formula	$C_{12}H_{16}F_{12}N_2O_2Sn$	
Formula weight	566.96	
Temperature	150.00(10) K	
Wavelength	1.54184 Å	
Crystal system	Monoclinic	
Space group	$P2_1/c$	
Unit cell dimensions	a = 18.5031(2) Å	α= 90°.
	b = 8.29960(10) Å	β= 94.4840(10)°.
	c = 12.5214(2) Å	γ = 90°.
Volume	1917.00(4) $Å^3$	
Z	4	
Density (calculated)	1.964 Mg/m^3	
Absorption coefficient	11.814 mm^{-1}	
F(000)	1104	
Crystal size	0.320 x 0.200 x 0.100 mm^3	
Theta range for data collection	4.795 to 73.407°.	
Index ranges	-22<=h<=22, -10<=k<=9, -11<=l<=15	
Reflections collected	13270	
Independent reflections	3815 [R(int) = 0.0343]	
Completeness to theta = 67.684°	100.0 %	
Absorption correction	Semi-empirical from equivalents	
Max. and min. transmission	1.00000 and 0.20108	
Refinement method	Full-matrix least-squares on F^2	
Data / restraints / parameters	3815 / 0 / 296	
Goodness-of-fit on F^2	1.044	
Final R indices [I>2sigma(I)]	R1 = 0.0339, wR2 = 0.0894	
R indices (all data)	R1 = 0.0353, wR2 = 0.0909	
Extinction coefficient	n/a	
Largest diff. peak and hole	0.998 and -0.474 $e.Å^{-3}$	

Table 7.11 – Crystal data and structure refinement for Complex 11.

Identification code	s17alj14	
Empirical formula	$C_{12}H_{26}F_6N_2OSi_2Sn$	
Formula weight	503.22	
Temperature	150.00(10) K	
Wavelength	1.54184 Å	
Crystal system	Triclinic	
Space group	P-1	
Unit cell dimensions	a = 7.06130(10) Å	α= 94.6970(10)°.
	b = 8.48480(10) Å	β= 98.7470(10)°.
	c = 18.7724(2) Å	γ = 110.7630(10)°.
Volume	1028.16(2) $Å^3$	
Z	2	
Density (calculated)	1.625 Mg/m^3	
Absorption coefficient	11.530 mm^{-1}	
F(000)	504	
Crystal size	0.400 x 0.298 x 0.230 mm^3	
Theta range for data collection	4.819 to 73.177°.	
Index ranges	-8<=h<=8, -10<=k<=9, -23<=l<=23	
Reflections collected	34240	
Independent reflections	4091 [R(int) = 0.0562]	
Completeness to theta = 67.684°	99.9 %	
Absorption correction	Semi-empirical from equivalents	
Max. and min. transmission	1.00000 and 0.20885	
Refinement method	Full-matrix least-squares on F^2	
Data / restraints / parameters	4091 / 0 / 225	
Goodness-of-fit on F^2	1.070	
Final R indices [I>2sigma(I)]	R1 = 0.0440, wR2 = 0.1184	
R indices (all data)	R1 = 0.0441, wR2 = 0.1185	
Extinction coefficient	n/a	
Largest diff. peak and hole	3.264 and -1.550 $e.Å^{-3}$	

Table 7.12 – Crystal data and structure refinement for Complex 12.

Identification code	s16alj18	
Empirical formula	$C_{16}H_{28}F_{12}N_4O_2Sn_2$	
Formula weight	773.80	
Temperature	150.01(10) K	
Wavelength	1.54184 Å	
Crystal system	Monoclinic	
Space group	$P2_1/c$	
Unit cell dimensions	a = 12.5872(3) Å	α= 90°.
	b = 8.5519(2) Å	β= 100.094(3)°.
	c = 12.5367(3) Å	γ = 90°.
Volume	1328.62(6) $Å^3$	
Z	2	
Density (calculated)	1.934 Mg/m^3	
Absorption coefficient	15.946 mm^{-1}	
F(000)	752	
Crystal size	0.180 x 0.150 x 0.030 mm^3	
Theta range for data collection	6.288 to 73.331°.	
Index ranges	-15<=h<=14, -10<=k<=6, -15<=l<=15	
Reflections collected	9233	
Independent reflections	2632 [R(int) = 0.0422]	
Completeness to theta = 67.684°	99.3 %	
Absorption correction	Semi-empirical from equivalents	
Max. and min. transmission	1.00000 and 0.29263	
Refinement method	Full-matrix least-squares on F^2	
Data / restraints / parameters	2632 / 0 / 167	
Goodness-of-fit on F^2	1.095	
Final R indices [I>2sigma(I)]	R1 = 0.0530, wR2 = 0.1362	
R indices (all data)	R1 = 0.0567, wR2 = 0.1385	
Extinction coefficient	n/a	
Largest diff. peak and hole	2.129 and -1.043 $e.Å^{-3}$	

Table 7.13 – Crystal data and structure refinement for Complex 19.

Identification code	s17alj12	
Empirical formula	$C_{26}H_{46}N_6Sn_2$	
Formula weight	680.07	
Temperature	150.01(10) K	
Wavelength	1.54184 Å	
Crystal system	Triclinic	
Space group	P-1	
Unit cell dimensions	a = 6.4317(4) Å	α= 69.302(6)°.
	b = 10.8638(7) Å	β= 76.868(6)°.
	c = 11.6000(7) Å	γ = 84.932(5)°.
Volume	738.35(9) $Å^3$	
Z	1	
Density (calculated)	1.529 Mg/m^3	
Absorption coefficient	13.626 mm^{-1}	
F(000)	344	
Crystal size	0.100 x 0.060 x 0.030 mm^3	
Theta range for data collection	4.167 to 73.505°.	
Index ranges	-7<=h<=7, -13<=k<=7, -14<=l<=13	
Reflections collected	8816	
Independent reflections	2939 [R(int) = 0.0501]	
Completeness to theta = 67.684°	100.0 %	
Absorption correction	Semi-empirical from equivalents	
Max. and min. transmission	1.00000 and 0.50530	
Refinement method	Full-matrix least-squares on F^2	
Data / restraints / parameters	2939 / 0 / 158	
Goodness-of-fit on F^2	1.048	
Final R indices [I>2sigma(I)]	R1 = 0.0296, wR2 = 0.0753	
R indices (all data)	R1 = 0.0312, wR2 = 0.0770	
Extinction coefficient	n/a	
Largest diff. peak and hole	0.552 and -1.266 $e.Å^{-3}$	

Table 7.14 – Crystal data and structure refinement for Complex 20.

Identification code	s17alj31	
Empirical formula	$C_{22}H_{34}N_4Sn$	
Formula weight	473.22	
Temperature	149.97(14) K	
Wavelength	1.54184 Å	
Crystal system	Monoclinic	
Space group	$P2_1$	
Unit cell dimensions	a = 5.99260(10) Å	α= 90°.
	b = 19.7872(5) Å	β= 90.003(2)°.
	c = 9.4828(3) Å	γ = 90°.
Volume	1124.44(5) $Å^3$	
Z	2	
Density (calculated)	1.398 Mg/m^3	
Absorption coefficient	9.123 mm^{-1}	
F(000)	488	
Crystal size	0.500 x 0.300 x 0.200 mm^3	
Theta range for data collection	4.469 to 72.887°.	
Index ranges	-5<=h<=7, -24<=k<=24, -11<=l<=11	
Reflections collected	9014	
Independent reflections	4221 [R(int) = 0.0393]	
Completeness to theta = 67.684°	100.0 %	
Absorption correction	Semi-empirical from equivalents	
Max. and min. transmission	1.00000 and 0.12460	
Refinement method	Full-matrix least-squares on F^2	
Data / restraints / parameters	4221 / 1 / 249	
Goodness-of-fit on F^2	1.116	
Final R indices [I>2sigma(I)]	R1 = 0.0554, wR2 = 0.1420	
R indices (all data)	R1 = 0.0554, wR2 = 0.1421	
Absolute structure parameter	-0.02(2)	
Extinction coefficient	n/a	
Largest diff. peak and hole	0.947 and -1.433 $e.Å^{-3}$	

Table 7.15 – Crystal data and structure refinement for Complex 21.

Identification code	s17alj17	
Empirical formula	$C_{33}H_{55}N_5Sn$	
Formula weight	640.51	
Temperature	150.01(10) K	
Wavelength	0.71073 Å	
Crystal system	Trigonal	
Space group	R-3	
Unit cell dimensions	a = 42.797(3) Å	α= 90°.
	b = 42.797(3) Å	β= 90°.
	c = 10.4350(8) Å	γ = 120°.
Volume	16552(3) $Å^3$	
Z	18	
Density (calculated)	1.157 Mg/m^3	
Absorption coefficient	0.720 mm^{-1}	
F(000)	6084	
Crystal size	0.450 x 0.120 x 0.090 mm^3	
Theta range for data collection	2.781 to 26.525°.	
Index ranges	-53<=h<=53, -53<=k<=53, -13<=l<=12	
Reflections collected	47754	
Independent reflections	7575 [R(int) = 0.1113]	
Completeness to theta = 25.242°	99.7 %	
Absorption correction	Gaussian	
Max. and min. transmission	1.000 and 0.609	
Refinement method	Full-matrix least-squares on F^2	
Data / restraints / parameters	7575 / 36 / 395	
Goodness-of-fit on F^2	1.053	
Final R indices [I>2sigma(I)]	R1 = 0.0475, wR2 = 0.1167	
R indices (all data)	R1 = 0.0690, wR2 = 0.1277	
Extinction coefficient	n/a	
Largest diff. peak and hole	1.570 and -0.483 $e.Å^{-3}$	

Table 7.16 – Crystal data and structure refinement for Complex 27.

Identification code	e18alj13	
Empirical formula	$C_{18}H_6F_{36}O_6Sn_3$	
Formula weight	1358.30	
Temperature	150.00(10) K	
Wavelength	0.71073 Å	
Crystal system	Monoclinic	
Space group	C2/c	
Unit cell dimensions	a = 18.8607(4) Å	α= 90°.
	b = 16.9876(3) Å	β= 101.102(2)°.
	c = 11.5664(2) Å	γ = 90°.
Volume	3636.50(12) $Å^3$	
Z	4	
Density (calculated)	2.481 Mg/m^3	
Absorption coefficient	2.265 mm^{-1}	
F(000)	2544	
Crystal size	0.400 x 0.150 x 0.150 mm^3	
Theta range for data collection	3.256 to 29.076°.	
Index ranges	-25<=h<=25, -22<=k<=23, -15<=l<=15	
Reflections collected	36783	
Independent reflections	4468 [R(int) = 0.0345]	
Completeness to theta = 25.242°	99.8 %	
Absorption correction	Semi-empirical from equivalents	
Max. and min. transmission	1.00000 and 0.84769	
Refinement method	Full-matrix least-squares on F^2	
Data / restraints / parameters	4468 / 0 / 285	
Goodness-of-fit on F^2	1.053	
Final R indices [I>2sigma(I)]	R1 = 0.0277, wR2 = 0.0611	
R indices (all data)	R1 = 0.0364, wR2 = 0.0638	
Extinction coefficient	n/a	
Largest diff. peak and hole	1.041 and -0.580 $e.Å^{-3}$	

Table 7.17 – Crystal data and structure refinement for Complex 28.

Identification code	e17alj10	
Empirical formula	$C_{16}F_{36}O_4Sn_2$	
Formula weight	1177.54	
Temperature	150.00(10) K	
Wavelength	0.71073 Å	
Crystal system	Monoclinic	
Space group	$P2_1/n$	
Unit cell dimensions	a = 11.3140(2) Å	α= 90°.
	b = 15.4271(3) Å	β= 93.1693(17)°.
	c = 17.2401(3) Å	γ = 90°.
Volume	3004.52(9) $Å^3$	
Z	4	
Density (calculated)	2.603 Mg/m^3	
Absorption coefficient	1.916 mm^{-1}	
F(000)	2208	
Crystal size	0.525 x 0.297 x 0.169 mm^3	
Theta range for data collection	3.327 to 27.507°.	
Index ranges	-14<=h<=14, -20<=k<=18, -22<=l<=22	
Reflections collected	28040	
Independent reflections	6878 [R(int) = 0.0307]	
Completeness to theta = 25.242°	99.8 %	
Absorption correction	Analytical	
Max. and min. transmission	0.967 and 0.919	
Refinement method	Full-matrix least-squares on F^2	
Data / restraints / parameters	6878 / 12 / 606	
Goodness-of-fit on F^2	1.041	
Final R indices [I>2sigma(I)]	R1 = 0.0295, wR2 = 0.0651	
R indices (all data)	R1 = 0.0374, wR2 = 0.0693	
Extinction coefficient	n/a	
Largest diff. peak and hole	2.543 and -0.441 $e.Å^{-3}$	

Table 7.18 – Crystal data and structure refinement for Complex 30.

Identification code	s18alj31	
Empirical formula	$C_{20}H_{44}O_8Sn_2$	
Formula weight	649.93	
Temperature	149.9(3) K	
Wavelength	1.54184 Å	
Crystal system	Triclinic	
Space group	P-1	
Unit cell dimensions	a = 7.0708(3) Å	α= 91.512(4)°.
	b = 9.8872(4) Å	β= 104.194(5)°.
	c = 10.2383(6) Å	γ = 102.918(4)°.
Volume	673.85(6) $Å^3$	
Z	1	
Density (calculated)	1.602 Mg/m^3	
Absorption coefficient	15.057 mm^{-1}	
F(000)	328	
Crystal size	0.180 x 0.060 x 0.040 mm^3	
Theta range for data collection	4.471 to 72.726°.	
Index ranges	-8<=h<=6, -11<=k<=12, -12<=l<=12	
Reflections collected	6613	
Independent reflections	2661 [R(int) = 0.0648]	
Completeness to theta = 67.684°	100.0 %	
Absorption correction	Semi-empirical from equivalents	
Max. and min. transmission	1.00000 and 0.21685	
Refinement method	Full-matrix least-squares on F^2	
Data / restraints / parameters	2661 / 0 / 142	
Goodness-of-fit on F^2	1.059	
Final R indices [I>2sigma(I)]	R1 = 0.0329, wR2 = 0.0829	
R indices (all data)	R1 = 0.0344, wR2 = 0.0846	
Extinction coefficient	n/a	
Largest diff. peak and hole	1.334 and -1.221 $e.Å^{-3}$	

Table 7.19 – Crystal data and structure refinement for Complex 31.

Identification code	e15alj10
Empirical formula	$C_{13}H_{29}N_3Si_2Sn$
Formula weight	402.26
Temperature/K	150.00(10)
Crystal system	monoclinic
Space group	P21/c
a/Å	11.8512(4)
b/Å	10.4036(3)
c/Å	15.6557(5)
α/°	90
β/°	96.431(3)
γ/°	90
Volume/Å3	1918.13(11)
Z	4
ρcalcg/cm3	1.393
μ/mm 1	1.451
F(000)	824.0
Crystal size/mm3	0.403 × 0.37 × 0.293
Radiation	MoKα (λ = 0.71073)
2Θ range for data collection/°	6.54 to 54.958
Index ranges	-15 ≤ h ≤ 9, -12 ≤ k ≤ 13, -19 ≤ l ≤ 20
Reflections collected	15655
Independent reflections	4329 [Rint = 0.0354, Rsigma = 0.0390]
Data/restraints/parameters	4329/0/180
Goodness-of-fit on F2	1.068
Final R indexes [I>=2σ (I)]	R1 = 0.0295, wR2 = 0.0561
Final R indexes [all data]	R1 = 0.0372, wR2 = 0.0596
Largest diff. peak/hole	0.42/-0.35 e Å-3

Table 7.20 – Crystal data and structure refinement for Complex 32

Identification code	e15alj08
Empirical formula	$C_{14}H_{22}N_4Sn$
Formula weight	365.04
Temperature/K	150.00(10)
Crystal system	monoclinic
Space group	P21/c
a/Å	9.3277(3)
b/Å	11.3766(4)
c/Å	14.9148(6)
α/°	90
β/°	98.662(4)
γ/°	90
Volume/Å3	1564.67(10)
Z	4
ρcalcg/cm3	1.550
μ/mm 1	1.627
F(000)	736.0
Crystal size/mm3	0.516 × 0.378 × 0.266
Radiation	MoKα (λ = 0.71073)
2Θ range for data collection/°	6.586 to 54.958
Index ranges	-11 ≤ h ≤ 12, -14 ≤ k ≤ 14, -19 ≤ l ≤ 19
Reflections collected	13218
Independent reflections	3586 [Rint = 0.0361, Rsigma = 0.0382]
Data/restraints/parameters	3586/0/176
Goodness-of-fit on F2	1.061
Final R indexes [I>=2σ (I)]	R1 = 0.0291, wR2 = 0.0563
Final R indexes [all data]	R1 = 0.0381, wR2 = 0.0607
Largest diff. peak/hole	0.33/-0.51 e Å-3

Table 7.21 – Crystal data and structure refinement for Complex 33.

Identification code	s16alj21	
Empirical formula	$C_{12}H_{14}N_4Sn$	
Formula weight	332.96	
Temperature	150(2) K	
Wavelength	1.54184 Å	
Crystal system	Monoclinic	
Space group	$P2_1/n$	
Unit cell dimensions	a = 13.7265(4) Å	α= 90°.
	b = 5.93000(10) Å	β= 104.195(3)°.
	c = 16.1287(4) Å	γ = 90°.
Volume	1272.76(6) $Å^3$	
Z	4	
Density (calculated)	1.738 Mg/m^3	
Absorption coefficient	15.833 mm^{-1}	
F(000)	656	
Crystal size	0.372 x 0.040 x 0.028 mm^3	
Theta range for data collection	3.797 to 72.307°.	
Index ranges	-16<=h<=16, -7<=k<=4, -19<=l<=19	
Reflections collected	13015	
Independent reflections	2487 [R(int) = 0.0405]	
Completeness to theta = 67.684°	100.0 %	
Absorption correction	Semi-empirical from equivalents	
Max. and min. transmission	1.00000 and 0.54331	
Refinement method	Full-matrix least-squares on F^2	
Data / restraints / parameters	2487 / 146 / 230	
Goodness-of-fit on F^2	1.128	
Final R indices [I>2sigma(I)]	R1 = 0.0260, wR2 = 0.0631	
R indices (all data)	R1 = 0.0291, wR2 = 0.0646	
Extinction coefficient	n/a	
Largest diff. peak and hole	1.008 and -0.401 $e.Å^{-3}$	

Table 7.22 – Crystal data and structure refinement for Complex 34.

Identification code	s17alj26	
Empirical formula	$C_{14}H_{18}N_4Sn$	
Formula weight	361.01	
Temperature	150.00(10) K	
Wavelength	1.54184 Å	
Crystal system	Monoclinic	
Space group	$P2_1$	
Unit cell dimensions	a = 8.5561(3) Å	α= 90°.
	b = 8.8998(3) Å	β= 93.866(3)°.
	c = 10.0193(3) Å	γ = 90°.
Volume	761.21(4) $Å^3$	
Z	2	
Density (calculated)	1.575 Mg/m^3	
Absorption coefficient	13.285 mm^{-1}	
F(000)	360	
Crystal size	0.320 x 0.150 x 0.030 mm^3	
Theta range for data collection	4.423 to 73.010°.	
Index ranges	-10<=h<=10, -10<=k<=6, -12<=l<=11	
Reflections collected	5956	
Independent reflections	2288 [R(int) = 0.0279]	
Completeness to theta = 67.684°	100.0 %	
Absorption correction	Gaussian	
Max. and min. transmission	1.000 and 0.336	
Refinement method	Full-matrix least-squares on F^2	
Data / restraints / parameters	2288 / 1 / 174	
Goodness-of-fit on F^2	1.077	
Final R indices [I>2sigma(I)]	R1 = 0.0336, wR2 = 0.0894	
R indices (all data)	R1 = 0.0338, wR2 = 0.0896	
Absolute structure parameter	0.001(14)	
Extinction coefficient	n/a	
Largest diff. peak and hole	1.203 and -0.788 e.$Å^{-3}$	

Table 7.23 – Crystal data and structure refinement for Complex 35.

Identification code	s16alj19	
Empirical formula	$C_{18}H_{26}N_4Sn$	
Formula weight	417.12	
Temperature	150.00(10) K	
Wavelength	1.54184 Å	
Crystal system	Monoclinic	
Space group	$P2_1/n$	
Unit cell dimensions	a = 12.1057(3) Å	α= 90°.
	b = 9.7711(2) Å	β= 95.487(2)°.
	c = 16.0995(4) Å	γ = 90°.
Volume	1895.62(8) $Å^3$	
Z	4	
Density (calculated)	1.462 Mg/m^3	
Absorption coefficient	10.746 mm^{-1}	
F(000)	848	
Crystal size	0.389 x 0.251 x 0.037 mm^3	
Theta range for data collection	4.375 to 73.438°.	
Index ranges	-15<=h<=14, -7<=k<=11, -19<=l<=18	
Reflections collected	12882	
Independent reflections	3772 [R(int) = 0.0598]	
Completeness to theta = 67.684°	100.0 %	
Absorption correction	Semi-empirical from equivalents	
Max. and min. transmission	1.00000 and 0.17713	
Refinement method	Full-matrix least-squares on F^2	
Data / restraints / parameters	3772 / 71 / 340	
Goodness-of-fit on F^2	1.090	
Final R indices [I>2sigma(I)]	R1 = 0.0495, wR2 = 0.1407	
R indices (all data)	R1 = 0.0536, wR2 = 0.1453	
Extinction coefficient	n/a	
Largest diff. peak and hole	1.728 and -0.965 $e.Å^{-3}$	

Table 7.24 – Crystal data and structure refinement for Complex 38.

Identification code	s16alj16
Empirical formula	$C_{34}H_{42}N_4Sn$
Formula weight	625.40
Temperature/K	150.00(10)
Crystal system	monoclinic
Space group	P21/n
a/Å	15.0740(1)
b/Å	11.8067 (1)
c/Å	18.2296(2)
α/°	90
β/°	106.6660(10)
γ/°	90
Volume/Å3	3108.11(5)
Z	4
ρcalcg/cm3	1.337
μ/mm 1	6.741
F(000)	1296.0
Crystal size/mm3	0.277 × 0.238 × 0.196
Radiation	CuKα (λ = 1.54184)
2Θ range for data collection/°	6.732 to 145.674
Index ranges	-17 ≤ h ≤ 18, -9 ≤ k ≤ 14, -22 ≤ l ≤ 22
Reflections collected	26377
Independent reflections	6142 [Rint = 0.0393, Rsigma = 0.0233]
Data/restraints/parameters	6142/0/360
Goodness-of-fit on F2	1.062
Final R indexes [I>=2σ (I)]	R1 = 0.0258, wR2 = 0.0697
Final R indexes [all data]	R1 = 0.0265, wR2 = 0.0702
Largest diff. peak/hole	0.73/-0.70 e Å-3

Not all those who wander are lost.